Epitaxial Rhenium, a clean limit superconductor for superconducting Qbits

Kitti Ratter

Communauté
UNIVERSITÉ Grenoble Alpes

THÈSE

Pour obtenir le grade de

DOCTEUR DE LA COMMUNAUTÉ UNIVERSITÉ GRENOBLE ALPES

Spécialité : NANOPHYSIQUE

Arrêté ministériel : 25 mai 2016

Présentée par

Kitti RATTER

Thèse dirigée par **Klaus HASSELBACH**
et codirigée par **Bruno GILLES**

préparée au sein du **Laboratoires Instutut Néel** et **SIMaP**
dans **l'École Doctorale Physique**

Epitaxial Rhenium, un supraconducteur en limite propre pour des Qbits supraconducteurs

Epitaxial Rhenium, a clean limit superconductor for superconducting Qbits

Thèse soutenue publiquement le **20 octobre 2017**,
devant le jury composé de :

Monsieur Grégory ABADIAS
Professeur, Université de Poitiers, Rapporteur et Président
Monsieur Dominique MAILLY
Directeur de Recherche, CNRS C2N-Saclay, Rapporteur
Monsieur Alain MARTY
Ingénieur de Recherche, Institut Nanosciences et Cryogénies CEA - GRENOBLE, Examinateur
Monsieur François LEFLOCH
Ingénieur de Recherche, Institut Nanosciences et Cryogénies CEA - GRENOBLE, Examinateur

Acknowledgement

It is not a secret that this journey was not easy. That this work is finished is not only my achievement. It would not have been possible without the support of my supervisors, colleagues, friends and family. I would like to express my gratitude to them in the following paragraphs.

I would like to start by thanking Dominique Mailly, Grégory Abadias, Alain Marty and François Lefloch for accepting to be part of my jury, and taking interest in my research.

I owe thanks to the Nanosciences Foundation, particularly Alain Fontaine, Marie-Anne Carré and Fériel Kouiten-Sahraoui for funding the project my PhD was part of. I am especially grateful for the one month (July 2017) I could spend in Grenoble to conclude the writing of this manuscript.

My sincere thanks go to my supervisors, Klaus Hasselbach and Bruno Gilles, for proposing a great project. The scope of it, encompassing two fields of research, is what attracted me to it in the first place. Admittedly, this made my work difficult at times, but now I know that it was good that I was constantly challenged, and never quite comfortable. After all, how boring life would be if there was nothing left to learn.

I am also grateful for my supervisors' kindness, guidance, their patient discussions with me and the encouragement they provided over the years. I consider myself lucky for having had supervisors who were generous with their time, and were available when I asked them to discuss. Above all, I am incredibly thankful that they did not give up on me during my long absences in the past year.

I owe thanks to Olivier Buisson and his group. A large part of my work was done with his group, and although I was formally not part of it, I felt like I belonged. I had several interesting discussions with Olivier, and he kindly advised me and guided me during my time at Institut Néel.

I am grateful to Cécile Naud for introducing me to cryogenics and lithography fabrication. It is thanks to her dedication that we succeeded in fabricating rhenium SQUIDs.

I would like to thank the whole NanoFab team for the training they gave me, and for

their help and advice on the fabrication of rhenium.

I thank Guillaume Beutier and Marc Verdier for introducing me to synchrotron experiments. I count our time in Diamond Light Source among the most exciting experiences during my PhD.

I would like to thank Stéphane Coindeau, Frédéric Charlot, Florence Robaut and Sabine Lay for contributing to my work with measurements, and for the help they gave me in the analysis of the data. I thank Pierre Rodière for his measurement on one of my samples, and for his input on my defence presentation. I thank Virginie Simonet for taking me on my first tour of Institut Néel, and introducing me to Klaus.

During my time in Grenoble I made many friends.

Eva and Rosen were not only my office mates, but were my neighbours, and we quickly became good friends. We shared dinners and games, sometimes several times a week. With Eva we learned to sew and perfected our knitting skills together. Eva, we have yet to make our big skirts and wear them on top of a windy hill.

I would like to thank again the hospitality of Andrew, Nat, Sarah and Amy. I spent a week with them before my defence, and had a really excellent time. I hope to visit them again soon.

I thank Markus for helping me out, and for arranging my inscription for the last year of doctoral school.

I had lots of beers and pizza at Brasserie du Carré with Kristijan, Daria, Marek, Hannu, Tilo, Ingo, Andrew and Markus. These were really great times, and I miss our dinners and their company a lot.

I had way too much coffee with Rémy, Javier, Luca, Etienne, Jorge and Farshad during my time at Institut Néel. I really did not need to drink all that coffee; I just enjoyed spending time with them.

I am also grateful to have met and spent time with John, Marian, Dipankar, Gyuri, Márti, Alex, Alexadre, Dibyendu, Ivy, Clément, Farida, Hanno, Benjamin, Hasan, Solène and Maxime.

I owe the greatest gratitude to my parents, Marianna and József Ratter. I only have the abilities which allowed me to pursue a PhD because they provided me with the opportunity to learn. They supported all my endeavours, and allowed me to make my own mistakes, for which I am grateful. Köszönet mindenért!

My parents-in-law Klazien and Dennis W. T. Nilsen were already familiar with the process of getting a PhD. They told me that it was hard for Dennis and for Gøran as well. It gave me a lot of comfort knowing that I was not alone. I also thank them for all of their encouragement and support and for their belief in me.

I thank the support of my brother Patrik and his new family Virág and Janka, and also my brothers-in-law and their families: Bengt, Monica, Derek, Miriam, Melina and Deana.

I spent the last five years being far away from my family, and I have not had the opportunity to see them as often as I wished. I hope I can change that soon.

Above all I would like to thank the support and encouragement of my husband, Gøran Nilsen. I honestly believe that without him I would not have had the strength and the courage to finish. I am incredibly grateful for his patience, his help, his soothing words and hugs through the tough times. Thank you.

"If you can see, look. If you can look, observe."

---

epigraph to Jose Saramago's Blindness

Abstract

The epitaxial growth conditions and superconducting properties of nanostructured devices made of rhenium (superconducting below T=1.7 K) on sapphire were explored. Epitaxial growth of rhenium thin films onto a single crystal α-Al_2O_3 substrate was realised using molecular beam epitaxy. The pressure in the MBE chamber was in the range of 10^{-10} Torr. The cleanness of the substrate was verified using XPS, and the growth of rhenium was monitored using RHEED. The orientations of the two crystals were $(0001)Al_2O_3//(0001)Re$ and $<2\bar{1}\bar{1}0>Al_2O_3//<01\bar{1}0>Re$, which was confirmed using X-ray diffraction. The in-plane misfit between the lattices is -0.43% at room temperature, which allows us to estimate the critical thickness of rhenium to be between 10 nm and 15 nm.

For deposition, rhenium was heated using an electron beam. A deposition rate of 0.1 Å/s was maintained. The temperature of the evaporating rhenium is estimated to reach approximately 3000°C. Substrates were heated during growth using either a Joule-heated W filament located behind the sample, or electron bombardment. Generally deposition temperatures of 800°C and 900°C gave reproducible results.

The effect of deposition temperature was studied on samples that had the same thickness but were deposited at different temperatures. Three thickness groups were selected: 25 nm, 50 nm and 100 nm. Every sample was dominated by the (0001) epitaxial orientation. Orientations $(11\bar{2}0)$, $(10\bar{1}0)$, $(10\bar{1}1)$ were present, but their intensities were small and decreased with increasing deposition temperature. Extensive AFM imaging was used to observe the morphology of the films. The 25 nm thick films were decorated with grains. The diameter of the grains ($\sim$ 50 nm) did not vary significantly on these samples, however, they became more uniform with increasing deposition temperature, and the surface became smoother. On the 50 nm and 100 nm thick films spirals and holes can be observed. The diameter of the spirals on the 50 nm thick film increased from 100 nm to 500 nm when the temperature of the deposition was increased from 800°C to 900°C. On the 100 nm thick sample the diameter of the spirals also increased with higher deposition temperature, but the increase was not as significant. XRD rocking curves measured on all

samples narrowed with increasing deposition temperatures, indicating reduced mosaicity among the (0001) crystallites. High-resolution θ-2θ scans evidenced disorder in the 50 nm thick film, corresponding to strain values in the range of 0.01. Deposition temperature of 1000°C lead to the dewetting of a 50 nm thick sample, and islands with atomically flat surfaces were formed.

The frequently observed spirals are most likely the result of screw dislocations. The origin of the holes that accompany the spirals is a dewetting process that starts when the thickness of the film reaches approximately 10 nm. We quantified the temperature evolution of the film during growth, taking into account emission, reflection and transmission between all surfaces. This thermal model confirmed that the temperature of the film increases as the rhenium film grows. The dewetting was studied using Mullins' theory of thermal grooving. A surface diffusion coefficient of 4×10^{-12} cm^2/s was obtained, which is consistent with the observed dimensions of the surface topography.

Wires with widths ranging from 100 nm to 3 μm and superconducting quantum interference devices were fabricated from the rhenium films. Transport measurements were conducted using a helium-3 refrigerator. It was found that the lithography process does not affect the superconducting properties of the rhenium. Critical temperatures between 1.43 K and 1.96 K were measured. We could correlate the superconducting transition temperature with the topography and the crystallinity of the films. The mean free path of electrons and the superconducting coherence length were obtained. For two of the films, both the mean free path and the effective coherence length were over 100 nm. These two films were in the clean limit, but the fabricated wires were in the dirty limit.

On one film, SQUIDs of 1 μm diameter with 50 nm and 20 nm wide nanobridges acting as Josephson junctions were fabricated. The SQUIDs were cooled down using a dilution refrigerator. Critical current oscillations were measured. The flux noise values obtained were as low as 2.6×10^{-5} $\Phi_0/\mathrm{Hz}^{1/2}$.

Contents

Introduction

The foundations of today's computers were laid down by Alan Turing in 1936, who developed a model for a programable machine, now known as the Turing machine. The first electronic computers appeared shortly after. With the invention of the transistor in 1947, hardware development took off, and computer power has been growing exponentially since, changing the world at an unprecedented pace and scale [1].

However, it is argued that conventional computers will not be able to keep up with this established trend much longer. Due to the decreasing size of the electronic components, quantum effects are beginning to interfere with their operation. Furthermore, the time required to solve a problem with a conventional algorithm grows exponentially with the number of operations. This puts constraints on the finesse in a simulation [1].

One path proposed is to redefine computation as we know it, and use quantum computers. In a quantum computer, bits are replaced by quantum bits or qubits. Unlike a bit, which can either be '0' or '1', a qubit can have a state which is the superposition of '0' and '1':

$$|\psi\rangle = \alpha\,|0\rangle + \beta\,|1\rangle\,,$$

where $\alpha^2 + \beta^2 = 1$. N bits in both a quantum and in a conventional computer can have a total of 2^N states. The qubits can occupy all these states simultaneously. Algorithms that can exploit the superposition of states already exist. An example of this is Shor's algorithm, which demonstrated that factorisation of large integers can be solved efficiently. It is believed that this problem has no efficient solution on a conventional computer [1, 2].

Bits in a computer are expected to preserve their states for a period of time. This is not different for a quantum computer either. However, the loss of coherence in qubits makes developing a quantum computer challenging.

One of the candidates to realise a qubit is based on Josephson junctions. Josephson junctions consist of two superconductors separated by a thin ($\sim$ 1 nm) insulator barrier.

They are described in more detail in section 3.3.1. The time scales over which a qubit preserves information are called the coherence times. These coherence times are limited by noise, which is ascribed to fluctuating charges in the insulator barrier. A frequently used material for the barrier is aluminium oxide. It is prepared by the subsequent deposition and oxidation of aluminium. The result is an amorphous layer, which is noted with the chemical formula AlO_x. It is suspected that the aluminium is not fully oxidised in this form, and that this is the origin of the two-level fluctuations that lead to decoherence [3].

Consequently, the path to the quantum computer goes via employing new or unconventional materials and exploring the parameter space of deposition and growth conditions, in order to obtain high quality superconductor-insulator-superconductor junctions, which prerequisite for qubits.

The aim of this project was to eliminate disorder by growing epitaxial films. For epitaxial growth, the lattice parameter match is an important criterion. The lattice of rhenium, which is superconducting below 1.7 K, has an excellent match with the lattice of Al_2O_3. Furthermore, crystalline rhenium is very stable, and does not oxidise.

Rhenium has been the subject of a few studies in the recent past. Oh et al. grew rhenium thin films onto Al_2O_3 using DC and RF sputtering. They observed the growth of epitaxial islands with spiral structure [4].

Welander grew rhenium films on niobium surfaces [5]. Niobium was first grown onto an Al_2O_3 substrate, and this growth has been shown to be epitaxial [6]. Rhenium films grown this way were smooth, and fully relaxed by 20 nm thickness.

The molecular beam epitaxy growth of rhenium onto Al_2O_3 substrate was started by B. Delsol in SIMaP [7]. These films were used to fabricate microwave resonators [2, 8], and to study the proximity effect with graphene [9].

Rhenium, indeed, grows epitaxially onto single crystal Al_2O_3. In the next step , crystalline aluminium would be deposited onto the flat surface of epitaxial rhenium, and oxidised. Our aim was that this would result in a crystalline, fully oxidised barrier. However, as is shown throughout this work, it is not so easy to produce a flat rhenium surface. The surfaces of our epitaxial films are decorated with spirals and deep holes. Such a topography is not adequate for the deposition of a second layer. Consequently, we achieved an understanding of the processes driving the growth mechanism, as we successfully identified dewetting as the culprit for the presence of holes.

The epitaxial growth of rhenium thin films onto single crystal Al_2O_3 substrates was realised using molecular beam epitaxy. Following the characterisation of the films, wires and SQUIDs (superconducting quantum interference device) were fabricated using laser and electron lithography. The transport properties of these devices were studied at low

temperatures.

Chapter 1 starts with a short description of the materials used in this work, rhenium and the single crystal Al_2O_3 substrate. Following that, the requirement of ultra-high vacuum in epitaxial growth is explained. Sections 1.3 and 1.4 describes the molecular beam epitaxy setup, and the characterisation techniques that were used to prepare and study the films presented in this work. The final section of this chapter deals with the theoretical background of crystal growth, spiral growth, and thermal grooving. These theories are referred to in chapter 2.

The first section of chapter 2 discusses several aspects of rhenium growth on Al_2O_3 specifically. The preparation procedure of the substrate is described first, then the temperature of the evaporating rhenium is estimated from the observed deposition rate. The critical thickness, above which dislocations are expected to appear, is also given here. The following section studies how the temperature of the sample during growth influences the surface topography and the crystallography of the film. Section 2.3 shows that rhenium undergoes dewetting during growth when approximately 10 nm thickness is reached. Finally, the thermal transfer model is described, which was developed to calculate the temperature of the growing film.

The first section of chapter 3 presents the phenomena of superconductivity, and explains the basic theories that were developed to describe it. In the following section superconducting devices, namely the Josephson junction and the SQUID, are described. The final section of this chapter gives a short description on the two refrigerators that were used to reach temperatures below 1 K, and measure the transport properties of our samples.

In the first two sections of chapter 4 the lithography process and the fabricated circuit designs are presented. Section 4.3 discusses the transport measurements on the wires. The shape and width of the superconducting transition with respect to the topography and crystallography is studied. The final section presents the critical current oscillations of two low-noise SQUIDs.

1

Molecular beam epitaxy

In this chapter, first rhenium and the substrate material are introduced, then the theoretical and experimental basis for molecular beam epitaxy and crystal growth is given. In the second section the motivation for the use of ultra-high vacuum environment is explained. After that, the molecular beam epitaxy setup, and the available characterisation techniques are described. The following section deals with the basic theories of crystal growth, and the roll of misfit strain on dislocation formation. Finally, Burton, Cabrera and Frank's theory on spiral growth, and Mullins' theory on thermal grooving is introduced. These theories will be referred to in chapter 2, where the experimental results are discussed.

1.1 Materials

1.1.1 Rhenium

History and occurrence

The existence of rhenium was predicted by Mendeleev. It is the last discovered element that has a stable isotope, and was first detected in platinum ore in 1925 by Walter Noddack, Ida Tacke, and Otto Berg in Germany [10]. It was named after the river Rhine.

In 1928 Noddack et al. were able to extract 1 g of pure rhenium by processing 660 kg of molybdenite (MoS_2) [11].

Rhenium is among the rarest elements in the Earth's crust. It has not yet been found in pure form, and the only known rhenium mineral, ReS_2 called rheniite, was described as recently as 1994. It was discovered condensing on the Kudriavy volcano, on the Iturup island, disputed between Japan and Russia [12]. The volcano discharges 20-60 kg rhenium per year mostly in the form of rhenium disulfide.

The primary commercial source of rhenium is the mineral molybdenite (MoS_2) which contains about 3% Re. Chile has the world's largest rhenium reserves and was the leading producer as of 2005. The total world production of rhenium is between 40 and 50 tons/year, and the main producers are in Chile, the United States, Peru, and Poland.

Physical and chemical properties

Rhenium is a silvery-white heavy metal from the third row of the transition metal block, with atomic number 75. Its melting point (3186 °C) and boiling point (5630 °C) are among the highest among the elements.

It crystallises in the hexagonal close-packed structure, shown in figure 1.1, with lattice parameters a = 0.2761 nm and c = 0.4456 nm [13].

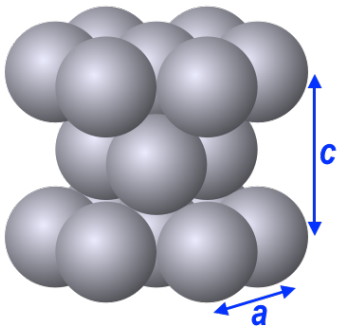

Figure 1.1: Hexagonal closed-pack structure.

The density of rhenium is also among the highest, with 21.02 g/cm^3 measured at room temperature.

Rhenium has one stable isotope, ^{185}Re, which is in minority. Naturally occurring rhenium is composed of 37.4% ^{185}Re, and 62.6% ^{187}Re. ^{187}Re is unstable but its half life is very long, about 10^{10} years [14].

Electron configuration of rhenium is [Xe] $4f^{14}$ $5d^5$ $6s^2$. Its oxidation state is known to vary between -3 and +7 skipping over -2, the most common being +7, +6, +4, and +2. There are several rhenium oxides, the most common is Re_2O_7, is colourless and volatile. Other oxides include ReO_3, Re_2O_5, ReO_2, and Re_2O_3 [15].

Pure rhenium is a superconductor, and its first recorded transition temperature was 2.42 K [16]. Rhenium alloys show higher transition temperatures: rhenium-molybdenum is superconductive under 10 K [17], and tungsten-rhenium at around 4-8 K [18].

Application

As a refractory metal, rhenium shows extraordinary resistance against heat and wear. Most of its applications are centred around this property.

Nickel based alloys that contain up to 6% of rhenium are used in jet engine parts or in industrial gas turbine engines. 70% of the worldwide rhenium production is used in this field. Tungsten-rhenium alloys are used as X-ray sources and thermocouples for temperatures up to 2200°C.

The low vapour pressure of rhenium makes it suitable to be used as filaments in mass spectrometers, gauges and photoflash lamps.

Alloyed with platinum, it is used as a catalysts in the production of lead-free, high-octane gasoline.

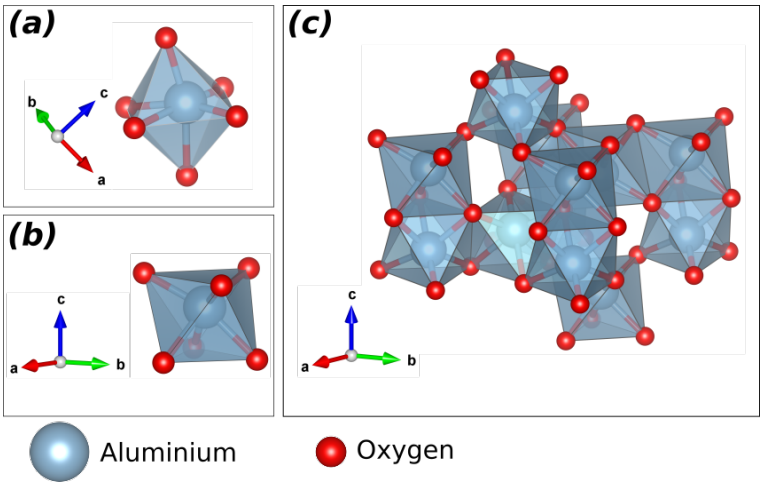

Figure 1.2: Lattice of Al_2O_3. (a) and (b) Six oxygen ions form a slightly distorted octahedron around an aluminium ion. (c) Stacking of the octahedra. The size of the atoms on the figure corresponds to their atomic radii [19].

1.1.2 Al_2O_3 substrate

Rhenium thin films were deposited onto single crystal α-Al_2O_3 substrates. Several polymorphs of Al_2O_3 exists, α-Al_2O_3 is the most stable, and is the only phase that occurs naturally. α-Al_2O_3 is called corundum. Corundum is a rock- forming mineral. It is transparent, and in its chemically pure form has a white hue. In nature, corundum is rarely pure, and can appear in many different colours depending on the impurities. Coloured corundum is frequently used as a gemstone, best known varieties of it are ruby and sapphire.

Synthetic Al_2O_3 crystals are prepared with the Czochralski growth process. A precisely oriented seed crystal is introduced into the molten Al_2O_3, and slowly pulled. The melt crystallises onto the seed matching its orientation.

Al_2O_3 crystallises in the trigonal crystal system, in the R$\bar{3}$c space group. Its lattice parameters are $a = 0.476$ nm and $c = 12.993$ nm [20]. In the lattice, six oxygen ions form a slightly distorted octahedron around an aluminium ion. Two octahedra are shown in two different orientations in figure 1.2(a) and 1.2(b). In figure 1.2(c) the stacking of the octahedra is shown, as they form the lattice.

Along the c-axis the structure is an alternation of one oxygen and two aluminium layers, shown in figure 1.3(a). The two neighbouring Al layers are separated by approx-

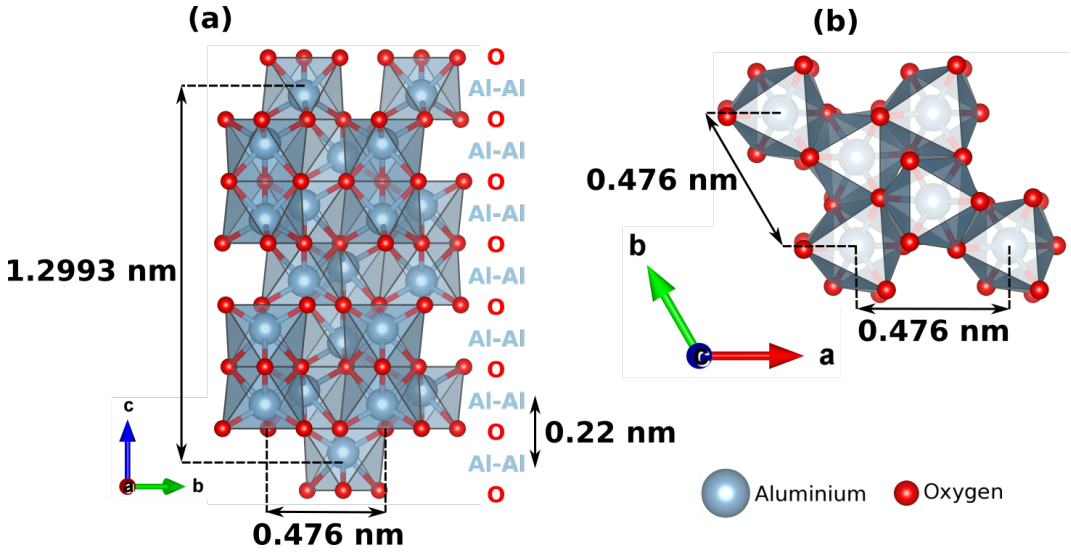

Figure 1.3: Lattice of Al_2O_3. (a) Alteration of one oxygen and two aluminium layers along the c axis. (b) View of the c plane. The size of the atoms on the figure corresponds to their atomic radii [19].

imately 0.06 nm and shifted laterally. The separation between two layers of oxygen is the sixth of the c lattice parameter, 0.22 nm. The double Al layers also have an average spacing of 0.22 nm.

In figure 1.3(b) the view of the c plane is shown, terminated by oxygen ions, that form triangles over the Al ions.

All our substrates were c-plane, they were cut perpendicular to the crystallographic c-axis, along the (001) plane.

1.2 The basics of molecular beam epitaxy

Epitaxy is a Greek composite word, epi meaning 'above', and taxis meaning 'an ordered manner'. It roughly translates 'arranging upon'. Epitaxy occurs when a metastable material nucleates onto a crystalline substrate in registry with its crystalline order, as shown on figure 1.4 [21]. This process allows the preparation of single crystal thin films.

Depending on the phase of the metastable material the epitaxy can be solid phase, liquid phase or vapour phase epitaxy. In chemical vapour deposition volatile precursors decompose onto or react with the substate to produce the layer. In other vapour epitaxy techniques the source is sputtered or ablated. These techniques allow fast growth of thin films therefore they are reliably used in the semiconductor industry and in research.

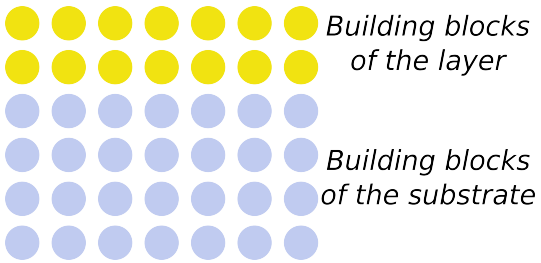

Figure 1.4: Epitaxy refers to the growth of a crystalline layer onto a crystalline substrate following its lattice.

Molecular beam epitaxy utilises beams of atoms or molecules in an ultra-high vacuum environment (10^{-10} Torr) that are incident upon a heated crystal whose surface is atomically flat and clean [21]. Depositions rates are much lower than in the above mentioned techniques, around 1 monolayer/minute, allowing the growth of single crystals and sub-monolayer composition control. The ultra-high vacuum conditions makes it possible to incorporate characterisation techniques, such as electron diffraction, X-ray

photoemission spectroscopy, and sample preparation techniques such as ion etching. All these make MBE the ideal research tool for developing new materials.

The development of MBE was driven by the decreasing dimensions of semiconductor devices [22], and by the interest in heterostructures made out of semiconductors with different energy gaps [23]. Several unsuccessful attempts were made to grow such structures [24, 25]. Breakthrough came from the field of surface sciences in 1968, when Arthur observed that growth rate is not only the function of vapour pressure, but is strongly influenced by vapour-surface interactions [26, 27]. His discovery paved the way for the stoichiometric growth of compounds where the components have very different vapour pressures. 1968 marks the birth of MBE.

The advance of the supporting techniques was essential to the rapid evolution of MBE. Quadruple mass spectrometry was used in the study of surface-vapour interactions by Arthur [26], and it remains a key component of MBE chambers to ensure a clean UHV environment. In 1969 A. Y. Cho was the first to use reflection high energy electron diffraction setup (RHEED) in the MBE chamber to investigate the growth process *in situ*. He showed that MBE is capable to produce atomically flat, ordered layers [28, 29]. During these years compact electron guns became available, which made it possible to routinely combine MBE with RHEED, allowing the study of wide range of materials. From then on MBE was an essential part of several important studies and discoveries:

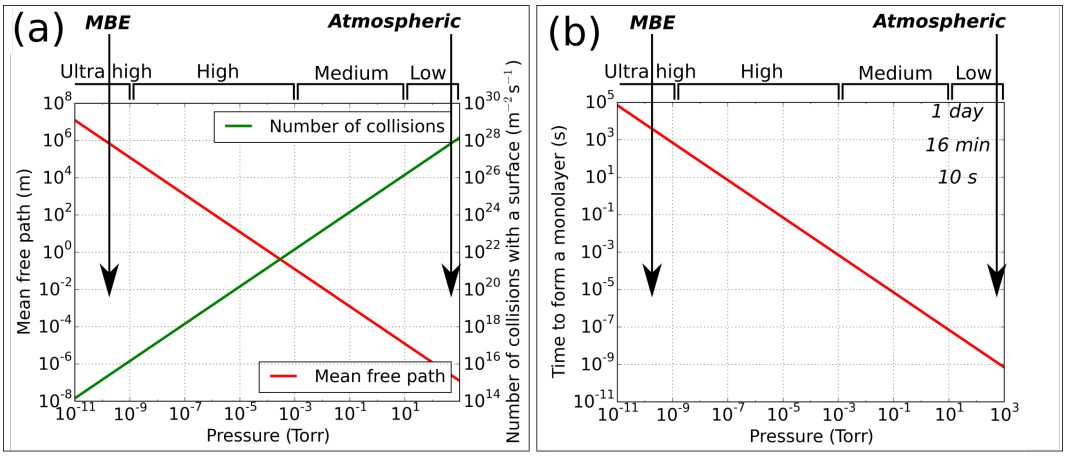

Figure 1.5: (a) Mean free path and number of collisions as the function of pressure. (b) Time required for the formation of a monolayer as the functions of pressure. In ultra-high vacuum, the mean free path is so long that collisions can be neglected, and it takes several hours for a monolayer to form from the residual molecules.

fractional Hall effect [30], band-gap engineering [31], quantum cascade laser [32], zero-dimensional structures [33], quantum dot lasers [34], giant magnetoresistance [35, 36]. In the following sections the operational principles of MBE and the supporting techniques are detailed, starting with the importance of ultra-high vacuum conditions.

MBE operates in ultra-high vacuum. To reach 10^{-10} Torr from atmospheric pressure, the chamber has to be evacuated by running high performance pumps for several days. After, the chamber walls, and all the instruments and surfaces are heated to aid the evaporation of molecules that were absorbed from the air. At the end of this procedure, in the ultra-high vacuum regime, the residual gas mainly consists of hydrogen molecules and methane. To maintain the low pressure, continuous pumping is necessary using ion pumps.

The kinetic gas theory demonstrates the necessity of ultra-high vacuum. The residual molecules are moving rapidly around the chamber, occasionally colliding with the wall, instruments, samples, or with each other. From the kinetic gas theory, the mean free path of the particles (λ) and the rate of collisions with a surface (N_{coll}) at pressure P can be calculated:

$$\lambda = \frac{k_B T}{\sqrt{2}\pi d^2 P}, \qquad N_{coll} = \frac{P}{\sqrt{2\pi k_b T m}},$$

where k_B is the Boltzmann constant, T is the temperature inside the chamber in kelvin, d is the diameter, and m is the mass of a molecule [37].

In figure 1.5(a) the mean free path and the rate of collisions are shown as the function of pressure. In the calculation a hydrogen molecule was considered. Values are in the same range for the residual molecules that are commonly found in ultra-high vacuum. At atmospheric pressure the mean free path is in the range of nanometers, but at pressures where MBE operates it is around 100 km. This means that in a chamber with dimensions of 1-2 meter the particles can move without collisions. The beam of molecules/atoms can reach the substrate without reacting with other species on the way. Another advantage is that ultra-high vacuum allows the use of electron beam at high or low energy, the beam will not be scattered even at long distances ($\sim$1 meter).

To calculate the time it takes for a monolayer to form from the residual molecules, the following is considered: on a surface of area of 1 m^2 there are approximately 10^{19} atoms. Using the collision rate and assuming the colliding molecule sticks to the surface, one can calculate how long it takes for a monolayer to form from the residual particles: $\tau[\mathrm{s}] = \frac{10^{19}}{N_{coll}}$. This time is plotted as the function of pressure in figure 1.5(b). In ultra-high vacuum τ can be measured in hours. In MBE deposition rates are low, therefore, deposition of a

sample can take hours. Keeping the rate of collisions low by keeping the pressure in the ultra-high vacuum range ensures the purity of the sample.

1.3 MBE instrumentation

The MBE setup used for this work is shown in figure 1.6. It consists of four interconnected chambers.

The introduction chamber, noted by label 1 in figure 1.6, is the only chamber that is brought to atmospheric pressure regularly, as it is used for the introduction of the substrates. It is pumped to 10^{-7} Torr before it is opened towards the other chambers with higher vacuum levels. Otherwise it is kept at static vacuum. Before opening it towards the atmosphere, it is flooded with nitrogen gas.

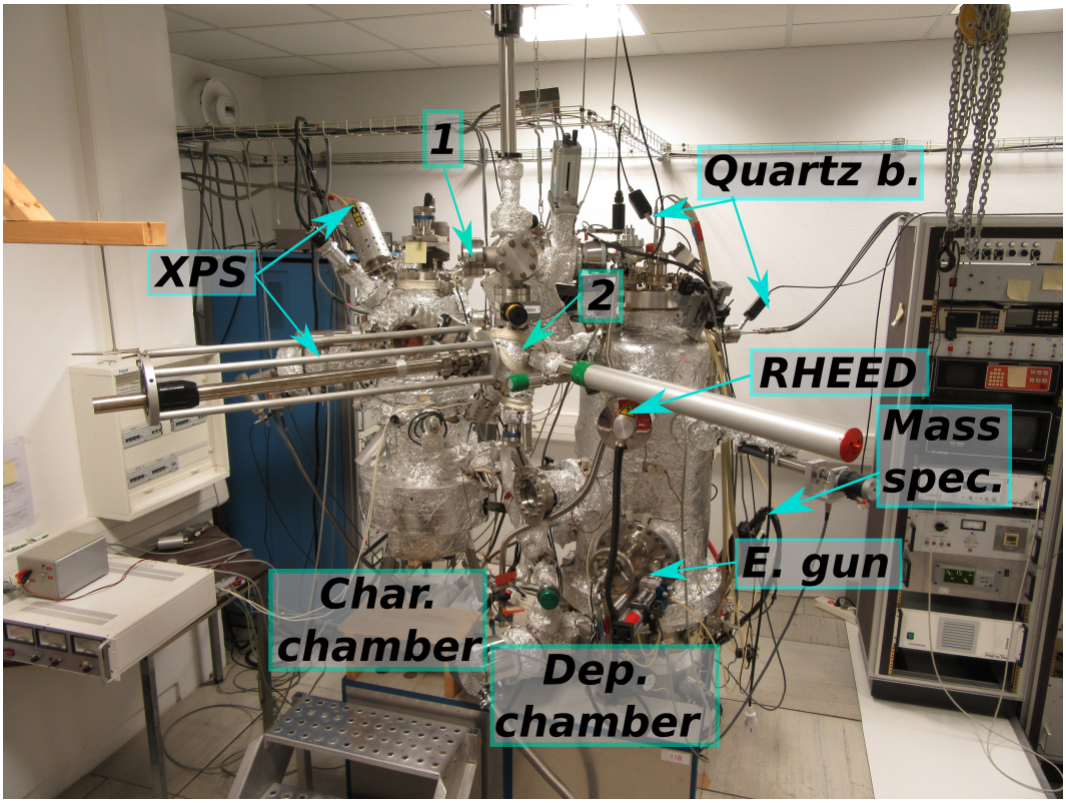

Figure 1.6: MBE setup in SIMaP. It consists of four chambers: 1 - introduction chamber, 2 - intermediate chamber, Dep. chamber - deposition chamber, Char. chamber - characterisation chamber.

The intermediate chamber, noted by label 2 in figure 1.6, connects the other three chambers together.

1.3.1 Deposition chamber

The deposition chamber, labeled as 'Dep. chamber' in figure 1.6, is where the thin films are deposited. It is equipped with a Leybold quadrupole mass spectrometer that is used to monitor the composition of the residual gas inside the chamber.

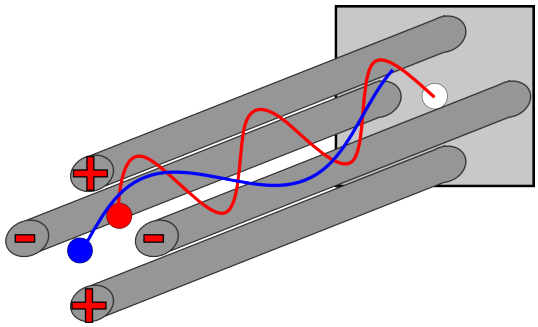

Figure 1.7: Schematics of the quadrupole mass spectrometer: four electrodes placed parallel, with voltage applied between them. Depending on the voltage, only the particles with the set mass-to-charge ratio will reach the detector.

The schematics of the spectrometer is shown in figure 1.7. A quadrupole mass spectrometer has three parts. The first part is an ioniser, that ionises the molecules passing through it by electron bombardment. The second part is a mass-to-charge ratio filter, and the third part is the detector. The mass-to-charge ratio filter consists of two pairs of cylindrical electrodes in quadrupolar arrangement, as shown in figure 1.7. A potential of $\pm(U + V\sin(\omega t))$ is applied between them, where U is a DC voltage and Vsin(ωt) is an AC voltage. The trajectory of ions travelling between the the four rods will be affected by the field, so that only ions with the set mass-to-charge ratio will reach the detector (red path in figure 1.7). The others will be thrown off course (blue path in figure 1.7). A mass-to-charge ratio spectrum is obtained by changing the voltage applied to the electrodes. From the spectrum, the composition of the residual gas can be determined.

The deposition chamber is also equipped with two Riber evaporation systems which consist of an electron gun, bending magnet, metal charges, and controlling electronics. The schematics of the evaporation system is shown in figure 1.8. The metal charge is heated with a 10 kV electron beam extracted from a tungsten filament. The beam scans the charge to ensure uniform heating. To adjust the heating power, and thus the rate

of deposition, the current of the beam can be adjusted. The metal charge used in the present studies was 99.95% rhenium supplied by Neyco. To achieve a deposition rate of 0.1 Å/s - 0.2 Å/s of rhenium, the beam current was set to approximately 200 mA.

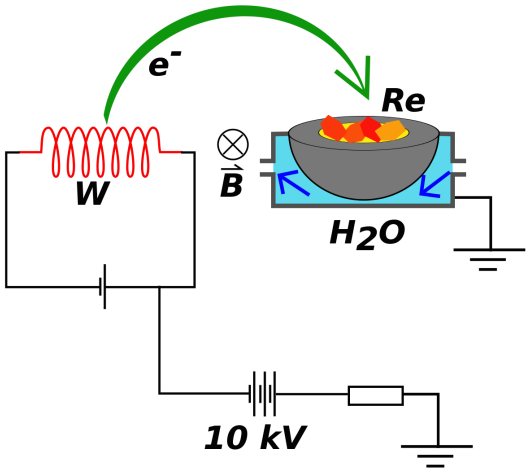

Figure 1.8: Schematics of the evaporation system: electrically heated tungsten wire biased by 10 kV ejects electrons that are directed onto a metal charge using a magnetic field.

The substrate is placed horizontally on a manipulator above the charge. At its position the flux of atoms arriving at the surface is homogeneous. The deposition can be turned on and off with the use of a shutter located below the substrate. The manipulator is equipped with a furnace that consists of a tungsten filament, shown in figure 1.9. The substrate can be heated in two ways using this furnace: either by thermal radiation, or by electron bombardment. Infrared radiation is emitted by the tungsten filament when it is heated by a current running through it (up to approximately 10 A). Increasing the current will increase the temperature of the substrate. We can reach around 900°C this way. When applying a voltage (400 V - 800 V) between the sample and the filament, electrons are emitted. The temperature of the substrate is adjusted by the emission current (up to approximately 100 mA). We can reach around 1000°C by electron bombardment.

The manipulator head is shown in figure 1.9. The temperature of the substrate is measured by a thermocouple that is located in the middle of the manipulator head, and is pressed against the back side of the substrate. There is an uncertainty in the contact between the thermocouple and the substrate, thus the value measured this way is an approximate of the real surface temperature. Also, the thermal and optical properties of the sample can change during growth, which affects the surface temperature. This change cannot be detected with the thermocouple.

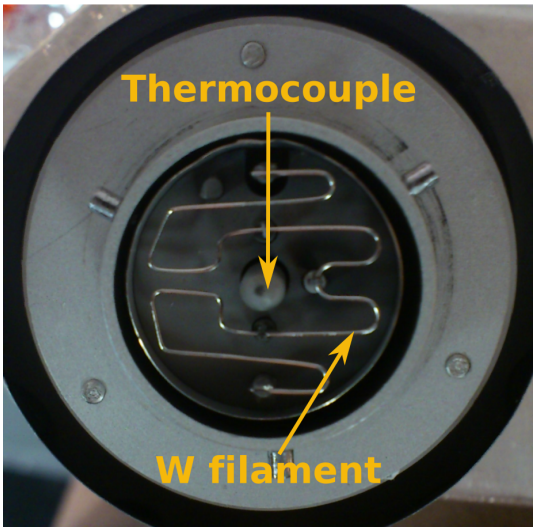

Figure 1.9: Furnace and thermocouple in the manipulator: the substrate is placed on top of the tungsten filament, the thermocouple is pressed against its back side.

Another way of measuring the temperature in an ultra-high vacuum environment, is to use a pyrometer. The pyrometer is located outside of the chamber, looking at the sample through a viewport. It measures the thermal radiation emitted by the material. For this method to give a reliable result, the viewport has to be made out of a material whose transmission as the function of wavelength is well known (usually Al_2O_3). Also, the sample surface has to be aligned parallel with the window of the pyrometer. In the deposition chamber we cannot fulfil these requirements due to geometric constraints. The only way to measure the temperature of the sample during growth is by the thermocouple.

Using molecular beam epitaxy, films with thicknesses ranging from a few Å to 100 nm are routinely deposited. To be able to prepare samples in this wide range of thickness, precise measurement of the deposition rate is necessary.

A microbalance made out of a quartz single crystal is the most commonly used tool to monitor the deposited thickness. The quartz microbalance consists of a quartz crystal, cut along a specific crystallographic orientation, with an alternating voltage applied to it. Due to the piezoelectric effect this voltage generates a standing wave in the crystal at a well defined frequency (resonance frequency) in the MHz range. When the mass of the crystal increases, the resonance frequency decreases. From the frequency shift the deposited mass and the thickness can be calculated. There are two Leybold quartz balances in our deposition chamber, located close to the sample, shown in figure 1.6.

The lifetime of a quartz microbalance is limited due to the deposit building up on it. To lengthen its lifetime, we are able to turn the measurement on and off using a shutter placed in front of the quartz crystal.

1.3.2 Characterisation chamber

There is a second ultra-high vacuum chamber connected to the deposition chamber. This is the characterisation chamber, labeled as 'Char. chamber' in figure 1.6. It is equipped with instruments that allow the investigation and preparation of the sample before or after the deposition, without exposing it to air. Instruments available in the chamber are the following: X-ray photoelectron spectroscopy (XPS), argon ion gun, low energy electron diffraction, a furnace that can reach over 2000°C, and a pyrometer to measure the temperature. In this work, only the XPS was used, only that technique is discussed in detail in the following section.

1.4 Thin films characterisation techniques

1.4.1 In situ characterisation techniques

Some investigative techniques are available without having to remove the sample from the vacuum chamber. XPS is used to check the chemical composition of the surface of the substrate or the deposited film before or after deposition. RHEED can be used before, after, or during deposition to monitor the crystallographic properties of the film.

X-ray photoelectron spectroscopy

XPS is used to study the chemical composition of the surface. The principle of the technique, shown in in figure 1.10(a), is the following: the sample is irradiated with a known energy X-ray beam, and the electrons (mostly photoelectrons) that escape the material are sorted by their kinetic energies, and counted.

The setup consists of an X-ray tube, shown by the upper arrow in figure 1.6, and a detector, shown by the lower arrow. The anode material in the X-ray tube is magnesium, and the radiation corresponding to its Kα line with an energy of 1253.6 eV is used. The detector has two parts: an energy analyser with an energy window that is scanned over a given voltage range, and an electron multiplier for amplifying the current of the electrons.

The binding energy of the electrons are the characteristics of an atom or a molecule. From the kinetic energy of an emitted electron its binding energy can be calculated as follows:

$$h\nu = E_B + \Phi + E_k \quad \rightarrow \quad E_B + \Phi = h\nu - E_k, \tag{1.1}$$

where h is the Planck constant, ν is the wavelength of the exciting X-ray beam, E_B is the binding energy of an electron, Φ is the work function that depends on the material and the instrument, and E_k is the kinetic energy of the electron. Precise value of Φ is not known but it is small [38].

A typical XPS spectra is shown on figure 1.11. Most of the peaks indeed correspond to photoelectrons that were excited from the core shells of the atoms. There is, however, an other process, called Auger effect, which can result in peaks: a photoelectron leaves a vacancy on an inner shell that is filled by an electron from a higher shell. Then a second electron, an Auger electron, is emitted, carrying off the excess energy, leaving behind a doubly-charged ion. Figure 1.10(b) illustrates the process. The kinetic energy of the second electron equals to the energy difference between the 1+ and 2+ ionisation status, and does not depend on the energy of the exciting X-ray beam. Auger electrons emitted by oxygen atoms are noted by O(KVV) in figure 1.11. The KVV notation indicates that

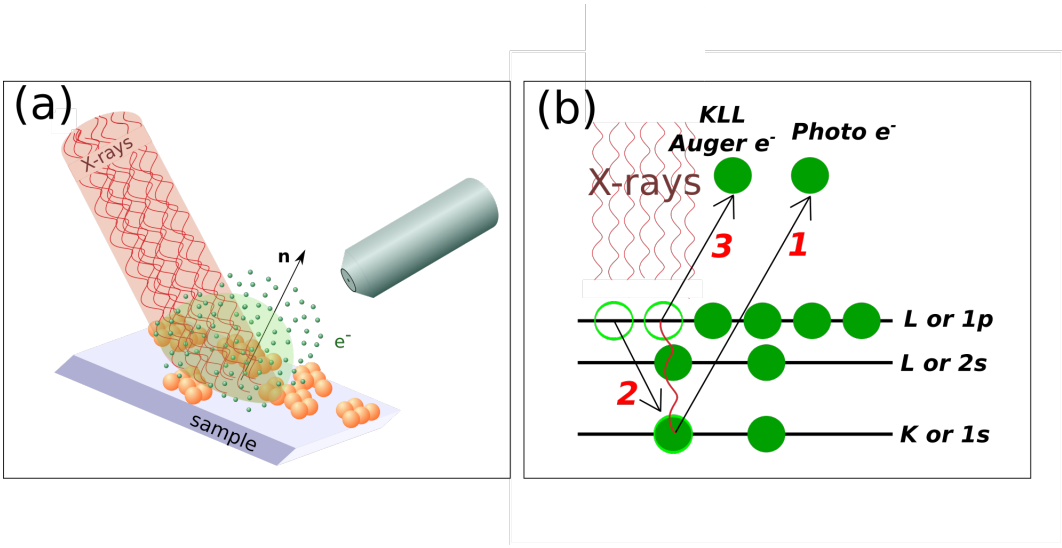

Figure 1.10: (a) Schematics of the XPS measurement: the sample is irradiated with a monochromatic X-ray beam. As a result electrons escape from the surface region, their energy is measured by the detector. (b) Auger effect: a vacancy left by a photoelectron is filled up by an other electron from a higher energy level, the excess energy is carried away by a second emitted electron, called Auger electron.

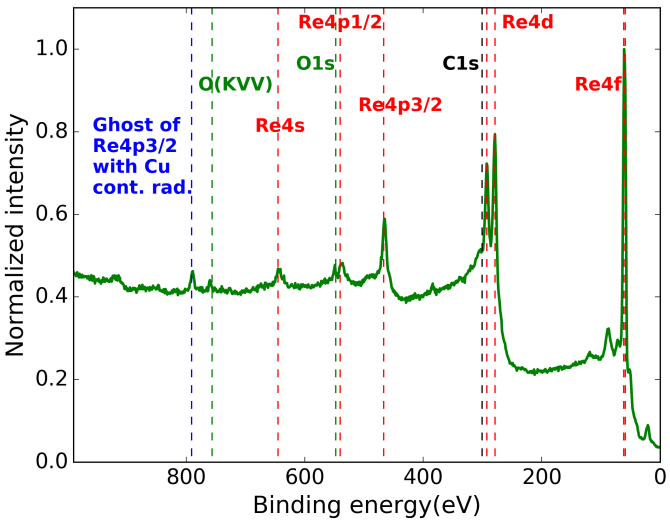

Figure 1.11: A typical XPS spectra recorded on a rhenium thin film.

the first electron, the photoelectron, originated from the K level, its place was taken by an electron from the valence level, and the Auger electron was also from the valence level [38].

A ghost peak is also noted in figure 1.11 in blue. This is the result of copper contamination in the anode. The energy of the X-ray photons emitted by the copper contamination are different, therefore, the kinetic energy of the electrons they excite from the same shells are different too. When calculating the binding energy, only the Kα line of magnesium is considered in equation 1.1. This gives small intensity peaks in the spectrum at a wrong binding energy [38].

Even though the penetrations depth of the X-rays are relatively large (1-10 μm), the mean free path of electrons at these energies is restricted to a few nanometers due to strong electron-electron scattering. Thus we only get information from the top few atomic layers. A significant number of electrons undergo inelastic scattering processes, losing some of their kinetic energy, and thus add to the background. This is the reason for the step-like structure of the graph, that can most clearly be observed between the peaks Re4d and Re4f.

From the intensity of the XPS peaks, the surface monolayer coverage can be calculated. We used this method in other projects, and the detailed derivation is given in appendix B.

Reflection high energy electron diffraction

The deposition chamber is equipped with a Staib RHEED setup. The technique has been widely used to monitor the surface structure of the films during growth since the '70s. The setup consists of an electron gun, shown in figure 1.6 by an arrow labeled as RHEED, and a phosphor screen on the opposite side. The electron gun produces an electron beam with an energy of 20 keV, that is directed onto the surface of the growing crystal at a grazing angle (1° - 3°). Geometry of the RHEED setup is shown in figure 1.12. From the diffraction pattern the physical state of the surface can be determined: in-plane lattice parameter, orientation, symmetry of reconstruction.

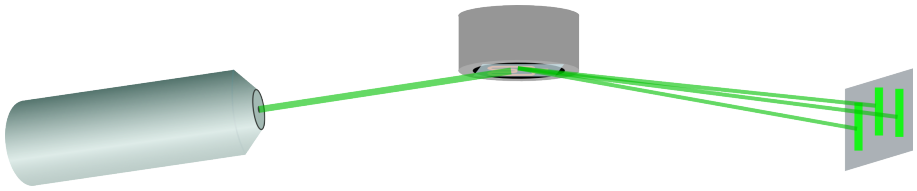

Figure 1.12: Geometry of RHEED: monochromatic electron beam is directed onto the growing crystal surface, the diffraction pattern is detected by a phosphor screen.

In an elastic scattering process the energy of the scattered particle is conserved:

$$E_I = E_F = \frac{\hbar^2 k_I^2}{2m} = \frac{\hbar^2 k_F^2}{2m} \quad \rightarrow \quad k_F = k_I = k, \tag{1.2}$$

where E_I and E_F are the energies of the incident and scattered electrons, $\hbar$ is the reduced Planck constant, k_I and k_F are the magnitudes of the wave vectors of incident and scattered electrons, and m is the electron mass. Laue's condition of diffraction states that the wave vector in diffraction can only change by a vector that is a reciprocal vector ($\mathbf{g_{hkl}}$) of a scattering crystal:

$$\mathbf{k_F} - \mathbf{k_I} = \mathbf{g_{hkl}}, \tag{1.3}$$

where

$$\mathbf{g_{hkl}} = h\mathbf{a_1^*} + k\mathbf{a_2^*} + l\mathbf{a_3^*} \quad \text{and} \quad \mathbf{a_i^*} = 2\pi \frac{\mathbf{a_j} \times \mathbf{a_k}}{\mathbf{a_i} \cdot (\mathbf{a_j} \times \mathbf{a_k})}. \tag{1.4}$$

$\mathbf{a_{i,j,k}}$ and $\mathbf{a_{i,j,k}^*}$ are real and reciprocal lattice vectors respectively, and h, k, and l are integers [39, 40]. A more detailed discussion on diffraction can be found in section 1.4.2.

The solutions of equations 1.2 and 1.3 can be obtained geometrically by the Ewald construction, where the vector $\mathbf{k_I}$ is placed in the reciprocal lattice of the diffracting volume so that its tail end is on a reciprocal point. Then a sphere with radius k is drawn around the head of the vector $\mathbf{k_I}$. Diffraction occurs in all the directions, where the sphere intersects a reciprocal lattice point [39, 40]. The detecter is placed in the forward direction, as shown in figure 1.12, thus we can only observe waves, that are diffracted forward.

The radius of the Ewald sphere can be calculated from the de Broglie wavelength of the electrons:

$$\lambda = \frac{h}{p}, \tag{1.5}$$

where h is the Planck constant, and p is the momentum of the electrons.

In case of high energy electron beams (>50 keV), relativistic effects have to be taken into account. For a 20 keV electron beam the relativistic correction in the wavelength is only 1%, but for the sake of completeness the relativistic calculation is shown here [40].

Energy (E) of a particle with rest mass of m_e (electron mass) is

$$E = \sqrt{p^2c^2 + m_e^2c^4} = T + m_ec^2, \tag{1.6}$$

where c is the speed of light, and T is the kinetic energy. From equation 1.6 the momentum can be expressed as follows:

$$p^2c^c = T^2 + 2Tm_ec^2. \tag{1.7}$$

Kinetic energy of a particle with charge e (electron charge) accelerated by a voltage U is the following:

$$T = \frac{1}{2}m_ev^2 = Ue. \tag{1.8}$$

Using equations 1.5, 1.7, and 1.8, choosing an accelerating voltage of 20 kV, the wavelength, and the magnitude of the wave vector is:

$$T = \frac{1}{2}m_ev^2 = Ue = 0.09\text{Å} \quad \rightarrow \quad k = \frac{2\pi}{\lambda} = 73\text{Å}^{-1}. \tag{1.9}$$

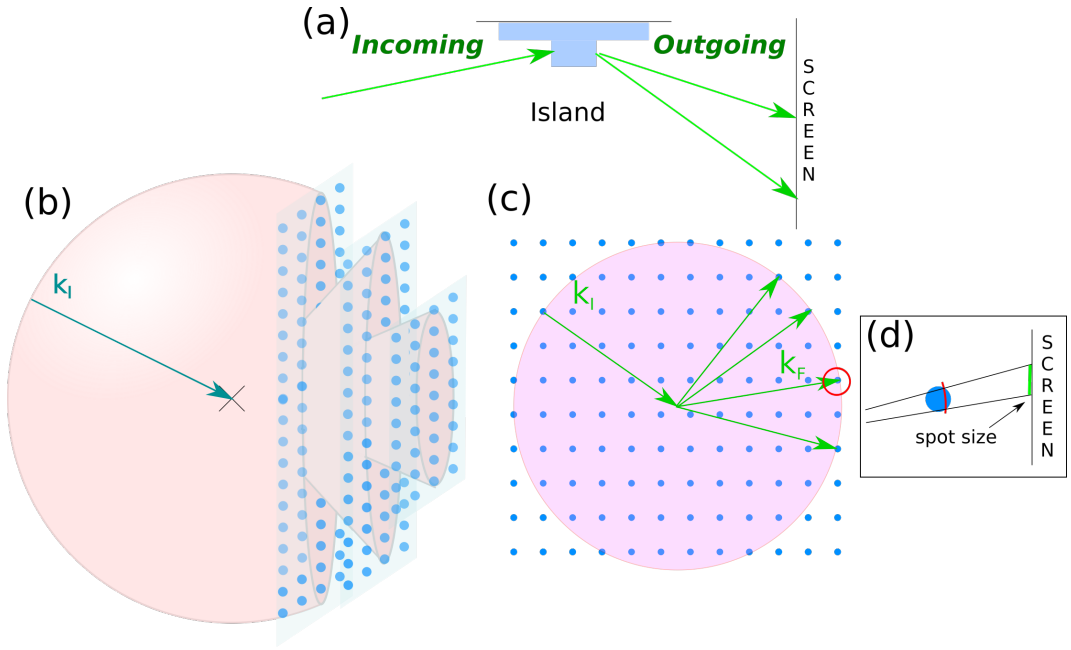

Figure 1.13: Electron diffraction from an uneven surface. (a) Diffraction happens in transmission through an island, a three dimensional object. (b) Sections of the Ewald sphere are shown in the reciprocal lattice, which consists of points. Constructive interference occurs in directions where the Ewald sphere intersects a reciprocal lattice point. (c) Cross section of the Ewald sphere is shown with the reciprocal lattice points and the wave vectors of the incoming and the outgoing, forward scattered waves. (d) The intersection of a reciprocal lattice point and the electron beam is projected onto the phosphor screen, which results in a spherical spot.

The advantage of grazing incidence is its sensitivity to the surface structure of the sample. Just by glancing at the diffraction pattern it can be determined whether the surface is flat or has grain structure. In the following, the construction of the diffraction patterns are discussed starting with the case of island growth.

In figure 1.13(a) diffraction from a surface, that is covered with islands, is shown, schematically in real space. The electron beam travels through these islands in transmission. The diffracting volume is extended in all three directions, which in reciprocal space corresponds to reciprocal lattice points. This reciprocal lattice is shown in figure 1.13(b) with the Ewald sphere. Constructive interference occurs in directions where the Ewald sphere intersects the reciprocal lattice points. In figure 1.13(c) a cross section of the Ewald sphere and the reciprocal lattice is shown. The points of intersections are clearly

visible, they will define all the possible directions of the outgoing wave vector ($\mathbf{k_F}$). The intersection of a reciprocal lattice point and the electron beam is projected onto the phosphor screen. Due to the finite crystallite size, the reciprocal lattice points have an finite width. This results in spherical diffraction spots with a finite diameter.

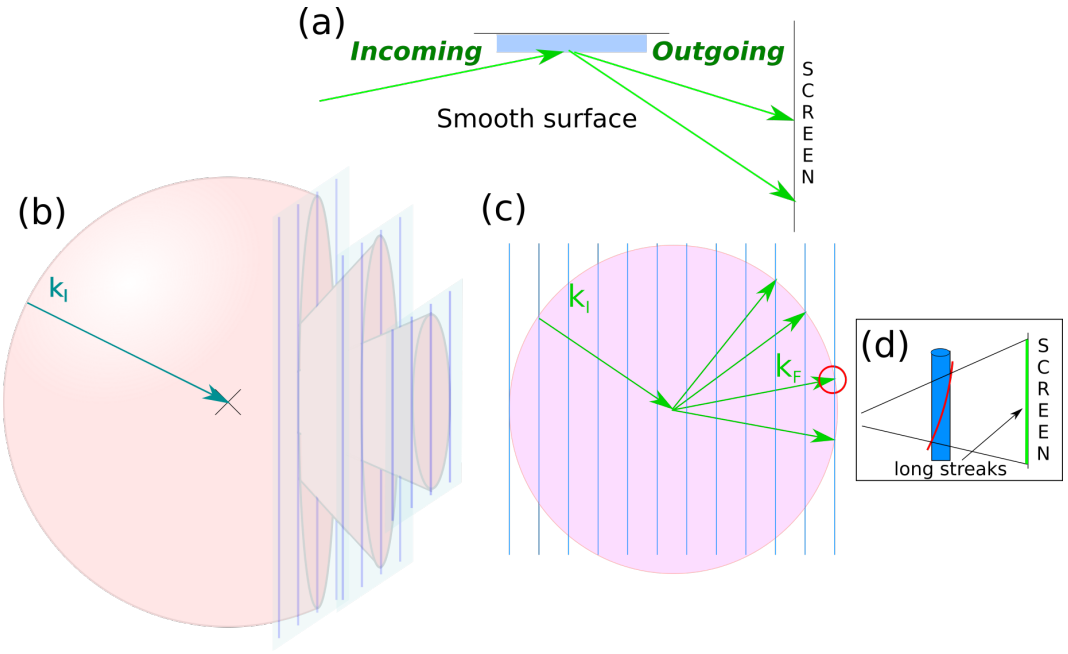

Figure 1.14: Electron diffraction from an even surface. (a) Diffraction happens in reflection, the third dimension is reduced. (b) Sections of the Ewald sphere are shown in the reciprocal lattice, which consists of rods. Constructive interference occurs where the Ewald sphere intersects the reciprocal lattice rods. (c) Cross section of the Ewald sphere is shown with the reciprocal lattice rods and the wave vectors of the incoming and the outgoing beams. (d) The intersection of a reciprocal lattice rod and the electron beam is projected onto the phosphor screen, which results in an elongated rod perpendicular to the surface.

In figure 1.14(a), diffraction from a smooth surface is shown schematically, in real space. Diffraction happens in reflection, and the penetration depth of the electron beam is restricted to a few atomic layers. The third dimension of the diffracting volume is reduced. The reciprocal lattice of a two dimensional periodic structure consists of rods, that are perpendicular to the surface. The distance between the reciprocal lattice rods corresponds to the inverse of the in-plane lattice constant.

In figure 1.14(b) the reciprocal lattice rods and the Ewald sphere are shown. Diffrac-

tion is observed in directions where the Ewald sphere intersects the reciprocal lattice rods. In figure 1.14(c) a cross section of the reciprocal lattice and the Ewald sphere are shown. Dimensions in the figures 1.14(b) and 1.14(c) are not accurate, the radius of the Ewald sphere is much larger than the spacing between the reciprocal lattice rods. Therefore, the intersections between them are extended along the direction of the surface normal. This is illustrated in figure 1.14(d). This is the reason why in the RHEED pattern of a film with a smooth surface and good crystalline quality sharp streaks are observed.

1.4.2 Ex situ characterisation techniques

Surface topography and the crystallographic properties of the substrates and the thin films were investigated using several techniques outside of the vacuum chamber. Atomic force microscopy was used to measure the topographic features; X-ray diffraction was used to check the orientations and verify the thicknesses of the films. These two techniques are described below.

Atomic force microscopy

Topography of the films and the substrates were measured using a Veeco Dimension 3100 atomic force microscope. Atomic force microscopy (AFM) belongs to the family of scanning probe microscopes. The AFM probe is an atomically sharp silicone tip attached to a cantilever. They have resonance frequency around 300 kHz.

The AFM cantilever is very flexible, and small forces that act between the sample and the tip can bend it according to Hook's law:

$$\mathbf{F} = k\mathbf{z}, \tag{1.10}$$

where k is the spring constant of the cantilever, and z is the displacement of the tip.

Forces can have different sources depending on the sample, mostly it is due to electrostatic interaction. What is important, that the magnitude of the force decreases with the distance. This allows imaging the topography, by keeping the interaction between the tip and the surface constant [41].

In this work, the AFM was used in tapping mode. In tapping mode the cantilever is oscillated so that it lightly taps on the surface of the sample at the lowest point of its swing. The frequency of the oscillation is near to the resonance frequency of the cantilever, where the amplitude is most sensitive to changes. The sample surface is scanned with the oscillating tip, while a feedback loop maintains a constant amplitude, ie. constant

surface-tip distance, by lowering or lifting the probe. The feedback signal on the vertical module is calibrated, so that it gives the vertical movement of the AFM tip. Plotting this over the scanned are gives the topographic image of the surface [41].

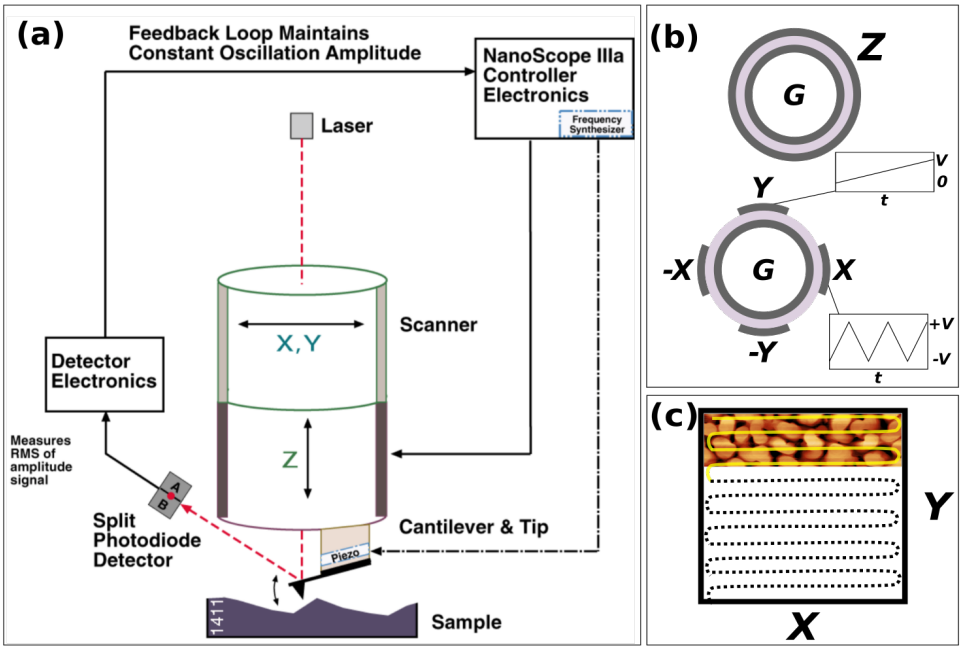

Figure 1.15: Schematics of Tapping Mode AFM and the feedback loop. (a) An oscillating cantilever is attached to a piezoelectric ceramic tube. Movement of the tip is detected by a split photodiode. The amplitude of the oscillation is kept constant by a feedback loop [41]. (b) Cross section of the modules of the piezoelectric tube, and the applied voltage. (c) The feedback signal is converted to height, phase or amplitude, and are plotted as the function of the coordinates of the scanned area.

The schematics of the AFM is shown in figure 1.15(a). The cantilever is connected to a tube made out of a piezoelectric ceramic. This tube is composed of two parts corresponding to the lateral (x, y), and the vertical (z) directions. The vertical module, shown in figure 1.15(b), consists of two cylindrical electrodes separated by the piezoelectric ceramic. The voltage applied to the piezoelectric ceramic is adjusted by the feedback loop, and causes the part to contract or to extend, lifting or lowering the tip, respectively [41].

The lateral module, also shown in figure 1.15(b), has four pairs of electrodes arranged around the piezoelectric ceramic tube. The ones opposite to each other receive the same

signal but with opposite sign, so while one side extends the other contracts, thus causing the tube to tilt. The shape of the signal applied to these electrodes to generate the scanning raster motion is shown in figure 1.15(b) [41].

The movement of the tip can be monitored with the use of a laser light that is directed onto the backside of the cantilever, as shown in figure 1.15(a). It is reflected towards a split photodiode detector that has two separate parts: A and B. The output of the detector is $\frac{I_A - I_B}{I_A + I_B}$, where I_A and I_B are the signals on each diode. From this value the vertical position of the tip can be reconstructed [41].

Three types of image can be obtained from an AFM scan: height, amplitude, and phase image. The height image is the one mentioned above, when the vertical position of the oscillating tip is adjusted to keep a constant amplitude. The vertical movement of the tip is plotted as the function of the coordinates of the scanned area, which directly corresponds to the topography of the surface [41].

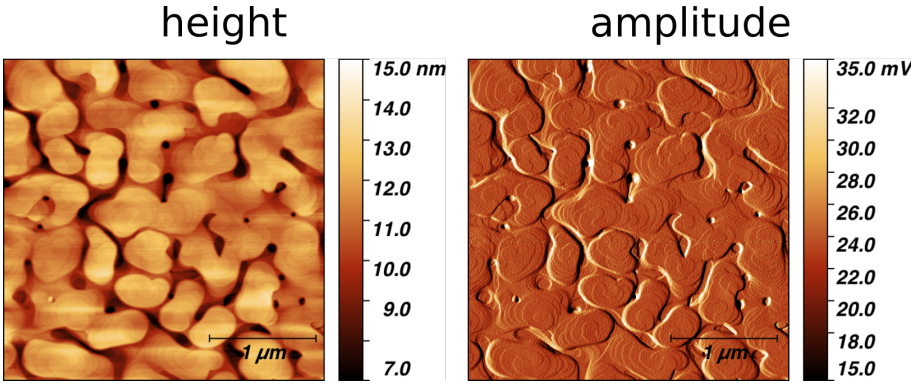

Figure 1.16: 3 µm x 3 µm height and amplitude image taken of the same area of a rhenium thin film: variation of height shows on the height image, but it is easier to observe the edges on the amplitude image.

The change in the signal on the photodiode detector can also be plotted, this corresponds to the changes in the amplitude of the oscillation, so it is referred to as amplitude image. The feedback loop should keep this value constant, but rapid changes in the topography will show in the amplitude image.

The third value that can be used to create an image is the phase difference between the driving AC signal, and the oscillation of the cantilever. This can show changes in the interaction between the tip and the sample. This is called phase image. Determining what causes the changes in the phase is a science in itself [41].

In figures 1.16 and 1.17 the differences between the height and amplitude image, and

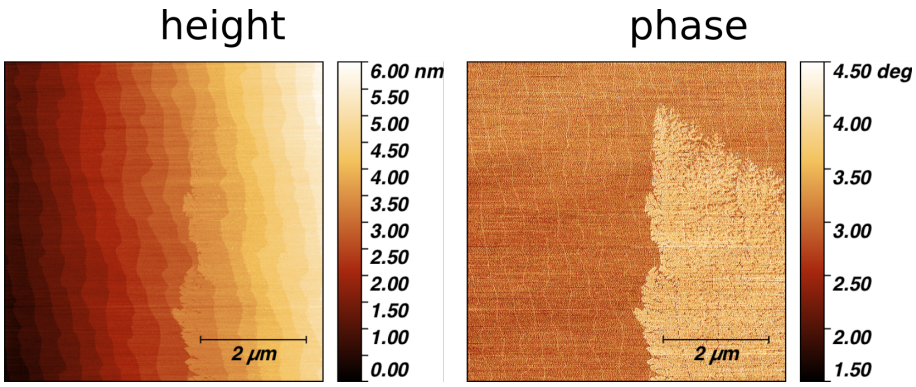

Figure 1.17: 6 µm x 6 µm height and phase image taken of the same area of a sapphire substrate: the phase image shows a contrast that is thought to be due to different chemical composition on the surface. Contrast is not visible on the height image.

height and phase image can be observed. Most of the images shown in this work are height images.

Images were analysed using the software Gwyddion [42]. Noise was reduced on all of them with in-built algorithms. Also, an algorithm called planefit was used on all of them, unless otherwise stated. Planefit is used to remove the slope across an image that could be caused by uneven mounting of the sample. In the case of stepped surfaces, which have a slope by nature, planefit has an effect that is illustrated in figures 1.18.

In figure 1.18(a), a simulated stepped surface is shown. The intensity of the colour is proportional to the surface height. A cross section of the surface is shown in figure 1.18(c) with the blue line. The plane fit algorithm determines the average slope of the surface,

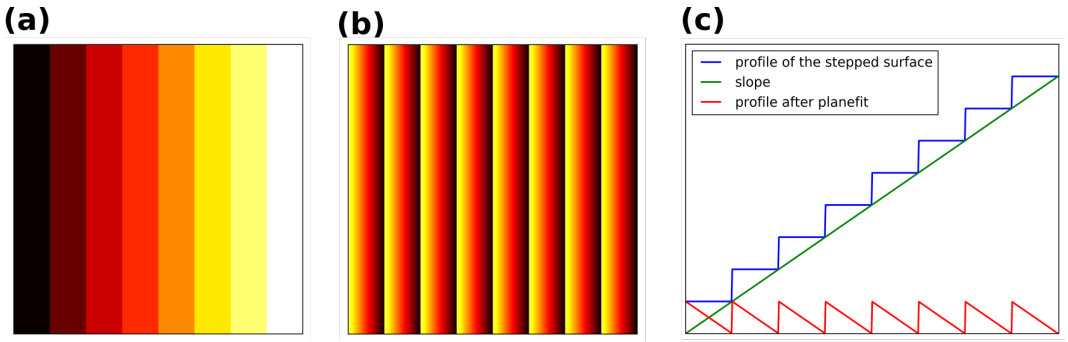

Figure 1.18: Effect of the planefit algorithm illustrated by a simulated stepped surface: the average slope of the image is subtracted, stepped surface appears to be jagged.

shown in green in figure 1.18(c), and subtracts it from the raw height data. The result is shown in figure 1.18(b), and its cross section in figure 1.18(c) in red.

After the slope is subtracted, the surface appears to be jagged. Nonetheless, it is preferred to use the planefit algorithm even on stepped surfaces, because it reduces the range of the vertical scale, making the features easier to observe.

Lateral resolutions of the AFM is ideally around 1 nm, but it strongly depends on the quality of the tip. The tip degrades over time, because it keeps touching the surface again and again. Vertical resolution is approximately 0.1 nm [41].

X-ray diffraction

X-ray diffraction (XRD) was used to determine the crystal structures of the deposited thin films. Diffraction of high energy electrons was discussed briefly already in section 1.4.1 using Laue's condition of diffraction, and the Ewald sphere. In this section a short summary is given on the hexagonal crystal structure, then the diffraction phenomena and XRD is described in more detail.

Notes on the hexagonal crystal system. In a crystalline material the atoms are arranged periodically in all three directions of space, forming a crystal lattice. The smallest volume that have the overall symmetry of the crystal is called the unit cell. The length of the vectors (lattice vectors: **a**, **b**, **c**) that define it are the lattice parameters. Rhenium crystallises in the hexagonal system. The **a** and **b** hexagonal lattice vectors make an angle of 120°, and the **c** vector is perpendicular to the $\mathbf{a} - \mathbf{b}$ plane. **a** and **b** are equal in length ($a = 0.2761$ nm), but **c** is longer ($c = 0.4456$ nm) [13].

Atoms on a crystal lattice form a series of crystal planes. Infinite number of such planes can be defined. A crystal plane intercepts the lattice vectors at points $\frac{a}{h}$, $\frac{b}{k}$, $\frac{c}{l}$. (hkl) are the Miller indexes and they define the orientation of a plane with respect to the coordinate system of the unit cell. Parallel planes are noted using the same Miller indices, and are spaced at equal distances (d_{hkl}). d_{hkl} for hexagonal crystals can be obtained using the following equation:

$$\frac{1}{d_{hkl}^2} = \frac{4}{3}\frac{h^2 + hk + k^2}{a^2} + \frac{l^2}{c^2}. \tag{1.11}$$

It is sufficient to use the three Miller indices to identify a plane or a direction in the hexagonal system, however, it does not have the same convenience, as it has in an orthogonal system.

In an orthogonal system, indices of equivalent planes and directions can be generated by the permutation of the three Miller indices. This does not work with the Miller indices of a hexagonal crystal. However, permutation does work with the Bravais-Miller indices.

In the Bravais-Miller coordinate system a fourth, redundant axis is introduced in the $\mathbf{a}-\mathbf{b}$ plane, with 120° apart from **a** and **b**. Crystal planes and directions are noted with the four Bravais-Miller indices, $(hkil)$. Equivalent directions and planes can, in this notation, be obtained by the permutation of the first three indices.

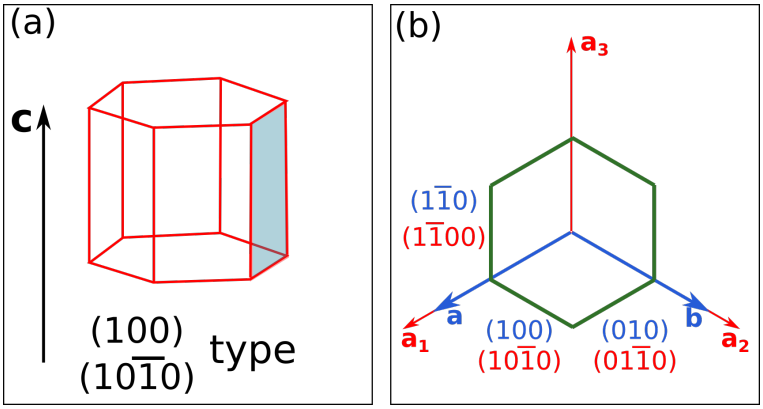

Figure 1.19: Miller indices and Bravais-Miller indices of the hexagonal system.

For example, a hexagonal prism is shown in figure 1.19(a). A plane parallel to the **c** axis is highlighted. All six of such planes around the prism are equivalent. Figure 1.19(b) shows the in-plane axes of the Miller coordinate system in blue (**a** and **b** axes), and the Bravais-Miller coordinate system in red ($\mathbf{a_1}$, $\mathbf{a_2}$, and $\mathbf{a_3}$ axes). The intersections of the planes with the axes give the indices in the two system. The Miller indices are: $(1\bar{1}0)$, (100), and (010). The Bravais-Miller indices are: $(1\bar{1}00)$, $(10\bar{1}0)$, and $(01\bar{1}0)$. This demonstrates that indices in the four axis notation can be obtained by the permutation of the first three indices. In this work, mostly the Miller indices are used.

Indices can be transformed from one notation to the other. In case of a plane, the fourth index (i) is obtained as follows:

$$i = -(h + k). \tag{1.12}$$

A direction $[UVTW]$ can be converted to the three indices $[uvw]$ as follows:

$$u = 2U + V, \quad v = 2V + U, \quad w = W. \tag{1.13}$$

X-ray diffraction. In an XRD experiment, the sample is subjected to an X-ray plane wave ($e^{-i\mathbf{k_i r}}$) with a known wave vector ($\mathbf{k_i}$), therefore known energy and propagation direction. We used two laboratory XRD setups: the Huber 4-cycle diffractometer and the Rigaku SmartLab high-resolution diffractometer. Both instruments use the Kα line of copper. The intensity of this emission is split in two: 2/3 Kα_1 with wavelength 1.540562 Å, and 1/3 Kα_2 with wavelength 1.544398 Å. In the Huber 4-cycle diffractometer both wavelengths were used, in the Rigaku SmartLab high-resolution diffractometer the Kα_2 line is removed.

The X-rays are scattered by the electrons in the sample. The scattering is assumed to be elastic, only momentum transfer occurs. This means, the outgoing wave vector has the same length as the incoming wave vector ($|\mathbf{k_i}| = |\mathbf{k_f}|$), and their vectorial difference is called the scattering vector:

$$\mathbf{q} = \mathbf{k_f} - \mathbf{k_i}. \tag{1.14}$$

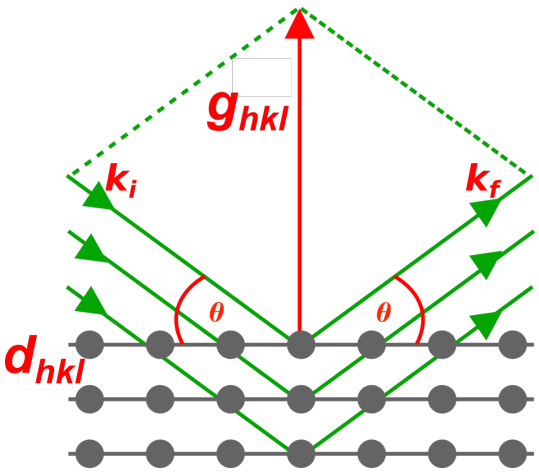

Figure 1.20: Bragg's and Laue's conditions of diffraction.

The scattered amplitude is the sum of the scattering from each atom in the illuminated volume, which, because X-rays are scattered by electrons, can be expressed as the Fourier transform of the electron density:

$$A(\mathbf{q}) = \int_V f(\mathbf{r}) e^{i\mathbf{qr}} d\mathbf{r}, \tag{1.15}$$

where the integral is taken across the illuminated volume [43].

The periodic arrangement of the atoms in a crystal lattice results in constructive (in specific cases destructive) interference whenever the scattering vector coincides with a reciprocal lattice vector ($\mathbf{g}_{hkl}$) [43]. This gives Laue's condition of diffraction:

$$\mathbf{g}_{hkl} = \mathbf{q}. \tag{1.16}$$

Laue's condition of diffraction is illustrated in figure 1.20.

$\mathbf{k_i}$, $\mathbf{k_f}$ and $\mathbf{g}_{hkl}$ form an isosceles triangle, where the angle enclosed by the two equal sides is 2θ, thus the following relation holds:

$$|\mathbf{g}_{hkl}| = 2|\mathbf{k_i}| \sin\theta. \tag{1.17}$$

Using the properties of the reciprocal lattice, it can be shown that $\mathbf{g}_{hkl}$ is perpendicular to the plane series with indices (hkl), and its length is related to the spacing d_{hkl}:

$$|\mathbf{g}_{hkl}| = m\frac{2\pi}{d_{hkl}}, \tag{1.18}$$

where m is an integer, which refers to the order of the reflection [39].

Substituting 1.18 in equation 1.17, and using relation $|\mathbf{k}| = 2\pi/\lambda$ we obtain Bragg's condition for diffraction:

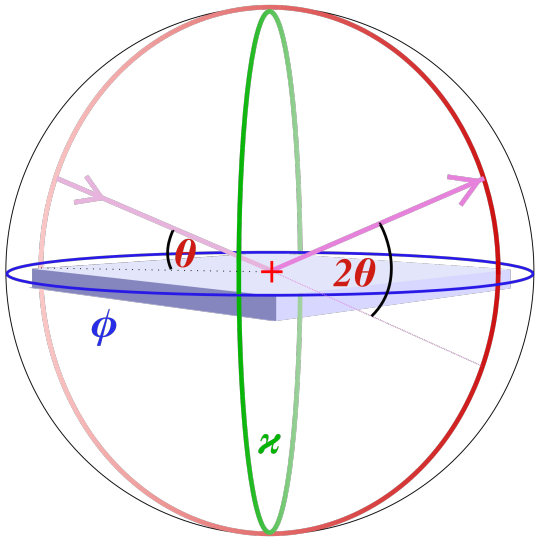

Figure 1.21: Circles and angels of a 4-cycle diffractometer.

$$m\lambda = 2d_{hkl} \sin\theta. \tag{1.19}$$

Bragg's condition of diffraction is also illustrated in figure 1.20.

Bragg's law shows a simple relationship between wavelength, angle of reflection, and lattice spacing. During an elastic diffraction experiment the angular distribution of the scattered intensity is measured. From the angles, the lattice spacings can be determined. Different lattice spacings correspond to different orientations, thus the texture of the film can be determined from a few measurements.

The schematics of a 4-cycle diffractometer is shown in figure 1.21. All circles are aligned so that their centres coincide with the centre of the sample. The detector and the source can move along the red circle. The angle between the incident beam and the surface of the sample is θ. In the symmetric, θ-2θ measurement, the angle between the incident beam and the detector is 2θ, and the source and the detector are moved symmetrically, as shown in figure 1.22(a). During this measurement the direction of the scattering vector remains perpendicular to the surface, and its length changes. The sample is scanned for all d_{hkl} values of planes that are parallel to the surface. Grains with different orientations are detected this way. Symmetric reflections are often called specular reflections.

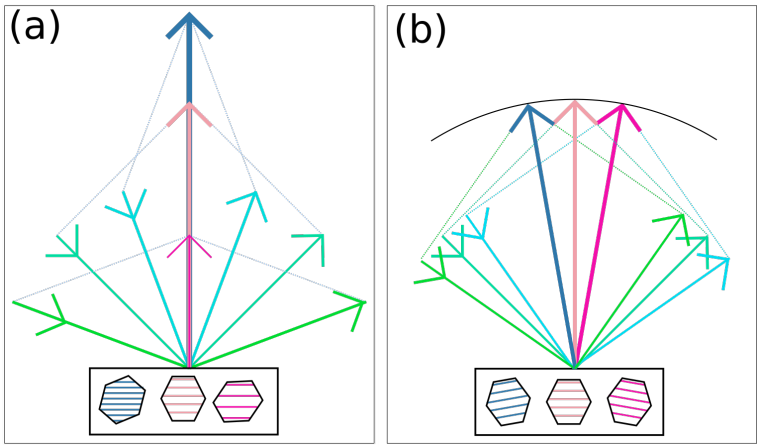

Figure 1.22: (a) Schematics of the θ-2θ scan. (b) Rocking curve measurement.

In the rocking curve measurement the detector and the source are fixed at a θ and a 2θ value where a specular peak was found. The sample is 'rocked' along the red circle in small steps. This is shown in figure 1.22(b). In this case, the length of the scattering vector is

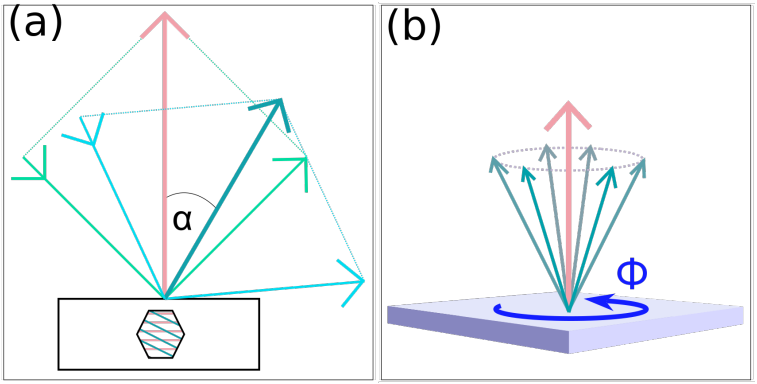

Figure 1.23: (a) Asymmetric reflection. (b) Φ scan.

fixed, and its direction changes. Small rotations of grains with the same orientation can be detected this way. This is called mosaicity.

It was mentioned above that infinite number of planes can be defined in a crystal lattice. This means that, besides the specular reflections, several asymmetric reflections can be found. This concept in shown in figure 1.23(a). The scattering vector shown in pink was found by a θ-2θ scan. α is the angle between the specular (pink), and the asymmetric (blue) reflections. For a hexagonal structure α can be computed using the following expression:

$$\cos\alpha = \frac{4}{2a^2}\left[h_1h_2 + k_1k_2 + \frac{1}{2}(h_1k_2 + h_2k_1) + \frac{3a^2}{4c^2}l_1l_2\right]d_{h_1k_1l_1}d_{h_2k_2l_2}. \tag{1.20}$$

Using the angle α, the source and the detector can be moved on the asymmetric reflection.

To verify the crystallinity of the sample in-plane, a Φ scan is conducted, which is shown in figure 1.23(b). The sample is rotated around the scattering vector of a specular reflection (|| surface normal), along the blue (Φ) circle in figure 1.21, while the detector is set on an asymmetric reflection. If the sample is crystalline, the number of reflections seen in a full rotation reflects the symmetry of the rotation axis. For example, rhenium grows epitaxially on Al_2O_3 with orientation (002). The (002) axis has hexagonal symmetry, so when we set the source and the detector on the (103) asymmetric reflection, and rotate the sample around the (002) direction we expect to observe 6 bright signals coming from the planes equivalent to (103). As an illustration of the technique, the above example is shown in figure 1.24. Here, Φ was scanned in a 180° interval, and in addition a χ scan was performed. A 2D projection of the diffraction peaks can be observed. Indeed, within half

a circle, 3 diffraction peaks appear. This shows that the rhenium film has a single in-plane orientation. This technique was used to determine the in-plane relationship between the substrate and the film which is presented in section 2.1.3.

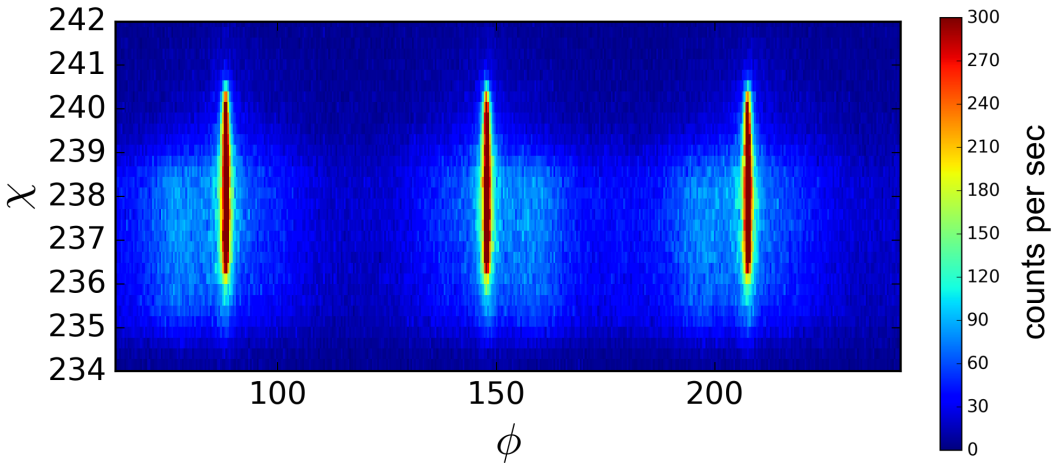

Figure 1.24: Φ and χ scan on the (103) equivalent reflections of rhenium grains with (002) orientation.

The interference function On a high resolution θ-2θ diffraction pattern fringes are often observed. Fringes appear when X-rays are scattered by a highly crystalline sample composed of N planes with equal distances (d) between them. This situation is shown in figure 1.25.

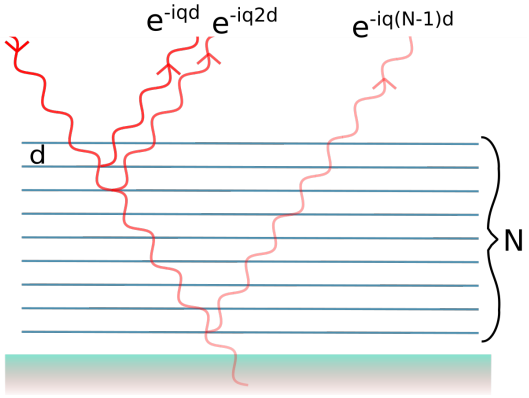

Figure 1.25: Scattering from N planes with equal distances.

The scattered amplitude (A_N) is the sum of amplitudes from each plane:

$$A_N(q) \propto \sum_{n=0}^{N-1} e^{-iqnd} \underset{\text{with } k=e^{-iqd}}{=} 1 + k + k^2 + ... + k^{N-1} = \frac{1-k^N}{1-k}. \tag{1.21}$$

Equation 1.21 can be arranged in the following form:

$$A_N(q) \propto \frac{\sin\frac{qNd}{2}}{\sin\frac{qd}{2}} \cdot e^{-iq(N-1)d}, \tag{1.22}$$

From this, the equation that describes the intensity is:

$$I_N(q) \propto \frac{\sin^2\frac{qNd}{2}}{\sin^2\frac{qd}{2}}. \tag{1.23}$$

Equation 1.23 is called the interference function, and was used to fit high-resolution X-ray data presented in chapter 2.

1.5 MBE growth

1.5.1 Adsorption and growth modes

During molecular beam epitaxy growth, a charge is heated to temperatures where it slowly evaporates. The deposition chamber contains the vapour phase of the material to-be-deposited and also a heated substrate in the solid phase. Crystal growth happens at the interface of the two phases [44]. Atoms of the vapour phase arrive on the surface of the solid phase. Growth will take place when the arriving atoms of the vapour phase attach to the solid phase at a higher rate than they reevaporate, which implies a departure from equilibrium conditions [44].

Atoms arriving at the substrate have a temperature distribution corresponding to the source (T_{source}). Upon arrival they either reach thermal equilibrium with the substrate at the substrate temperature ($T_{\text{substrate}}$), or reevaporate at a temperature T_{reevap}. This process is quantitatively described by the accommodation coefficient [44]:

$$\alpha = \frac{T_{\text{source}} - T_{\text{reevap}}}{T_{\text{source}} - T_{\text{substrate}}}. \tag{1.24}$$

Thus equation 1.24 expresses the extent to which the arriving atoms reach thermal equilibrium with the surface. α equals zero when $T_{\text{reevap}} = T_{\text{source}}$, which means that

the atoms reevaporate immediately, before they had time to loose from their energy and lower their temperature. The other limit is when $T_{\text{reevap}} = T_{\text{substrate}}$, and $\alpha = 1$. In this case thermalisation is perfect, the arriving atoms cool to the temperature of the substrate. Atoms that have reached the equilibrium do not necessarily remain on the surface permanently. It is still possible for them to reevaporate at the temperature of the substrate. Sticking or condensation coefficient gives the probability that an atom will adhere to the surface [44]. It is defined as the number of adhered atoms (N_{adh}) over the total number of arriving atoms (N_{tot}):

$$s = \frac{N_{\text{adh}}}{N_{\text{tot}}}, \tag{1.25}$$

where for the accommodation coefficient only the temperatures are considered, in the sticking coefficient the nature of the physical or chemical bond is also included.

Absorption of an atom can be chemical, when ionic or covalent bonds are formed between the adsorbate and the adsorbent: electrons are transferred. It can be physical, when there is no electron transfer, van der Waals bond connects the two parts. Usually in MBE growth both of them are present subsequently [44].

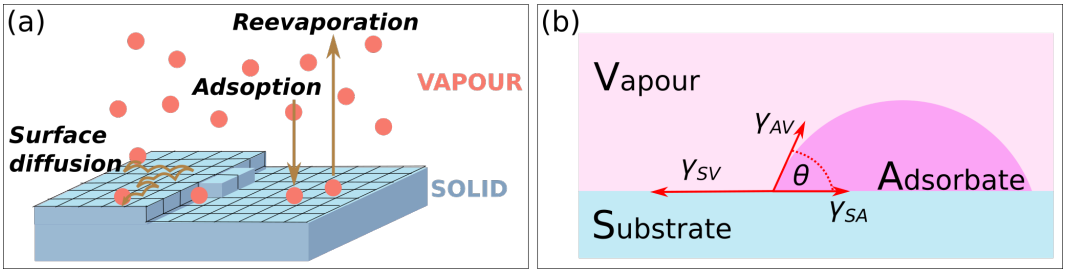

Figure 1.26: (a) Processes that can occur when an atom reaches the surface of the growing crystal or the substrate. (b) Surface tensions that act between the adsorbate island (A), substrate (S), and vapour (V).

Once atoms are adsorbed on the surface three things can happen: they can be incorporated into the crystal where they are, they can diffuse to find an energetically more favourable location, or they can reevaporate. This is shown in figure 1.26(a). What an energetically favourable location for an adsorbate is, depends on the surface tensions between the interfaces, and the amount of material that has already been deposited. The relation developed by Young, which explains the shapes of liquid droplets on solid surfaces, is valid for solid adsorbate too. It demands that the forces acting on the surfaces are in balance:

$$\gamma_{SV} - \gamma_{SA} - \gamma_{AV}\cos\theta = 0 \quad \rightarrow \quad \cos\theta = \frac{\gamma_{SV} - \gamma_{SA}}{\gamma_{AV}}, \tag{1.26}$$

where γ_{SV} and γ_{SA} are the surface tensions between substrate and vapour, and substrate and adsorbate, respectively. $\gamma_{AV}\cos\theta$ is the projection of the surface tension between the adsorbate and vapour to the plane of the substrate surface. θ is the angle between the surface of the substrate and the adsorbate. Geometry is shown in figure 1.26(b).

When $\gamma_{SV} < \gamma_{AV} + \gamma_{SA}$, θ has a finite value, and it is energetically favourable to keep the area of the substrate-vapour interface at maximum, which will force the adsorbate to form islands. This is called Vollmer-Weber island growth mode, and is depicted in figure 1.27(b). This growth mode is often observed when metal is grown on an insulator [44].

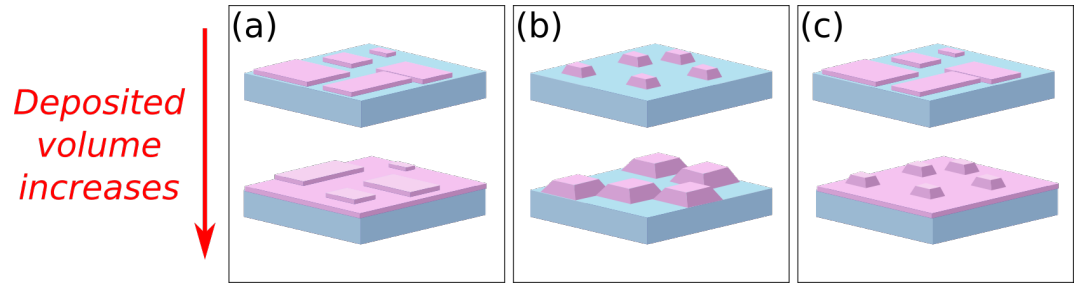

Figure 1.27: Three growth modes: (a) Frank-van der Merve layer-by layer growth mode, (b) Vollmer - Weber island growth mode, (c) Stranski-Krastanov layer-plus-island growth mode.

When the relation is reversed, $\gamma_{SV} > \gamma_{AV} + \gamma_{SA}$, θ angle cannot be defined. It is now favourable to reduce the substrate-vapour interface by the formation of an adsorbate layer. This is called Frank-van der Merve layer-by layer growth mode, shown in figure 1.27(a). This growth mode is observed in the case of adsorbed gases on metals, semiconductors grown on semiconductors, or in metal-metal systems [44].

There is a third growth mode, which is called Stranski-Krastanov layer-plus-island growth mode, and is shown in figure 1.27(c). In this case the growth starts layer by layer. After a few monolayer was deposited the growth mode changes into island growth. The change in the growth mode is triggered by the changing of the surface tension with increasing thickness. Surface tension is affected by many factors including strain or surface reconstruction [44].

1.5.2 Dislocations and misfit

Dislocations

Dislocations are two dimensional defects in crystals. Depending on the orientation of the Burgers vector with respect to the dislocation line, edge and screw dislocations can be defined.

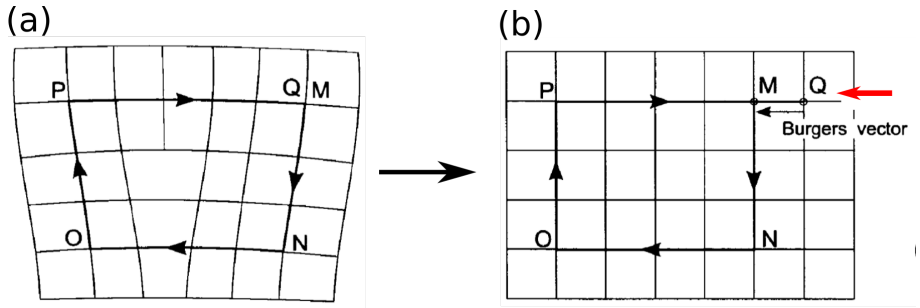

Figure 1.28: (a) Schematic representation of an edge dislocation with the Burgers circuit. A closed loop ($MNOPQ$) is drawn in the crystal that encloses the dislocation. (b) Burgers circuit is copied into a perfect crystal, where it is not closed. Burgers vector connects the starting point (M) and the final point (Q) of the Burgers circuit [45].

In case of an edge dislocation, shown in figure 1.28(a), an extra half plane is present in the crystal. A screw dislocation, shown in figure 1.29(a), can be imagined by cutting the crystal in half but not all the way, and displacing one half of the crystal by one lattice spacing relative to the other half. If a screw dislocation reaches the surface of the crystal, a step appears [45].

Dislocations can be characterised by their Burgers vectors. A Burgers circuit is any atom-to-atom path which forms a closed path. Burgers circuits are shown in figures 1.28(a) and 1.29(a). In figure 1.28(a), the circuit $MNOPQ$ encloses an edge dislocation, in figure 1.29(b), a screw dislocation. If the same path is taken in a dislocation free crystal, as shown by the arrows in figure 1.28(b) and 1.29(b), and the path does not close, it must contain at least one dislocation. The vector required to close the loop, is called the Burgers vector. In figures 1.28(b) and 1.29(b), vectors pointing from points Q to M are the Burgers vectors. It can be observed, that the Burgers vector of a pure edge dislocation is perpendicular to the line of the dislocation. In case of a pure screw dislocation, it is parallel [45].

Dislocations in real materials are neither pure edge nor pure screw type. They are a mixture of both.

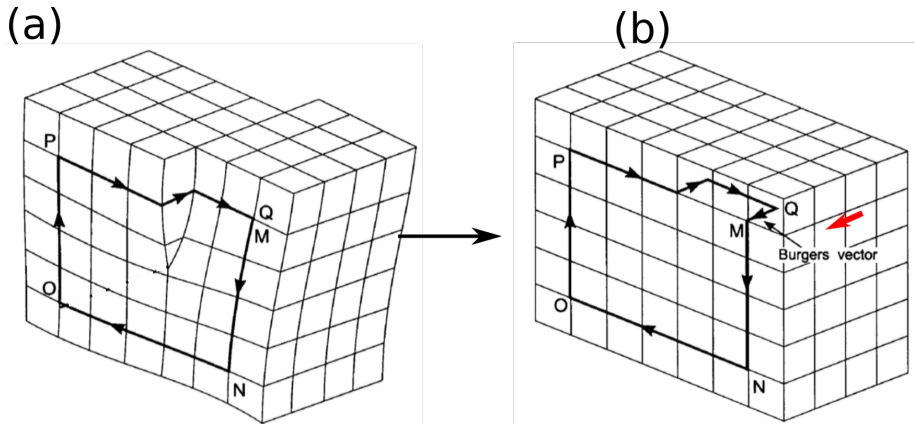

Figure 1.29: (a) Schematic representation of a screw dislocation with the Burgers circuit. A closed loop (MNOPQ) is drawn in the crystal that encloses the dislocation. (b) Burgers circuit is copied into a perfect crystal, where it is not closed. Burgers vector connects the starting point (M) and the final point (Q) of the Burgers circuit [45].

Dislocations distort the crystal lattice, they induce elastic stress in the material. The stress around a dislocation scales with $\frac{1}{r}$, where r is the distance from the dislocation. When $r = 0$, the stress in infinite which is not possible. This divergence is caused by the break down of the elastic theory at the vicinity of the dislocation. The elastic theory neglects the atoms, and treats the material as a continuum. To avoid infinite stress, an arbitrary cutoff radius, core radius (r_0) is defined, and calculations are stopped there. Reasonable values for the core radius are in the range of 1 nm [45].

Misfit

Heteroepitaxy refers to the growth of a layer onto a chemically different material. Due to the chemical difference they favour different interatomic distances, i.e. their bulk lattice parameters are different. This is shown in figure 1.30(a). The difference can be expressed by the misfit:

$$\epsilon_i = \frac{a_{\mathrm{s}i} - a_{\mathrm{l}i}}{a_{\mathrm{l}i}}, \quad i = x, y \tag{1.27}$$

where a_{s} and a_{l} are the lattice parameters in the two directions (x, y) perpendicular to the growth direction. This means that if the layer grows epitaxially, its structure matches perfectly with the substrate. Thus, the layer experiences a homogeneous strain.

Strain energy scales with the volume, it increases with thickness. Above a critical thickness it becomes energetically favourable to release part of the strain by the spontaneous formation of dislocations, shown in figure 1.30(b).

Critical thickness

The existence of the critical thickness, where misfit dislocations appear, was first predicted by Frank and van der Merwe. It was treated theoretically by several authors and confirmed experimentally.

Formula for the critical thickness can be derived by comparing the work that is required to form a dislocation (W_d), and the work that can be gained from the stress field when a dislocation is formed (W_m). The thickness where the work gained equals to the work required, defines the critical thickness.

The geometry of a misfit dislocation is shown in figure 1.31(a). The coordinate system is taken so that the y axis is perpendicular to the surface. The dislocation line lies along the z axis, at the interface between the film and the substrate. Along this axis the strain is uniform. The grey plane is the plane where the dislocation can glide, and it divides the crystal in two, signed as $(+)$ and $(-)$ [46].

To calculate the work that is required for the formation of a dislocation, the following is considered: a stress free crystal is cut along the glide plane from the surface to the dislocation, and material with radius r_0 is removed, centred on the eventual dislocation line. The path of the cut is shown in figure 1.31(b) by a dotted line. Surfaces (Γ^+ and Γ^-)

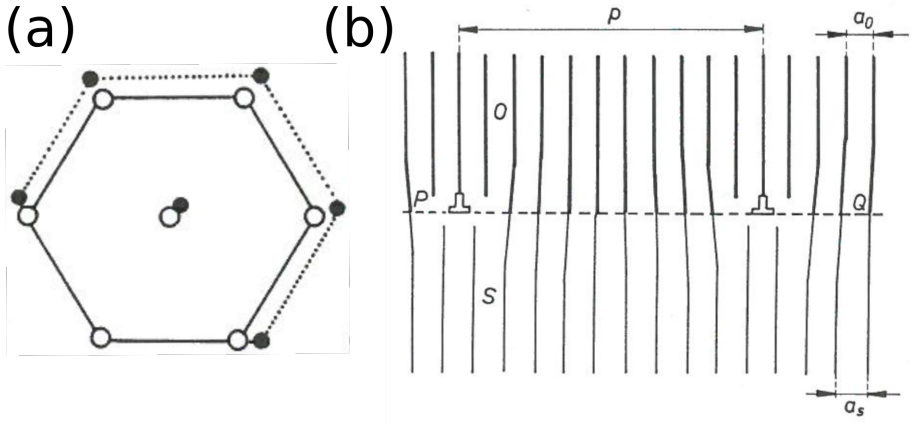

Figure 1.30: (a) Misfit of two hexagonal crystal lattices. (b) Due to the misfit, dislocations spontaneously appear in the film [44].

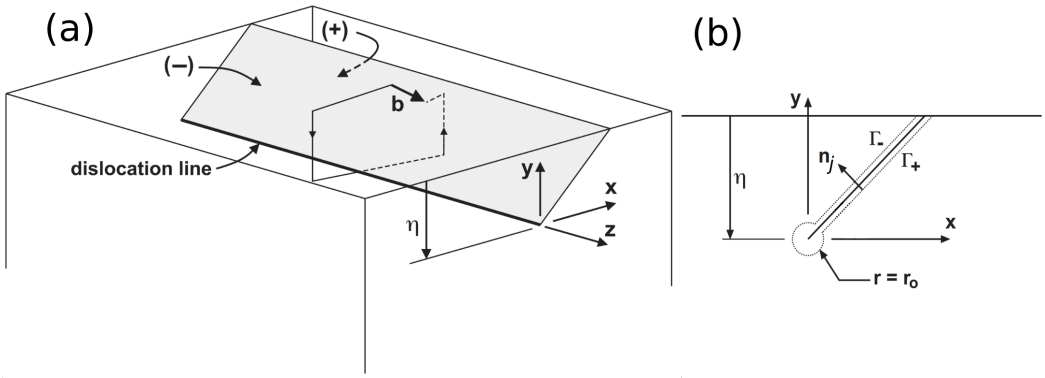

Figure 1.31: (a) A dislocation lies η distance away from the surface, along axis z. Its glide plane divides the crystal in two: (+) and (−). (b) Sideview of (a): surfaces Γ^+, Γ^- are on the two sides of the glide plane. A volume around the dislocation line, with radius $\mathbf{r_0}$ is excluded from the calculation [46].

created by the cut are displaced by on offset defined by the Burgers vector ($\mathbf{b}$) of the dislocation. The energy per unit length that is stored in the material as the result of these operations is the following:

$$W_d(\eta) = \int_\Gamma \frac{1}{2} T_i u_i dl, \tag{1.28}$$

where index i denotes the x, y, z coordinates of the corresponding vectors, Γ is the boundary of the region created by the cuts in the material, l is the arc length along this boundary, and T is the traction required to maintain the imposed displacement. Traction is related to the stress tensor (σ_{ij}) and the surface normal (n_j): $T_i = \sigma_{ij} n_j$. Evaluation of the integral is lengthy and beyond the scope of this work. More details can be found in reference [46]. The following expression is a good approximation of the final result:

$$W_d(\eta) = \frac{\mu[b_x^2 + b_y^2 + (1-\nu)b_z^2]}{4\pi(1+\nu)} ln \frac{2\eta}{r_0}, \tag{1.29}$$

where b_x, b_y, and b_z are the components of the Burgers vector, η is the distance of the dislocation from the surface of the crystal. μ is the elastic sheer modulus, it is the property of the material defined as the ratio of sheer stress to the sheer strain. Finally, ν is the Poisson ratio, it is also the property of the material, defined as the transversal strain over the axial strain. Poisson ratio is the measure of the Poisson effect: when a

material is compressed in one direction, it tends to expand in the two other perpendicular directions. Most often Poisson ratio is negative [46].

Next, the work done by the background stress field in forming a dislocation, where the stress is caused by the the misfit, is calculated. The same thought process, shown in figure 1.31(b), is followed, except this time the crystal is strained by misfit, and the stress field is considered to be unaffected by the formation of the dislocation. The work done by the field can be calculated by the same formula as before:

$$W_m(\eta) = \int_\Gamma \frac{1}{2} T_i u_i dl. \tag{1.30}$$

The difference here is that the stress is the misfit stress, not the stress caused by the dislocation. In this case, the formula for the stress is simply $\sigma_m = \mu\epsilon_m$, where ϵ_m is the misfit strain from equation 1.27. The result of the integration is the following:

$$W_m(\eta) = -b_x \sigma_m \eta. \tag{1.31}$$

Dislocations spontaneously appear in the film when $W_d(h_c r) + W_m(h_c r) = 0$. The full expression for the critical thickness can be found in reference [46]. An approximation, which is valid when the critical thickness is larger than the magnitude of the Burgers vector is the following:

$$\frac{b_x^2 + b_y^2 + (1-\nu)b_z^2}{8\pi(1+\nu)b_x h_{cr}} \ln \frac{2h_{cr}}{r_0} = \epsilon_m \quad h_{cr} \gg b. \tag{1.32}$$

Positive critical thickness can only be defined, when the misfit and b_x have the same sign, which means that only dislocations that relive the strain are allowed [46].

Equation 1.32 was used to derive the critical thickness of rhenium on Al_2O_3. This is presented in section 2.1.3

1.5.3 Growth on a stepped surface and spiral growth

The best way to grow a good quality film is to use a single crystal substrate which was cut along a low energy crystal plane. It is impossible to cut a substrates from a bulk precisely along a certain direction, there will always be a miscut angle, which is usually in the range of 0.1°. This small deviation from the low energy configuration is going to drive the atoms in the surface region to rearrange themselves and form steps with one

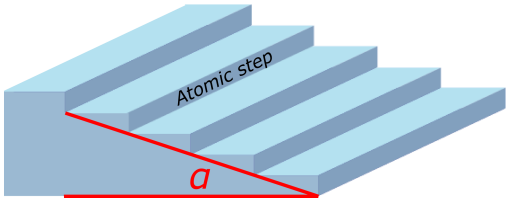

Figure 1.32: A low energy crystal surface with miscut of α tends to rearrange itself into a stepped structure.

atomic height, as shown in figure 1.32. The widths of the steps are equal, and are defined by the angle of the miscut [47].

The step edges provide efficient nucleation sites for the adatoms. They allow a so called step flow growth, shown schematically in figure 1.33. This was first described by Burton, Cabrera and Frank before MBE existed. In this growth mode, growth only happens at the step edges, and the terraces move or flow as more and more atoms are deposited [47].

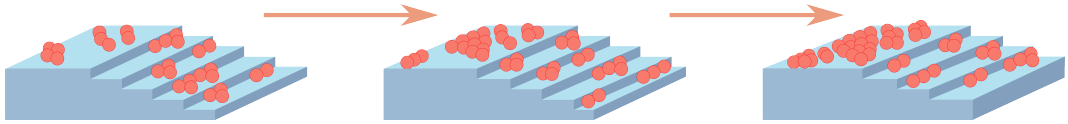

Figure 1.33: Step flow growth mode: steps are providing nucleation sites for the adatom, and the growth happens only at the step edges.

Without the presence of steps, the adatoms diffuse on the surface until enough of them meet, and a critical nucleus is formed. The critical nucleus contains the minimum number of adatoms that can be stable on the substrate surface. They can capture further atoms and initiate the growth of islands. The size of the critical nucleus depends on the temperature. At low temperature a single adatom can be stable, at higher temperature two or three or more atoms are needed. These islands grow according to the mode defined by the surface free energies, and when they are big enough they coalesce. Along the line of coalescence defects can easily occur, such as grain boundaries or holes. Step flow growth overcomes these issues as arbitrary lines of coalescence have no time to form [47].

The presence of steps is not enough for step flow growth to occur. If adatoms have no time to reach a step edge before forming a critical nucleus, islands grow on the terraces. Diffusion length defines the length an adatom can travel, before meeting an other adatom.

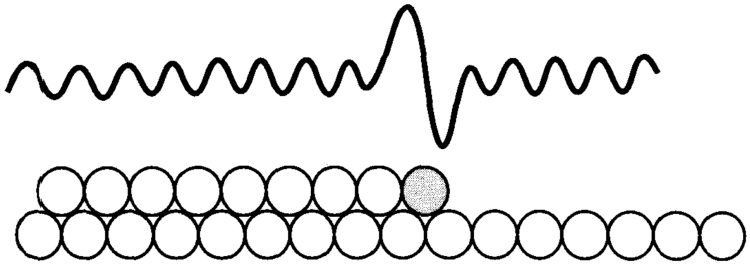

Figure 1.34: Schwoebel barrier: theoretical potential felt by an adatom (shown in grey) on a step edge [47].

Assuming a dimer is stable, it can be said that the requirement for step flow growth to occur is to have larger diffusion length than step width [47].

When discussing growth on a stepped surface, an important effect has to be mentioned: the Schwoebel barrier. Schwoebel barrier is the energy potential an adatom has to overcome when diffusing over a step.

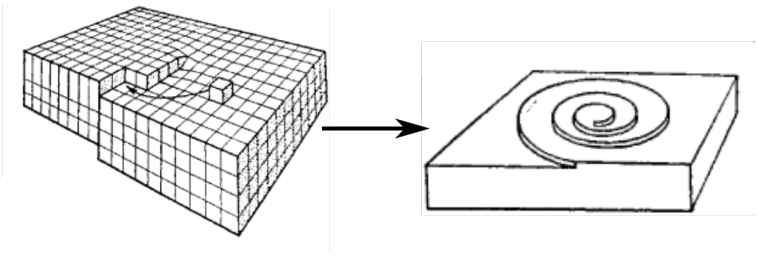

Figure 1.35: An edge dislocation produces a slanting step on the surface, which will act as a nucleation site for the arriving atoms. Nucleating adatoms keep creating steps, as a result the surface will grow in a spiral manner [48].

Schwoebel barrier is explained in figure 1.34. The adatom is show in grey. The potential felt by the adatom is shown schematically in this figure. The potential has a maximum at the step edge. When an adatom reaches the end of a terrace, to step down to the terrace below, it has to pass through a position where it does not have many neighbours. This is what creates the potential barrier [47].

The Schwoebel barrier is felt by an adatom diffusing from a lower to a higher terrace as well. In this case the adatom is in a potential well when it reaches the step edge, as the coordination number is the highest there.

A special case of step flow growth was described by Burton, Cabrera and Frank in

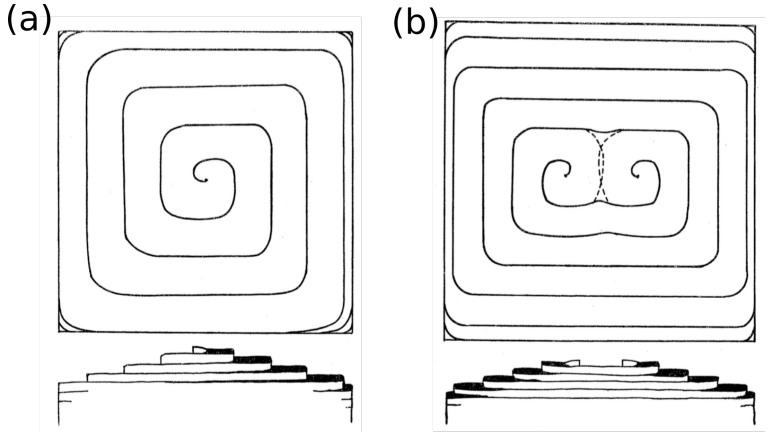

Figure 1.36: (a) Single spiral grown around a single dislocation. (b) Double spiral that grew around a dislocation pair of opposite signs [48].

1951 [48]. It occurs when a screw dislocation reaches the surface, and creates a step. This step will act as a nucleation site, and the adatoms arrange themselves along it. Because the step created by the screw dislocation slopes, and disappears into the crystal, the adatoms perpetually create steps as they nucleate. This is shown in figure 1.35. Growth around such step creates a spiral structure.

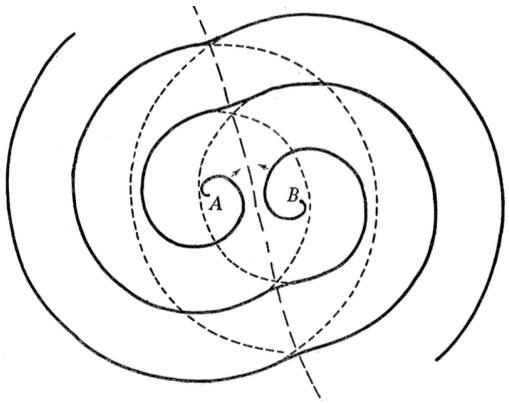

Figure 1.37: Growth of spirals initiated by a pair of screw dislocations of like sign [48].

Topology of the spirals depends on the sign of the screw dislocation that initiated the growth. A single spiral is created by a single dislocation, shown in figure 1.36(a). If there are two dislocations present with opposite signs, separated by a distance larger than $2\pi\rho_c$, where ρ_c is the critical radius, they start to grow independently, and form a

double spiral when they overlap. This is shown in figure 1.36(b). If the distance between them is smaller, no spiral growth occurs [48].

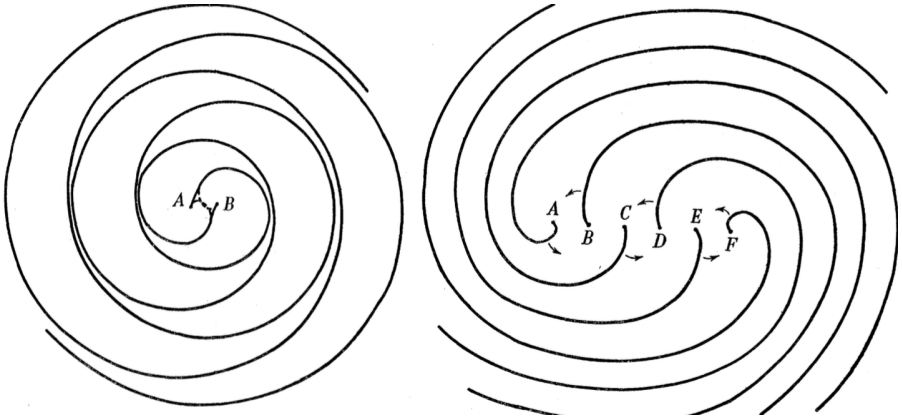

Figure 1.38: Growth of spirals initiated by dislocations within a $2\pi\rho_c$ distance [48].

Dislocation pairs of like signs separated by larger than $2\pi\rho_c$ exhibit similar growth to opposite sign pairs. They turn separately until they meet. Following that, they grow as one spiral, as it is shown in figure 1.37 [48].

When the dislocations of like sign are closer, growth still occurs. These spirals have no intersection point except in the origin, which means that they will grow separately. Turns of both spirals reach the whole area. This statement is true for any number of dislocations within a $2\pi\rho_c$ distance. This case is illustrated in figure 1.38 [48].

The shape of the spirals are determined by the dependence of the growth rate on crystallographic orientation. In the case when it is independent, the shape is circular, when it is dependent, spirals are deformed into polygons [48].

1.5.4 Thermal grooving

In polycrystalline thin films grooves can spontaneously develop along grain boundaries at elevated temperatures. This process is called thermal grooving, or dewetting, and was theoretically investigated by W. W. Mullins [49]. He derived the time dependent profile of a surface around a grain boundary during thermal grooving. Two cases were considered: one where the transport of the matter was driven by evaporation-condensation, and one where it was driven by surface diffusion. For both cases partial differential equations are derived, solved and the results are compared.

In the case of evaporation-condensation, it is shown that evaporation is proportional to the surface area. Therefore, the flux of atoms emitted by a curved surface is higher

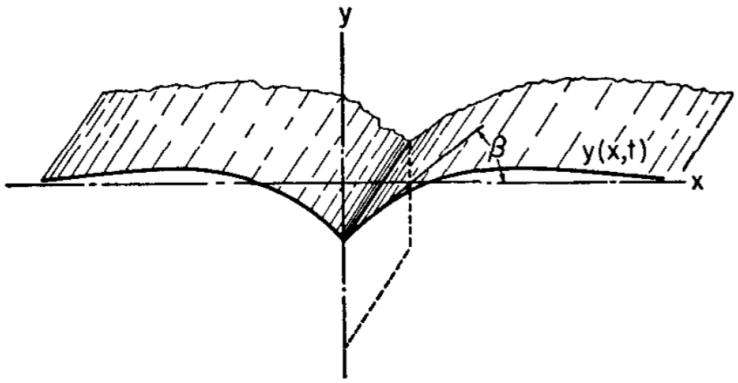

Figure 1.39: Grain boundary groove with angle β [49].

than by a flat surface. On the other hand, the mean free path of the metal atoms in the vapour phase is large, thus the density of metal vapour is equal all across the surface. The result is that less atoms condensate on the curved surface than evaporate, the grain boundary walls shift away from their original position, and the groove deepens [49].

The partial differential equation is derived from the approximation of the Gibbs-Thompson formula, which gives the equilibrium vapour pressure ($p = \Delta p + p_0$) of a surface segment with curvature K:

$$\frac{\Delta p}{p_0} = K\frac{\gamma\Omega}{k_B T}, \tag{1.33}$$

where p_0 is the equilibrium vapour pressure of a plane surface, γ is the surface free energy, Ω is the molecular volume, k_B is the Boltzmann constant, and T is the temperature. This approximation is valid when p/p_0 is close to 1 [49].

The number of atoms emitted by the surface can be calculated from the equilibrium pressure. It is required that the densities of the vapour over the flat and the curved surfaces are equal. The net loss of atoms of the curved surface equals the difference between the number of atoms leaving the curved surface and the number of atoms leaving the flat surface. From this, the rate of advance of a profile element can be obtained. Using the definition of curvature, the differential equation for the time evolution of the surface profile is the following:

$$\frac{\partial y}{\partial t} = Ay'', \quad \text{where} \quad A = \frac{p_0\gamma\Omega^2}{(2\pi M)^{\frac{1}{2}}(k_B T)^{\frac{3}{2}}}, \quad y'' = \frac{\partial^2 y}{\partial x^2}, \tag{1.34}$$

and M is the molecular mass. This partial differential equation is solved with boundary conditions $y(x,0) = 0$, and $y'(0,t) = \tan\beta = m$, where β is the angle of the surface, shown is figure 1.39 [49].

The solution is the following:

$$y_{ec}(x,t) = -2m(At)^{\frac{1}{2}}\,\mathrm{ierfc}\left(\frac{x}{2(At)^{\frac{1}{2}}}\right), \quad \text{where} \tag{1.35}$$

$$\mathrm{ierfc}\,(t) = \int_t^\infty \mathrm{erfc}\,(u)du = \frac{2}{\sqrt{\pi}}\int_t^\infty\int_u^\infty e^{-z^2}dz.$$

The time evolution of the surface profile is plotted in figure 1.40. Parameter A was arbitrarily chosen as 5000, β was 5 degrees. The units along the x, and y axis are a measure of length, the numbers in the legend are a measure of time.

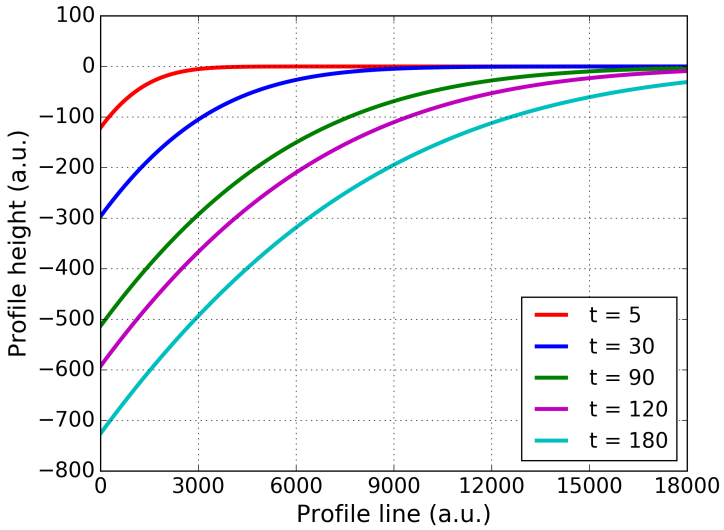

Figure 1.40: Surface profile when shaped by evaporation-condensation plotted for different time intervals. The units along the x, and y axis are a measure of length, the numbers in the legend are a measure of time.

When surface diffusion drives the transfer of matter, the partial differential equation is derived from the dependence of the chemical potential (μ) on the surface curvature:

$$\mu(K) = K\gamma\Omega. \tag{1.36}$$

Nernst-Einstein relation gives the average velocity of the surface atoms in the presence of a chemical potential gradient:

$$v = -\frac{D_s}{k_B T}\frac{\partial \mu}{\partial s} = -\frac{D_s \gamma \Omega}{k_B T}\frac{\partial K}{\partial s}, \tag{1.37}$$

where D_s is the surface diffusion coefficient, and s is the arc length along the profile [49].

Equation 1.37 multiplied by the number of atoms per unit area (ν) gives the surface current. Divergence of the surface current gives the increase of the number of atoms per surface area. From this, the partial differential equation for the surface profile is the following:

$$\frac{\partial y}{\partial t} = -B\frac{\partial}{\partial x}\left[\frac{1}{\sqrt{(1-y'^2)}}\frac{\partial}{\partial x}\left(\frac{y''}{(1+y'^2)^{\frac{3}{2}}}\right)\right], \quad \text{where} \quad B = \frac{D_s \gamma \Omega^2 \nu}{k_B T}. \tag{1.38}$$

An approximation of equation 1.38 was solved. The approximation is valid in cases when m is small, and is referred to as small slope approximation:

$$\frac{\partial y}{\partial t} = -By''''. \tag{1.39}$$

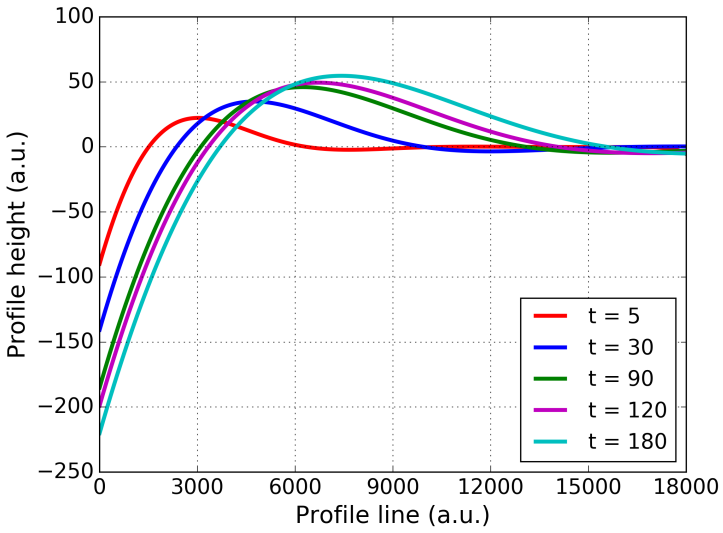

Figure 1.41: Surface profile when shaped by surface diffusion plotted for different time intervals.. The units along the x, and y axis are a measure of length, the numbers in the legend are a measure of time.

The boundary conditions were: $y(x,0) = 0$, $y'(0,t) = \tan\beta = m$, and $y'''(0,t) = 0$. The solution of equation 1.39 is the following function:

$$y_{sd}(x,t) = m(Bt)^{\frac{1}{4}}\mathrm{Z}\left(\frac{x}{(Bt)^{\frac{1}{4}}}\right), \quad \text{where} \quad Z(u) = \sum_{n=0}^{\inf} a_n u^n. \tag{1.40}$$

The a_n coefficients are:

$$a_0 = -\frac{1}{2^{\frac{1}{2}}\Gamma\left(\frac{5}{4}\right)} = -0.7801, \quad a_1 = 1, \quad a_2 = -\frac{1}{2^{\frac{3}{2}}\Gamma\left(\frac{3}{4}\right)} = -0.2885,$$

$$a_3 = 0, \quad a_{n+4} = a_n \cdot \frac{n-1}{4(n+1)(n+2)(n+3)(n+4)} \tag{1.41}$$

The time evolution of the surface profile is plotted in figure 1.41. Parameter B was arbitrarily chosen as 10^{10}, and β was 5 degree. The units along the x, and y axis are a measure of length, the numbers in the legend are a measure of time.

For both cases the groove ($x = 0$) deepens as time passes. The overall shape of the surface profile does not change with time. The most important difference is that while evaporation-condensation profile increases monotonously along the profile line, surface profile that was shaped by surface diffusion shows a local maxima close to the groove, after which it flattens [49]. These results are used to describe our films in section 2.3.

2

Growth and characterisation of rhenium thin films

In this chapter the growth of rhenium onto single crystal Al_2O_3 is presented. First the preparation of the substrate, then the evaporation of rhenium is described. From the frequently observed deposition rates, the temperature of the evaporating rhenium is estimated. Next, the epitaxial relationship between the rhenium and the substrate is presented, and the critical thickness of the rhenium is calculated from the misfit strain. In the following section, the effect of temperature on the properties of the film is studied on samples with 3 different thicknesses, then it is shown that rhenium undergoes dewetting, when its thickness reaches approximately 10 nm. Lastly, a model to calculate the temperature of the growing film is presented.

2.1 Growth procedure

2.1.1 Preparation of the substrate

Single crystal α-Al_2O_3 substrates were purchased from Neyco. They were all 0.5 mm thick, and measured either 15 mm x 15 mm or 13 mm x 13 mm in the plane.

Al_2O_3 is a frequently used substrate material, as many preparation procedures as users can be found in literature [50–62]. Based on these examples, we have also developed our own predeposition treatment.

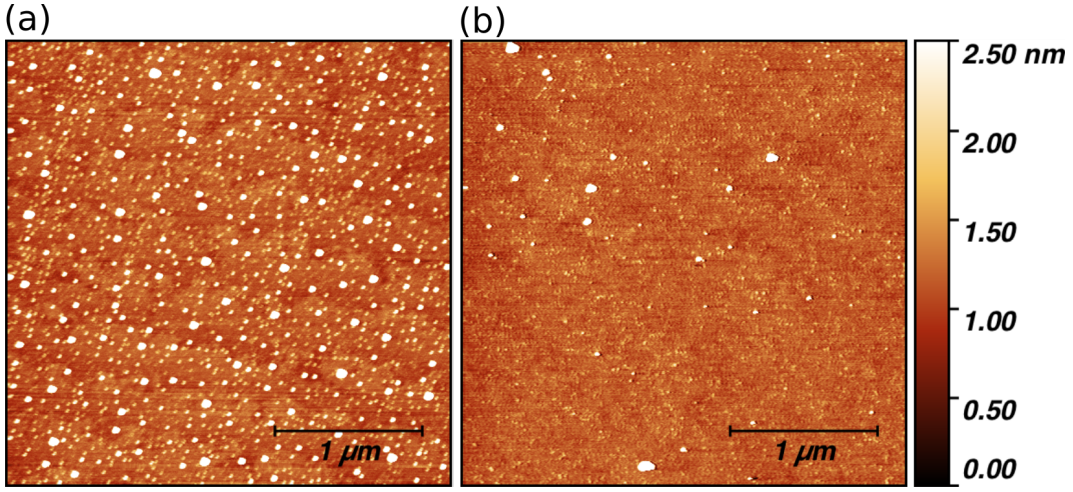

Figure 2.1: (a) 3 μm x 3 μm AFM height image taken of the Al_2O_3 substrate as received. The surface is covered with particles of various sizes. (b) 3 μm x 3 μm AFM height image taken of the Al_2O_3 substrate after cleaning, before annealing. A few larger particles are still visible, but their density is significantly reduced.

AFM height image taken of a substrate as received is shown in figure 2.1(a). The surface is covered with particles of various sizes. From analysing the profile of the surface, the height of the larger particles was found to be approximately 10 nm. Number density measured on a 6 μm x 6 μm AFM image was 130 per μm^2. These small islands can influence the growth of rhenium by acting as a nucleation site. They have to be removed.

Substrates were first washed in an RBS detergent solution purchased from Chemical Products then rinsed with deionised water. Afterwards, they were cleaned with acetone in ultrasonic bath. Finally, they were put in ethanol and dried in nitrogen flow. An AFM height image taken after the cleaning procedure is shown in figure 2.1(b). A few larger particles are still visible but their density is reduced ten fold, to only 10 per μm^2.

After the cleaning, substrates were placed in a clean quartz tube to be annealed in a muffle furnace in air atmosphere. Quartz at this temperature can get soft, and deform due to creeping. For this reason, we designed a special tube: the inner quartz tube is supported by an outer alumina tube. A drawing of our design is shown in figure 2.2.

The temperature was raised linearly to 1100°C from room temperature in 7 hours. Substrates were annealed at this temperature for an hour, then the furnace was switched off and let to cool. It took 4-5 hours to reach room temperature.

AFM height image taken after the heat treatment is shown in figure 2.3. As a result

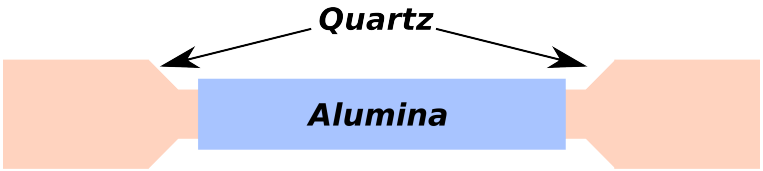

Figure 2.2: Schematics of the tube used for the heat treatment of the substrates: the quartz tube is supported by an outer alumina tube to prevent deformation.

of the high temperature annealing and the inherent misalignment of the surface, regular arrangement of steps develops. The planefit procedure, described in section 1.4.2, was not applied to the data, it shows the real surface structure. The steps have heights corresponding to the spacing between the consecutive layers along the c axis in Al_2O_3, 0.22 nm. This is highlighted in figure 2.4, where the surface profile extracted from figure 2.3 along a line, is shown. The true miscut of the substrate can be determined from the width (w) and the height (h) of the steps as follows: $\arctan \alpha = h/w$. The sample shown in figure 2.3 had a miscut of 0.034°. Miscuts were always found to be smaller than 0.1°.

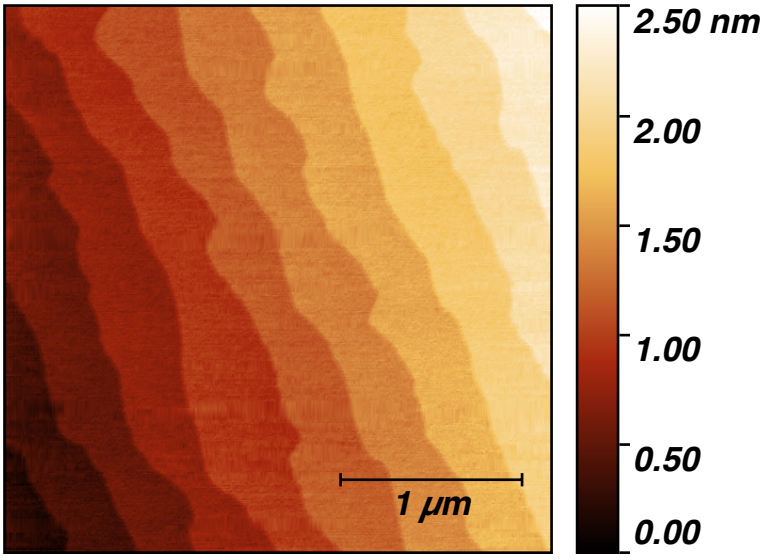

Figure 2.3: 3 µm x 3 µm AFM height image showing the steps that develop on the substrate as a result of the heat treatment. The planefit procedure was not applied to the data.

To find the two good temperature and time parameters of the heat treatment, annealing experiments were conducted where only one parameter, either the temperature or

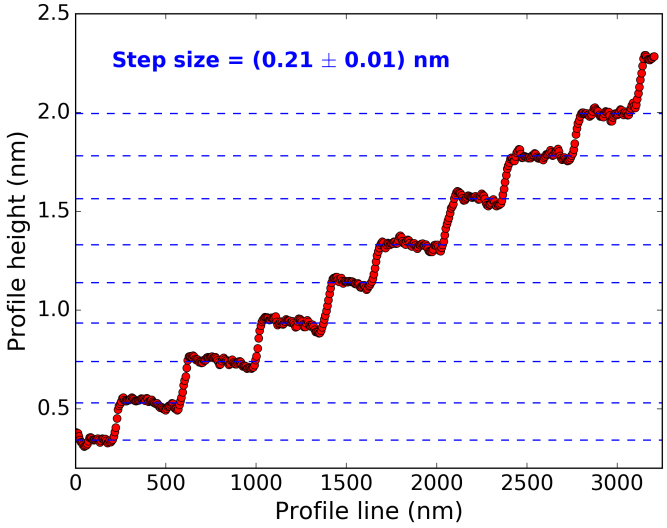

Figure 2.4: Surface profile extracted from the AFM height image showing the step structure.

the time, was changed. Examples of the surfaces that develop are shown in figures 2.5(a) and 2.5(b).

For the sample shown in figure 2.5(a), the annealing time was reduced to 30 minutes. Monoatomic steps began to form on the substrate, but small islands can be observed along the edges. The time was not long enough to complete the development of the steps.

In case of the example shown in figure 2.5(b), the temperature of the annealing was reduced to 1000°C. The step edges appear to be sharp, well defined but they are decorated with kinks, and large islands can be observed in-between. The temperature does not appear to be high enough to straighten the steps, and atoms do not have enough energy to reach the edges, so they form islands. If islands grow large enough they coalesce with the step edge, and form a structure similar to a peninsula.

On a nominally flat (001) Al_2O_3 surfaces only steps with single atomic height develop when they are annealed under 1200°C. The coalescence of steps occurs at higher temperatures [50, 51, 54, 55]. Our setup was limited to 1100°C.

As was described before, in crystalline Al_2O_3 along the c axis two Al layers and an O layer alternate. This means three different surface terminations are possible: single Al, double Al, or O. Which dominates in single crystal substrates, has been the subject of

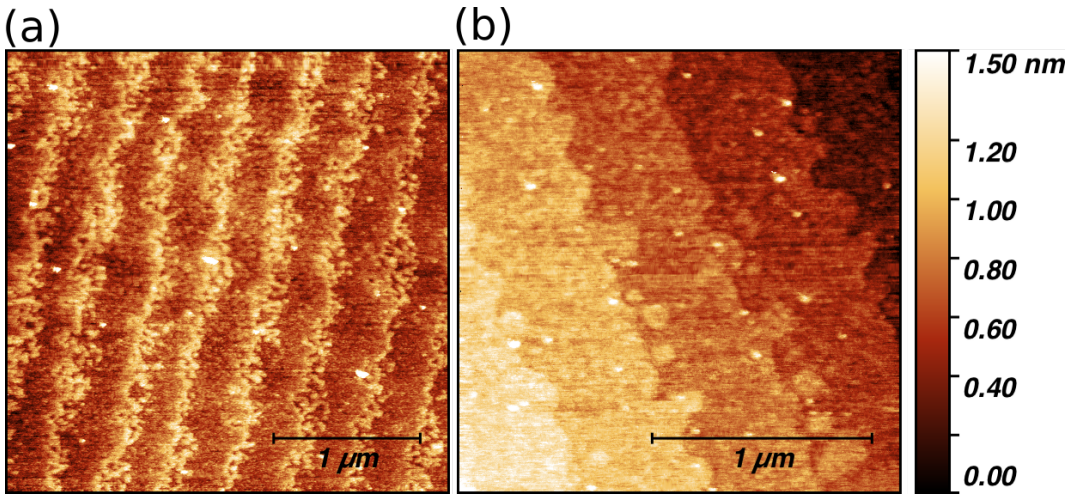

Figure 2.5: (a) Surface after annealing at 1100 °C for 30 minutes. (b) Surface after annealing at 1000 °C for an hour. The planefit procedure was not applied to the data.

extensive experimental and theoretical studies [56–62], and so far has yielded no agreement. Walters et al. found the termination to be single Al layer based on low energy electron diffraction patterns, regardless the treatment preceding the measurement [61]. Sang et al. claims to have been able to manipulate the termination of the Al_2O_3 substrate by different surface treatments in ultra high vacuum: annealing resulted in Al layer, O-plasma treatment produced OH termination, and O-plasma treatment following Ar^+ ion etching yielded O rich top layer [59]. A theoretical study by Wang et al. states that Al is the most stable termination even in O_2 atmosphere at high pressures, and oxygen can only be stable if hydrogen is present at the surface, in which case the termination is hydroxide [56]. We followed the same substrate preparation procedure for all our substrates and the resulting properties of the substrates and the deposited thin films were reproducible. We do not know what the terminations of the substrates are but we expect them to be consistent.

2.1.2 Evaporation of rhenium

Rhenium has a low vapour pressure, and is therefore difficult to evaporate. As such, it needs to be heated to high temperatures (∼3000°C) to achieve a reasonable deposition rate.

The first investigation of liquid evaporation of mercury into vacuum was conducted by Hertz in 1882 [63]. He concluded that the evaporation rate of a liquid cannot exceed a

maximum value at a certain temperature, and this theoretical maximum is obtained only when as many atoms or molecules leave as would be required to exert the equilibrium vapour pressure (P_v) on the surface, and none of them return. This means that the number of atoms/molecules (dN_{source}) evaporating from a surface area A_{source} during time dt has to be equal to the impingement rate on the surface corresponding to the pressure inside the chamber (P):

$$\frac{dN_{\text{source}}}{dt} = A_{\text{source}}(P_v - P)\sqrt{\frac{N_A}{2\pi M k_B T}}, \tag{2.1}$$

where N_A is the Avogadro number, M is the molar weight, k_B is the Boltzmann constant and T is the temperature measured in K [44].

The observed evaporation rates are generally below the theoretical maximum. Based on this Knudsen argued that a certain fraction of the molecules contribute to the vapour pressure but not to the evaporation rate. The theoretical evaporation rate should be multiplied by the thus defined evaporation coefficient, α. This form of equation 2.1 is known as Hertz-Knudsen equation. α is measured experimentally, and here is considered to be 1. Later Langmuir showed that the Hertz-Knudsen equation applies to the evaporation from the surface of a solid as well [44].

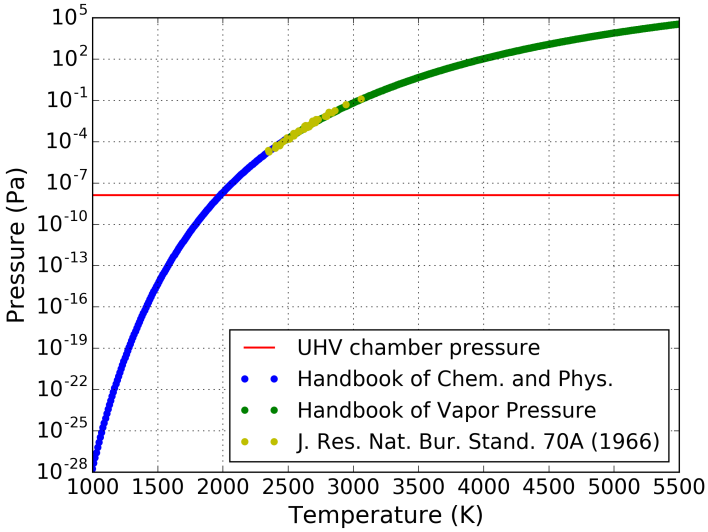

Figure 2.6: Vapour pressure of rhenium found in references [64], [65], and [66].

The vapour pressure can be calculated using the empirical equations 2.2 and 2.3. The parameters and their range of validity for rhenium is listed below.

Between 298 K - 2500 K [64]:

$$\log P_v(\text{Pa}) = 5.006 + A + BT^{-1} + C\log T,$$
$$\text{where } A = 11.543, \quad B = -40726, \quad C = -1.1629. \tag{2.2}$$

Between 2480 K - 5915 K [65]:

$$\log P_v(\text{Pa}) = (A + BT^{-1} + C\log T + DT + E^2)\cdot 133.322,$$
$$\text{where } A = -31.5392, \quad B = -3.2254\text{e}4, \quad C = 12.215,$$
$$D = -1.2695\text{e}{-3}, \quad E = 3.7363\text{e}{-8}. \tag{2.3}$$

The vapour pressure of rhenium was measured by Plante et al. in a narrow temperature range that overlaps with the range of validity of equations 2.2 and 2.3 [66]. This experimental data was used to check the values given by the equations. The results of equations 2.2 and 2.3, and the values found in reference [66] are shown in figure 2.6. The calculated data from both equations and the experimentally measured data match well.

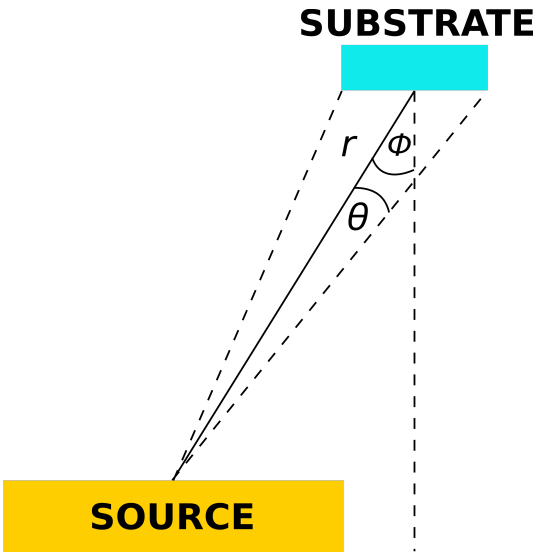

Figure 2.7: Geometry of the source and the substrate.

The deposition rate is given by the evaporated particles that reach and stick to the substrate. For the sake of simplicity, the assumption is that the sticking coefficient is 1. Every particle reaching the substrate sticks to it.

The number of particles that reach the surface of the substrate depends on the geometry of the setup. To calculate the arrival rate, the following equation can be used for

the Knudsen cell, which is an evaporation cell, where the source material is enclosed, and its vapour can escape through a small hole:

$$\frac{dN_{\text{sub}}}{A_{\text{sub}}dt} = \frac{dN_{\text{source}}}{dt}\frac{1}{\pi r^2}\cos\theta\cos(\theta+\phi), \tag{2.4}$$

where r is the distance between the source and the substrate, and the angles are shown in figure 2.7 [37].

In the MBE setup used, an open crucible was employed rather than a Knudsen cell, but equation 2.4 can be used to provide an estimate. The distance between the the substrate and the source is about 40 cm. The angles are small, and therefore considered to be 0 for this calculation.

The deposition rate was calculated using equation 2.4, and it is shown in figure 2.8. The deposition rate reaches the frequently observed values at around 3000°C.

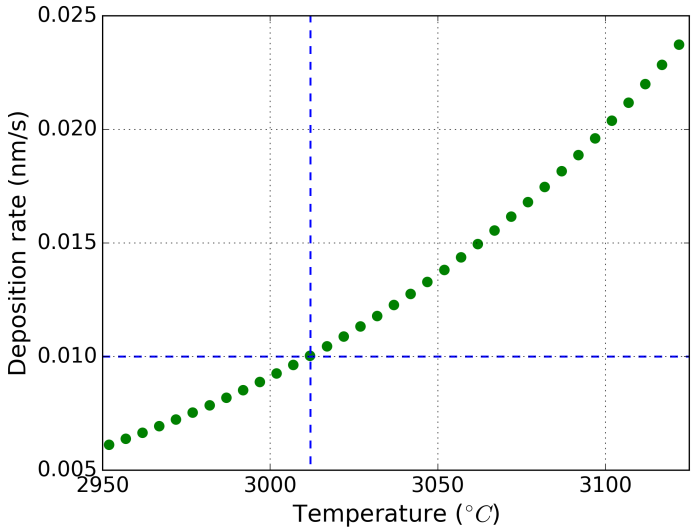

Figure 2.8: Deposition rate of rhenium. The observed deposition rate is shown with the blue dashed line.

It is possible to reach deposition rates higher than 0.1 Å/s, but small droplets are occasionally ejected from the charge over this value. The reasons behind this process are not yet understood. The ejection of droplets was recorded through a view port on the MBE setup, and a photo from this recording is shown in figure 2.9a.

The approximate position of the rhenium charge is shown in the figure with an arrow.

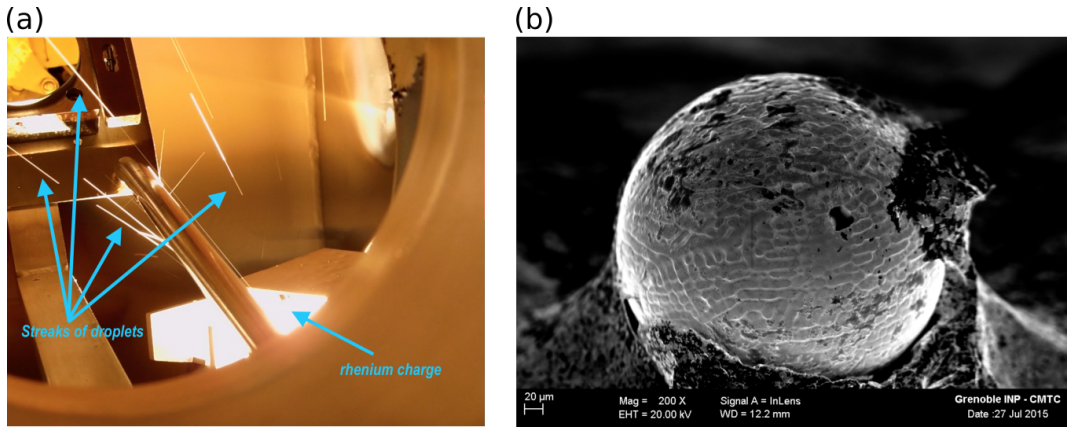

Figure 2.9: (a) Rhenium droplets ejected from the charge. (b) SEM image of a droplet found in the chamber.

Several streaks are visible, caused by the white-hot rhenium particles leaving the charge at high speed.

Several of these droplets were found when the chamber was opened. They are all perfectly round and have a smooth surface. A scanning electron microscope (SEM) image taken on one of them is shown in figure 2.9b. The analysis of the emitted characteristic X-rays induced by the electron beam in the SEM confirmed that the metal ball is indeed rhenium. The shape and the surface of the ball suggests that part of the rhenium is molten during deposition, and that the ejected droplets most likely to come from the liquid phase.

2.1.3 Rhenium on Al_2O_3

The aim of this section is to study the epitaxial relationship between rhenium and Al_2O_3, and to determine the thickness above which dislocations are expected to appear in the film.

The atomic arrangement in the first layers of the growing film mimics the lattice of the substrate, and thus the film is under a strain, induced by the substrate. This strain is called misfit, and its consequences in the relationship between Re and Al_2O_3 are discussed below.

In figures 2.10(a) and 2.10(b) the lattices of rhenium and Al_2O_3 are depicted with the epitaxial orientations. Figure 2.10(a) shows a single layer of rhenium on top of a single layer of Al - O octahedra viewed along the c axis. The rhenium atoms can be

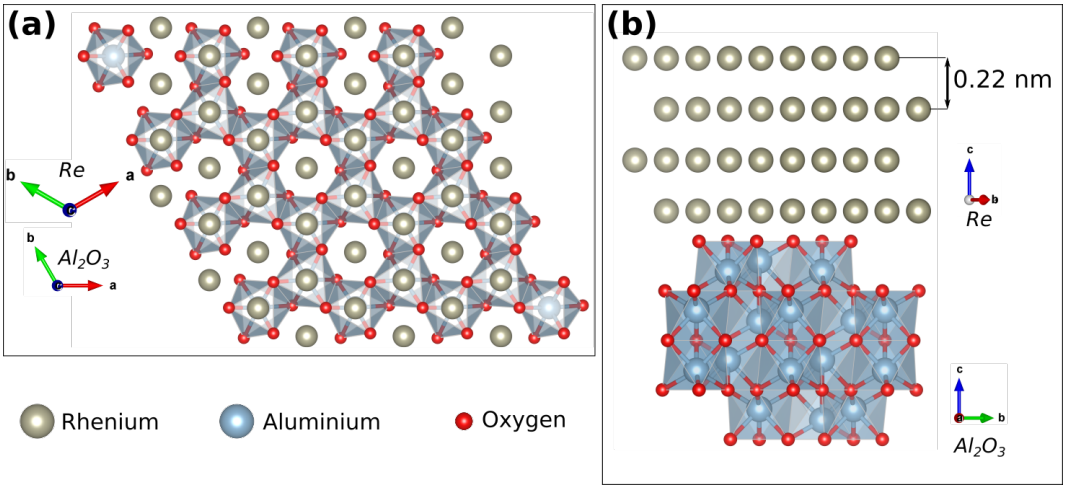

Figure 2.10: (a) A single layer of rhenium on top of a single layer of Al - O octahedra viewed along the c axis. (b) The view of the Re and Al_2O_3 lattices along the a axis of the substrate [19].

positioned on top of the Al atoms, and are thus neighboured by 3 oxygen atoms at each surface site. The number density of the rhenium atoms is higher in the lattice than the aluminium density in Al_2O_3, where only 2/3 of the octahedral positions are filled. This is why rhenium can be observed to be positioned in the empty hexagonal spaces as well. These sites have the same oxygen coordination as the Re atoms on top of the Al_2O_3 octahedra. We note that 3 out of 6 oxygens that are visible around the Re atoms belong to the lower plane of oxygens, and do not coordinate the rhenium atoms.

In figure 2.10(b) the view of the two lattices are shown viewed along the *a* axis of the substrate. The spacing between two rhenium planes is 0.22 nm.

The rhenium and the Al_2O_3 lattices match very well. There is an epitaxial relationship between the lattices, which with the Bravais-Miller indices is $(0001)Al_2O_3//(0001)Re$ and $<2\bar{1}\bar{1}0>Al_2O_3//<01\bar{1}0>Re$. The two lattices are rotated by 30° in-plane with respect to each other, which can be observed in figure 2.10(a). The angle of rotation was confirmed using XRD. The Φ scans measured on a film and its substrate are shown in figure 2.11. The (102) reflection of rhenium and the (104) reflection of the substrate were located, and the sample was rotated around the specular (001) direction. (001) axis of the substrate has trigonal symmetry, and indeed the equivalent reflections appear 120° apart. For rhenium this axis has sixfold symmetry, and its equivalent reflections are 60° apart. The angular separation between the reflections of the two materials is consistent with the 30°

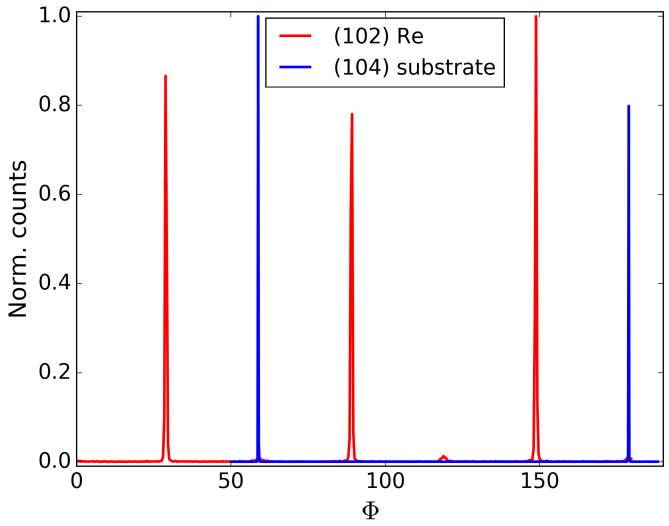

Figure 2.11: XRD Φ scans on the (102) equivalent reflections of rhenium, and (104) equivalent reflections of Al_2O_3 show the 30° rotation between the two lattices.

the rotation.

The 30° rotation is taken into account when calculating the misfit. Furthermore, the a lattice parameter of the the Al_2O_3 lattice was divided by 2. The misfit strain at room temperature is the following:

$$\epsilon_a(\mathrm{RT}) = \frac{a_s/2 - a_{\mathrm{Re}} \cos 30^\circ}{a_{\mathrm{Re}} \cos 30^\circ} = \frac{a_s - \sqrt{3} a_{\mathrm{Re}}}{\sqrt{3} a_{\mathrm{Re}}} = -0.0043. \tag{2.5}$$

This value corresponds to a very small misfit strain. As a comparison, ZnSe grown on GaAs has a lattice mismatch of 0.27%, BeTe on GaAs has -0.48%, and both are said to be nearly lattice-matched. The lattice mismatch and the elastic properties of the rhenium defines how thick it can grow in registry with the substrate, without defects [37].

The negative sign means that the rhenium lattice in bulk has a larger a lattice parameter than the substrate, and therefore when grown pseudomorphically on Al_2O_3, is compressed in-plane. As a result of the compression along both in-plane directions, the lattice extends out-of-plane. The strains are connected via the Poisson's ratio ν, which is 0.2894 for rhenium [67]:

$$\epsilon_c(\mathrm{RT}) = -\frac{2\nu}{1-\nu}\epsilon_a = 0.0035. \tag{2.6}$$

The sample is heated during deposition, which means both lattices are expanded. The value of misfit is therefore different at the deposition temperature than it is at room temperature. The high temperature lattice parameters can be obtained from the thermal expansions of the two materials along the a axis, which are the following:

Rhenium from 293 K to 1900 K [68]:

$$\frac{\Delta L}{L}(\%) = -0.195 + 6.513\text{e}{-4} \cdot T + 5.412\text{e}{-8} \cdot T^2 - 1.652\text{e}{-11} \cdot T^3. \tag{2.7}$$

Al_2O_3 from 239 K to 1900 K [69]:

$$\frac{\Delta L}{L}(\%) = -0.176 + 5.431\text{e}{-4} \cdot T + 2.150\text{e}{-7} \cdot T^2 - 2.810\text{e}{-11} \cdot T^3. \tag{2.8}$$

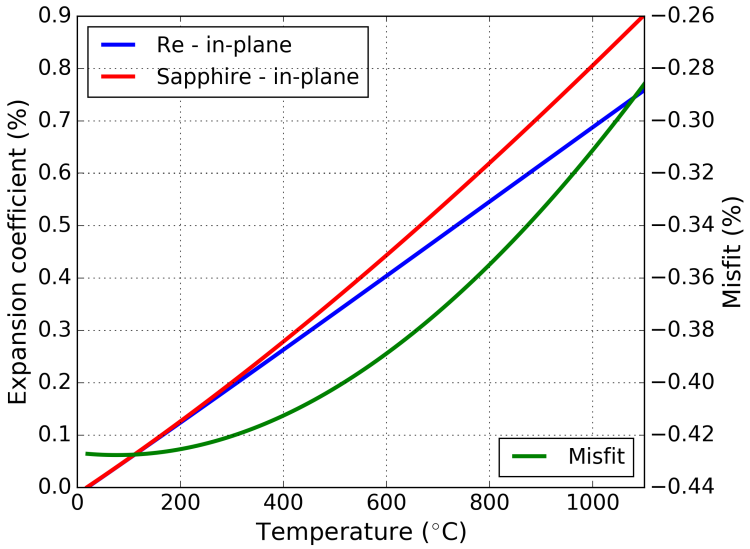

Figure 2.12: Thermal expansion coefficient of rhenium and Al_2O_3 and the obtained misfit as the function of temperature.

The misfit was calculated for a wide temperature range, and it is shown in figure 2.12 by the green curve. Figure 2.12 also shows the thermal expansion coefficients of the two materials along the crystal axis a. The sample temperature is between 700°C - 1000°C during deposition. The misfit changes one tenth of a percent between room temperature and 1000°C.

The strain caused by the misfit can only be accommodated by the growing film up to the critical thickness. When the critical thickness is reached, dislocations spontaneously appear to relieve the strain. The derivation to obtain the critical thickness was given in

section 1.5.2. The obtained formula is an approximation, which is valid until the critical thickness is larger than the magnitude of the Burgers vector. It is the following:

$$\frac{b_x^2 + b_y^2 + (1-\nu)b_z^2}{8\pi(1+\nu)b_x h_{cr}} \ln\frac{2h_{cr}}{r_0} = \epsilon_m \quad h_{cr} \gg b, \tag{2.9}$$

where b_x, b_y, and b_z are the components of the Burgers vector, ν is the Poisson ratio, r_0 is the dislocation core radius, h_{cr} is the critical thickness, and ϵ_m is the misfit strain.

In equation 2.9 the Burgers vectors of the dislocations are given by their Cartesian coordinates. How to obtain the Cartesian coordinates from Miller or Bravais-Miller indices of directions is explained in appendix C.

Six different Burgers vectors can exist in a hexagonal close-packed system. Four of them have the correct direction to relieve in-plane strain: $1/3 < 11\bar{2}0 >$, $1/3 < 11\bar{2}3 >$, $1/3 < \bar{1}100 >$, and $1/6 < \bar{2}203 >$ [45]. Each of these four Burgers vectors include six equivalent directions, which can be obtained by the permutation of the first three indices. Of these, the ones where the second index is negative, can relieve compressive strain.

The misfit strain as the function of the critical thickness calculated using equation 2.9 is shown in figure 2.13 for the four Burgers vectors. The core radius of the dislocation was chosen to be half the magnitude of each Burgers vector [46]. The horizontal line shows the misfit strain calculated for the temperature during deposition.

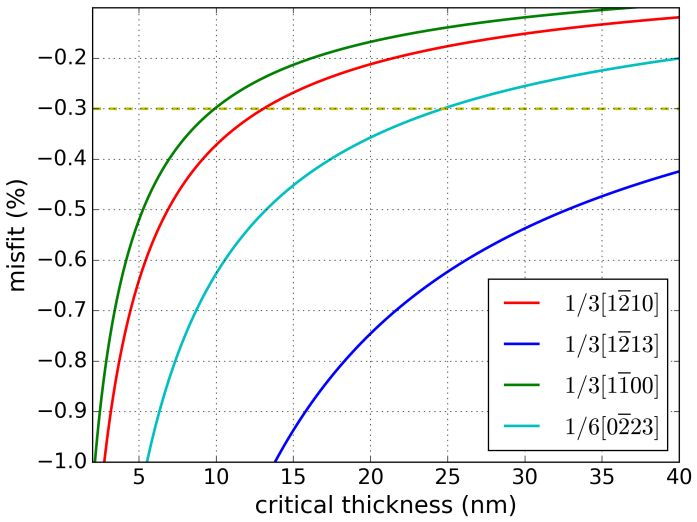

Figure 2.13: Misfit as the function of the critical thickness calculated using equation 2.9.

According to the calculation, rhenium grows pseudomophically up to approximately 10 nm thickness onto the Al_2O_3 substrate. The critical thickness obtained with Burgers vectors $1/3[1\bar{1}00]$ and $1/3[1\bar{2}10]$ are very close to each other, 10 nm and 13 nm, respectively. These dislocations are expected to be present above the critical thickness.

We observe spirals on films that are thicker than 20 nm. Screw dislocations can cause spirals to grow by creating a step on the surface. To create a step, the Burgers vector needs to have a nonzero final (Bravais-)Miller index. Burgers vector $1/6[0\bar{2}23]$ gave a critical thickness slightly below 25 nm. These dislocation can be present in the relaxed film and can be responsible for spiral growth.

The fourth Burgers vector $1/3[1\bar{2}13]$ has too high energy cost to be expected in the films.

2.1.4 Thin film growth

The instruments mentioned below are described in detail in section 1.3.1.

During the deposition of rhenium the substrate has to be heated to provide kinetic energy for the adatoms. There are two ways to heat the substrate, either by infrared radiation or by electron bombardment. Al_2O_3 is an insulator. If we applied electron bombardment, the sample would become charged because the excess electrons cannot be removed. The substrate cannot be heated with infrared radiation either, because it is transparent in that wavelength range. To overcome these issues 300 nm of tungsten is deposited onto the back side of the substrates.

After, the substrate is mounted on a sample holder with a hole in the middle. This way thermocouple is in contact with the back side, and also, the sample is heated directly, not through the sample holder. After the substrate is mounted, it is transferred to the deposition chamber, where it is degassed for a few hours at approximately 350°C. Figure 2.14 was taken through a view port of the MBE setup. The sample holder with the sample is mounted on the manipulator inside the chamber, and it is in position for deposition.

Before starting the deposition, the temperature of the substrate is set using the furnace in the manipulator head.

A 10 kV electron gun is used for the evaporation of rhenium. To achieve a deposition rates between 0.1 Å/s and 0.2 Å/s, the electron emission current of the gun is slowly increased to about 150 mA - 200 mA. When the deposition rate is stable, the shutter covering the substrate is opened, and the deposition begins.

The deposition rate is monitored, and kept constant by manually adjusting the emission current of the electron gun. The time required to deposit the desired thickness is

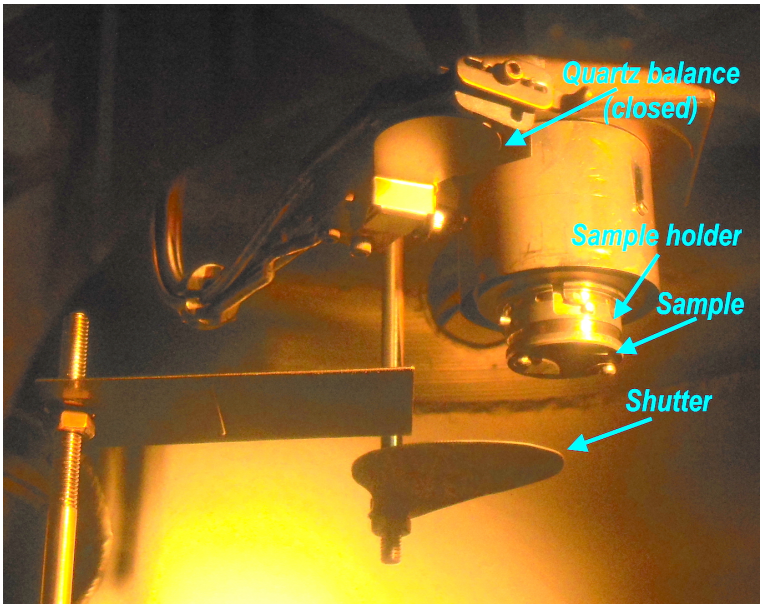

Figure 2.14: Sample inside the chamber, shutter and the quartz balance are also shown.

calculated and measured with a stopwatch. When the thickness is reached, the shutter is closed, and the electron gun is turned off. The temperature of the sample is slowly decreased, the heating electronics are turned off, and the sample is left to cool to room temperature before removing it from the vacuum.

2.2 Influence of the growth temperature

The influence of the substrate temperature on the surface topography and crystallographic properties of the thin film was investigated. 7 samples were deposited: two with 25 nm, three with 50 nm, and two with 100 nm thickness. Temperatures during the deposition of all the samples from each thickness group were different. Thicknesses and temperatures are summarized in table 2.1.

At the lowest temperature the current running through the heating filament behind the sample was set to 7.5 A. The thermocouple that touched the back side of the sample measured 800 °C. Based on the model described in [7], the actual surface temperature is estimated to be 700°C. At the second temperature the current was set to 8.5 A, the thermocouple measured 900°C, and according to the model the surface temperature was 770°C. For the highest deposition temperature, which was only used for sample E, the sample was heated by electron bombardment. 600 V was applied between the heating

filament and the sample, and the emission current was set to 50 mA. The temperature of the sample was approximately 1000°C.

Sample	A	B	C	D	E	F	G
Thickness (nm)	25	25	50	50	50	100	100
Temperature (°C)	800	900	800	900	1000	800	900

Table 2.1: Thicknesses and deposition temperatures of the samples discussed in this section.

Surfaces of these samples were investigated with AFM, and their crystallography was studied with X-ray diffraction. In this section, the results of these measurements are organized and discussed according to the thickness of the films.

Sample A and sample G was used to fabricate microwave resonators by Dumur et al. From the resonance frequency at a low temperature, the London penetration depth was determined [8].

2.2.1 25 nm thick films

Two samples with 25 nm thickness were prepared: sample A at 800°C and sample B at 900°C.

AFM study of the surfaces

AFM images taken of sample A and sample B are shown in figures 2.15(a) and 2.15(b), respectively.

The two surfaces are similar, both are covered with grains that have two distinct geometries: small ones, with approximately spherical shape, and larger ones with elongated, polygonial shape. The diameter of these grains are very similar also. Measuring 10 of both types, and averaging, it was found that the diameter of the larger ones is (96 ± 28) nm, and the smaller ones is (45 ± 12) nm on sample A. On sample B, the larger ones have diameter (73 ± 13) nm, and the smaller ones have (26 ± 4) nm. Grain sizes are more uniform, their standard deviations are smaller, on the sample which was deposited at higher temperature. This is visible in figure 2.15(b) in case of the small grains, which are almost identical, and appear to form a continuous, smooth layer.

Both samples are relatively flat, and aside from a few holes, there are no large deviations in height. However, the surface of sample A is jagged, it is rougher than sample B. The average roughness (R_a) can be measured by the arithmetical mean deviation. The

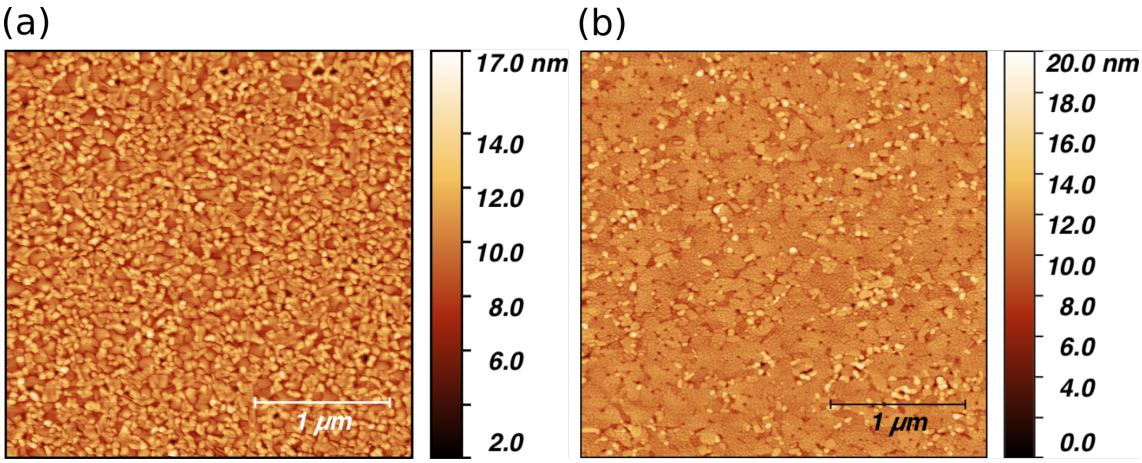

Figure 2.15: (a) 3 μm x 3 μm AFM height image shows the surface of the 25 nm thick sample deposited at 800°C, sample A. (b) 3 μm x 3 μm AFM height image shows the surface of the 25 nm thick sample deposited at 900°C, sample B.

average deviation of all points from a mean height value ($R_a = 1/N \sum_{j=1}^{N} |r_j|$) is calculated. This value for sample A is 1.27 nm, for sample B it is smaller, 0.98 nm.

Measurements on figures 2.15(a) and 2.15(b) are summarised in table 2.2.

25 nm		
	800°C (A)	900°C (B)
Diameter of larger grains (nm)	96 ± 28 (29 %)	73 ± 13 (18 %)
Diameter smaller grains (nm)	45 ± 12 (27 %)	26 ± 4 (15 %)
Average roughness (nm)	1.27	0.98

Table 2.2: Surface features measured in figures 2.15(a) and 2.15(b).

Higher deposition temperature results in a smoother surface, with more uniform grain size. However, on the sample deposited at 900°C there are still two distinct types of grains. They most likely have different orientations.

XRD θ-2θ measurements

θ-2θ scans of both samples are shown in figure 2.16. Both curves were normalised with respect to the (002) peak of rhenium, so that the differences can be read more easily. Both graphs are dominated by the (001), epitaxial orientation, which is signalled by the

large, higher order (002) and (004) peaks. There are 5 much lower intensity rhenium peaks, corresponding to 3 different orientations. Peak (110) is only present in the lower temperature sample. Orientation (101) is featured in both samples. Peaks from this orientation, (101) and (202), have a slightly lower intensity on the sample B. Finally, the intensity of (100) and (200) are higher on the sample B.

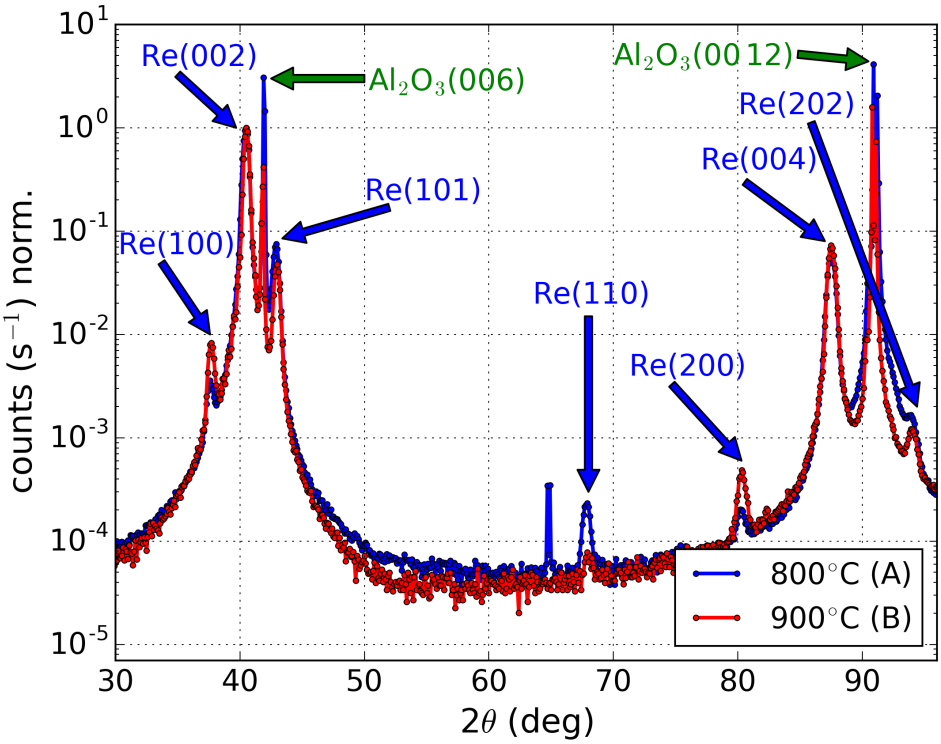

Figure 2.16: θ-2θ of the two 25 nm thick samples.

It is confirmed that rhenium grown on the (001) plane of Al_2O_3 prefers to grow along the (001) direction. Two orientations remain present in the sample grown at 900°C: (100) and (101). This could either mean both these orientations are stable as well, or it could be an anomaly. It could have been caused by contamination on the substrate, which decreased the mean free path of rhenium adatoms, and caused nucleation and growth along these direction. Conclusion can only be drawn after looking at more samples.

The shape of the (002) diffraction peaks appear similar on both samples. To verify this, they were fitted, and the fitting procedure is described below.

A close up of the (002) peak of rhenium measured on sample A is shown in figure 2.17.

The sample was probed with the copper Kα radiation. The intensity of the incoming X-ray beam is composed of two parts Kα1 radiation with wavelength 1.540562 Å, and one part Kα2 with wavelength 1.544398 Å. The substrate peaks are double, which can be observed on the (00 12) reflection in figure 2.16. A slight asymmetry can be observed in case of the rhenium peak as well. For this reason the sum of 2 functions was used to fit the data shown in figure 2.17: one corresponding to the copper Kα_1 radiation, the other to the Kα_2.

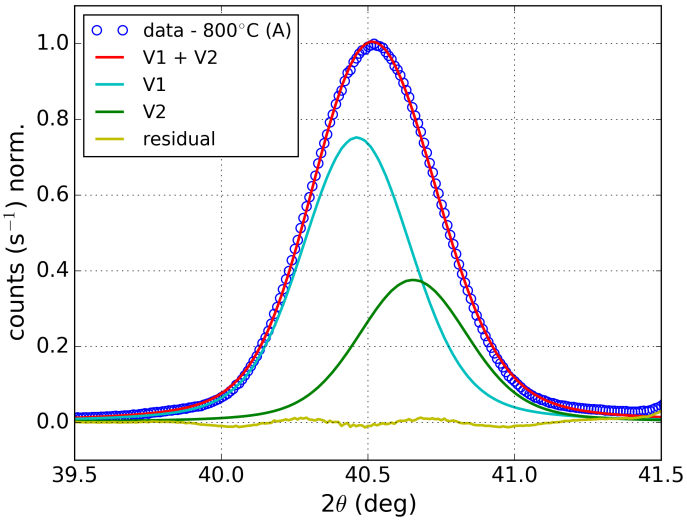

Figure 2.17: (002) reflection of sample A fitted with the sum of two Voigt functions.

As mentioned, the intensity ratio of the two components of the incoming beam is Kα1:Kα2 = 2:1. Thus, the integrated intensity ratio of the respective diffraction peaks ($I_{K\alpha_1}/I_{K\alpha_2}$) has to be 2:1. The integrated intensity of a peak depends on its amplitude and its full width half maximum (FWHM), both of which depend on the resolution of the diffractometer. The resolution of the diffractometer depends on the 2θ angle. The two peaks, corresponding to Kα_1 and Kα_2, are so close to each other, that resolution can be considered constant in that range. Their full width half maxima are expected to be equal, and the ratio of their amplitudes is expected to be 2:1. In the fitting procedure the ratio of amplitudes were fixed at the expected value, the full with half maxima were set to be equal, and the position of the Kα_2 peak was calculated from the Kα_1 peak using Bragg's law, equation 1.19.

The angular separation between the two peaks increases with the Bragg angle. In the

interval shown in figure 2.17 its value is around 0.1°. A few degrees of misalignment in the experimental setup can cause variations in the second digit after the decimal point of the separation. A parameter (ϵ) was allowed to correct the position of the second peak in the fitting procedure.

Two model functions are used for the fit of diffraction peaks. These two functions are the Gauss function ($G(x)$) and the Cauchy or, as it is also known, the Lorentz function ($L(x)$). The copper Kα emission line of the X-ray tube have a Lorentzian shape. Broadening due to small crystal size is also associated with a Lorentzian shape. However, broadening due microstrains is described by a Gauss function, because microstrain fields often exhibit a normal distribution of lattice spacing values around an average d_0 value. Therefore, diffraction peaks are usually well described by a mixture of these two functions [70].

The (002) rhenium peaks were fitted with the sum of two Voigt functions. The Voigt function is the convolution of a Gauss (G) and a Lorentz (L) function:

$$V(x) = \int_{-\infty}^{\infty} G(x')L(x-x')dx' \quad \text{where} \tag{2.10}$$

$$G(x) = \frac{1}{\sigma\sqrt{2\pi}} e^{-\frac{(x-x_0)^2}{2\sigma^2}}, \quad FWHM_G = 2\sqrt{2\ln 2}\sigma$$

$$L(x) = \frac{1}{\pi\gamma\left[1+\frac{(x-x_0)^2}{\gamma^2}\right]}, \quad FWHM_L = 2\gamma$$

The fit of the (002) rhenium peak of sample A is shown in figure 2.17. The individual Voigt curves corresponding to the two wavelengths are also shown. The results of the fits with their standard deviations are summarised in table 2.3.

XRD line profile analysis of epitaxial thin films is not straightforward. The film has a preferred orientation determined by the substrate that will reduce the number of diffraction peaks. A Williamson-Hall plot would allow us to separate size and strain contribution to peak broadening [71]. In this approach the parameters of each diffraction peak are plotted in a coordinate system with axis FWHM$\cdot\cos\theta$ and $2\sin\theta/\lambda$, and a straight line is fitted across the points. In our case, the film has a single dominant orientation, that results in two peaks which can reliably be fitted. This is not sufficient for the Williamson-Hall plot, this method is not suitable for epitaxial films.

The Warren-Averbach method makes use of the Fourier coefficients of at least two harmonic reflections [72]. For this, first, the 2θ scattering angle has to be transformed to

25 nm (002) Voigt fit		
	800°C (A)	900°C (B)
Peaks @	40.462 ° ± 0.001° 40.654° ± 0.007°	40.474° ± 0.004° 40.64° ± 0.02°
$FWHM_G$	0.372° ± 0.006°	0.31° ± 0.01°
$FWHM_L$	0.122° ± 0.004°	0.127° ± 0.009°

Table 2.3: Parameters of the Voigt functions fitted to the (002) rhenium peaks of the 25 nm samples

the magnitude of the scattering vector (q) using the following expression: $q = 4\pi \sin\theta/\lambda$. The presence of a secondary wavelength makes this transformation uncertain.

The analysis that relies on a single line takes advantage of the observation that was mentioned above: size broadening has Lorentzian shape, strain broadening has Gaussian shape. Based on this, the Lorentz and Gauss fractions in the fitted Voigt functions are interpreted to signal effects of size and strain, respectively [73].

Particle size can be determined from the FWHM using the Scherrer equation [74]. This equation can be derived from the interference function, given in equation 1.23, and gives a lower limit to the size of cubic shaped crystallites in the direction perpendicular to the reflecting planes. In our case this size is the thickness (t). The Scherrer formula is the following:

$$t = \frac{K\lambda}{\mathrm{FWHM} \cdot \cos\theta}, \tag{2.11}$$

where K is a geometrical factor approximately unity, and FWHM is taken in radians.

Thicknesses calculated from the Lorentzian width of the (002) peaks are 72 nm for sample A and 70 nm for samples B. This cannot be correct, because thickness was measured during deposition, and and is known to be approximately 25 nm.

The Gaussian contribution is thought to carry the strain broadening. Strain is a dimensionless quantity, that describes the variations of interplanar spacings in the crystal relative to the undistorted lattice parameter, d_0: $\epsilon = \Delta d/d_0$. The relationship between line broadening and strain can be obtained by differentiating Bragg's law:

$$\frac{\Delta d}{\Delta(2\theta)} = -\frac{d_0}{2}\cot\theta \quad \rightarrow \quad \langle\epsilon^2\rangle^{1/2} = \frac{\Delta(2\theta)}{2}\cot\theta. \tag{2.12}$$

$\Delta(2\theta)$ is identified as the integral breadth of the Gaussian part of the Voigt function, which can be converted to the FWHM: $\text{FWHM}_G = \Delta(2\theta)/\sqrt{2\pi}$ [70]. Thus the root mean square of the strains calculated from the (002) reflections are:

$$\langle \epsilon_A^2 \rangle^{1/2} = 0.004, \quad \langle \epsilon_B^2 \rangle^{1/2} = 0.003. \tag{2.13}$$

The obtained strains are in the range where misfit strain is expected to be.

What we can safely conclude based on the θ-2θ scans presented above is that the shape of the main (002) diffraction peak, ie. arrangement of the lattice planes parallel to the surface, is not greatly affected by temperature during deposition at these temperature values. We can see a slight decrease in the Gaussian width with the temperature increasing (table 2.3), which can mean there are less defects present in sample B. The nature of these defects cannot be established based on these measurement.

The Lorentzian widths are equal within the error bar, which is good sign considering that this width is expected to carry the size component of the broadening, and the two films have the same thickness. However, the calculated thickness is not what we know it is. The Scherrer equation was derived for cubic materials and cubic shaped grains. It is possible that rhenium thin films fall outside of its limits.

Discrepancies could arise when one tries to deconvolve the effect of size and strain on X-ray diffraction peaks. Soleimanian et al. used several methods to extract the crystallite size and strain from the same set of lines. The values they obtained from different methods differed by a factor of 2 or 3, but were of the same order. They did not obtain the same strain value for harmonic reflections either. Voigt profile fitting, the one used above, gave them the largest values [75].

XRD rocking curve measurements

The rocking curves of the (002) rhenium peaks of sample A and B were measured. Rocking curve measurement probes the angle distribution of the reflecting lattice planes around the lattice normal. The lateral coherence length, ie. lateral grain size also contributes to the broadening.

To compare the widths of the rocking curves of the two samples, the data was fitted using a function which is also a mixture of a Gauss and a Lorentz function, but easier to compute than the Voigt function. This is the Pearson VII function ($P(x)$), or as also known, the modified Lorentz function, and given by the following equation:

$$P(x) = \left[\frac{1}{1+(\sqrt[m]{2}-1)\frac{(x-x_0)^2}{w^2}}\right]^m, \quad FWHM_P = 2w. \tag{2.14}$$

This function is a Lorentz function in the $m = 1$ limit, and a Gauss function in the $m \to \infty$ limit [70].

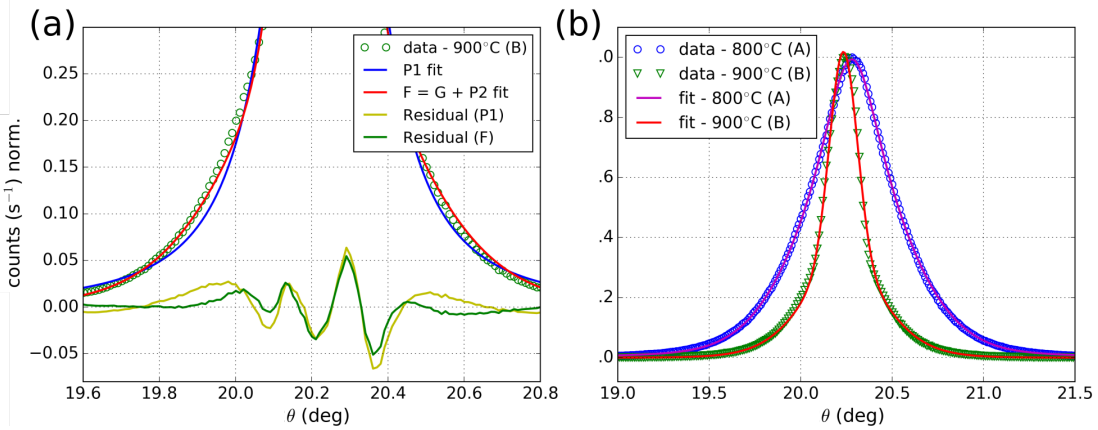

Figure 2.18: (a) Rocking curve of the (002) peak of rhenium on sample B fitted with a Pearson VII (blue) and Pearson VII plus Gaussian (red). The red curve describes the wide tails of the data better. (b) Rocking curves of the 25 nm samples fitted with the sum of a Pearson VII and a Gaussian.

The lower part of the rocking curve of the (002) rhenium reflection measured on sample B is shown in figure 2.18(a). The single Pearson VII function that was first fitted to the data is shown in blue, and it does not describe the data well. The tails of the experimental data exceed the tails of the model function. To account for the tail, a Gaussian contribution was added to the Pearson VII. This is shown in red in figure 2.18(a). This curve describes the data well, however, it is still not perfect. The measured peak is slightly asymmetric due to the two wavelengths. To perfectly describe the rocking curve, the number of functions would need to be doubled. Since the parameters are only used to compare between samples, to describe growth qualitatively, and not to extract quantitative parameters, the blue and the red curves in figure 2.18(a) are both deemed satisfactory.

The rocking curves of both samples A and B are shown in figure 2.18(b), with the sum of a Pearson VII and a Gaussian fitted to each. The data was normalised to help com-

parison. Parameters of the fits (both single Pearson VII and Pearson VII plus Gaussian) are listed in table 2.4.

25 nm (002) Rocking curves				
	800°C (A)		900°C (B)	
	P	P + G	P	P + G
χ^2	0.03	0.006	0.06	0.03
I_{ratio}	-	$I_P/I_G = 0.95$	-	$I_G/I_P = 0.75$
Peak @ (°)	20.2797 ± 5e−4	20.2799 ± 2e−4	20.2340 ± 4e−4	20.2338 ± 3e−4
$FWHM_G$ (°)	-	0.731 ± 0.004	-	0.178 ± 0.002
$FWHM_P$ (°)	0.531 ± 0.002	0.384 ± 0.003	0.225 ± 0.002	0.52 ± 0.02
m	1.84 ± 0.03	1.21 ± 0.02	1.20 ± 0.02	5 ± 1

Table 2.4: Parameters of the rocking curves measured on the 25 nm thick films.

It is immediately apparent from figure 2.18(b) that the rocking curve of sample B is significantly narrower. The single Pearson VII full width half maximum of this sample is less than half than that of sample A. This signals that the grains have lower mosaicity.

In figure 2.18(b) the $G + P$ fit is shown. For both samples one of the functions has a smaller width and a larger amplitude contributing mainly to the peak (peak contribution), and the other function has a larger width and a smaller amplitude contributing to the tail (tail contribution). These functions are not the same for the two samples. Where one is a Pearson VII, the other is a Gaussian. This was taken into account when comparing the parameters. The widths of the tail contribution has decreased from 0.731 to 0.52, the widths of the peak-function decreased over two folds, from 0.384 to 0.178, when the deposition temperature was increased.

The integral of the two components were calculated for both samples, and the peak-to-tail contribution ratios are listed in table 2.4. The ratios have a similar value for both samples. As it will be shown in the following sections, fitting of rocking curves measured on thicker samples does not require the addition of a second function. This means that the pronounced tails we see in case of these samples are due to the small thickness of the films. It is possible that it is caused by an intermediate layer of rhenium on the Al_2O_3. The volume fraction of this layer is reduced as the thickness grows, thus its effect cannot be observed on the rocking curves of thicker samples.

Conclusion on the 25 nm thick films

AFM study of the surfaces of the two samples revealed that higher deposition temperature results in a smoother surface with more uniform grains. XRD data shows that the dominant orientation is the epitaxial (001). There are three other orientations present in the films, intensities of two decrease with higher deposition temperature, rhenium favours the epitaxial orientation. The width of the rocking curve decreased by half on the film which was deposited at higher temperature. This means that the out-of-plane orientation of the grains are more uniform on sample B, it has lower mosaicity.

2.2.2 50 nm thick films

AFM study of the surfaces

Three samples with thickness 50 nm were investigated. Sample C, was deposited at 800°C, sample D at 900°C, and sample E at 1000°C.

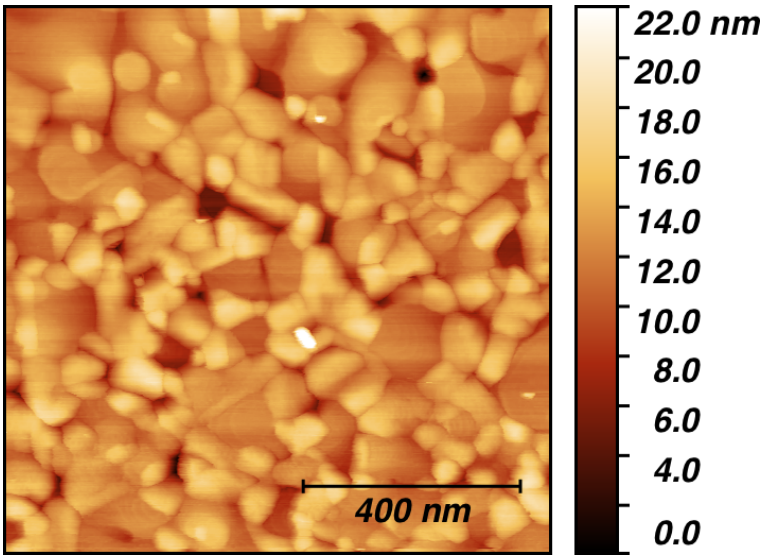

Figure 2.19: 1 μm x 1 μm AFM height image shows the surface of the 50 nm thick sample deposited at 800°C (sample C).

Their surfaces were studied with AFM. The topographies of sample C and sample D are shown in figure 2.19 and 2.21, respectively.

The surface of sample C is covered with grains. There are small grains with irregular shape and uneven surface, and there are larger grains with flat terraces. A closer look, in figure 2.20(b), reveals that the flat terraces are spirals. The height profile was measured

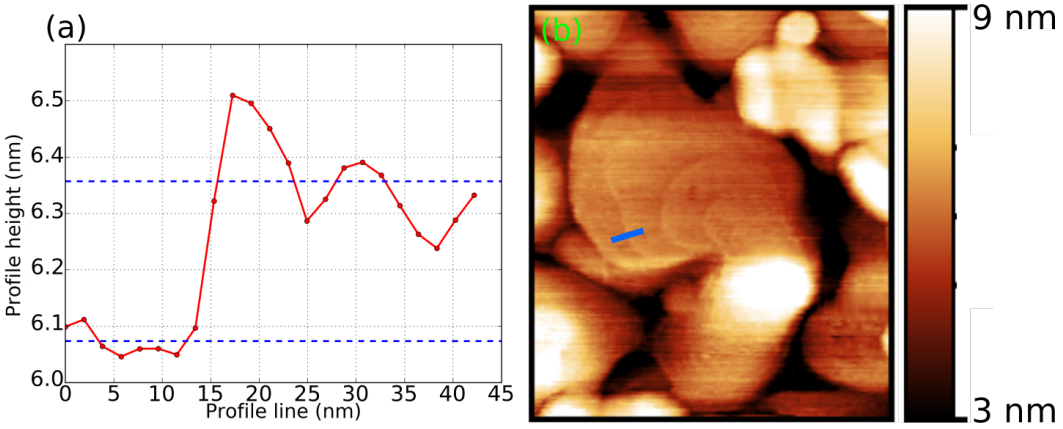

Figure 2.20: Sample C: 350 nm x 400 nm AFM height image showing an irregular spiral with the profile measured along the blue line.

along the blue line shown in figure 2.20(b), and is plotted in figure 2.20(a). The height difference between the two terraces is 0.28 nm which is in agreement with the spacing of atomic planes along the c axis of the rhenium lattice, 0.22 nm. Some of these spirals have irregular shapes, like the one shown in figure 2.20(b), others have regular concentric arms. They are all very small, they measure less than 100 nm across.

The surface of sample D is covered with large, even spirals, that are connected to each other by ridges. There are deep holes in between them. The profile of the holes cannot be determined using AFM, as they are too steep. Only the shape of the probe is measured.

A double spiral is shown in figure 2.22(b). The profile was measured along its slope, shown with the white line, and is plotted in figure 2.22(a). It shows several regular steps, and flat terraces. The average step height between consecutive turns extracted from this profile is 0.24 nm, which corresponds to the atomic spacing in the rhenium lattice along the c axis. The spirals on this sample are larger than on sample C, they measure up to 500 nm - 600 nm across.

The surface of the third sample, sample E, is shown in figure 2.23, and is very different than the others discussed before. The sample has partially dewetted during the deposition. The film is not continuous, but composed of large islands. The discontinuous nature of the film has been confirmed by transport measurement [7].

The surface of sample E appears to be very smooth, but in fact it is decorated by steps and terraces. An AFM image is shown in figure 2.23(b), where the colour scale was set to highlight the topography of the topmost surface. It shows large flat terraces and

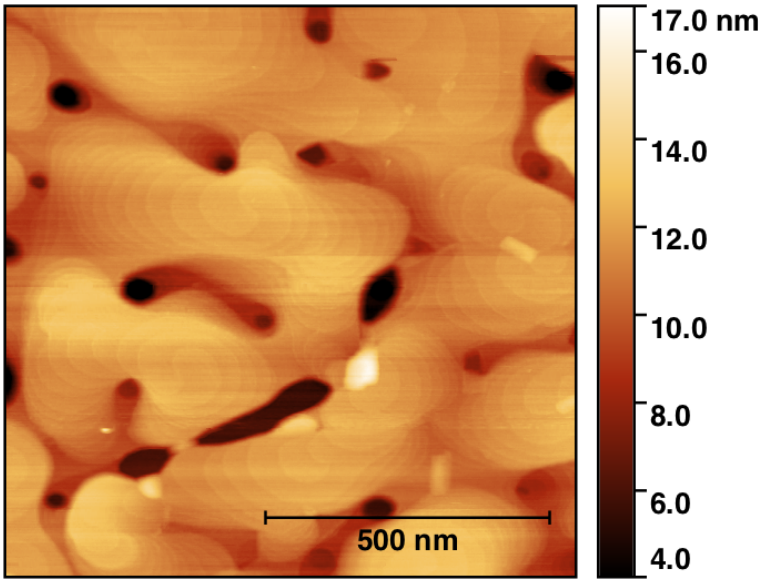

Figure 2.21: 1 µm x 1 µm AFM height image shows the surface of the 50 nm thick sample deposited at 900° C (sample D).

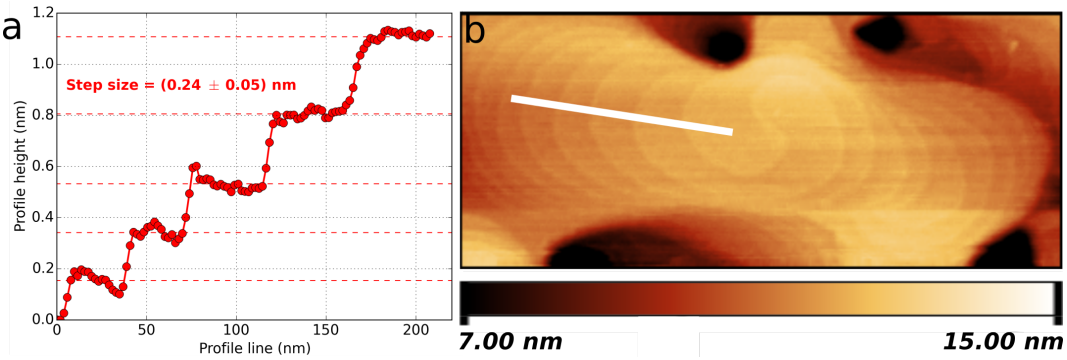

Figure 2.22: Sample D: 600 nm x 250 nm AFM height image showing a double spiral with the profile measured along the white line.

sharp steps. These steps are either monoatomic (0.22 nm) or an integer multiples of that.

The channels between the islands are wide enough on this sample to see the surface of them. A close up AFM image in shown in figure 2.24(b). Several small grains can be observed. The depth of the channel was measured along the three lines, shown in figure 2.24(b). The profiles are shown in figure 2.24(a) in corresponding colours. The profile of the drop itself cannot be determined because its shape is convolved with the

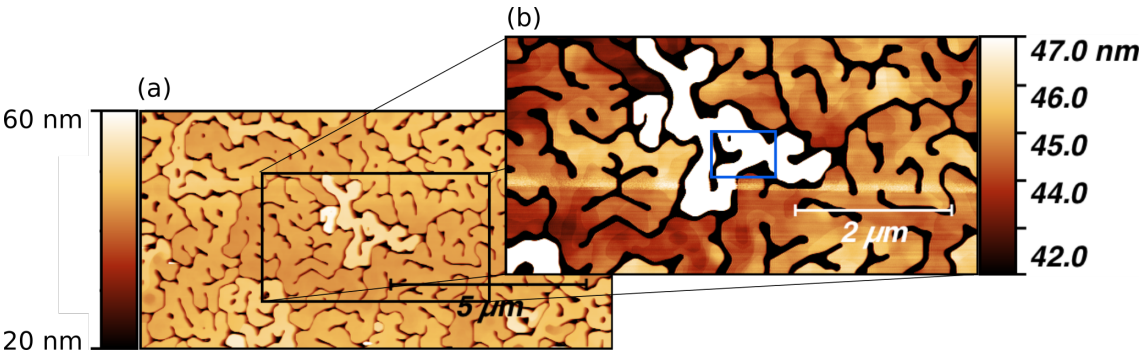

Figure 2.23: (a) 12 µm x 6 µm AFM height image showing the surface of the 50 nm thick sample deposited at 900° C (sample E). (b) 3 µm x 1.5 µm AFM height image. The colour scale was set to highlight the terrace structure of the topmost surface.

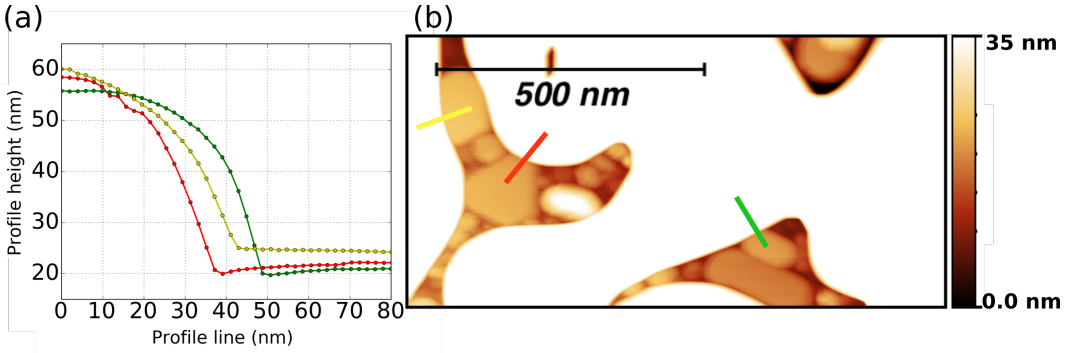

Figure 2.24: (b) 1 µm x 0.5 µm AFM image, a magnification of the area marked by the blue square in figure 2.23(b). The colour scale was set to highlight the bottom of the channels. (a) Surface profiles were measured along the coloured lines, and are plotted in corresponding colours.

shape of the AFM tip. The depth, however, can be measured, and it is 40 nm. This suggests that the whole thickness of the film took part in the dewetting process, and formed large islands.

On all three samples there are steps with heights corresponding to the spacing of planes in the lattice of rhenium along the c axis, which suggests that these objects have (001) orientation. Higher deposition temperature resulted in larger spirals on sample D, and in the reduction of the uneven grains that were present on sample C. Also, deep holes appeared in between the spirals when deposition temperature was increased. Sample E,

where the temperature was further increased partially dewetted. Islands formed that are not connected to each other. There are no signs of spirals, which suggests that dewetting eliminated the dislocations which, we assume, are responsible for spiral growth.

XRD θ - 2θ measurements

Standard resolution data. The crystallographic properties of the films were studied with X-ray diffraction. θ-2θ scan of all three samples are shown in figure 2.25. Graphs were normalized to the (002) peak of rhenium to help comparison.

The (001) orientation is the dominant in this case as well. Besides, there is a small peak corresponding to the (101) orientation on sample C which is not present in the spectrum of sample D or E. The (100) reflection, and its higher order (200) reflection are only featured on sample D. Finally, the (110) peak gradually decreases as the deposition temperature is increased. Samples E does not show any other orientation but the (001).

The (002) peak of rhenium was was fitted with the sum of two Voigt functions,

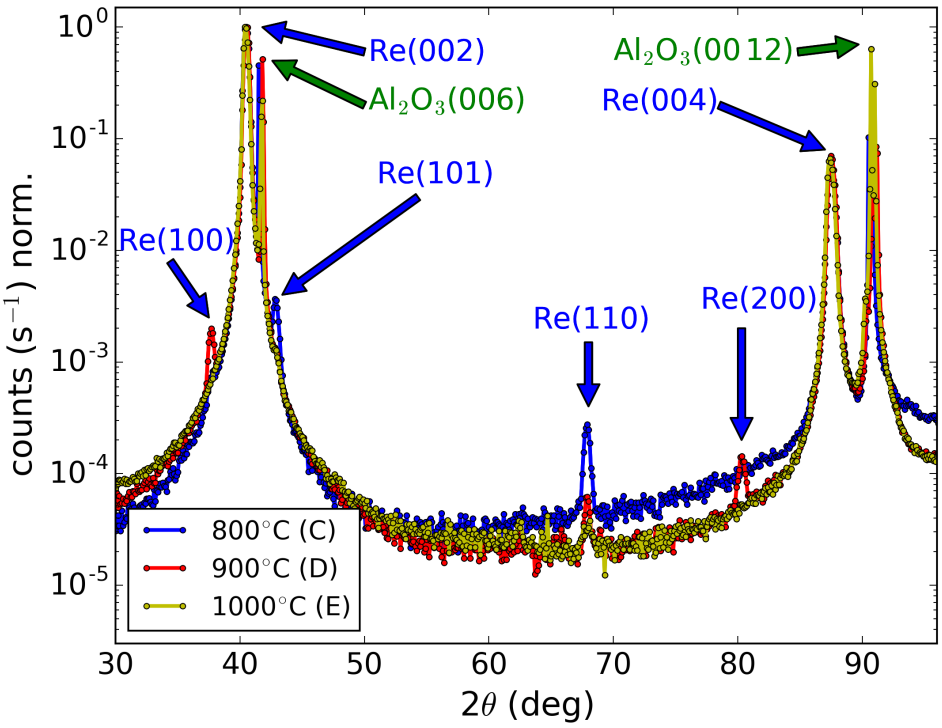

Figure 2.25: θ-2θ of the three 50 nm thick samples.

equation 2.10. The same fitting procedure was applied, as described previously for the 25 nm thick films. Parameters of the fits are summarized in table 2.5.

50 nm (002) Voigt fit			
	800°C (C)	900°C (D)	1000°C (E)
Peaks @ (°)	40.454 ± 0.001	40.478 ± 0.001	40.4185 ± 0.0004
	40.640 ± 0.007	40.625 ± 0.006	40.624 ± 0.002
$FWHM_G$ (°)	0.386 ± 0.006	0.364 ± 0.004	0.246 ± 0.003
$FWHM_L$ (°)	0.028 ± 0.004	0.043 ± 0.003	0.092 ± 0.003

Table 2.5: Parameters of the Voigt fits of the (002) rhenium peaks measured on the 50 nm thick samples.

The Lorentzian widths are increasing with the deposition temperature. The reason behind this increase is unknown. The Scherrer equation (eq. 2.11) used with the Lorentzian width does not give correct results for the film thickness.

The Gaussian widths decrease significantly with the increasing deposition temperature. This is expected, especially in case of the dewetted sample, sample E.

The root mean square of the strains can be calculated from the Gaussian widths using equation 2.12. The following strain values were obtained:

$$\langle \epsilon_C^2 \rangle^{1/2} = 0.004, \quad \langle \epsilon_D^2 \rangle^{1/2} = 0.003, \quad \langle \epsilon_E^2 \rangle^{1/2} = 0.002. \tag{2.15}$$

All three of them are in the range where misfit strain is expected.

High-resolution data. Samples C and D were also measured using the Rigaku SmartLab high-resolution diffractometer.

In figure 2.26 the θ-2θ scan on the (002) rhenium peak of sample D is shown. The sharp, lower intensity peak at the higher angle side in figure 2.26 is the (006) reflection of the substrate.

On both sides of the largest, central peak oscillations can be observed. The frequency of these oscillations is inversely proportional to the number of lattice planes scattering in phase. The presence of these clear fringes indicates that the layer is highly crystalline, with a well-defined lattice spacing throughout the thickness.

The experimental data was first fitted with the interference function ($I(q)$), given in equation 1.23. This function describes the scattering by N number of parallel lattice

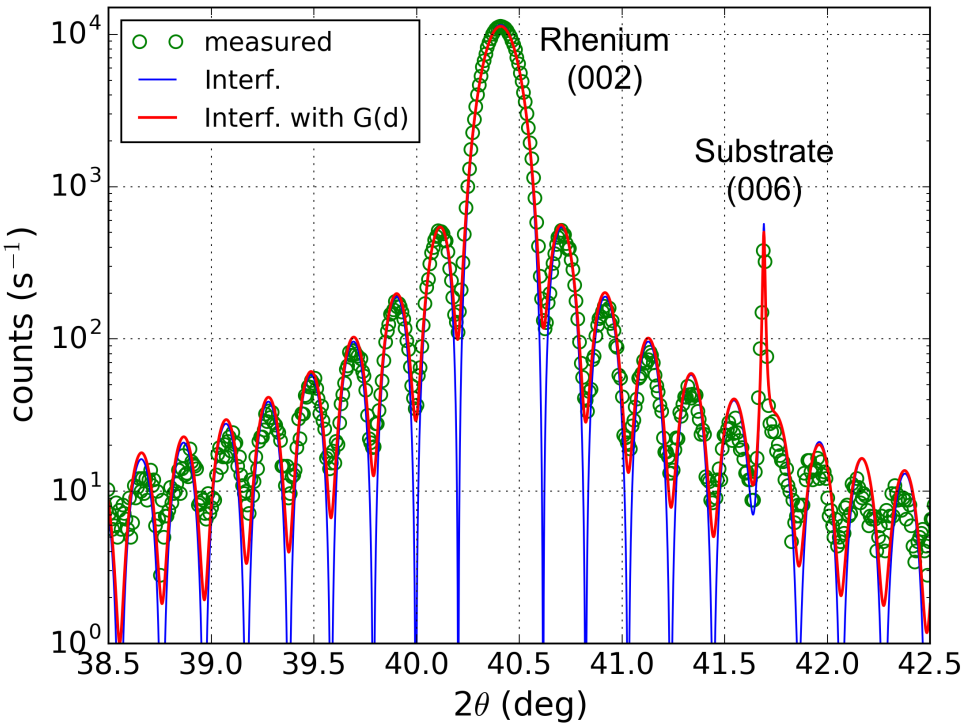

Figure 2.26: High-resolution X-ray scan of the (002) peak of rhenium with the (006) peak of the substrate (sample D). Only every fifth datapoint is shown.

planes with d spacing. To use equation 1.23, 2θ angles had to be converted to scattering vector q using the following formula:

$$q = \frac{4\pi \sin\theta}{\lambda}. \tag{2.16}$$

The (006) peak of the substrate was included in the fit, a Lorenz function was used to describe it.

The fit of the interference function is shown with the blue line in figure 2.26. It looks almost perfect at the scale of the plot: the periodicity matches the data, the intensity of each peak looks correct, and also the shoulder that appear on the side of the substrate peak is well described.

However, upon magnification, the shortcomings of this model appear. This is shown in figure 2.27. A definite broadening can be observed on the main peak, and on the

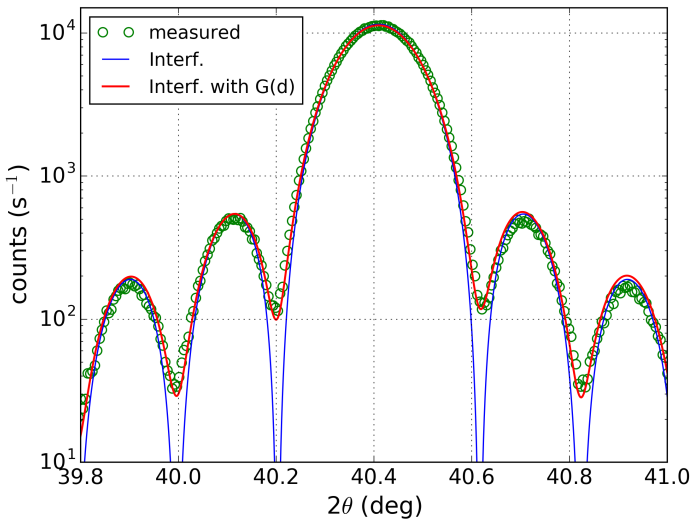

Figure 2.27: A magnification of figure 2.26, the (002) peak of rhenium on sample D. Only every third datapoint is shown.

fringes too. This is the reason that while the positions of the minima align well between the measurement and the blue curve, the maxima are slightly shifted. The intensities at the minima are at larger values on the measured data, while the model function minima go to zero.

To account for the broadening, disorder was introduced in the model lattice in the form of a Gaussian distribution of crystal plane spacings. This concept is shown in figure 2.28. The lattice is composed of N lattice planes, all with slightly different spacings. To achieve the Gaussian distribution of lattice parameters, a constant Δd multiplied by a random number was added to the average d_0. This random number was chosen from a Gaussian distribution centred on 0, with standard deviation 1.

The structure factor was then calculated by adding up the scattered plane wave from each lattice planes with a phase factor, which was calculated from the distance the radiation travels in the crystal. The scattered intensity was obtained by taking the absolute square of the structure factor. The formula describing this is the following:

$$I_{\mathrm{mod}}(q) = \left| \sum_{i=1}^{2000} \left[1 + e^{-iqd_1} + e^{-iq(d_1+d_2)} + \cdots + e^{-iq(d_1+d_2+d_3+\cdots+d_{N-1})} \right] \right|^2, \qquad (2.17)$$

where $d_i = d_0 + \Delta d \cdot \mathrm{rand}(0,\, 1)$.

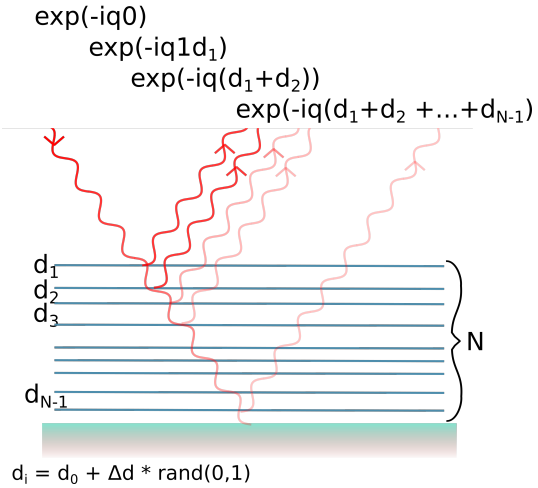

Figure 2.28: Scattering of X-ray wave from parallel planes that are slightly disordered.

Due to the random number generator, the resulting curves are not consistent. To improve this, a summation running from 1 to 2000 was introduced. This can have a physical interpretation as well: it can account for inhomogeneities that are inevitable in the sample. This aspect is not investigated further here, the number of sampling was increased until the resulting curves were consistent.

Function 2.17 was fitted by hand, because it is a demanding calculation. Parameters were adjusted to the last digit until improvement could be observed on the fit and in the value of χ^2. The errors listed in table 2.6 were taken as 1 on the last digit. Results and standard deviations of the parameters obtained from both fits are listed in table 2.6.

50 nm (002) fit by equation 2.17		
	800°C (C)	900°C (D)
N	215 ± 0	204 ± 0
d_0	(0.22302 ± 1e−6) nm	(0.22303 ± 1e−6) nm
$FWHM_d$	(0.0093 ± 1e−4) nm	(0.0065 ± 1e−4) nm

Table 2.6: Parameters of the fit of the high-resolution (002) rhenium peaks with the modified interference function, equation 2.17.

The fit is shown by the red curve in figure 2.26 and 2.27. It perfectly describes the intensity variations of the fringes, and the broadening as well.

In figure 2.29 the (002) peaks of both samples are shown. The fringes are denser on sample C, more lattice planes take part in the scattering process. Also, the intensity difference between the minima and the maxima is smaller on this sample, which is a sign of a more disordered film.

It is visible on figure 2.29 that the disorder introduced in the system does not destroy the fringes on the diffraction pattern. The agreement between the thus modified interference function and the experimental data is improved with the disorder. The widths and positions of the peaks and fringes, and the vertical positions of the minima and maxima are all well matched.

The distributions of d lattice parameters used in the calculation are shown in a histogram in figure 2.30. The full width half maximum of the distribution used for sample C is indeed wider.

The root mean square strains can be calculated from the full width half maxima using the following formula: $\langle \epsilon^2 \rangle^{1/2} = \mathrm{FWHM}_d / d_0 \cdot 1/(2\sqrt{2 \ln 2})$. The obtained strain values are the following:

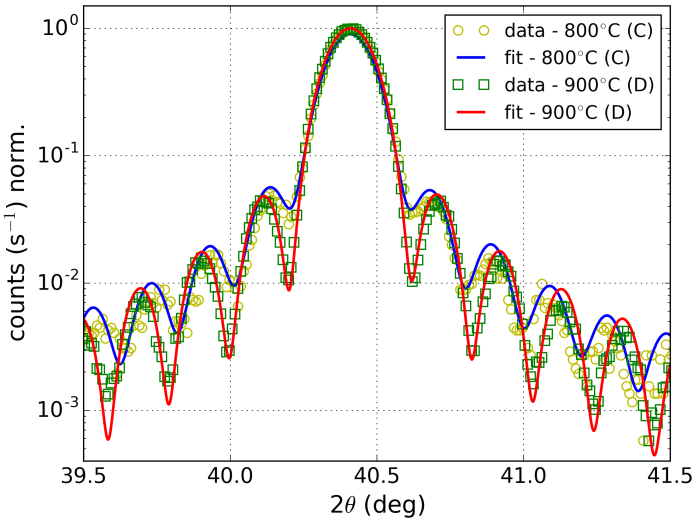

Figure 2.29: The high-resolution (002) peaks of rhenium measured on the 50 nm samples and fitted with the modified interference function, equation 2.17. Only every sixth datapoint of both datasets is shown.

$$\langle \epsilon_C^2 \rangle^{1/2} = 0.018, \quad \langle \epsilon_D^2 \rangle^{1/2} = 0.012 \tag{2.18}$$

The strain values calculated here are a magnitude larger than the ones obtained from the low-resolution measurement, shown in equation 2.15.

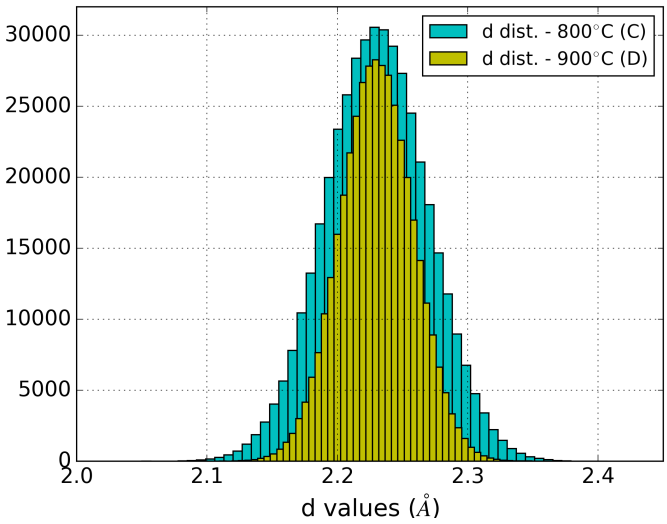

Figure 2.30: The distributions of lattice plane spacings used for the fits shown in figure 2.29, to describe the intensity variation of the fringes, and the slight broadening of the main peak.

By multiplying N and d the average rhenium thickness that takes part in the scattering can be calculated:

$$t_C = 47.9 \text{ nm} \quad t_D = 45.5 \text{ nm}. \tag{2.19}$$

Thickness values confirm the thickness expected from the quartz balance measurement during deposition.

Simulation of the standard resolution data. To verify the validity of the modified interference function, the standard resolution data was simulated from the fitted modified interference function curves.

The substrate is a high quality single crystal, and its (006) peak is very close to the (002) peak of the rhenium. The (006) reflection of the Al_2O_3 should only show the

instrumental broadening. As an approximation, its Lorenzian fit shifted to the rhenium (002) peak position (θ_1) was used as the resolution function of the instrument.

The modified interference function fitted to the high-resolution (002) peak of sample D ($I_{\mathrm{mod}}^{\mathrm{film}(002)}(\theta,\theta_1)$), and the Lorentz function fitted to the Cu Kα_1 (006) peak on the standard resolution data ($L^{\mathrm{sub}(006)}(\theta,\theta_1)$) were convolved. The result of the convolution is what would have been measured with the standard resolution instrument, using only the Cu Kα_1 radiation ($S_{\lambda_1}(\theta,\theta_1)$). The Cu K$\alpha_2$ contribution ($S_{\lambda_2}(\theta,\theta_2)$) needs to be added. The result of the convolution was divided by two, as dictated by the intensity ratio of the two wavelengths, and then it was shifted by the angular difference corresponding to the secondary wavelength ($\Delta\theta$). This is the Kα_2 contribution. The two parts were then added.

The following formulation attempts to summarise the procedure described above:

$$S(\theta) = S_{\lambda_1}(\theta,\theta_1) + S_{\lambda_2}(\theta,\theta_2), \text{ where} \tag{2.20}$$

$$S_{\lambda_1}(\theta,\theta_1) = \int_{-\infty}^{\infty} I_{\mathrm{mod}}^{\mathrm{film}(002)}(\theta,\theta_1) L^{\mathrm{sub}(006)}(\theta-\theta',\theta_1)\,d\theta', \text{ and}$$

$$S_{\lambda_2}(\theta,\theta_2) = 0.5\, S_{\lambda_1}(\theta,\theta_1+\Delta\theta).$$

All the functions above have two arguments, the first argument (θ) is a running parameter, the second argument refers to the position of the maximum. The thus computed curve ($S(\theta)$) should look similar to the (002) reflection measured by the low-resolution instrument.

The result of this simulation is shown in figure 2.31. The fringes are still visible, but significantly damped. The shape of the simulated curve matches well the shape of the measured data. The width of the simulated (002) is narrower than the measured, but the difference is small. The shape of the low-resolution data is reproducible from the high-resolution data.

We see the signature of lattice distortions on the high-resolution data. These measurements do not tell what the source of the lattice distortion are, or where in the lattice they may be. The lattice mismatch can only account for some of the strain, but it only affects the bottom part of the film, in proximity of the substrate. Spirals cover the surface of the sample D, and some can be observed on sample C too. This suggests, according to the theory of spiral growth [48], the presence of screw dislocations. The strain field of a screw dislocation is proportional to $b/(4\pi r)$ with a cosine or sine coefficient depending

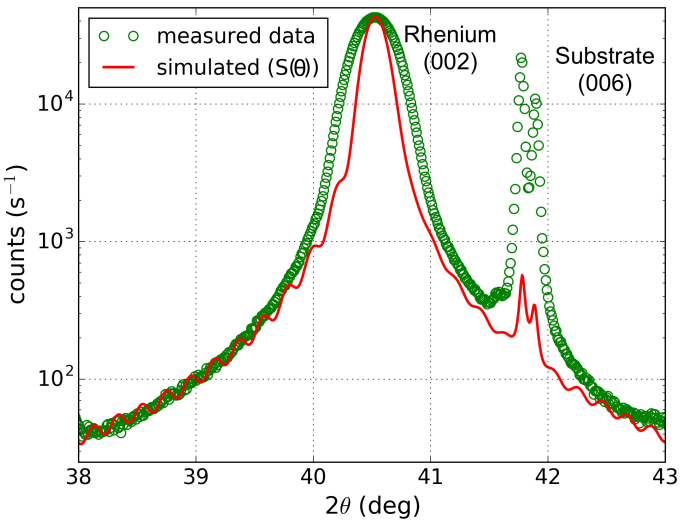

Figure 2.31: Standard resolution data simulated from the high-resolution data of the (002) peak of rhenium (sample D). As an approximation, the substrate peak was used as the resolution function. The red curve is the result of the convolution of the fitted high resolution curve, and the approximate resolution function (equation 2.20).

on the component of the strain. Here b is the Burgers vector of the dislocation, which is in the range of the lattice parameter, and r is the distance measured from the core of the dislocation. The strain a few nanometers away from a dislocations can be in the range calculated in 2.18, thus dislocations could account for the at least some of the strain.

XRD rocking curve measurements

The rocking curves of samples C, D, and E were measured. All three of them are shown in figure 2.32. They were fitted with Pearson VII function, equation 2.14. The fits are also shown in figure 2.32.

A single Pearson VII function describes these rocking curves well, the addition of a second function was not necessary this time. The parameters of the fits are listed in table 2.7.

The rocking curves are becoming significantly narrower with the increasing deposition temperature. This is consistent with the larger objects observed on the AFM images of sample D and E. This result also suggests that the mosaicity of the film is decreased.

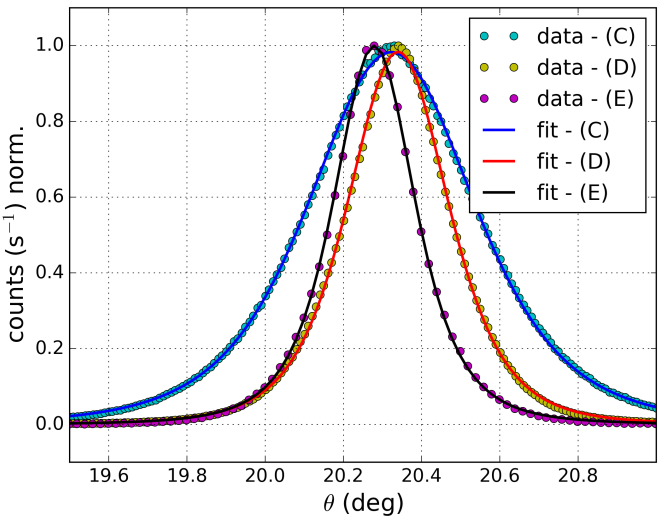

Figure 2.32: Rocking curves measured on the (002) peaks of the 50 nm samples.

50 nm (002) Rocking curves			
	800°C (C)	900°C (D)	1000°C (E)
Peaks @ (°)	20.3227 ± 0.0002	20.3397 ± 0.0002	20.2789 ± 0.0002
$FWHM$ (°)	0.4991 ± 0.0006	0.3035 ± 0.0005	0.2455 ± 0.0007
m	2.62 ± 0.02	2.50 ± 0.03	2.10 ± 0.04

Table 2.7: Parameters of the Pearson VII fit of the (002) rocking curves measured on the 50 nm samples.

Conclusion on the 50 nm thick films

AFM study of the surfaces showed spirals on both C and D films. On the lowest temperature sample several grains could be observed also. These grains disappeared from sample D. The size of the spirals grew 5 fold when 900°C temperature was applied, compared to 800°C. The third sample, which was deposited at he highest temperature dewetted, and formed atomically flat islands, which are not connected to each other. XRD data shows that the dominant orientation is the epitaxial (001). The three other orientations, which were observed on the 25 nm thick samples also, had low intensities, which decreased with higher deposition temperature. The only exception was the (100) peak, which was present only on sample D. The high-resolution (002) curves measured on

samples C and D evidenced less disorder in the higher temperature sample. The width of the rocking curves decreased with increasing deposition temperature.

2.2.3 100 nm thick films

AFM study of the surfaces

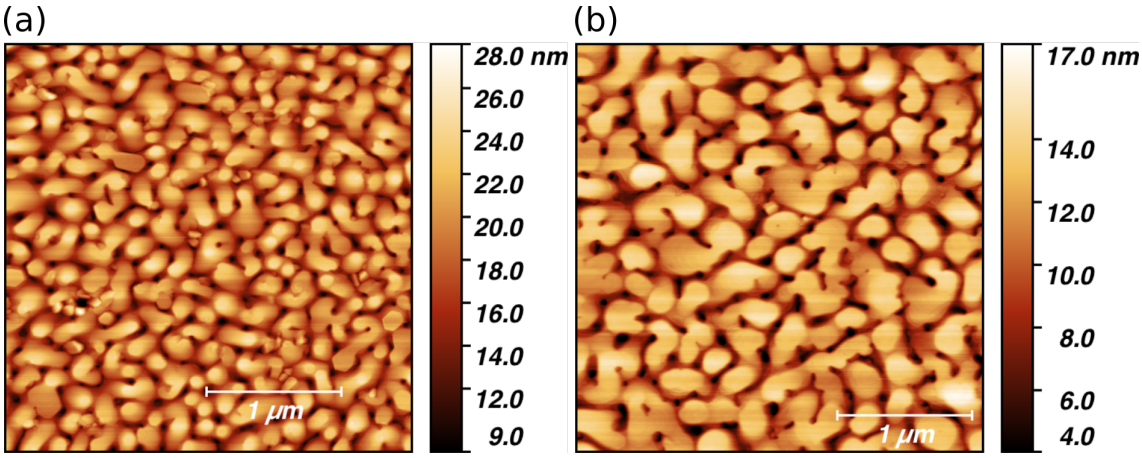

Figure 2.33: (a) 3 µm x 3 µm AFM height image shows the surface of the 100 nm thick sample deposited at 800°C (sample F). (b) 3 µm x 3 µm AFM height image shows the surface of the 50 nm thick sample deposited at 900°C (sample G).

Two 100 nm samples were deposited, one at 800°C (sample F) and the other at 900°C (sample G). AFM images taken on the surface of both sample F and G are shown in figures 2.33(a) and 2.33(b), respectively.

The structure of the surfaces look very similar: they are both covered with spirals that have atomic step heights. Spirals are connected to each other by ridges, and there are deep holes around them. On sample F there are a few grains in between the spirals, and the spirals are slightly smaller. However, the difference in size is not as pronounced as it was on the 50 nm samples. While spirals on sample G measure about 200 nm - 400 nm, on sample F they measure about 100 nm - 300 nm.

XRD θ-2θ measurements

The θ-2θ scan of both samples are shown in figure 2.34. The graphs were normalized to the (002) peak of rhenium.

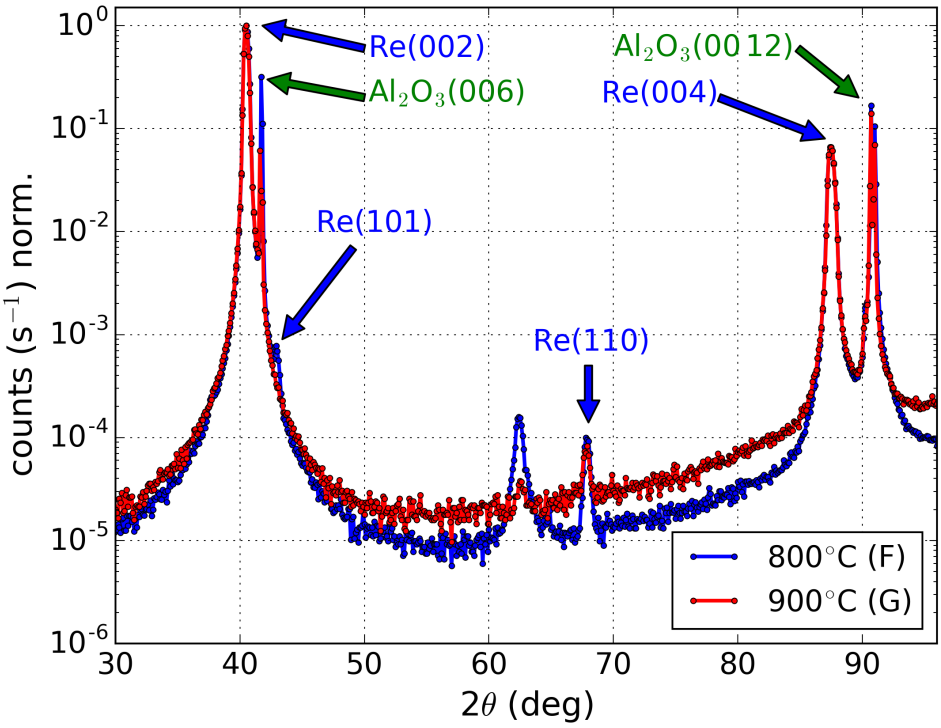

Figure 2.34: θ-2θ scan of the 100 nm samples.

The dominant orientation on both films is (001). Aside from that, there is a low intensity (101) peak on sample E that is not present on sample F. There is also a low intensity (110) peak on both samples. The broad unindexed peak on sample F between 60° and 70° does not belong to rhenium nor to the substrate. It is possible that that it is a reflection from ReO_2.

In figure 2.35(a) a close up of the (002) Re and (006) Al_2O_3 peaks of both samples are shown. The peaks look almost identical. Neither reflection can be described by the sum of two Voigt functions (equation 2.10) well because of the clear asymmetry of the peaks. Asymmetry is expected as they were measured using two wavelengths. However, on these samples, the angles of the higher and lower intensity contributions are reversed. It appears that they have a lower intensity contribution towards the lower angles. The unusual shape could be due to the relaxation of the film. As the film grows the lattice spacing gradually becomes what it is in bulk rhenium. Adjusting the function to describe such a situation would require the addition of several extra parameters, which would

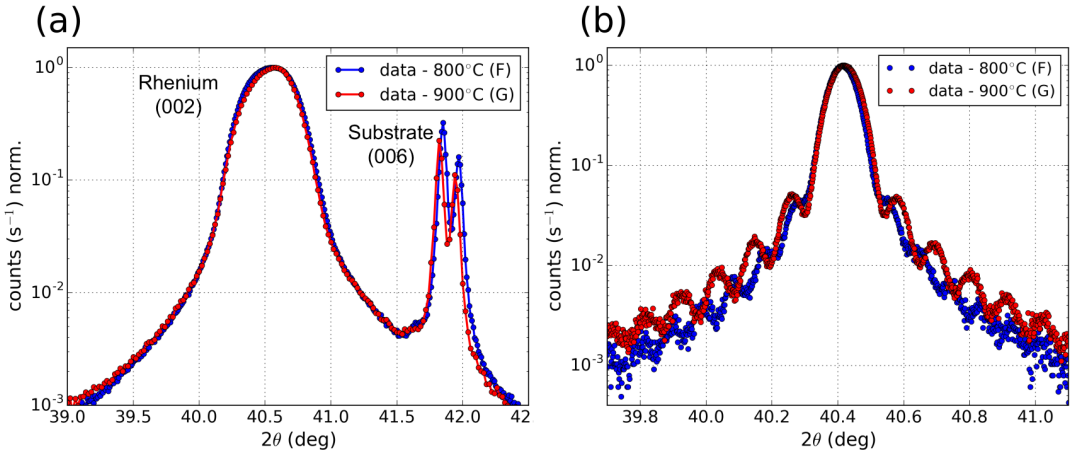

Figure 2.35: (a) The (002) peak of rhenium measured on the 100 nm samples. The curves measured on the two films are asymmetric, and almost identical. (b) High-resolution scan of the same (002) peaks of both 100 nm samples. The fringes on the curve of sample G are more pronounced.

reduce the reliability of the fit.

Samples F and G were also measured using the Rigaku SmartLab high-resolution diffractometer. The measured curves are shown in figure 2.35(b). The interference function, equation 1.23, was used to fit the data. Parameters are listed in table 2.8. This model has the same shortcomings as was seen before. The peaks are broad on both of these samples, and the minima are shallow. However, the number of scattering planes and average lattice parameter can accurately be determined.

The thickness of the films calculated from the fit parameters are:

$$t_F = 99 \text{ nm}, \quad t_G = 86 \text{ nm}. \tag{2.21}$$

The thicknesses are in agreement with what was measured during deposition.

An attempt was made to fit the high-resolution data with the modified interference function. In this case, the model fails to accurately describe the intensity variations of the experimental data and the broadening of the main peak. The reason why this simple model fails could be that there are defects in the film that cannot be described by a single Gaussian distribution of lattice planes.

Even without the parameters to compare, it is visible in figure 2.35(b) that the fringes are more damped on sample F than on sample G. This suggests that the film which was deposited at lower temperature (sample F) is more disordered.

100 nm (002) High-resolution data		
	800°C (F)	900°C (G)
N	448 ± 0	387 ± 0
d_0	(0.2230084 ± 6e−7) nm	(0.222972 ± 7e−6) nm
100 nm (002) Rocking curves		
Peaks @ (°)	20.28330 ± 6e−5	20.2668 ± 3e−5
$FWHM$ (°)	0.3384 ± 0.0002	0.2794 ± 0.0001
m	3.15 ± 0.02	3.83 ± 0.02

Table 2.8: Parameters of the fit of the high-resolution (002) rhenium peaks with the interference function, equation 1.23, and the parameters of the fit of the rocking curves with the Pearson VII function, equation 2.14.

XRD rocking curve measurements

The rocking curves of the 100 nm samples were fitted with the Pearson VII function, equation 2.14. The parameters of the fit are summarised in table 2.8.

The rocking curve of the sample which was deposited at higher temperature is narrower. This is consistent with our previous observations, and with the presence of larger objects on the surface.

Conclusion on the 100 nm thick films

The trend observed in case of the 25 nm thick films and the 50 nm thick films continues with 100 nm thick films. AFM revealed that spirals decorate the surface of both films. The spirals grew in size with higher deposition temperature, however, the difference is not as significant as for the 50 nm thick film. XRD data shows that the dominant orientation is the epitaxial (001). Two additional orientations appear with low intensities. Only one of them persists on the higher temperature sample. On the lower temperature sample there is a broad, unidentified peak. It is possible that it comes from an oxide of rhenium. No difference can be observed between the standard resolution (002) peaks, however, they have a distinct asymmetric shape, which might be due to the relaxation of the films. Fringes of the high-resolution data are more pronounced on the higher temperature sample, which indicates less disorder. We could not confirm this with the modified interference function. The width of the rocking curves decreased with increasing deposition temperature for these films as well.

2.2.4 Conclusions on the effects of the temperature

Higher deposition temperature resulted in more uniform grain sizes, smoother surface on the 25 nm thick films, and larger spirals on the 50 nm and 100 nm thick films. Overall, surfaces deposited at 900°C appear more homogeneous. However, with the spirals, holes appeared also. The presence of holes is explained in the following section.

The 50 nm sample that was deposited at 1000°C dewetted, which resulted in a surface covered with large, atomically flat islands, comparable to a mesa landscape.

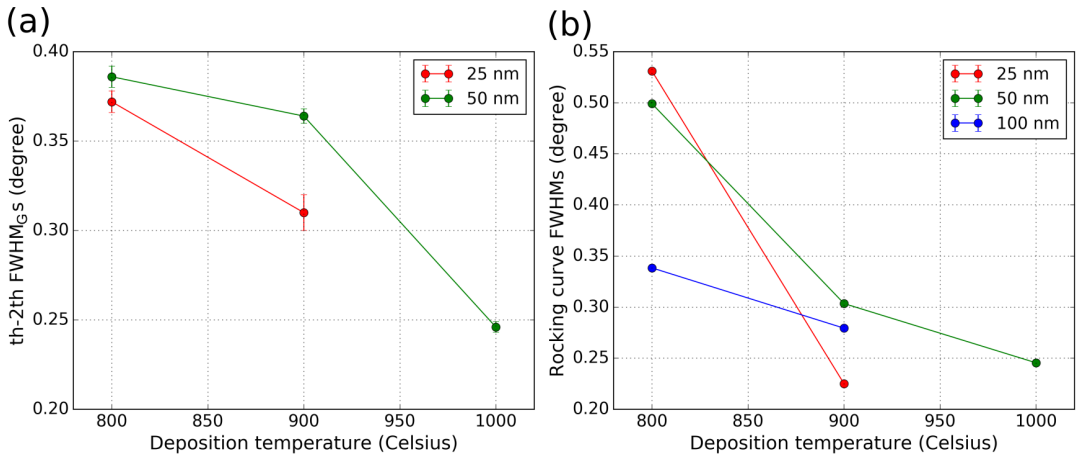

Figure 2.36: (a) Gaussian widths of the θ-2θ peaks as the function of temperature. (b) Pearson VII widths of the rocking curves as the function of temperature.

Every sample had a single dominant orientation, (001), in accordance with the substrate lattice. Several other orientations appeared on the graphs, but for almost every thickness, their intensity decreased or vanished with increasing deposition temperature.

The detailed study of the (002) reflections revealed that for every thickness the higher temperature deposition resulted in less disorder in the lattices. Less disorder is indicated by the decreasing Gaussian FWHMs of the Voigt functions. These values are shown as the function of temperature in figure 2.36(a). Disorder was quantified for two of 50 nm thick films (samples C and D), by the introduction of a distribution of lattice parameters. As was shown in figure 2.30, the distribution was narrower for the higher temperature film.

For every thickness the rocking curves of the higher temperature samples were significantly narrower. The Pearson VII FWHM values obtained from the fits are shown as the function of temperature in figure 2.36(b). The improvement of rocking curves is consistent with the larger objects observed on the AFM images, and they also indicate

that the mosaicity of the epitaxial grains is reduced by higher temperature deposition.

2.3 Thermal grooving of the surface

During the deposition of the rhenium thin films, the crystallography of the surface is monitored by reflection high energy electron diffraction. The technique is described in chapter 1.4.1. Prior to evaporation, Kikuchi lines corresponding to the lattice of the Al_2O_3 can be observed on the screen. As the rhenium deposition starts, the Kikuchi pattern gradually changes to broad rings on a diffuse background, indicating the growth of crystalline islands with different orientations. Then spots appear, indicating 3D growth. When the thickness reaches approximately 10 nm, the RHEED pattern changes again, suddenly rods appear. This is a sign that electrons are diffracted by a volume with single orientation and flat surface.

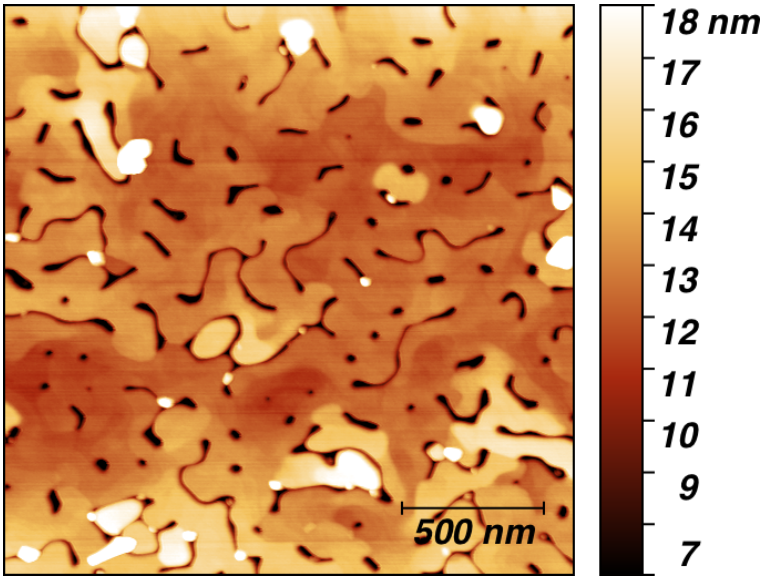

Figure 2.37: 2 μm x 2 μm AFM hight image of the rhenium thin film with approximately 15 nm thickness, showing signs of dewtting.

To understand the reason behind this transition, a sample was deposited. Temperature was set to 900°C, and the thickness of this sample was determined by the change in the RHEED pattern during deposition: evaporation was stopped when the diffraction rods were detected, at approximately 15 nm. The film was studied using AFM and XRD.

AFM height image of the sample is shown in figure 2.37. The image shows a surface

that is flat but not continuous. The film has dewetted. The large ridges are interrupted by circular or elongated holes. The ridges show a stepped structure. The heights of the steps correspond to single or double interatomic spacing along the c axis in the rhenium structure. An example for both are shown in figure 2.38. The height profile of the surface was extracted along the paths shown by the purple and the blue lines on the insets in figure 2.38(a). The profiles themselves are shown in corresponding colours in figure 2.38(b). The minima of the graphs were set to 0 nm on the plot. The mean step height along the purple path is (0.22 ± 0.07) nm which corresponds to single interatomic spacing. Along the blue line it is (0.43 ± 0.14) nm, which is the double of the previous value.

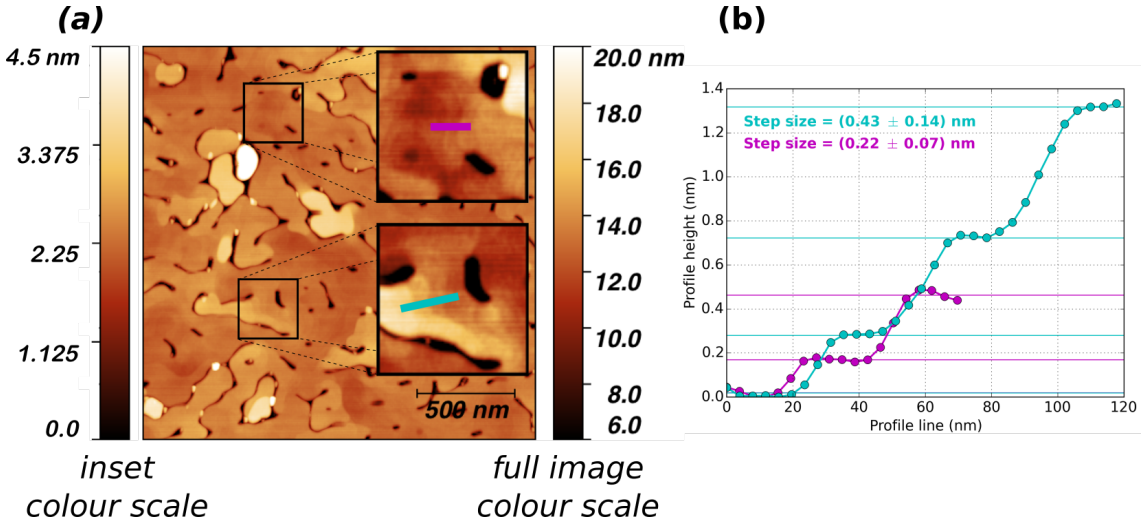

Figure 2.38: (a) 2 µm x 2 µm AFM hight image taken on the same sample as shown in figure 2.37 with two insets. The colour scale of the insets was adjusted to show the step structure of the ridges. (b) Profiles extracted from the AFM hight image, showing singe and double steps. Minima of both curves were set to 0.

The depth and the true shape of the holes that interrupt the ridges cannot be determined. Due to the restrictions of AFM imaging, these holes reflect the shape of the probe. They may reach all the way to the substrate.

Many of the ridges show a slight increase in height around the holes, as shown by two examples in figure 2.39(b). Height profiles were extracted along the paths that are drawn on the insets of figure 2.39(a) for this plot.

The patterning that can be observed in figure 2.37, and is highlighted in figure 2.39 resembles curves of thermal grooving, where the transport of the matter was driven by

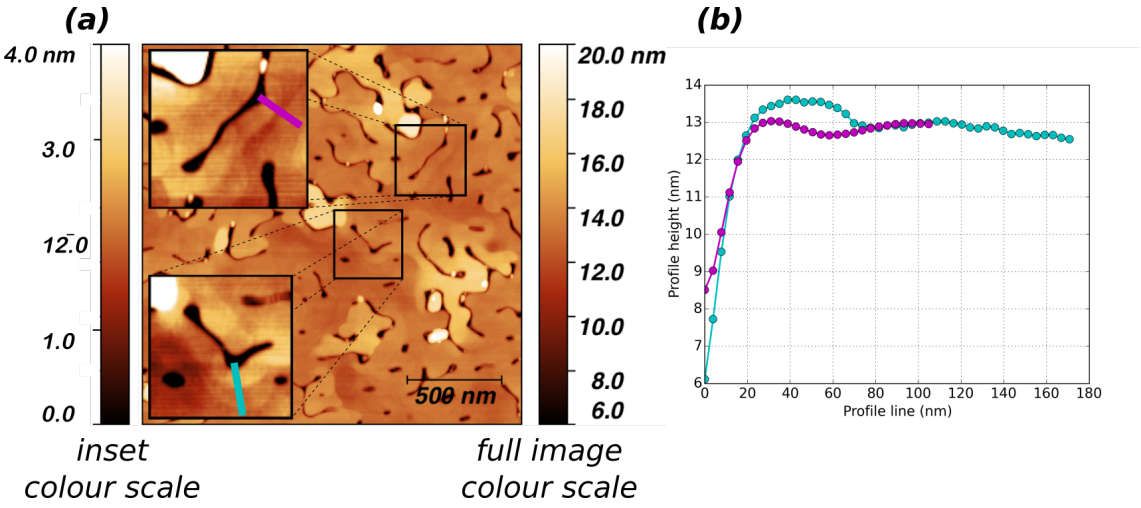

Figure 2.39: (a) 2 µm x 2 µm AFM hight image taken on the same sample as shown in figure 2.37 with two insets. The colour scale of the insets was adjusted to show the slight maximum in height around the holes. (b) Profiles extracted from the AFM hight image. The slight bump that appears around the holes resembles curves of thermal grooving driven by surface diffusion.

surface diffusion. Mullins' theory of thermal grooving was described in chapter 1.5.4. The theoretical profile, that develops along a grain boundary in case of surface diffusion, also shows a maxima. The equation of the surface profile ($y_{sd}(x,t)$) was given in equation 1.40, and was used to fit the height graphs extracted from the AFM data.

An example of a fit is shown in figure 2.40 with the parameters. The theoretical curve describes the shape of the measured profile well, our observation is consistent with the theory of thermal grooving. However, the atomic steps, that can be observed on the tail of the measured data cannot be reproduced. Mullins' model is a continuous model, and cannot account for discontinuities, such as steps, that develop on a low energy crystal surface at high temperatures.

One of the parameters of the fit was $(Bt)^{\frac{1}{4}}$, which equals to the following:

$$(Bt)^{\frac{1}{4}} = \left(\frac{D_s \gamma \Omega^2 \nu t}{k_B T}\right)^{\frac{1}{4}}, \tag{2.22}$$

where D_s is the surface diffusion coefficient, γ is the surface free energy, Ω is the molecular volume, ν is the number of atoms per unit area, t is the time, k_B is the Boltzmann constant, and T is the temperature.

From the $(Bt)^{\frac{1}{4}}$ parameter, the surface diffusion coefficient of rhenium can be determined, and compared to the value found in reference [76].

t was taken as the time it took to deposit the sample, approximately 1000 seconds. The growth temperature was 1150 K. The molecular volume is the volume of a rhenium atom, which can be calculated from the atomic radius: $\Omega = 3/4\,\pi r^3 = 3/4\,\pi(0.137\,\mathrm{nm})^3 = 6.059 \cdot 10^{-3}\,\mathrm{nm}^3$. The number of atoms per unit area was calculated from the rhenium hexagonal closed packed unit cell. Considering (001) orientation, the surface is covered with hexagons, and rhenium atoms are placed in the corners, and in the middle of each hexagon. The area of one such unit can be obtained using the lattice parameter a: $A_{\mathrm{hexa}} = 3\sqrt{3}/2\,a^2 = 3\sqrt{3}/2\,(0.276\,\mathrm{nm})^2 = 0.198\,\mathrm{nm}^2$. All rhenium atoms on the corners are shared by three hexagons, so there are $6 \cdot 1/3 + 1 = 3$ atoms on the area calculated above. The number of atoms per unit area can be calculated by a division: $\nu = 3/A_{\mathrm{hexa}} = 15.147\,\mathrm{nm}^{-2}$.

The value of the surface free energy can be found in references [77], [78], and [79]. Tyson and Miller calculated the surface free energy from liquid surface tension measurement data. They obtained a value of 3.626 Jm^{-2} [77]. Surface free energy found in reference [78] is in good agreement with Tyson and Miller, 3.600 Jm^{-2}. In a more recent article, Vitos et al. determined the surface free energy of low-index surfaces of 60 metals,

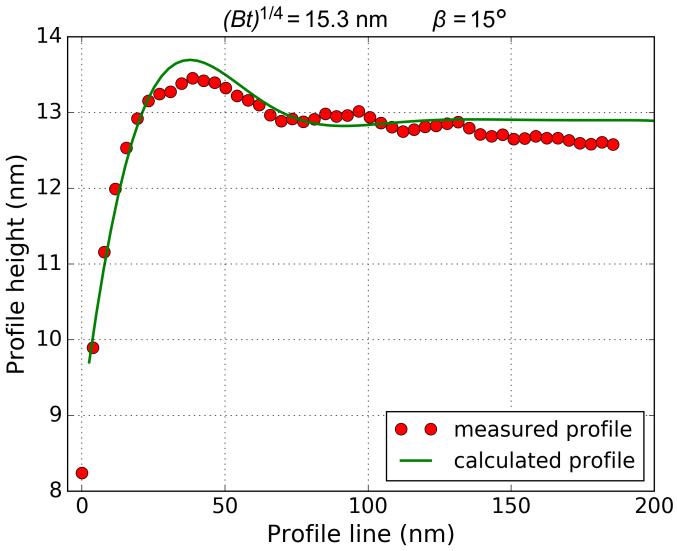

Figure 2.40: Extracted height profile fitted by Mullins' theoretical curve. Parameters of the fit are shown above the plot.

including rhenium, using density functional theory [79]. For the (001) surface of rhenium they found a value of 4.214 Jm^{-2}.

The value reported by Vitos et al. was used to determine the surface diffusion coefficient from the averaged $(Bt)^{\frac{1}{4}}$ parameters. We obtained the following value:

$$D_s = 4.06 \cdot 10^{-12}\,\mathrm{cm}^2/\mathrm{s}. \tag{2.23}$$

It can be determined from the surface diffusion coefficient how far an atom can travel in one second ($\lambda = \sqrt{D_s t}$). λ is approximately 20 nm/s. This is in good agreement with the width of the atomically flat terraces, which measure a few tens on nanometers across.

Temperature dependence of the surface diffusion coefficient of the Re(001) surface was measured by Goldstein and Ehrich in the 210 K - 235 K temperature range [76]. Temperature dependence of the diffusion coefficient follows the Arrhenius law:

$$D_s(T) = D_0\, e^{-\frac{E_a}{k_B T}}, \tag{2.24}$$

where E_a is the activation energy. The parameters reported in reference [76] are the following:

$$E_a = 11.11 \pm 0.43\,\mathrm{kcal/mol} \text{ and } D_0 = 6.13(\cdot 2.6 \pm 1) \cdot 10^{-6}\,\mathrm{cm}^2/\mathrm{s}. \tag{2.25}$$

Using these values, the surface diffusion coefficient was calculated at the temperature of the deposition. It is plotted in the relevant temperature range in figure 2.41. According to this, surface diffusion coefficient should be in the order of 10^{-8} cm^2/s at 1000 K. This value corresponds to a λ of 1μm/s. 1μm is much larger than the size of the terraces on the film, and the reported surface diffusion coefficient is four orders of magnitude higher, than what we obtained.

The authors of reference [76] conducted their experiments at much lower temperatures, at a relatively small temperature range: 210 K - 235 K. Extrapolated values in the region of 1000 K should be taken with caution.

In our experiment, the sample was an extremely thin film, 15 nm, and the full thickness dewetted. Holes that developed as a result probably reach the substrate. Their profile cannot be determined but it can be assumed, that they have a similar stepped structure as observed on the ridges. Steps provide an energy barrier known as the Schwoebel barrier against the atoms diffusing through them. The effect was described in section 1.5.3. This can lower the diffusion coefficient we obtain.

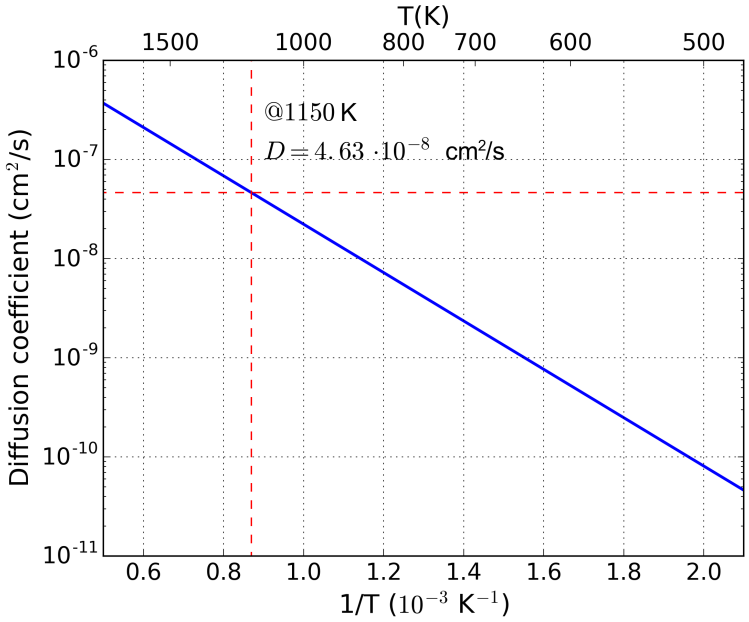

Figure 2.41: Temperature dependence of the diffusion coefficient according to the measurements of Goldstein and Ehrich [76].

Lastly, the theoretical curve cannot account for the steps observed on the surface, but describe the overall shape well. The results should be viewed as qualitative due to the restrictions of Mullins' theory. He based his paper on the observations in copper samples that were polycrystalline and bulk. Our rhenium samples, on the other hand, had thickness about 15 nm. One of his assumptions was that the properties of the interface are independent of the orientations of the crystals. The orientations of the rhenium grains are very close to a low energy surface (001), thus this assumption cannot be valid in our case. Recrystallisation of the whole sample competes with thermal grooving. Recrystallisation to a low-index orientation flattens the surface. On the low-index surface steps develop, which provide a diffusion barrier, and stop the process of thermal grooving. The step structure can be observed on the ridges, highlighted in figure 2.38. It is also visible on the tail of the measured profile in figure 2.40. Recrystallisation also causes the maxima after the hole to flatten, most visible on the blue profile in figure 2.39(b).

That the dewetting process is accompanied by recrystallisation is confirmed by the transformation of the RHEED pattern during growth. The initial concentric rings correspond to grains with random orientation, and the regularly spaced rods that appear after, to a single orientation and a flat surface. X-ray diffraction data acquired on the

sample further confirms that the layer has a single orientation, which is the epitaxial (001) orientation.

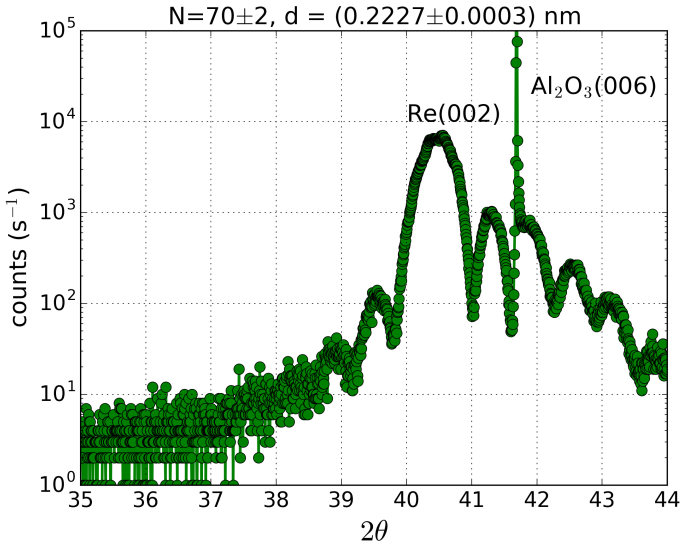

Figure 2.42: θ-2θ scan of the Re(002) peak measured on the 15 nm thick rhenium film. Several fringes on both sides of peak show that the X-ray beam was diffracted by regularly arranged lattice planes.

The high-resolution θ-2θ scan around the Re(002) peak is shown in figure 2.42. The sharp, unresolved peak between 41 and 42 degrees corresponds to the Al_2O_3 (006) orientation, the broader peak between 40 and 41 degrees is the rhenium (002) peak. A few fringes can be observed on both sides of the rhenium peak which is a sign that the X-ray beam was diffracted by well-arranged, parallel lattice planes. The interference function, equation 1.23 was fitted, to determine the number of lattice planes (N) and their spacing (d). N is related to the periodicity of the fringes, d is to the angular position of the central peak. The fit is not shown in figure 2.42, because it fails to describe the intensity ratio of fringes and the main peak. The film is very thin, so the fringes are damped. However, this does not affect the position of the peak, and the periodicity. Parameters obtained from the fit are also shown in figure 2.42. By multiplying N and d, the thickness of the layer can be determined. We obtain (15.5 ± 0.5) nm.

Conclusion thermal grooving

The surface which develops as the result of the dewetting can be described by Mullins' theory of thermal grooving, where the matter was driven by surface diffusion. Dimensions observed on the topography are consistent with the surface diffusion coefficient we obtain from Mullins' model. Changes in the RHEED pattern indicate the coalesce of initial islands and the full recrystallisation of the film. This was confirmed by high-resolution X-ray diffraction.

We believe that dewettting and recrystallisation happens on most rhenium samples when they reach approximately 10 nm -15 nm thickness. This leaves behind a flat surface with a single orientation, and deep holes and ridges. Initially holes observed on the samples with spirals were thought to be the result of impurities on the substrate [7]. We now believe that the holes are the result of dewetting during the early stages of growth. Spiral will grow onto the terraced ridges, that can be observed in figure 2.37.

2.4 Thermal transfer during crystal growth

Measurement of temperatures in a vacuum chamber is not a trivial task. Its difficulties were discussed in chapter 1.3.1.

To estimate the temperature of the surface of the growing rhenium, a model was developed by Delsol [7]. His model is outlined here, and modifications are introduced, that can explain the thermal grooving that occurs when thickness of 10 nm - 15 nm is reached by an increase in temperature.

Theory outlined here is described in more detail in reference [80].

2.4.1 Elements of the model

Definitions

Thermal radiation is modelled by the ideal radiator, the black body, which absorbs all and reflects none of the radiation arriving at its surface. Planck predicted the emitted power flux (monochromatic emissive power) black body at temperature T at wavelength λ:

$$M_{\lambda,bb}(\lambda,T) = \frac{2\pi hc^2}{\lambda^5}\frac{1}{\exp\left(\frac{hc}{k_B T\lambda}\right)-1}, \tag{2.26}$$

where h is the Planck constant, c is the speed of light in vacuum, and k_B is the Boltzmann constant.

The total emissive power is obtained by an integration over the wavelengths, and its temperature dependence is given by the Stephan-Boltzmann law:

$$M_{bb}(T) = \int_0^\infty M_{\lambda,bb}(\lambda, T)d\lambda = \sigma T^4, \tag{2.27}$$

where σ is the Stephan-Boltzmann constant.

Thermal radiation of a real body is given by a comparison to the black body. Emittance (ϵ) is the ratio of the emitted radiation by the real and the black body:

$$\epsilon_\lambda(T) = \frac{M_\lambda(\lambda, T)}{M_{\lambda,bb}(\lambda, T)} \quad \text{and} \quad \epsilon(T) = \frac{M(T)}{M_{bb}(T)}. \tag{2.28}$$

Thus the Stephan-Boltzmann law for a real body is modified as follows:

$$M(T) = \epsilon\sigma T^4. \tag{2.29}$$

In general, emittance is the function of the wavelength. A body whose emittance is independent of the wavelength is a grey body ($\epsilon = \epsilon_\lambda$).

Besides the radiations that is emitted by a body, it is also important to discuss how it interacts with radiation that arrives at its surface. This is shown in figure 2.43.

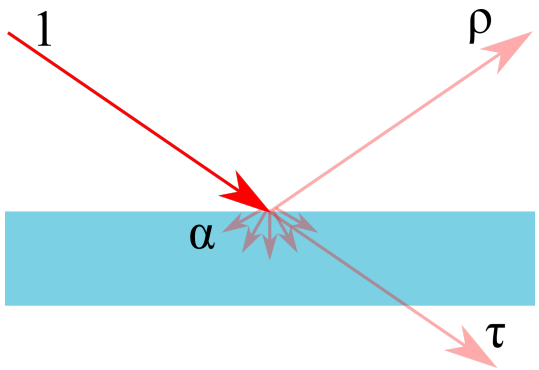

Figure 2.43: Radiation arriving on a surface (1). Proportions of it are reflected (ρ), transmitted (τ) or absorbed (α).

To simplify the problem, let us consider the incoming radiation to be 1. The fraction of the radiation that is absorbed is called absorbance (α). ρ is reflectance, and it measures the fraction that is reflected, and τ is the transmittance, gives the portion that is transmitted. In equilibrium, the following condition is fulfilled:

$$1 = \alpha + \rho + \tau \quad \rightarrow \quad \alpha = 1 - \tau - \rho. \tag{2.30}$$

Kirchhoff's law connects the absorbance and the emittance. It states that a body in equilibrium absorbs as much energy as it emits in every direction and at each wavelength:

$$\epsilon_\lambda(T, \theta, \phi) = \alpha_\lambda(T, \theta, \phi), \tag{2.31}$$

where θ and ϕ are angular coordinates.

When the surface is diffuse, emittance and absorbance does not depend on the direction. Furthermore, if the body is grey, wavelength dependence can be neglected as well. Kirchhoff's law then simplifies to the following:

$$\epsilon(T) = \alpha(T). \tag{2.32}$$

Oppenheim's electrical analogy

An analogy to electric circuits was developed to study heat exchange between grey diffuse bodies by Oppenheim. Two new quantities need to be defined. Irradiance (H) is the flux of energy that irradiates the surface, and radiosity (B) is the flux leaving a surface. The flux of energy leaving a surface is the sum of reflected irradiance and the emitted flux:

$$B = \rho H + \epsilon \sigma T^4. \tag{2.33}$$

The net flux leaving a surface can be expressed as

$$Q = B - H = \frac{\epsilon}{\rho}\sigma T^4 - \frac{1-\rho}{\rho}B. \tag{2.34}$$

If the body is opaque ($\tau = 0$) and grey, using equations 2.30 and 2.32, equation 2.34 takes the shape of Ohm's law:

$$Q = \frac{\sigma T^4 - B}{\frac{1-\epsilon}{\epsilon}}, \tag{2.35}$$

where Q takes the place of the current, $(\sigma T^4 - B)$ acts as the potential difference, and $\frac{1-\epsilon}{\epsilon}$ is the resistance. This analogy makes heat transfer problems easier to handle. For example, heat transfer between two planes can be described as two resistors connected in series.

Heat conduction

The above analogy is restricted to planes with diffuse, opaque, grey surface. Our system consists of 4 parts: furnace, tungsten, substrate-rhenium, and the chamber wall. The approximation can be valid to all but one part: the substrate. Al_2O_3 is transparent not opaque, and thick relative to the tungsten and rhenium. Heat conduction through the substrate has to be considered.

Heat transfer between two surfaces with temperatures T_1 and T_2 can be expressed as follows:

$$Q_C = \frac{T_1 - T_2}{t/k}, \tag{2.36}$$

where t is the distance between the two surfaces (thickness), and k is the thermal conductivity of the material.

Heating of the sample in UHV

The sample is heated with a tungsten filament that is located behind it. The setup is shown in figure 1.9. It can be operated in two modes: either emits infrared radiation as a result of Joule heating, or a voltage is applied between the filament and the sample, and electrons are emitted and bombard the backside of the substrate.

When the filament is heated by a current, the dissipated power is the product of the resistance of the wire and the square of the current:

$$P = R(T)I^2. \tag{2.37}$$

Some of this heat is lost through the hooks that keep the wire in place. It is estimated that 30% of the power heat the sample.

When electron bombardment is applied, it is assumed the all the power carried by the electrons heat the sample, thus the power is the product of the voltage applied between the filament and the sample and the electron current that is extracted from the filament (I_e):

$$P = UI_e. \tag{2.38}$$

2.4.2 Heat transfer during growth

Delsol used the elements discussed above to build a model to calculate the temperature of the rhenium surface during growth.

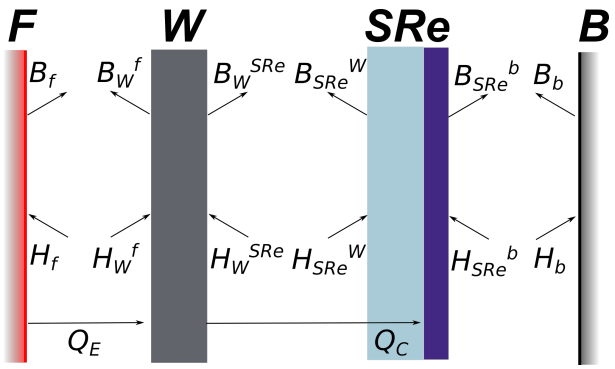

Figure 2.44: The model consists of a series of planes: furnace (F), tungsten (W), substrate-rhenium (SRe), and chamber (B). Irradiance and radiosity of the planes is considered.

The model is shown in figure 2.44. All the parts of the system was assumed to be an infinite plane. The plane noted with F is the furnace. Besides radiosity, which is the result of the hot filament, Q_E has to be included in the equations for experiments when electron bombardment is applied. W refers to the tungsten backing on the substrate. SRe is the substrate and rhenium, which is considered as one unit, and conduction of heat through the substrate (Q_C) is included in the model. Finally, B denotes the wall of the vacuum chamber ('bâtiment'), which is at room temperature.

The problem has three unknowns: the temperature of the tungsten (T_W), the temperature of the substrate-rhenium (T_{SRe}), and the heat flux between the surfaces, which in equilibrium have to be equal (Q). Three equations can be be written down to define Q using the radiosities of the surfaces:

$$Q = B_f - B_W^f + Q_E, \tag{2.39}$$

$$Q = B_W^{SRe} - B_{SRe}^W + Q_C, \tag{2.40}$$

$$Q = B_{SRe}^b - B_b. \tag{2.41}$$

The radiosities have to be expressed as the function of only the three unknown. To do this further equations have to defined. The heat exchange on each surface also have to be equal to Q. Writing these down as the difference between radiosity and irradiance gives further 6 equations.

Radiosity of a surface is the sum of the thermal radiation due to its temperature ($\epsilon\sigma T^4$), the reflected irradiance (ρH), and transmitted irradiance (τH). All except the

substrate-rhenium is considered opaque, which means $\tau = 0$. The radiosities can then be expressed as follows:

$$B^W_{SRe} = \rho_{SRe} H^W_{SRe} + \epsilon_{SRe}\sigma T^4_{SRe} + \tau_{SRe} H^b_{SRe}, \tag{2.42}$$

$$B^b_{SRe} = \rho_{SRe} H^b_{SRe} + \epsilon_{SRe}\sigma T^4_{SRe} + \tau_{SRe} H^W_{SRe}, \tag{2.43}$$

$$B_f = \rho_f H_f + \epsilon_f \sigma T^4_f, \tag{2.44}$$

$$B_b = \rho_b H_b + \epsilon_b \sigma T^4_b, \tag{2.45}$$

$$B^f_W = \rho_W H^f_W + \epsilon_W \sigma T^4_W, \tag{2.46}$$

$$B^{SRe}_W = \rho_W H^{SRe}_W + \epsilon_W \sigma T^4_W. \tag{2.47}$$

Using the 6 heat exchange equations and equations (2.42) - (2.47) the equation system (2.39), (2.40), (2.41) can be expressed as the function of only the three unknowns. The derivation is long but not complicated. It is shown in detail in appendix D. The final form of the equation system is the following:

$$Q = \frac{\sigma T^4_f - \sigma T^4_W}{1 + R_f + R_W} + Q_E, \tag{2.48}$$

$$Q = \frac{\sigma T^4_W - \sigma T^4_{SRe}}{1 + R_W + R_{SRe}} + \left(\frac{r_{SRe}}{1 + R_W + R_{SRe}} + 1 \right) Q_C, \tag{2.49}$$

$$Q = \frac{\sigma T^4_{SRe} - \sigma T^4_b}{1 + R_B + R_{SRe}} - \frac{r_{SRe}}{1 + R_B + R_{SRe}} Q_C, \tag{2.50}$$

where the following notations were used:

$$R_f = \frac{\rho_f}{\epsilon_f}, \qquad R_b = \frac{\rho_b}{\epsilon_b}, \qquad R_W = \frac{\rho_W}{\epsilon_W},$$

$$R_{SRe} = \frac{\rho_{SRe} - \tau_{SRe}}{\epsilon_{SRe} + 2\tau_{SRe}}, \qquad r_{SRe} = \frac{\frac{\tau_{SRe}}{\epsilon_{SRe}}}{\epsilon_{SRe} + 2\tau_{SRe}}.$$

Substrate and rhenium was is treated as a single object. The common transmittance and emittance was calculated as follows:

$$\tau_{SRe} = \tau_S \tau_{Re}, \qquad \epsilon_{SRe} = (1 - \tau_{Re})\epsilon_{Re} + \tau_{Re}\epsilon_S. \tag{2.51}$$

2.4.3 Thermal and optical properties of the materials

Thermal conductivity of the substrate

Thermal conductivity of Al_2O_3 is listed in reference [81]. It was fitted with a 5th degree polynomial. The fit is given by the equation below:

$$k_{Al_2O_3}(T) = 97.155 - 0.32723 \cdot T + 5.3582\text{e}{-4} \cdot T^2 - 4.8283\text{e}{-7} \cdot T^3 + \\ + 2.2971\text{e}{-10} \cdot T^4 - 4.4808\text{e}{-14} \cdot T^5,$$

where the temperature is measured in Kelvin.

Optical properties of the substrate-rhenium plane and tungsten

Transmittance be calculated from the complex refraction index (κ), which can be found tabulated for rhenium in reference [82]. In the calculation the 0.1 eV - 2 eV energy range was used which corresponds to a wavelength range of 0.62 μm - 12.4 μm. This is the lower (in wavelength) end of the infrared range.

If we assume that the total emissive power (equation 2.27) falls on the surface of a material with complex refraction index κ, the intensity that persists down to thickness z

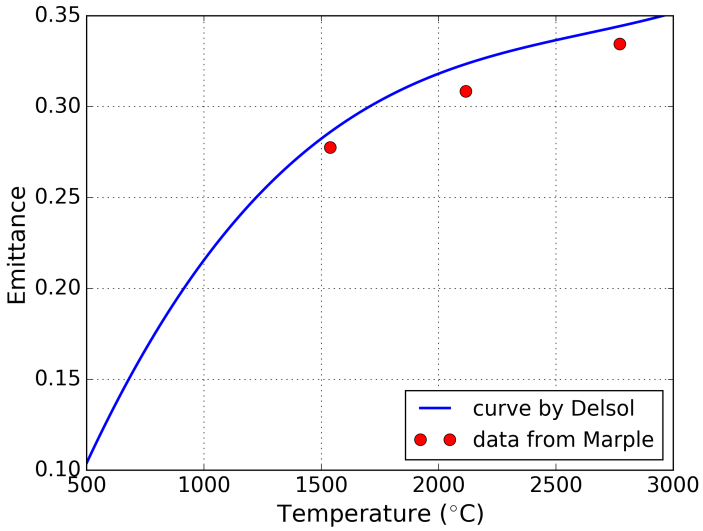

Figure 2.45: Emittance of rhenium: values calculated from reference [83] (red points) compared to curve used by Delsol [7] (blue line).

is obtained as follows:

$$M_{\lambda,t}(z) = M_{\lambda,bb}\, e^{\frac{-4\pi\kappa z}{\lambda}}, \tag{2.52}$$

Transmittance of material with thickness d can then be expressed as the ratio of the total transmitted intensity through depth d and the total emissive power (equation 2.27):

$$\tau = \frac{\int M_{\lambda,t}(z=d)\, d\lambda}{M_{bb}}. \tag{2.53}$$

Emittance of rhenium was measured by Marple [83], but the temperatures they worked at (>1500 °) are much higher than what we can achieve in the vacuum chamber. Their range of wavelength was 0.4 μm - 3 μm. In the model by Delsol the following expression was used to calculate the emittance of rhenium [7]:

$$\epsilon_{\mathrm{Re}}(T) = -0.18906 + 4.9151\mathrm{e}{-4}\cdot T - 1.5979\mathrm{e}{-7}\cdot T^2 + 1.8357\mathrm{e}{-11}\cdot T^3, \tag{2.54}$$

where the temperature is measured in Kelvin.

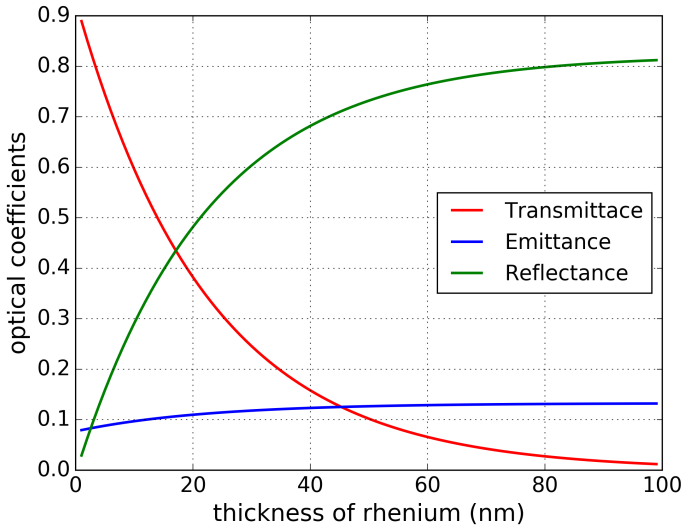

Figure 2.46: Optical coefficients of the substrate-rhenium plane as function of the rhenium thickness.

The emittance curve is shown in figure 2.45 with the solid line. The three red dots are the emittance values calculated from the curves found in reference [83]. The two datasets are in agreement.

Emittance is related to the full surface area of a body. Our thin films are smooth on a nanometer scale, thus their total surface area is smaller than the sand blasted rhenium sheet which was used for emissivity measurements by Marple [83]. Thus, we expect that emission from our rhenium films is smaller than what was presented in reference [83]. For this reason, the $\epsilon_{Re}(T)$ curve was reduced by 25%.

Emittance and transmittance of sapphire were taken to be 0.077 and 0.93, based on references [84–86].

The common transmittance, emittance and reflectance can now be computed using equations 2.51. The results are shown in figure 2.46 as the function of the thickness of the rhenium film. The temperature was fixed at 800 °C.

Emittance of tungsten is given by the following expression:

$$\epsilon_{\mathrm{W}} = -2.6875\mathrm{e}{-2} + 1.819696\mathrm{e}{-4} \cdot T - 2.1946163\mathrm{e}{-8} \cdot T^2, \tag{2.55}$$

where the temperature is measured in Kelvin [87]. This equation is valid between 400 K (127°C) and 3600 K (3327°C).

2.4.4 Results and discussion

The temperature of the rhenium was calculated for two cases: with or without tungsten backing on substrate. The current through the furnace filament was set to 8.5 A, and no electron bombardment was applied. This is a setting we used most frequently.

The temperature of the rhenium is shown in figure 2.47 as the function of its thickness. The effect of the tungsten is clear. The substrate is almost completely transparent for infrared radiation, thus it cannot be heated effectively. Rhenium heats as the thickness builds up, and its transmittance decreases. Compared that to the case when tungsten backing is applied to the substrate, the temperature is relatively stable.

An increase in temperature, that starts around 10 nm, can be observed in on the red curve. This is consistent with the dewetting described in section 2.3. The temperature of the rhenium surface is not constant during growth, but increases significantly, which induces changes in the growth process. To eliminate the holes, the dewetting process needs to be avoided. To achieve this, the tendency for the temperature increase has to be compensated by manually lowering the power of heating. This calculation allows us to

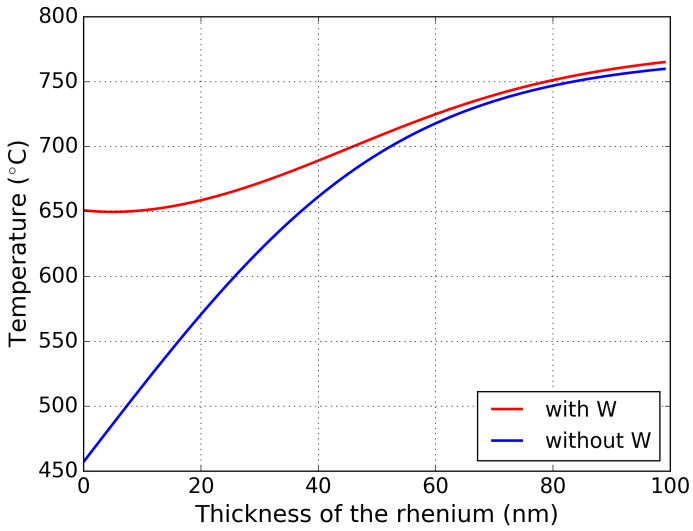

Figure 2.47: Temperature of the rhenium thin film with and without tungsten backing as the function of its thickness calculated from the model.

deduce how much we have to reduce the thermal power to achieve a constant temperature during the growth.

3

Superconductivity

This chapter starts with the short history of the discovery of superconductivity, following which the basic theories that describe this phenomena are introduced. In the third section superconducting devices, namely Josephson junction and the superconducting quantum interference device are explained. Finally, a description is given on the two refrigerators that were used to measure our superconducting circuits.

3.1 History of superconductivity

In 1908 Heike Kamerlingh Onnes succeeded in liquefying a cup of helium for the first time, which opened the door for low temperature physics [88]. It was also he, who, in order to study the conduction of metals at low temperatures, measured the abruptly vanishing resistivity of mercury at 4.2 K in 1911 [89].

The concept of phonons did not exist at the time, but it was accepted that electrons are responsible for electrical conductance and that scattering by ions causes resistivity. What was not known is how the electron-ion scattering amplitude and the mobility of electrons change upon approaching absolute zero. (The lowest temperature achieved before 1908 was 14 K using liquid hydrogen.) It was also observed that impurities have an effect on resistivity. The Leiden laboratory, where Onnes worked, had a lot of experience in

purification of mercury by distillation, therefore it was a convenient choice of a pure sample to measure. Onnes' cryostat was made out of glass, and was able to cool below 2 K. Interestingly, on the day when the first superconducting transition was measured, 8th of April 1911, in his notebook Onnes described the superfluid transition of helium as well, without realising that what he saw was also something brand new and equally as baffling as superconductivity [90].

After the experiments on mercury, Onnes' team discovered that tin and lead are also superconductors [91], and that magnetic field destroys superconductivity [92].

Zero resistivity is the first, most obvious hallmark of superconductivity. The second, which is more important for today's applications, was discovered over 20 yeas later [93]. The magnetic induction is zero inside a superconductor as long as the magnetic field is below a certain critical field, regardless the order of the following procedures: cooling below T_c, turning on magnetic field. This is called Meissner-Ochsenfeld effect. The expulsion of an applied field is what distinguishes the superconductor from a perfect conductor.

A few years after the discovery of the Meissner-Ochsenfeld effect, the London brothers described the electrodynamic properties of superconductors by introducing modifications in the Maxwell equations [94]. They assumed the existence of superconducting electrons, that can move in the lattice without resistance and their density increases from zero as temperature decreases below T_c. A "simple, but unsound derivation" [95] of the London equations is presented in section 3.2.1.

In another 15 years phenomenological description of superconductors was developed based on Landau's theory of second order phase transitions [96]. This allowed the investigation of spatial variations in the superconducting electron density, among others, that led to the discovery of flux quantisation [97].

The understanding the underlying microscopic physics came in the '50s in the form of the Bardeen-Cooper-Schreiffer (BCS) theory [98, 99]. Cooper showed that even a small attractive interaction between the electrons causes the Fermi sea to become unstable against the formation of two-electron bound states, Cooper pairs, which are responsible for superconductivity [100].

3.2 Theories of superconductivity

3.2.1 London equations

The London brothers assumed that in superconductors, besides the normal electrons, there are also superconducting electrons with charge e^*, mass m^*, and density n_s^* [94].

These superconducting electrons, unlike the normal electrons, are not scattered by the ions of the metal, accelerate freely in the electric field. Their equation of motion is the following:

$$m^* \frac{d\mathbf{v}}{dt} = -e^* \mathbf{E}. \tag{3.1}$$

Using the expression for current density, $\mathbf{j_s} = -e^* n_s^* \mathbf{v_s}$, the first London equation is:

$$\frac{d\mathbf{j_s}}{dt} = \frac{n_s^* e^{*2}}{m^*} \mathbf{E}, \tag{3.2}$$

which shows infinite conductance.

The second London equation can be obtained by combining the first, 3.2, with the Maxwell equation $\nabla \times \mathbf{E} = -\partial \mathbf{B}/\partial t$:

$$\frac{d}{dt}\left(\nabla \times \mathbf{j_s} + \frac{n_s^* e^{*2}}{m^*} \mathbf{B} \right) = 0, \tag{3.3}$$

and assuming the expression in the bracket is not only independent on time but zero, we obtain

$$\nabla \times \mathbf{j_s} = -\frac{n_s^* e^{*2}}{m^*} \mathbf{B}. \tag{3.4}$$

This is the second London equation.

When the second London equation is combined with another one of the Maxwell equations,

$$\frac{1}{\mu_0} \nabla \times \mathbf{B} = \mathbf{j_s}, \tag{3.5}$$

we get the following differential equation:

$$\Delta \times \mathbf{B} = -\frac{1}{\lambda_L^2} \mathbf{B}, \tag{3.6}$$

where λ_L is called London penetration depth. When solving equation 3.6 in one dimension, where $x = 0$ in the boundary of a superconductor, and $x > 0$ is the inside of a superconductor, we get an exponentially decreasing function: $B(x) = B_0 e^{-\frac{x}{\lambda_L}}$. This

equation describes the Meissner-Ochsenfeld effect: magnetic field inside a superconductor exponentially decreases. Characteristic length of this screening is the London penetration depth. Knowing that the superconducting electrons are electron pairs with charge $2e$, mass $2e$ and density $n_s/2$, the London penetration depth is:

$$\lambda_L^2 = \frac{m^*}{n_s^* e^* 2\mu_0} = \frac{m}{n_s e^2 \mu_0} \tag{3.7}$$

3.2.2 Ginzburg-Landau theory

In 1950 Ginzburg and Landau used Landau's previously developed theory for second order phase transitions [101] to describe the superconducting phase transition [96]. The theory assumes the existence of an order parameter, $\Psi(\mathbf{r}) = \psi_0(\mathbf{r})e^{-i\theta}$, that is zero in the normal state and increases to a finite value in the superconducting state. This order parameter describes the superconducting electrons, and their local density, $n_s(\mathbf{r}) = |\Psi(\mathbf{r})|^2$. A further assumption is that, in the vicinity of the transition, free energy can be defined, and it can be expressed as the series expansion of the order parameter, as follows:

$$\begin{aligned} f_s = f_n + \alpha(T)|\Psi(\mathbf{r})|^2 + \frac{1}{2}\beta(T)|\Psi(\mathbf{r})|^4 + \\ + \frac{1}{2m^{*2}}\left|\left(\frac{\hbar}{i}\nabla + e^*\mathbf{A}(\mathbf{r})\right)\Psi(\mathbf{r})\right|^2 + \frac{1}{2\mu_0}\mathbf{B}(\mathbf{r})^2, \end{aligned} \tag{3.8}$$

where f_n and f_s are the free energy density in the normal and the superconducting state, respectively, $\alpha(T)$ and $\beta(T)$ are coefficients of the expansion. The second to last term is the kinetic energy of superconducting electrons (with m^* mass and e^* charge) in magnetic field ($\mathbf{A}$ is the vector potential), and the last term is the energy of the magnetic field ($\mathbf{B}$). It is a requirement that the energy minimum in the normal state be at $\Psi(\mathbf{r}) = 0$, and below the transition temperature the energy has to reduce. Form this the coefficients are chosen as follows: $\alpha(T) \sim (T - T_c)$ and $\beta(T) = \beta > 0$. The energy minimum is found by taking the variational derivatives with respect to $\Psi^*(\mathbf{r})$ and $\mathbf{A}(\mathbf{r})$, which results in two differential equations, respectively:

$$\frac{1}{2m^*}\left(\frac{\hbar}{i}\nabla + e^*\mathbf{A}(\mathbf{r})\right)^2\Psi(\mathbf{r}) + \alpha\Psi(\mathbf{r}) + \beta|\Psi(\mathbf{r})|^2\Psi(\mathbf{r}) = 0, \tag{3.9}$$

$$\mathbf{j}(\mathbf{r}) = \frac{1}{\mu_0}\nabla \times \mathbf{B}(\mathbf{r}) = -\frac{e^*}{2m^*}\Psi^*(\mathbf{r})\left(\frac{\hbar}{i}\nabla + e^*\mathbf{A}(\mathbf{r})\right)\Psi(\mathbf{r}) + \text{c. c.} \tag{3.10}$$

Equation 3.9 is the non-linear Schrödinger equation of the superconducting electrons, where the non-linear term can be interpreted as a repulsive potential. 3.10 is the quantum mechanical current carried by the superconducting electrons.

Ginzburg-Landau theory was derived phenomenologically, 7 years before the microscopic origins of superconductivity were understood. In 1959 Gorkov derived the the Ginzburg-Landau equations from the microscopic theory [102], and showed, what is well known today, that e^* and m^* is the charge and mass of two electrons.

3.2.3 Bardeen-Cooper-Schrieffer theory

In 1950 it was experimentally shown by two groups that the critical temperature and field of mercury is sensitive to the isotope mass, which is today known as the isotope effect [103, 104]. Shortly after, Fröhlich submitted his paper, where he proposed that superconductivity is the result of the interaction of ions and electrons [105], predicting the isotope effect, and claiming he came to this conclusion independently, without the knowledge of the experimental confirmation [106]. A stance that is today generally accepted [107]. The idea that ions could be responsible for superconductivity, and the discovery of the isotope effect were the foundation stones of the first successful theory, the BCS theory.

The first step towards BCS theory was the realisation that the normal ground state of the electron gas, the Fermi sea, becomes unstable when an attractive interaction, however small it may be, acts between the electrons, and two-electron bound states appear [100]. In the derivation of the Cooper instability the Schrödinger equation with an attractive potential is solved for two electrons that are added to the Fermi sea. When evaluating the two-electron wave function, an important observations can be made. The lowest energy state is expected to have zero momentum, which means the electrons have equal and opposite momenta. To ensure that the wave function is antisymmetric, the electron spins must be opposite. This is an s-wave state, and indeed all conventional superconductors were found to have s-wave Cooper-pairs.

It might sound surprising to assume an attractive interaction between electrons at first. Coulomb interaction is repulsive, and even when considering screening that occurs in metals, the potential remains repulsive. Motions of the ions have to be considered to get an effective attractive interaction. An intuitive image could be the following: the first electron that passes through the lattice, polarises it by attracting the positive ions, then these positive ions attract the second electron. If this attraction can override the repulsion between the two electrons, an effective attractive potential occurs [95].

Characteristic vibrational frequency of the ions, phonon frequency, is the Debye fre-

quency, ω_D. It is assumed, that only the electrons whose energies are in the $2\hbar\omega_D$ interval around the Fermi level (E_F), experience the attractive potential.

The energy eigenvalue of the two-electron Schrödinger equations is the following:

$$E \approx 2E_F - 2\hbar\omega_D e^{-\frac{2}{N(0)V}}, \tag{3.11}$$

where $N(0)$ is the density of states at the Fermi level, and $-V$ is the attractive potential. The energy is negative with respect to the Fermi level, no matter how small V is. This means that there is a bound state of two electrons with lower energy than the ground state in the normal phase. This is called Cooper instability. The only conclusion that can be drawn from the calculation outlined above is that the Fermi sea is not a stable state anymore. To find what the new ground state of electrons is, the Schrödinger equation of all electrons in the material must be solved, and that is what the BCS theory does.

The most important results are the prediction of the energy gap (Δ) that opens in the electron spectrum around the Fermi energy, and linking that to the transition temperature (T_c). Both depend on Debye frequency, which signals the isotope effect:

$$k_B T_c = 1.14\hbar\omega_D e^{-\frac{1}{N(0)V}}, \tag{3.12}$$

$$\Delta(0K) \approx 2\hbar\omega_D e^{-\frac{1}{N(0)V}}. \tag{3.13}$$

From equations 3.12 and 3.13, the relation between T_c and $\Delta(0)$:

$$\Delta(0) = 1.754 k_B T_c. \tag{3.14}$$

BCS theory was a ground breaking theory, since it was the first microscopic theory that described superconductivity. Nonetheless, there are several experimental situations that cannot be explained by it, and thus it needs to be generalised. Processes other than electron-phonon scattering need to be considered. The reason for this are the several assumptions that are made to simplify the already complicated derivation. A few of these are: Fermi surface is assumed to be spherical, electron-phonon interaction is constant for all energies around the Fermi energy, and only singlet Cooper pairs are considered. Superconductors that can be described by the BCS theory are called conventional superconductors. Rhenium, alongside other pure metal superconductors, belongs to this group.

3.2.4 Characteristic lengths

One of the important characteristic lengths of a superconductor has already been defined in equation 3.7, it is the London penetration depth, which gives how deep the magnetic field can penetrate into a superconductor. Due to the limitations of the theory behind the London equations, λ_L is a theoretical limit of the effective penetration depth at $T \to 0$. The effective penetration depth is always larger, and diverges close to T_c.

A coherence length can be defined based on the uncertainty principle arguing that only electrons within $\sim k_B T_c$ interval of the Fermi energy can play a role. The momentum of these electrons are $p \approx k_B T_c / v_F$, where v_F is the Fermi velocity. For this the uncertainty of the location can be expressed as

$$\Delta x \gtrsim \frac{\hbar}{\Delta p} \approx \frac{\hbar v_F}{k_b T}, \tag{3.15}$$

which can be identified as the coherence length, and the numerical factor (α) can be obtained from the BCS theory:

$$\xi_0 = \frac{\hbar v_F}{\pi \Delta(0)} = \alpha \frac{\hbar v_F}{k_b T}, \tag{3.16}$$

where α is about 0.18.

Another characteristic length can be defined based on the Ginzburg-Landau theory [95]. From equation 3.9 the equilibrium value of the order parameter (Ψ_0) can be determined:

$$0 + \alpha \Psi_0 + \beta |\Psi_0|^2 \Psi_0 = 0 \quad \to \quad |\Psi_0|^2 = -\frac{\alpha}{\beta} \tag{3.17}$$

Using the normalised wave function $f = \Psi / \Psi_0$, equation 3.9 ($\mathbf{A} = 0$) can be rewritten in the following form:

$$-\frac{\hbar^2}{2m^* \alpha} \nabla^2 f + f - |f|^2 f = 0. \tag{3.18}$$

The coefficient of the gradient term is defined as the characteristic length. This is referred to as Ginzburg-Landau coherence length:

$$\xi_{GL}^2(T) = -\frac{\hbar^2}{2m^* \alpha(T)} \propto \frac{1}{T_c - T} \tag{3.19}$$

ξ_{GL} is different from ξ_0, however for pure materials, far below T_c they are equal.

The Ginzburg-Landau theory introduces the order parameter (Ψ), that was said to be related to the density of superconducting electrons ($n_s = |\Psi|^2$). It was shown in equation 3.17 that the equilibrium value of the order parameter is $-\alpha/\beta$. Writing this in the expression of the London penetration depth (equation 3.7), we can see that the penetration depth has the same temperature dependence as the Ginzburg-Landau coherence length, and they both diverge upon approaching T_c [95].

$$\lambda_L^2(T) = \frac{m^*}{4\mu_0 e^{*2}|\Psi_0|^2} = -\frac{\beta m^*}{4\mu_0 e^{*2}\alpha(T)} \propto \frac{1}{T_c - T}. \tag{3.20}$$

The dimensionless and temperature independent Ginzburg-Landau number is introduced, it shows the relation between the penetration depth and the coherence length [95].

$$\kappa = \frac{\lambda_L(T)}{\xi_{GL}(T)}. \tag{3.21}$$

Its significance will be discussed in chapter 3.2.7.

3.2.5 Dirty and clean superconductors

The term 'dirty superconductor' was coined by P. W. Anderson in his 1959 paper, where he "sketched" a BCS type theory for "very dirty superconductors" [108]. It has been observed that superconductivity is often insensitive to the amount of impurities present in the material. These impurities include crystal defects and non-magnetic chemical impurities: beryllium was shown to display superconductivity in amorphous state with T_c twenty times higher than in crystalline state [109, 110]. He divided superconductivity in two regions: clean superconductors that are sensitive to the introduction of additional impurities; and dirty superconductor that are insensitive.

Impurities cause conduction electrons to scatter. This scattering quantitatively is described by the mean free path (l). In the clean limit the electrons are rarely scattered, the mean free path is longer than the superconducting coherence length ($l \gg \xi$). In the dirty limit, however, electron scattering is strong, electron mean free path is shorter than the coherence length ($l \ll \xi$). The effective coherence length in dirty superconductors is reduced. Its value near the transition temperature can be obtained from the BCS theory [95]:

$$\xi_{\text{clean}} = 0.74\frac{\xi_0}{\left(1-\frac{T}{T_c}\right)^{\frac{1}{2}}}, \qquad \xi_{\text{dirty}} = 0.855\left(\frac{\xi_0 l}{1-\frac{T}{T_c}}\right)^{\frac{1}{2}}. \tag{3.22}$$

3.2.6 Fluxquatization

It has been observed that inside a superconductor ring the magnetic field cannot take an arbitrary value, but it must be an integer multiple of the so called flux quantum, $\Phi_0 = h/2e$ [111].

Flux passing through a surface area (S with normal $\mathbf{n}$) can be calculated by integrating the magnetic induction vector ($\mathbf{B}$) over that surface [112]. Using Stokes theorem the surface integral becomes a line integral running around the boundary of the area ($\mathbf{l}$), and the induction vector is replaced by the vector potential ($\mathbf{A}$):

$$\Phi = \int \mathbf{B}\cdot\mathbf{n}\,dS = \int \mathbf{A}\cdot d\mathbf{l}. \tag{3.23}$$

The vector potential in the superconducting regime can be expressed from one of the Ginzburg-Landau differential equations, equation 3.10. Current is 0 deep inside the superconductor, where the integration is considered. The order parameter is assumed to have the form $\Psi(\mathbf{r}) = \psi_0(\mathbf{r})e^{-i\theta}$, where ψ_0 is thought to have the equilibrium value, and does not change along the integral. Only the phase can change. Using these, the vector potential, and the flux inside the superconducting ring, respectively, is:

$$\mathbf{A} = -\frac{\hbar}{e^*}\nabla\theta, \qquad \Phi = -\frac{\hbar}{e^*}\int \nabla\theta\, d\mathbf{l}. \tag{3.24}$$

Phase must be a single valued function of space, $\theta(\mathbf{r})$, so, along a closed loop it can only change by integer multiples of 2π. The solution of the integral is then

$$\Phi = -\frac{\hbar}{e^*}n2\pi = n\frac{h}{2e} = n\Phi_0, \quad \text{where} \quad \Phi_0 = \frac{h}{2e} = 2.067\cdot 10^{-7}\,\text{Gauss}\cdot\text{cm}^2. \tag{3.25}$$

Φ_0 is called the flux quantum.

3.2.7 Two types of superconductors

In chapter 3.2.4 the dimensionless Ginzburg-Landau number was introduced, and its importance was promised to be explained. To recap, κ is defined as the ratio of the

penetration depth (λ) and the coherence length (ξ). The penetration depth describes the disappearance of the magnetic field at the boundary of the superconductor, and the coherence length is related to the decay of the order parameter. Therefore, their relative value describes the properties at the superconducting-normal interface. In figure 3.1 the magnetic field curve (h) and the order parameter (Ψ) are shown on the boundary of a superconductor for the two extreme cases of κ.

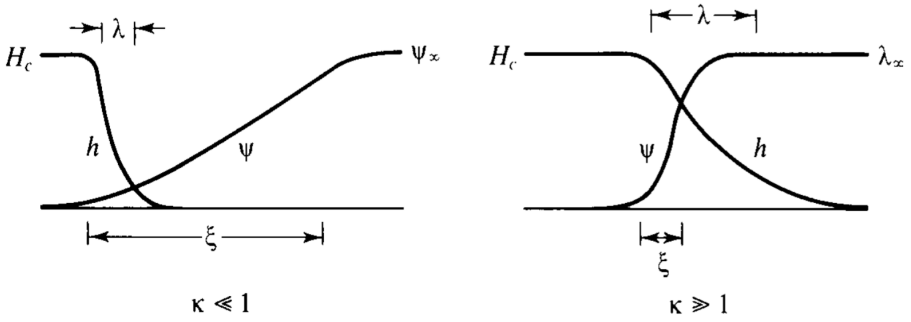

Figure 3.1: The superconducting order parameter and the magnetic field at a normal(left)-superconducting(right) interphase. [95].

When κ is smaller than 1, the coherence length is longer than the penetration depth, and there is a region where the magnetic field and the order parameter are both small. Expelling the magnetic field costs energy, and this energy is not compensated by the condensation to the superconducting phase, thus this interface has a positive energy. However, in the case when κ is larger than 1, following the same argument, interfacial energy can become negative, meaning that walls of this type can spontaneously appear. The crossover between positive and negative interfacial energy is at $\kappa = 1/\sqrt{2}$. This value for κ was already mentioned in Ginzburg and Landau's original paper [96], but it was Abrikosov who predicted how the magnetic field behaves in such superconductors [97], which will be briefly discussed below [95].

Since the penetration depth and the coherence length are material properties, we can talk about two types of superconductors. Type I are the ones with $\kappa < 1/\sqrt{2}$. Superconductivity is completely destroyed, and magnetic field enters the material at a certain critical filed $H_c(T)$.

Type II superconductors have $\kappa > 1/\sqrt{2}$. These materials have two critical fields, H_{c1} and H_{c2}. Their phase diagram is shown in figure 3.2. The Meissner phase, is the homogeneous superconducting phase, where the magnetic field is fully expelled. When the magnetic field is increased exceeding H_{c1}, type II superconductors transit to a so

called vortex phase, where magnetic field and superconductivity mix. Above H_{c2}, the superconductor transits to the normal phase [112].

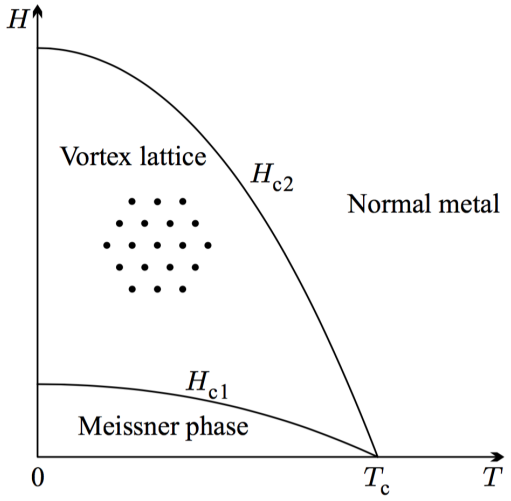

Figure 3.2: H-T phase diagram of a type II superconductor. [112].

In the vortex phase, that is unique to type II superconductors, magnetic flux is present in the sample in the form of tubes, vortices, around which the superconducting phase persists. The profile of the magnetic induction (B) and the order parameter around a core of a vortex (r=0) is shown in figure 3.3. The order parameter drops in the core of the vortex, while the magnetic induction reaches its maximum. The supercurrent is circulating around the core of the vortex. One vortex can only contain integer multiples of the flux quanta ($\phi_0 = h/2e$), where the integer is energetically favoured to be 1. When the magnetic field is increased, the density of the vortices increases. Due to the repulsion that acts between the vortices, they arrange themselves in a regular array, which is has trigonal symmetry in most cases.

The vortex phase was predicted by Abrikosov in 1957 [97], and it was first directly observed in 1967 by electron microscope using, magnetic particles for contrast [113].

3.3 Superconducting devices

3.3.1 Josephson junction

In 1962 Josephson pointed out that Cooper pairs can tunnel between two superconductors separated by a thin ($L < \xi$) barrier [114]. This construction is called a Josephson junction.

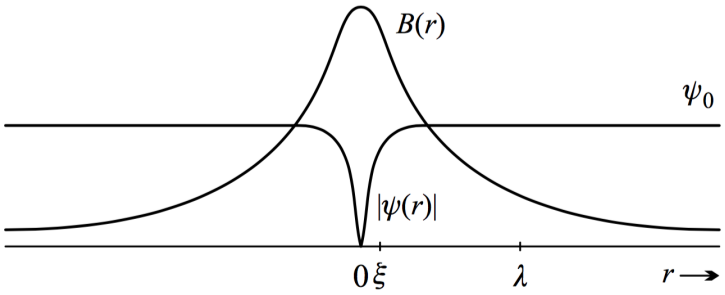

Figure 3.3: Order parameter and magnetic induction across a vortex. [112].

The thin barrier can be an insulating layer, as it was originally imagined by Josephson, or a thin metallic constriction with dimensions below the coherence length. The tunnelling current can be derived from the Ginzburg-Landau equations, and it is outlined below.

Recalling equation 3.18 in one dimension:

$$\xi^2 \frac{d^2 f}{dx^2} + f - f^3 = 0, \tag{3.26}$$

where $f = \Psi/\Psi_0$. The superconductors on the two sides of the bridge are assumed to be in equilibrium, giving $|f| = 1$, but the phase of the superconducting wave function can still differ. An absolute phase cannot be defined without loss of generality, it can be chosen to be 0 at one end of the bridge and $\Delta\theta$ at the other, which then gives the boundary conditions: $f(x = 0) = 1$; $f(x = L) = e^{i\Delta\theta}$. When $L \ll \xi$, equation 3.26 is dominated by the first term, in which case the problem is reduced to Laplace's equation:

$$\xi^2 \frac{d^2 f}{dx^2} = 0. \tag{3.27}$$

The most general solution in one dimension is $f = a + bx$, which after satisfying the boundary conditions gives:

$$f = \left(1 - \frac{x}{L}\right) + \frac{x}{L} e^{i\Delta\theta}. \tag{3.28}$$

The current running through the bridge can be obtained by inserting 3.28 into the Ginzburg-Landau expression of current, equation 3.10:

$$I_j = I_c \sin\Delta\theta, \quad \text{where} \quad I_c = \frac{e^* \hbar \Psi_0^2}{m^*} \frac{A_{cs}}{L}. \tag{3.29}$$

A_{cs} is the cross-sectional area of the bridge.

This means that the tunnelling superconducting current is the function of the relative phase of the wave function in the two superconducting regions, and is limited by the critical current, which is dependent on the bridge dimensions [95].

3.3.2 Superconducting quantum interference device

A superconducting quantum interference device (SQUID) is superconducting ring that is interrupted by at least one Josephson junction, shown in figure 3.4. Their current-magnetic flux characteristics are very sensitive to small changes of the magnetic field, therefore they are used as magnetometers. In scanning SQUID microscopy, SQUIDs are the scanning probes, and they map the magnetic field across a magnetic or superconducting sample.

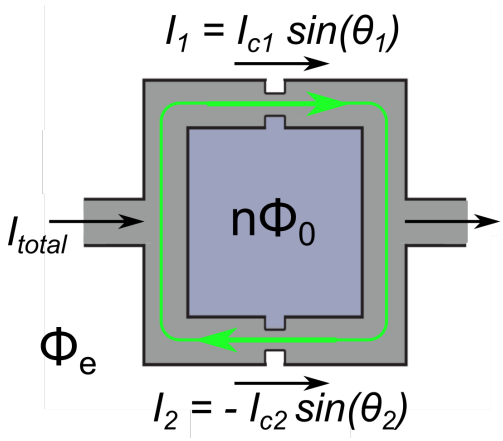

Figure 3.4: Schematic illustration of a SQUID containing two Josephson junctions. I_1 and I_2 currents running through the two junctions are modulated by the phase drops θ_1 and θ_2 [115].

In most SQUIDs the superconducting ring is interrupted by two junctions, as shown in figure 3.4. The ring is put in magnetic field such that the flux through it is Φ_e. As a result of the magnetic field, a current will circulate in the ring. From equation 3.29, the current through the junctions is defined by the phase drop across, θ_1 and θ_2:

$$I_1 = I_{c1} \sin\theta_1 \qquad I_2 = -I_{c2} \sin\theta_2, \tag{3.30}$$

where I_{c1} and I_{c2} are the critical currents.

The total current through the ring is the sum I_2 and I_1:

$$I_{\text{total}} = I_1 + I_2 = I_{c1} \sin\theta_1 - I_{c2} \sin\theta_2. \tag{3.31}$$

The sum of the phase differences across the two junctions is the integral of the vector potential along the ring:

$$\theta_1 + \theta_2 = \frac{2e}{\hbar} \int \mathbf{A} d\mathbf{l} = 2\pi \frac{\Phi_e}{\Phi_0}. \tag{3.32}$$

Using this in equation 3.31, the total current in the ring is:

$$I_{\text{total}} = I_{c1} \sin\theta_1 + I_{c2} \sin\left(\theta_1 - 2\pi \frac{\Phi_e}{\Phi_0}\right). \tag{3.33}$$

To find the maximum current through the ring, equation 3.33 has to be minimised with respect to θ_1:

$$\frac{dI_{\text{total}}}{d\theta_1} = I_{c1} \cos\theta_1 + I_{c2} \cos\left(\theta_1 - 2\pi \frac{\Phi_e}{\Phi_0}\right) = 0 \tag{3.34}$$

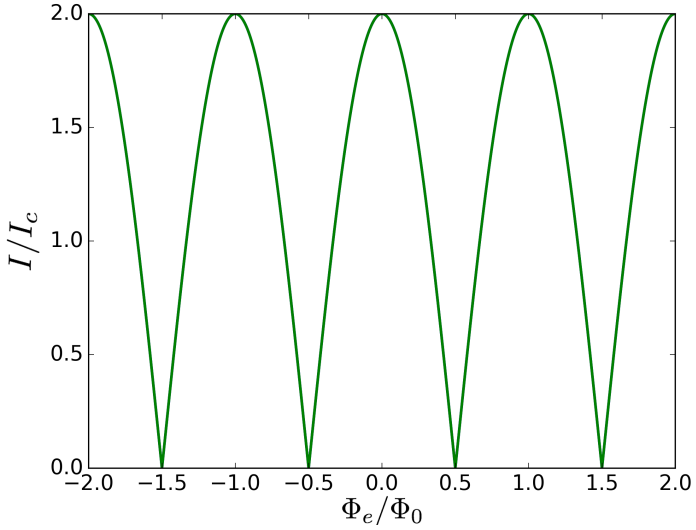

Figure 3.5: $I(\Phi_e)$ characteristic of a symmetric SQUID with zero inductance.

Summing the squares of equations 3.33 and 3.34:

$$I_{\text{total}}^2 = I_{c1}^2 + I_{c2}^2 + 2I_{c1}I_{c2}\cos\left(2\pi\frac{\Phi_e}{\Phi_0}\right). \tag{3.35}$$

Using the identity $\cos\delta = 2\cos^2\frac{\delta}{2} - 1$, equation 3.35 can be rearranged as follows:

$$I_{\text{total}} = \sqrt{(I_{c1} - I_{c2})^2 + 4I_{c1}I_{c2}\cos^2\left(\pi\frac{\Phi_e}{\Phi_0}\right)}. \tag{3.36}$$

If the junctions are assumed to be identical with equal critical currents ($I_{c1} = I_{c2} = I_c$), the critical current takes the following form:

$$I_{\text{total}} = 2I_c\left|\cos\left(\pi\frac{\Phi_e}{\Phi_0}\right)\right|. \tag{3.37}$$

The flux dependence of the current is shown in figure 3.5. The current changes periodically as the flux increases or decreases. These devices can be used to detect small magnetic fields [116].

The above calculation is only valid if the inductance of the SQUID (L_{SQUID}) is zero, which is not true in general. When L_{SQUID} is not zero, the flux inside the ring is modified

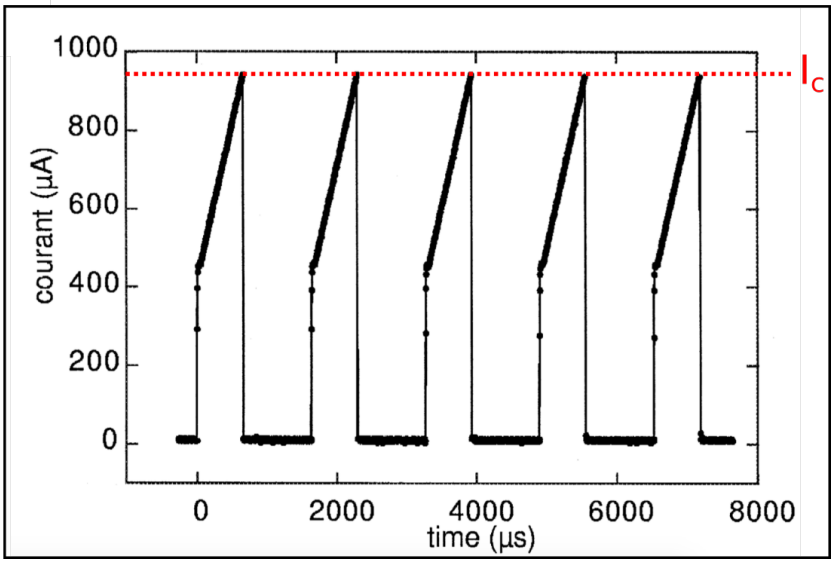

Figure 3.6: Oscilloscope reading of the current ramp repetitions applied to a Nb SQUID [116].

by the current running through it: $\Phi_L = \Phi_e + IL_{\mathrm{SQUID}}$. The critical current can be determined numerically. The inductance of the SQUID depends on its size.

To measure the critical current of a SQUID, one end is connected to a current source, the other to the ground, and the current is increased until it reaches the critical current.

In our setup, the SQUID is biased by a current which is ramped up from 0 with a given slope. At the start of the current ramp, a 40 MHz quartz clock is starts, simultaneously. When the critical current is reached, voltage appears across the SQUID, and the $\partial V/\partial t$ pulse is detected, the clock is stopped and the current is set back to zero. The time laps measured by the clock is registered, and the ramp starts again. The biasing current versus time is shown in figure 3.6. One critical current data point is plotted after averaging 30 critical current measurements.

SQUIDs have a hysteric V(I) characteristic due to Joule heating in the normal state. When the critical current is reached, the voltage pulse heats the SQUID, and after the bias current is switched off, it takes time to cool down, and return to the superconducting state. This limits the frequency at which the current ramp can be repeated [116].

3.4 Refrigerators

Temperature and magnetic field dependence of transport properties of complete films and nanostructures were measured. For the low temperature measurements two different refrigerators were used: a table top Helium-3 cryostat where only the temperature can be adjusted, and a dilution refrigerator where magnetic field can be applied as well.

3.4.1 Table-top helium-3 cryostat

Low temperature resistivity measurement on the rhenium wires were performed in a table-top helium-3 cryostat, which was designed and built at Institut Néel [117].

This cryostat, as its name suggests, is a compact, easy-to-use refrigerator, is able to cool down to 300 mK in about 3 hours. A simplified schematics, and a photograph of the inside is shown in figure 3.7, and in figure 3.8, respectively. It consist of a vacuum chamber that houses two interlocked helium circuits: one open circuit for helium-4 (blue line in figure 3.7), that runs through the cryostat from the reservoir to the recovery exhaust; and a closed circuit for helium-3 (orange line in figure 3.7). The volume of the fridge is divided by two radiation shields: an 80 K one (red in figure 3.7), and a 4 K one (green in figure 3.7). The coldest point is at the top, this is where the sample is placed, shown by purple in figure 3.7, and by an arrow in figure 3.8.

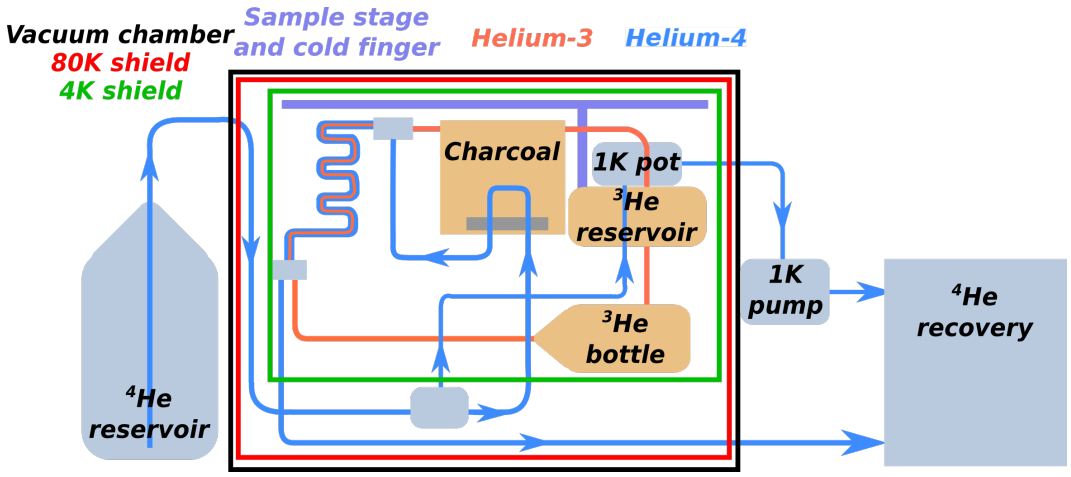

Figure 3.7: Schematic diagram of the table-top Helium-3 cryostat. It contains two circuits: ^{4}He shown in blue, ^{3}He shown in orange. Coldest temperature, 300 mK is achieved by internal pumping using charcoal on the ^{3}He reservoir.

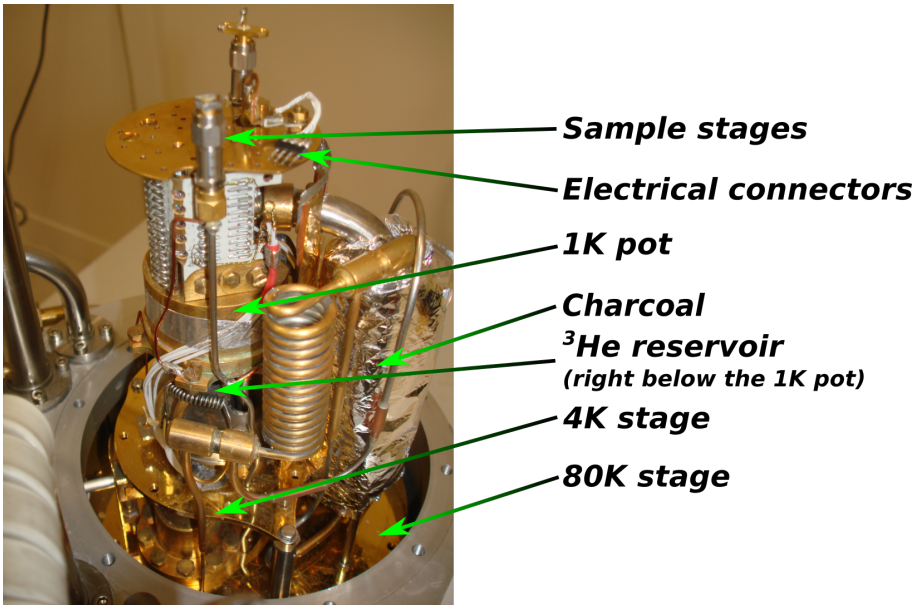

Figure 3.8: Photograph of the inside of the table-top helium-3 cryostat.

The fridge can be cooled down to approximately 1.2 K by circulating only helium-4, and pumping on it in the 1 K pot, shown in figures 3.7 and 3.8. At this temperature the vapour pressure of ^{4}He is too small, the rate of evaporation is too low to reduce the

temperature further.

Below 3.19 K helium-3 starts to condense in its reservoir. The condensation process can be monitored by measuring the pressure in the helium-3 circuit. When the condensation is complete, the helium-3 liquid is pumped by an internal sorption system, which is activated charcoal placed in the neighbouring container, labeled as charcoal in figures 3.7 and 3.8. This way the temperature of the reservoir can be further reduced to 300 mK, where we meet the same limitation: the vapour pressure is too low for evaporation to cool down further. This is the minimum temperature that can be achieved using pure helium-3. Once all the helium-3 is adsorbed, the charcoal can be heated to 40 K to release the gas, and the condensation-adsorption cycle can be repeated.

The temperature of the sample can be adjusted by ohmic heating, running current through a resistor placed on the sample stage.

3.4.2 Inverted dilution refrigerator

A dilution refrigerator contains several circuits, one of which is a closed circuit, containing a mixture of helium-4 and helium-3. Using the other, only helium-4 circuits, the fridge is able to reach the 1.2 K mentioned above, by strong pumping on the liquid ^{4}He. At

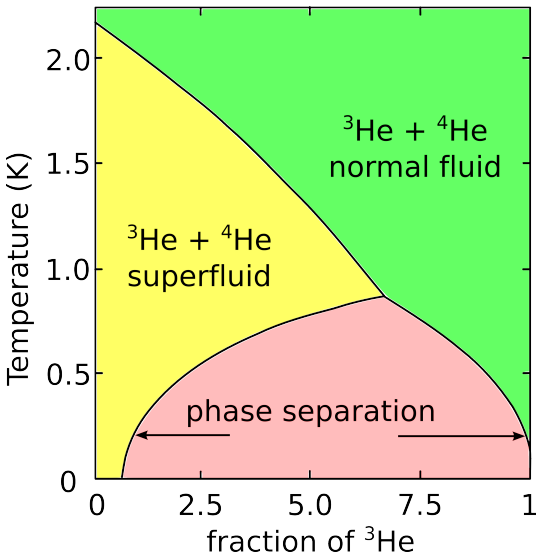

Figure 3.9: Phase diagram of the ^{3}He and ^{4}He mixture. Below 800 mK the mixture spontaneously separates into a diluted (yellow) and a concentrated in ^{3}He phase (green) Image is from reference [118].

this temperature the mixture has condensed, and by pumping on it, the temperature is decreased further. Upon reaching 800 mK, the mixture spontaneously undergoes a phase separation, as shown in the phase diagram in figure 3.9: the pink region is forbidden, the liquid separates into two phases. The one marked with yellow is still a mixture of ^{4}He and ^{3}He, but contains only a small amount of ^{3}He. This is the diluted phase. The other phase marked with green is also a mixture of the two isotopes, but it is rich in ^{3}He, this is the concentrated phase.

The volume of the mixture and the concentration of ^{3}He is set so that the phase boundary between the diluted phase and the concentrated phase occurs in the mixing chamber, and the liquid surface of the concentrated phase is in the still. A simplified mixture circuit is shown in figure 3.10, noting the mixing chamber and the still. Diluted phase is marked with blue, concentrated phase with orange. The lighter shade of orange corresponds to the gaseous phase, the darker to the liquid.

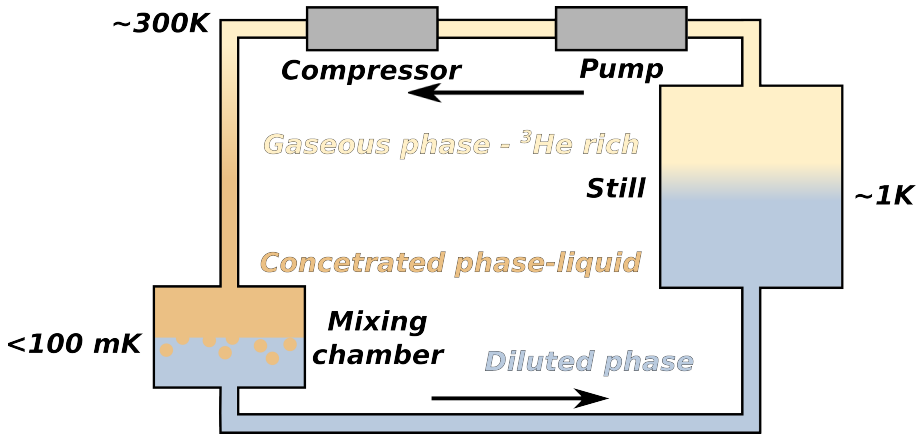

Figure 3.10: Simplified diagram of the mixture circuit of a dilution refrigerator. After the mixture separates to a diluted (blue) and a concentrated (orange) phase, ^{3}He is extracted from the still and resupplied to the mixing chamber. Cooling power is provided by the diffusion of ^{3}He from the concentrated to the diluted phase in the mixing chamber.

In the mixing chamber the concentrated phase floats on top of the denser diluted phase. The vapour in the still contains higher concentration of the component that has a lower boiling point. This is the helium-3, and is continuously pumped. The concentration of ^{3}He in the diluted phase drops as a result. To compensate the decreasing concentration, ^{3}He diffuses from the concentrated phase into the diluted phase in the mixing chamber. Dilution of helium-3 in the superfluid helium-4 requires heat absorption, superfluid helium-4 acts like vacuum. Dilution can be compared to evaporation, since the

^{3}He leaves a phase where the atoms are densely packed, like in a liquid, for a phase where they are further apart like in a gas. As a result, the mixing chamber, and everything thermally connected to it (sample) cools down.

The diagram in figure 3.10 is grossly simplified. The mixture circuit is interlocked with the helium-4 circuit. On the left the vapour leaving the still is warmed up by running through the incoming liquid helium-4, reaches room temperature by the time it gets to the pump. After the compressor the mixture runs through a liquid nitrogen bath, that removes the contamination that might be present, then in enters the fridge through the outgoing helium-4 pipes, which pre-cools it. On its way to the mixing chamber it runs in close contact with the vapour that is leaving the still, that aids further cooling. To liquify it, its pressure is increased by driving it through narrow pipe sections called impedance.

Dilution fridges are limited by the increasing viscosity and thermal conductivity of the circulating fluids as the temperature is lowered. For this reason the lower the temperature the larger the diameter of the tubes must be which increases the cost. The lowest temperature where they are still practical to use is 2 mK.

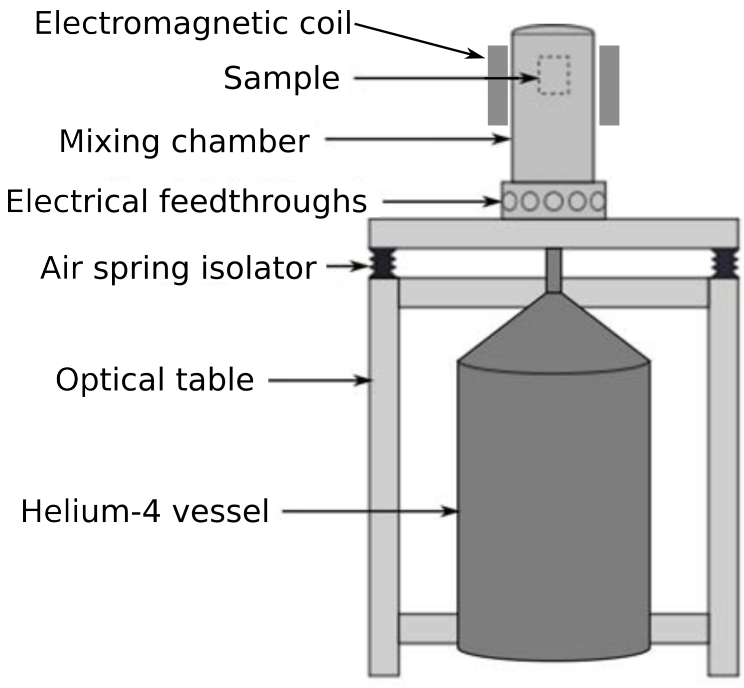

Figure 3.11: Diagram of the SIONLUDI inverted dilution fridge. The coldest part is on the top, the sample is loaded there, placed under concentric bells. Helium-4 is supplied from the bottom. Modified image from reference [115].

In conventional dilution fridges, the coldest part, the mixing chamber is at the bottom. We used an inverted dilution fridge, SIONLUDI, where the mixing chamber is at the top. Its schematic is shown in figure 3.11, it was designed and built in Institut Néel. The sample is easy to load, it is placed under concentric bells which are, from the outside: vacuum seal, and temperature shields for 300 K, 80K, 20 K, and 4 K. Helium-4 is fed from the bottom, and the fridge is placed on a vibration free table. The magnetic field can be adjusted by changing the current in the copper coil, which is outside of the vacuum bell.

"The world's wealth would be won by the man who,
out of the Rhinegold, fashioned the ring
which measureless might would bestow."

Richard Wagner, Das Rheingold, Der Ring des Nibelungen

4

Transport properties of rhenium wires and SQUIDs

Rhenium thin films have shown long superconducting coherence lengths (up to 170 nm) and electron mean free paths (up to 200 nm)[7]. This makes them suitable to study the effect of the decreasing size on the superconducting properties by reducing the dimensions of the samples to the vicinity of those two length scales. To explore this, and to study the effect of lithography on the superconducting properties of rhenium thin films, wires with width from 100 nm to 3 μm were fabricated. We have also successfully fabricated SQUIDs. In this chapter it is shown that superconductivity is unaffected by the lithography process. Sensitivity of T_c to lattice imperfections and orientation is studied. Finally, low noise SQUIDs are presented.

4.1 Fabrication

4.1.1 Circuit designs

3 different patterns were fabricated using laser and electron beam lithography.

The first design is shown in figure 4.1(a). It features a long wire that has 7 parts with different widths, ranging from 50 μm to 3 μm. This is shown in blue. The electrodes

that allow 2-point or 4-point resistivity measurements are shown in pink. Electrodes are connected to the ends of all the 7 parts, thus they can be measured independently of each other. External electrodes can be connected to the large pads shown in purple. This design was fabricated with laser beam lithography. The smallest object it included was the 3 μm wire, due to the resolution limitations of laser light ($\sim 1\mu$m).

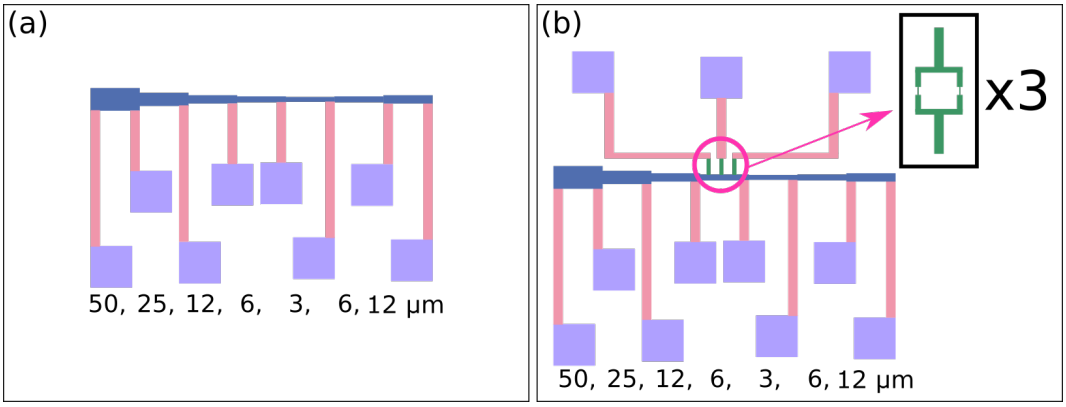

Figure 4.1: (a)Lithography design I: long wire with parts that have different widths (blue). Drawing is not to scale. (b) Lithography design II: long wire with parts that have different widths (blue), and 3 SQUIDs (green). Drawing is not to scale.

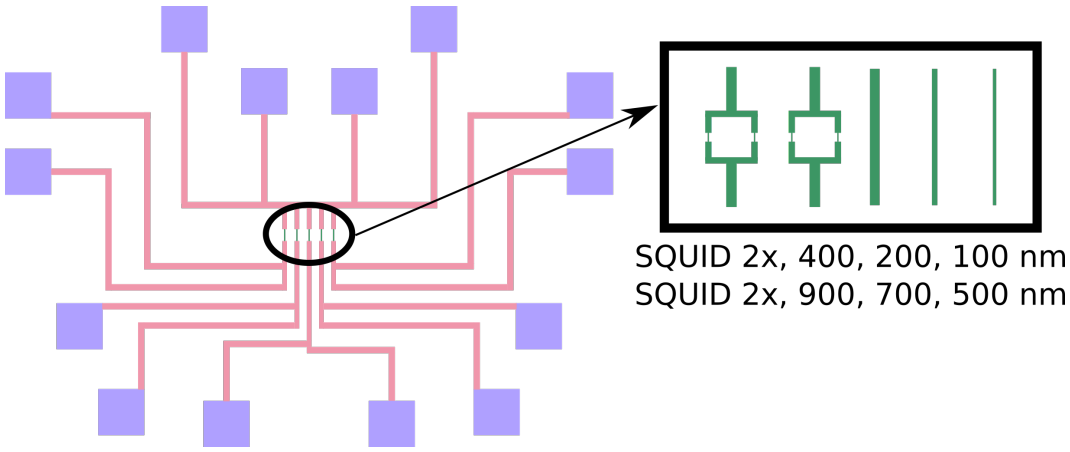

Figure 4.2: Lithography design III: 2 SQUIDs and 3 wires, each have two electrodes at the bottom, and one common electrode on top. Drawing is not to scale.

The second design is shown in figure 4.1(b). It features the same long wire as was shown in figure 4.1(a). This pattern was fabricated using electron beam lithography,

which allowed us to reduce the dimensions to the nanometer range. SQUIDs were included in this pattern. They are attached to the middle of the wire, and are shown in green in figure 4.1(b).

The third design is shown in figure 4.2. This pattern was also fabricated using electron beam lithography. Widths of the wires were reduced below 1 μm. The pattern included 2 SQUIDs as well, with different bridge widths: 50 nm and 20 nm. In this design each wire and SQUID is connected to two pads on the bottom, and there is a common electrode on the top with four pads. Two versions of the design were fabricated alternating on the film. The first version had wire widths 100 nm, 200 nm, and 400 nm; the second had 500 nm, 700 nm, and 900 nm.

Drawings shown in figures 4.1(a), 4.1(b), and 4.2 are not to scale.

4.1.2 Lithography

Steps of the lithography process are shown in figure 4.3.

First, the sample is spincoated with the resist. For laser beam lithography, S1818 resist was used, which forms a layer with thickness in the range of 1 μm on the surface of the sample. For electron beam lithography, PMMA (polymethyl methacrylate) resist was used, with a thickness in the range of 100 nm. After spincoating, the sample is baked to evaporate the solvent from the resist.

In the next step, the surface was exposed to a laser or electron beam along the pattern lines. Both of the resists are so called positive resists. They consist of long polymer chains,

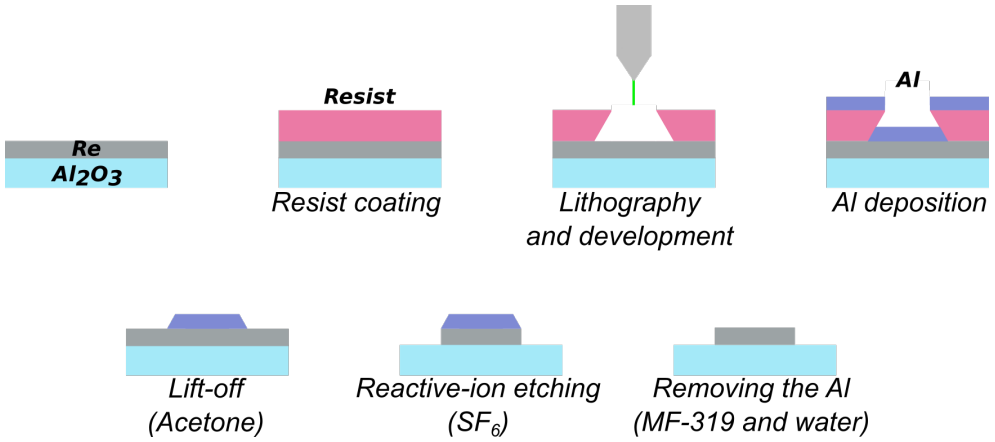

Figure 4.3: Steps of the lithography process used to fabricate wires and SQUIDs on rhenium thin films.

which break up to smaller fragments when exposed to light/electron beam. The smaller fragments can be dissolved easily in the developer, leaving behind a positive imprint of the pattern in the resist [119].

	Laser beam	Electron beam
Resist	S1818	PMMA
Thickness	~ 1 μm	~ 100 nm
Bake	115°C	180°C
Instrument	Heidelberg DWL66FS	Léo 1530
Developer	MF-319	1:3 MIBK:IPA methyl isobutyl ketone:isopropyl alcohol

Table 4.1: Resists, instruments and developers used for lithography.

In the case of electron beam lithography, the designs had to be patterned without moving the sample stage. This was done in two steps. In the first step, a 1 mm^2 writing field was chosen, and the pads and the electrodes were written using a beam current (I) of a few mA. In the second step, the writing field was reduced to 50 μm^2, and the wires and the SQUIDs were patterned using a beam current of 12-14 pA. The dose (D), charge received by unit area, can be obtained from the beam current using the formula $D = It/A$, where t is the exposure time, and A is the area. For the bridges in the SQUIDs, the dose was increased, and they were scanned only once.

After the development, the resist was removed from the surface of the rhenium where it was exposed. In the next step, 20 nm of aluminium was deposited using a Plassys MEB 550S evaporator. During lift-off, the sample was placed in acetone, which dissolved the remaining resist. The aluminium on top of the resist was also removed. To protect the thin bridges of the SQUIDs, we did not use ultrasonic bath at this step, only a pipette to stir the liquid a few times. Lift-off took approximately 2 hours. After the lift-off, aluminium only covered the rhenium film along the pattern lines. In the penultimate step the rhenium was removed everywhere by reactive ion etching (SF_6) using an RIE Plassys, except where it was protected by the aluminium. Finally, the aluminium covering the structures was removed by first immersing the sample in a developer called MF-319 developer (app. 3 % solution of $N(CH_3)_4^+OH^-$ in water), then rinsing it in distilled water and drying under nitrogen flow.

4.2 Description of the samples

Three rhenium films with different thicknesses, surfaces and crystallographic structures were patterned as described above, and transport measurements were conducted at low temperature. Before patterning the samples were studied with AFM and XRD techniques. The details of the measurements and analysis are described in chapter 2.2. A summary of the results and the patterns fabricated are listed in table 4.2.

	Sample B	Sample D	Sample F
Film thickness	25 nm	50 nm	100 nm
Deposition temp.	900°C	900°C	800°C
AFM image	figure 2.15(b)	figure 2.21	figure 2.33(a)
Features	grains	spirals	spirals
Diameter	$<$ 100 nm	$\sim$ 500 nm	$\sim$ 200 nm
XRD	figure 2.16 red curve	figure 2.25 red curve	figure 2.34 blue curve
Orientations	**(002)** (101), (110)	**(002)** (100), (110)	**(002)** (101), (110)
Lithography	design III	design II	design I
Measured wires	100 nm - 400 nm	3 μm	3 μm
SQUID	✓	×	×

Table 4.2: Crystallography and surface information on the samples that were used for the fabrication.

4.2.1 50 nm thick sample

Ten copies of design II, shown in figure 4.1(b), was patterned onto the 50 nm thick sample using electron beam lithography, as described in section 4.1. An image taken with an optical microscope of a completed pattern unit is shown in figure 4.4.

The pattern is not perfect, as some rhenium remained on the sides of some of the electrodes, and in some corners. This is due to wrong electron dose used during patterning. Electrons are scattered in the resist, are backscattered, and excite secondary electrons from the film. All these processes affect the size and shape of the patterned volume, this is called proximity effect. In the third step shown in figure 4.3, the ideal shape of the imprint in the resist is shown. It is a trapezoid. If the shape of the imprint is correct,

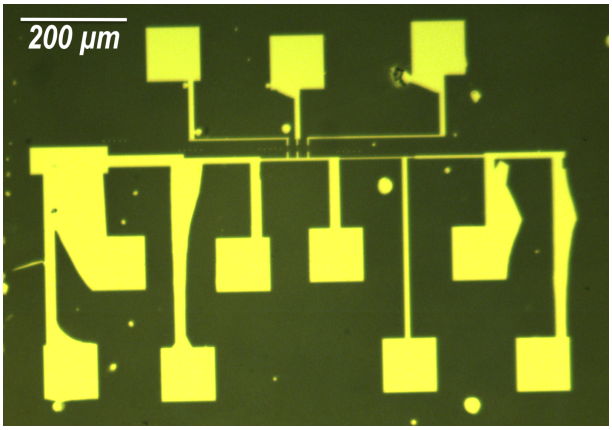

Figure 4.4: Optical microscopy image taken on the completed pattern fabricated from the 50 nm thick sample.

the deposited aluminium is not continuous, and is removed with the resist during lift-off. However, if the dose is wrong, and the imprint does not have the correct shape, the aluminium layer can be continuous, thus harder or impossible to remove with the resist during lift-off. Where aluminium is left, rhenium cannot be etched. The remaining rhenium created shortcuts and thicker wires on some of the patterns. These were excluded from the measurement.

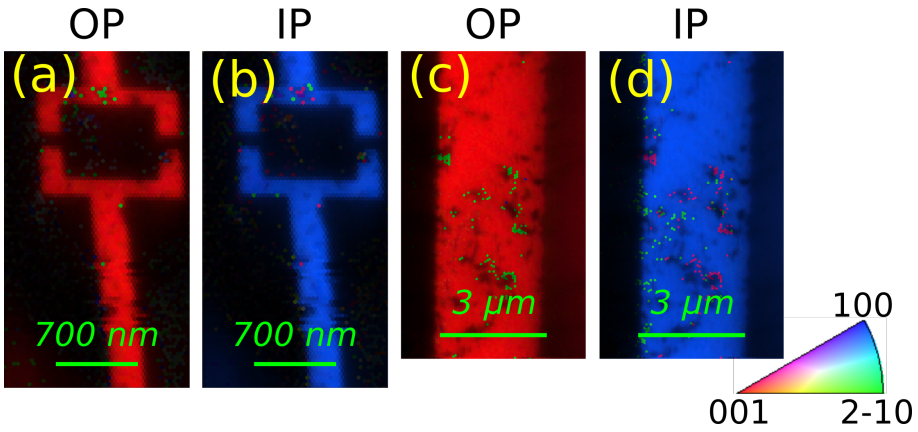

Figure 4.5: (a), (c) Out-of-plane (OP) orientation maps show that the orientation of rhenium along the 3 µm line and the SQUID is (001). (b), (d) In-plane orientation maps taken on the same areas as (a) and (c) shows that the in-plane orientations are also uniform.

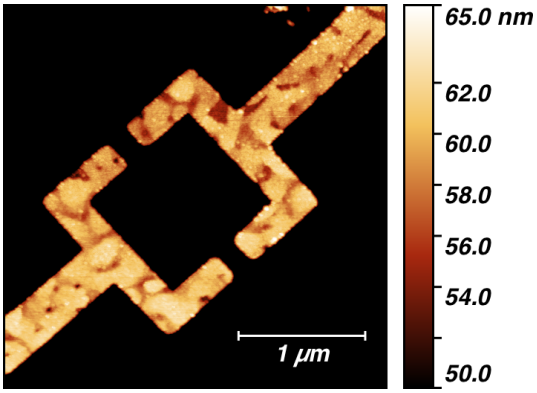

Figure 4.6: AFM height image taken on a SQUID. The spirals were left intact, however the bridges connecting the two forks of the SQUID are missing.

The correct dose can only be found by experimentation.

To verify the crystallography of the patterned area, EBSD measurements were carried out in SiMaP on the circuits after the lithography process using a FEG Zeiss scanning electron microscope.

Figures 4.5(a) and 4.5(c) show the out-of-plane (OP) orientation maps of a SQUID and a 3 μm line. The colour red is uniform along the measured area except in a few points. The red colour corresponds to the orientation (001), which is consistent with the results of the XRD.

Figures 4.5(b) and 4.5(d) show the in-plane (IP) orientation maps of the same areas. Here the colour is uniformly blue.

The intensity of the colour red and blue in these figures scales with the IQ, which measures the quality of the Kikuchi pattern recorded at a position [120]. In the areas where the intensity of red/blue is lower, points with the non-uniform colour can also be found. The low IQ of this area suggests that the orientations of these points were wrongly identified by the software due to weak contrast or blur in the Kikuchi patterns.

The surface was also investigated with AFM after the patterning. A SQUID is shown in figure 4.6. On the surface of the SQUID, a few nanometers of height variation can be observed. It corresponds to the spirals. They were left intact during the lithography process.

Unfortunately, the thin bridges that are the weak links between the two forks of the SQUID are not present on this sample. The dose during electron beam exposure was too low. The resist at the nanowire level was removed during development. For later samples the dose was adjusted.

4.2.2 25 nm thick sample

The two versions of design III were fabricated onto the sample using electron beam lithography. Version one had wires widths 100 nm, 200 nm and 400 nm, version two had 500 nm, 700 nm and 900 nm. The two version were alternating, and were repeated 18 times all over the sample.

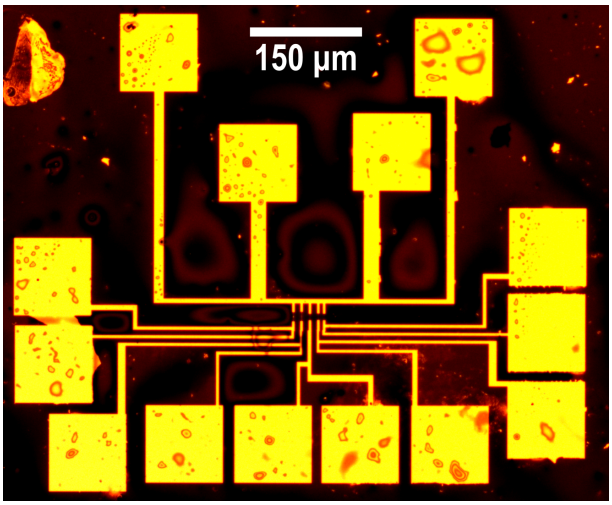

Figure 4.7: Optical and electron microscopy image taken on the completed design patterned onto the 25 nm thick sample.

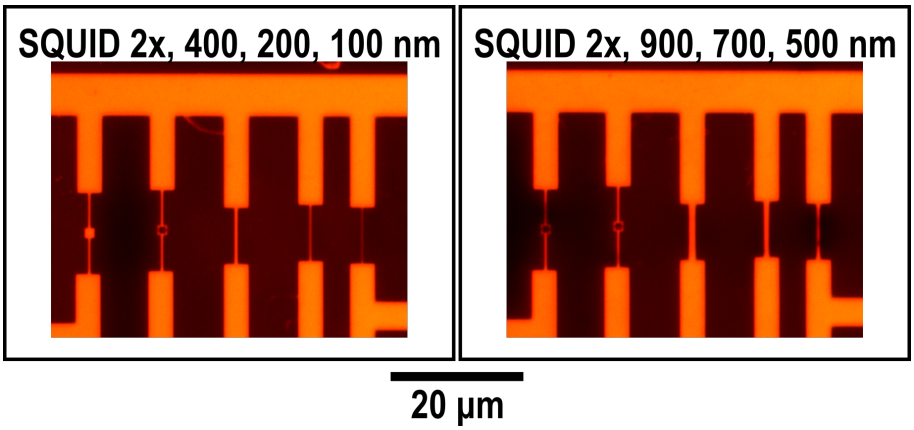

Figure 4.8: Optical microscopy images taken on the central parts of the two versions of the completed design on the 25 nm thick film.

Figure 4.7 shows an optical microscopy image of one of the full, completed patterns. In figure 4.8, the wires and the SQUIDs are shown.

As with the previous sample, the electron dose was not perfectly set, and it caused short cuts in some places. Because the pattern was repeated many times all over the sample, there were a sufficient number to choose from, where the left-over rhenium did not cause a short circuit.

4.2.3 100 nm thick sample

Design I was patterned onto the 100 nm thick film, using the laser lithography technique. An optical image of the fabricated pattern is shown in figure 4.9

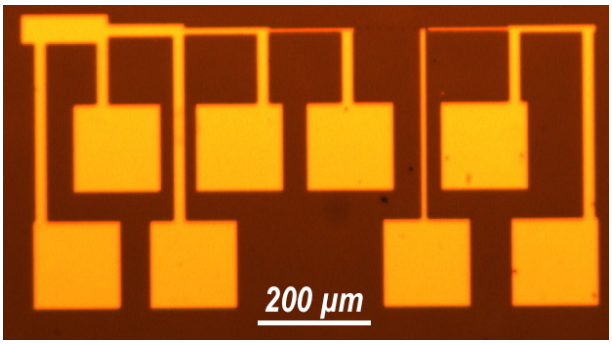

Figure 4.9: Optical microscopy image of the completed design patterned onto the 100 nm thick sample.

4.3 Transport measurements of the wires

4.3.1 The experimental setup

The resistances of the wires were measured using four-terminals. The principle of the technique is shown in figure 4.10.

Current is supplied to terminals 1 and 4, shown in blue, that are connected to the ends of the wire. The voltage is measured between terminals 2 and 3, shown in green, placed between the current electrodes. The separation of the voltage and current terminals means that only the resistance of the part of the wire that falls between the voltage electrodes is measured. The resistances of the electrodes, and contacts are excluded. This allows accurate measurement of low resistance values.

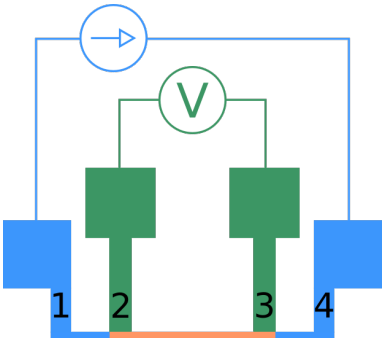

Figure 4.10: Four-terminal resistivity measurement.

The sample is glued on a sample holder with copper leads deposited onto it, as shown in figure 4.11. Connections were made between the copper electrodes of the sample holder and the large pads of the sample using a West Bond ultrasonic wire bonder with 25 μm diameter aluminium wire. There are 4 sets of 4 connectors inside the fridge, one of which is visible in figure 3.8, labeled as 'electrical connections'. They lead to the current source and the voltage probe outside the fridge, which was a TRMC2 controller.

The resistances of all three films before patterning was measured by B. Delsol, and was presented in detail in reference [7]. Some of his results, along with the results of the

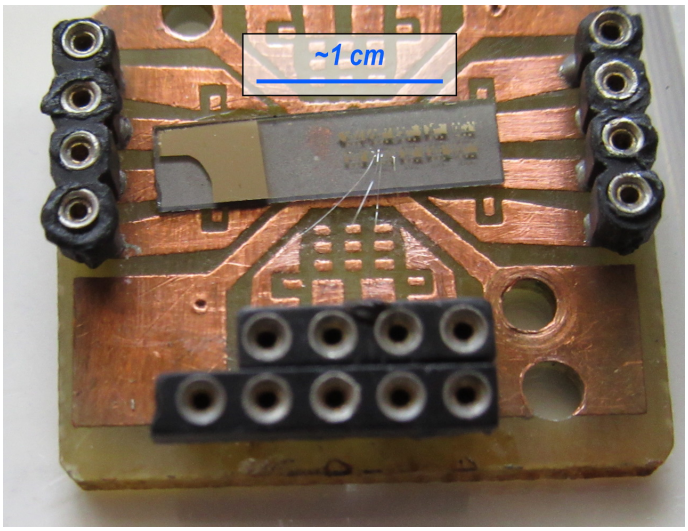

Figure 4.11: Sample is glued on the sample holder, and is connected by 25 μm diameter aluminium wires.

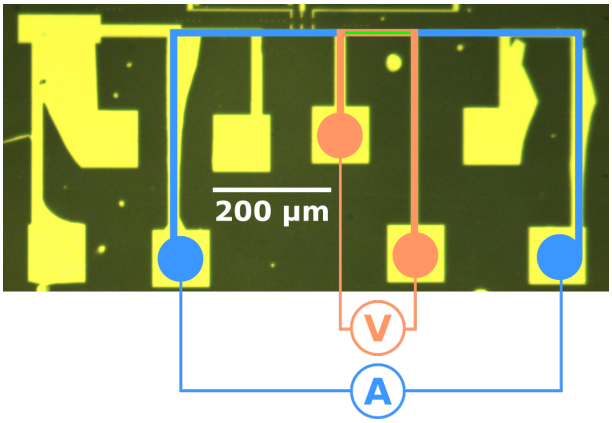

Figure 4.12: Connection for resistance measurement of the 3 µm wide rhenium wire on the 50 nm thick sample.

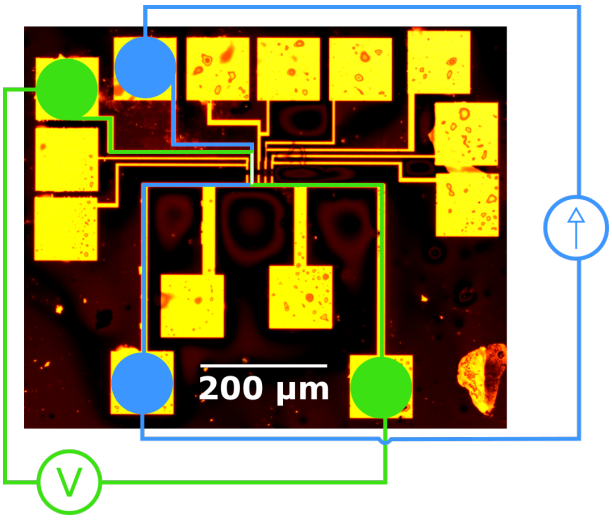

Figure 4.13: Connection for resistivity measurement of the 200 nm wide rhenium wire on the 25 nm thick sample.

wire measurements are listed in tables 4.3 and 4.4.

The resistance of the thinnest (3 μm) wires was measured on the 50 nm and the 100 nm thick films. An optical microscope image of one of the connections made on the 50 nm thick sample is shown in figure 4.12. The voltage probe was connected to the two ends of the 3 μm part of the pattern, while the current source and the ground to points further to the sides. The resistivity was only characterised along the green line in

figure 4.12.

On the 25 nm samples the 400 nm, 200 nm and the 100 nm wires were measured. The connections made for one of these experiments is shown in figure 4.13. The current source and ground were connected to the pads marked by the blue circles, and the voltage was measured between the two green circles. This allows the measurement of the 200 nm wide wire.

4.3.2 Calculation of the resistivity

The setup detailed above measures the resistance (R). Resistance depends on the geometry: the thickness of the film (d), the width of the wire (w), and the length, where the path of the current overlaps with the path of the voltage probe (l). If the geometry is known, resistivity (ρ), which depends only on material, can be calculated, as follows:

$$\rho = R\,\frac{wd}{l}. \tag{4.1}$$

Calculating the resistivity of the 3 μm wire is easy. It is shown in figure 4.12 that only the resistance of the wire is probed, and all its dimensions are known.

Resistivities in case of design II (figure 4.13) are more difficult to obtain. Magnified images of the pattern in figure 4.8 show that the thin wires are connected to thicker wires. Resistances of these thick parts are included in the measurement:

$$R_{\mathrm{output}} = R_{\mathrm{wire1}} + R_{\mathrm{wire2}} = \frac{\rho}{d}\left(\frac{l_{\mathrm{wire1}}}{w_{\mathrm{wire1}}} + \frac{l_{\mathrm{wire2}}}{w_{\mathrm{wire2}}}\right). \tag{4.2}$$

Thus the resistivity can computed as follows:

$$\rho = \frac{dR_{\mathrm{output}}}{\frac{l_{\mathrm{wire1}}}{w_{\mathrm{wire1}}} + \frac{l_{\mathrm{wire2}}}{w_{\mathrm{wire2}}}}. \tag{4.3}$$

There is a significant uncertainty ($>$10%) in the obtained resistivity values of the 100 nm, 200 nm and 400 nm wires, because their precise thicknesses were not verified with SEM. Due to the proximity effect, they can be thicker then designed.

4.3.3 Transport characteristics of rhenium wires

Normal state properties

Resistivity is the result of the scattering of the conduction electrons. According to Matthiessen's empirical rule, resistivities corresponding to independent sources of scatter-

ing add up. Dominant sources in metals are scattering on impurities and electron-phonon scattering, thus at room temperature:

$$\rho_{\mathrm{RT}} = \rho_{\text{el-ph}} + \rho_{\mathrm{imp}}. \tag{4.4}$$

Resistivity due to electron-phonon scattering is $\propto T$ at temperatures above the Debye temperature, and is $\propto T^5$ below [112]. At low temperatures, electron-phonon scattering becomes negligible, and impurity scattering dominates, which is independent of the temperature [112]:

$$\rho_{\mathrm{res}} = \rho_{\mathrm{imp}}. \tag{4.5}$$

Resistivity settles at a constant value, the residual resistivity.

The residual resistivity ratio (RRR) is defined as the ratio of the room temperature and the residual resistivity (RRR $= \rho_{\mathrm{RT}}/\rho_{\mathrm{res}}$). As equations 4.4 and 4.5 show, it strongly depends on the magnitude of impurity scattering. It is used as the measure of sample quality. Higher RRR indicates, less impurity.

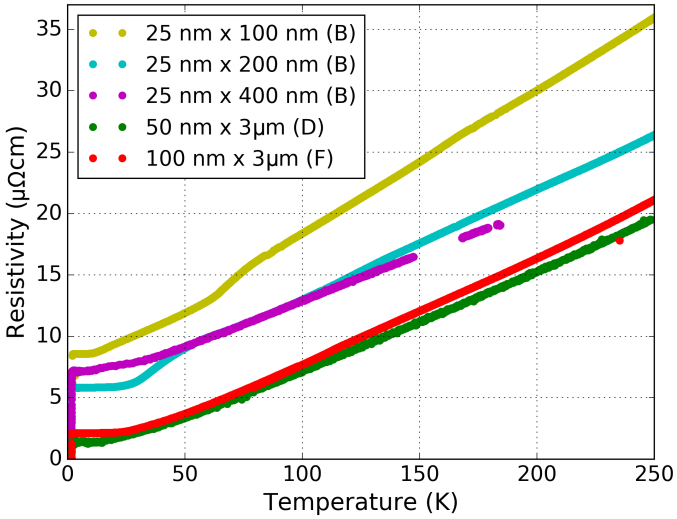

Figure 4.14: Resistivity the wires measured with decreasing temperature.

In the case of rhenium, when lowering the temperature further, below the critical temperature (T_c) the resistivity vanishes. This corresponds to the superconducting transition.

Film thickness	50 nm (D)		100 nm (F)	
	film	wire: 3 μm	film	wire: 3 μm
ρ_{RT} ($\mu\Omega$cm)	15.0 [7]	24.1	19.75 [7]	25.68
ρ_{res} ($\mu\Omega$cm)	1.1	1.4	0.915 [7]	2.14
RRR	15.0 [7]	17.2	21.6 [7]	12.0
T_c (K)	1.66	1.48	1.85 [7]	1.77
ΔT (K)	0.43	0.03	0.10 [7]	0.01
$\Delta(0)$ (meV)	0.25	0.22	0.28	0.27
l (nm) [121]	172	142	217	88
ξ_0 (nm)	167	187	150	157
	clean	dirty	clean	dirty
$\xi_{eff}(0)$ (nm)	124	139	111	100

Table 4.3: Values obtained for the 50 nm and the 100 nm films, and the 3 μm wide wires fabricated onto them.

Film thickness	25 nm (B)			
	film	wire: 400 nm	wire: 200 nm	wire: 100 nm
ρ_{RT} ($\mu\Omega$cm)	15.0 [7]	27.98 (extrapol.)	30.99	41.76
ρ_{res} ($\mu\Omega$cm)	3.8	7.16	5.82	8.57
RRR	4.0 [7]	3.9	5.3	4.9
T_c (K)	1.89	1.95	1.89	1.96
ΔT (K)	0.17	0.13	0.15	0.17
$\Delta(0)$ (meV)	0.29	0.29	0.29	0.3
l (nm) [121]	47	25	31	21
ξ_0 (nm)	147	142	147	141
	dirty	dirty	dirty	dirty
$\xi_{eff}(0)$ (nm)	71	51	58	47

Table 4.4: Values obtained for the 25 nm film, and the wires fabricated on it.

The resistivity of the wires measured at temperatures ranging from 250 K down to 300 mK is plotted in figure 4.14.

As the Debye temperature of rhenium is relatively high, 413 K [122], the graphs shown in figure 4.14 should display a T^5 temperature dependence down to about 30 K. This

could not be verified, because the thermocouples in the fridge are not calibrated for this temperature range.

The curves of the 200 nm and the 100 nm wires are not smooth around 50 K. Those are artefacts of the measurement, not real effects.

Below approximately 30 K, all the curves settle on a constant resistivity value, but these values are different for each wire. Between 1 K and 2 K the wires become superconducting.

The critical temperature, the width of the transition, the resistivity, and other calculated values are summarised in tables 4.3 and 4.4 for all the samples. Room temperature was considered 300K, and the residual resistivity was measured at 2.4 K. The critical temperature is taken where the resistivity decreases to half of the residual resistivity. The width of the transition was defined as the temperature interval between 90% and 10% of the residual resistivity.

Resistivity values measured at room temperature and at low temperature are in a similar range between the wires and the films they were fabricated on. Values of RRR are also very close for film and wire of the 50 nm and 25 nm thick sample. There is, however, a roughly 40% drop in the RRR value measured on the 100 nm film and the wire. The reason for this drop is unclear. One possible explanation is that the wire was fabricated on spot where impurity concentration was high. Another possibility is that the wire was damaged by the fabrication process. To determine the cause of the drop in the RRR value requires more experiments.

For the majority of samples, however, the fabrication did not alter their transport properties.

Properties of the superconducting transition

In this section the critical temperatures and the widths of the superconducting transitions of the films and the wires are compared to each other. The films were measured in a different cryostat by Delsol [7].

Figure 4.15(a) shows the superconducting transitions of the 3 μm wide wire on the 50 nm film in green. In red, the transition of the full film is shown. The superconducting to normal transitions start at about the same temperature in both cases, however, the transition of the film is over ten times broader than that of the wire. In the case of the wire, the transport measurement probes only an area 3 μm wide and 120 μm long. The sharp transition of the wire indicates that the film is homogeneous in that small region. In comparison, in case of the film, the area probed is several millimetres long and wide. The transition reflects the lowest resistivity along a filament. The observed broadening

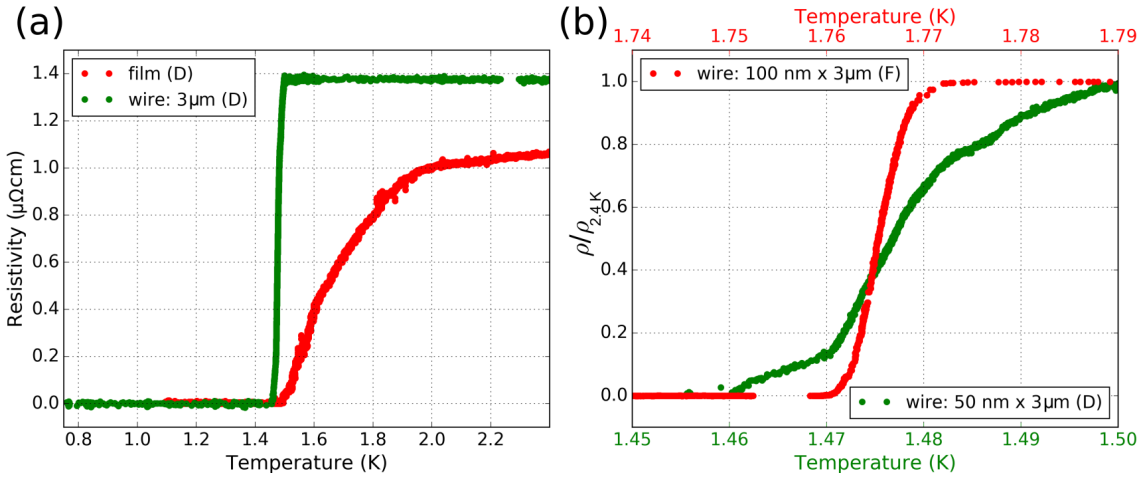

Figure 4.15: (a) Superconducting transitions of the 3 μm wide wire, and the 50 nm thick film it was fabricated on (Sample D). (b) Superconducting transitions of the 3 μm wide wires fabricated on the 50 nm (D) and the 100 nm (F) thick samples with normalised resistivities

reveals inhomogeneity in the probed region.

The 3 μm wide wire that was fabricated on the 100 nm thick sample was measured and its transition is shown in figure 4.15(b) in red, along with the previously discussed 3 μm wide wire on the 50 nm thick film in green. To be able to compare the two curves, the resistivities were normalised with respect to their residual resistivities. The temperature scales are different for the two curves. The transition of the 100 nm thick film is 10 times broader than that of the 3 μm wide wire fabricated on it (from table 4.3). The transition of the wire made of the 100 nm thick film is also significantly narrower and smoother than the wire made of the 50 nm thick film. This can be observed in figure 4.15(b).

The critical temperature of the wire fabricated onto the 100 nm film is the closest to what is expected for a bulk sample.

On the third, 25 nm thick sample, the 400 nm, 200 nm, and 100 nm wide wires were measured, their transitions, and the transition of the film is shown in figure 4.16. The transition curves were normalised with respect to their residual resistivity. The temperature axis was left unchanged.

About half way through the transition curve of the film a step can be observed. This suggests that the volume measured has two distinct transition temperatures. Similar steps can be observed in the same temperature region on the 100 nm wide wire. This curve has a third step also at a lower temperature. The 200 nm wide wire appears

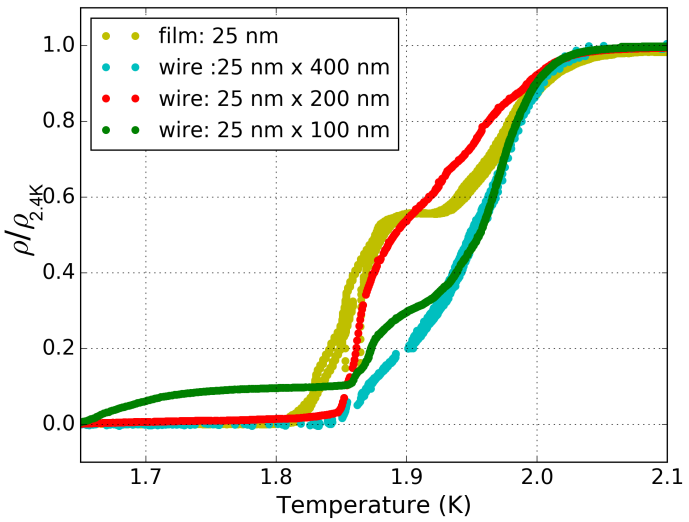

Figure 4.16: Superconducting transitions of the 100 nm, 200 nm, and the 400 nm wide wires, and the 25 nm thick film they were fabricated on (Sample B).

smoother compared to the film, and to the 100 nm wide wire, however, it is broad and perfectly envelopes both curves. The transition of the 400 nm wide wire is the sharpest of the four and relatively featureless.

Conclusions on the $\rho(T)$ curves

In the literature, previously reported critical temperatures of rhenium vary in a wide range. They can be found anywhere between 0.9 K and 5.5 K. After characterising several samples prepared with different methods, Hull and Goodman concluded that the correct critical temperature of a strain free rhenium single crystal is 1.699 K. They reported an increase of 1 K in the critical temperature after surface grinding [123].

Alekseevskii et al. reported an increase in the critical temperature, and the κ parameter (defined in equation 3.21) of deformed, bulk rhenium samples. Increase of the κ parameter signals that bulk rhenium changes from a type-I to a type-II superconductor upon deformation [124].

Kopetskii et al. suggested that dislocations increase the critical temperature, but do not affect the residual resistivity after studying deformed, annealed and quenched rhenium single crystals. Point defects, however, do affect both T_c and the residual resistivity. They stated that planar defects, such as twin boundaries have an insignificant effect on

both parameters [125]. Their last statement is in contrast with observations of localised superconductivity along twin boundaries, with critical temperatures higher than that of bulk [126].

Haq et al. conducted annealing experiments on rhenium thin films, and, consistently with the previous authors, concluded that vacancies and dislocations are responsible for the increased residual resistivity and transition temperature, and that grain boundaries do not contribute to this effect [127].

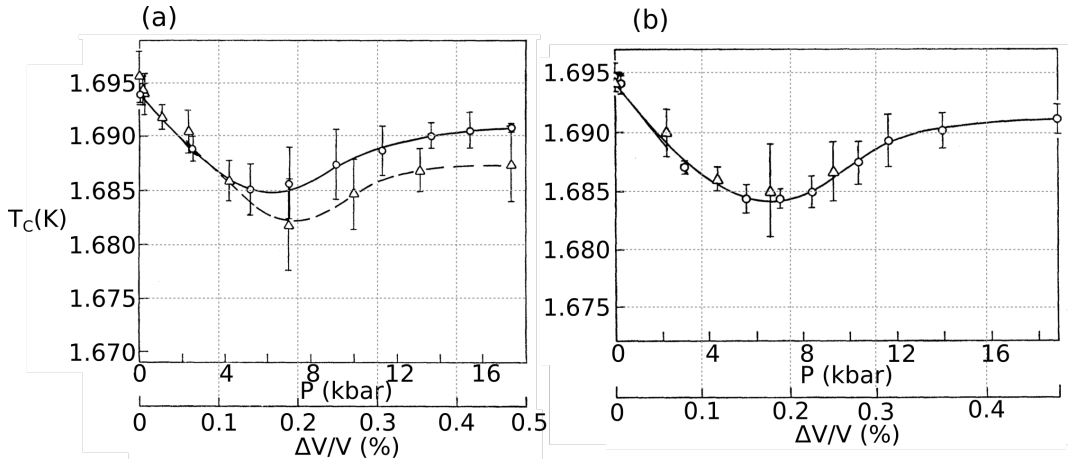

Figure 4.17: Critical temperature as the function of pressure/relative change of volume measured by Chu et al. (a) for two polycrystalline samples and (b) for two single crystal samples [128].

Chu et al. studied the effects of pressure on the critical temperature of rhenium. They observed a non-linear dependence: the critical temperature decreases steeply initially, passes through a minimum, then levels off, as shown in figure 4.17 [128]. Here, the pressure directly translates to strain, and thus the expected transition temperature can be calculated from the strain measured in our films.

In figure 4.17, instead of strain the relative volume change is given. Relative change of the hexagonal unit cell volume can be calculated from the strain as follows:

$$\frac{\Delta V}{V_0} = \frac{\frac{3\sqrt{3}}{2}\left((a_0+\Delta a)^2(c+\Delta c) - a_0^2 c\right)}{\frac{3\sqrt{3}}{2}a_0^2 c} = \epsilon_a^2 + \epsilon_a^2\epsilon_c + 2\epsilon_a\epsilon_c + 2\epsilon_a + \epsilon_c, \text{ where}$$

$$\epsilon_a = \frac{\Delta a}{a_0}, \quad \epsilon_c = \frac{\Delta c}{c_0} = -\frac{2\nu}{1-\nu}\epsilon_a.$$

The misfit strain results in a relative change in volume of 0.5%. The strain obtained from the high resolution X-ray scans give a much larger value, $\sim$ 1%. As can be read from figure 4.17, the critical temperature only changes 0.1 K before it levels off on a value close to the bulk. If only strain were present in our samples, we would measure critical temperatures closer to the bulk value. Thus, we can conclude, in agreement with previous authors and our previous measurements, that dislocations (and possibly vacancies, though this cannot be confirmed at this point) are present in our films, which cause an increase in the residual resistivity and the critical temperature.

In figure 4.18 the residual resistivity ratios of the wires are shown as the function of their critical temperatures. The two are inversely proportional which further confirms, that the increase of the critical temperature is caused by crystallographic defects in the sample.

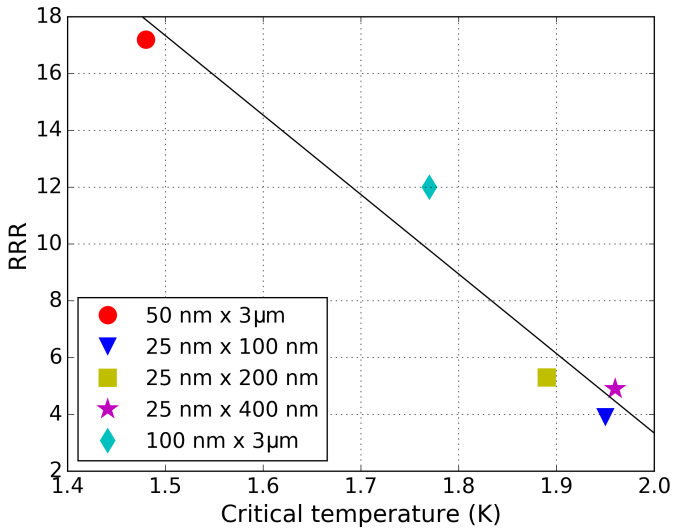

Figure 4.18: Residual resistivity ratio as the function of the critical temperature.

The widths of the transition in case of the 100 nm and 50 nm thick samples are broader on the film. This is a sign that the films are composed of domains, that transit to the superconducting phase at slightly different temperatures. The samples are not homogeneous on the mm^2 scale, which is the size of the region probed by the transport measurement on the full film. The areas of the wires are 360 μm^2, however. The narrower transition suggests that the domains are larger than the size of the wires. Inhomogeneity was reduced with the reduction of the size.

The transition curves of the 25 nm thick sample (film and wires) display a very clear structure. It was shown by the AFM images and by the XRD measurements that this film has a grainy structure, with two distinct grains that likely have two different orientations. Figure 4.17(a) and figure 4.17(b) shows that while the critical temperature of two polycrystalline samples behave slightly differently under applied pressure, the T_c of two single crystal samples can be described by a single curve. This could indicate that crystal properties, such as orientation, could affect the critical temperature. The possible cause of the steps in figure 4.16 is thus that the two types of grains have slightly different transition temperatures. When fabricating the wires, their volume ratio changes, which affects the 'height' of the step in the transition curve. The sizes of the grains are much smaller than the width of the narrowest wire (see table 4.2), therefore the measured volume remains inhomogeneous. The widths of all the transitions measured on the 25 nm thick sample, listed in table 4.4, are in close agreement.

The critical temperature of a superconductor calculated from the BCS theory is given in equation 3.12, the important parameters are the density of states at the Fermi level and the pairing potential. The band structure of rhenium was calculated for the first time by Mattheiss [129]. The introduction of crystal defects can lead to an increased unit cell volume and thus to increased density of states at the Fermi level in Re [130], as well as a change in the pairing potential which affects the critical temperature. Mito and collaborators observed T_c as high as 3.2 K for Re polycrystals submitted to shear strain leading to a volume expansion of 0.7%.

The critical temperature of the 3 μm wire on the 50 nm film stands out. It is over 0.2 K lower than the bulk critical temperature, 1.7 K, which is tantalising. This film is decorated by large spirals and deep holes. We can only speculate how these affect T_c: is there a Re wetting layer underneath, is the stress the same over the thickness of the film and in the spirals? These questions need further investigation.

Mean free path and coherence length

The electron mean free path and the superconducting coherence length can be obtained from the measured residual resistivity and critical temperature values.

According to the Drude model, the expression to calculate resistivity is the following:

$$\rho = \frac{m_e}{n_e e^2 \tau} = \frac{m_e v_F}{n_e e^2 l}, \tag{4.6}$$

where n_e is the density, e is the charge, m_e is the weight of electrons. τ is the time between collisions, which is equal to l/v_F, where v_F is the Fermi velocity and l is the

mean free path of the electrons [39]. Multiplying both sides with l shows that the product of the resistivity and the mean free path is nominally a constant:

$$\rho l = \frac{m_e v_F}{n_e e^2}. \tag{4.7}$$

This product was measured by several authors for rhenium, yielding the following values: 4.5e−5 $\mu\Omega\text{cm}^2$ [127], 2.16e−5 $\mu\Omega\text{cm}^2$ [131], and an average of 2.01e−5 $\mu\Omega\text{cm}^2$ [121]. The last two values reported by Tulina et al. are in good agreement, but the first is very different. In the expression 4.7 the density of electrons is the only parameter that can change between samples. In reference [121], the resistivities and mean free paths of several rhenium samples were measured separately. Their RRRs are also listed. From reference [121], samples with the closest RRR values to our samples were chosen, and their ρl product was used to calculate the mean free paths of our samples. These values are listed in tables 4.3 and 4.4.

To calculate coherence length, the superconducting energy gap ($\Delta(0)$) needs to be obtained first using equation 3.14. Values for all the samples are listed in tables 4.3 and 4.4.

From the energy gap, the coherence length of the superconducting electrons (ξ_0) can be calculated using equation 3.16. A Fermi velocity was obtained by averaging the values published in reference [121], which gave $2. \cdot 10^5$ m/s. The coherence lengths are listed in tables 4.3 and 4.4.

The coherence length can be compared to the mean free path of the electrons to determine whether the sample is in the clean or in the dirty limit. In the clean limit, the electrons can travel the characteristic distance of superconductivity without scattering.

The 50 nm and the 100 nm thick film were in the clean limit, but after fabrication, the 3 μm wires are in the dirty limit. Whether this is due to the fabrication process or to the ageing of the sample is not known. However, the three characteristic lengths of both wires and both films are all larger or equal to 100 nm, except one.

The 25 nm thick film and its wires are in the dirty limit.

The effective coherence length is obtained from equations 3.22, which takes into account the effect of the electron mean free path. It is shorter than the coherence length.

In our study, we reached the clean limit with the 100 nm and the 50 nm thick film. In addition, the mean free path is larger than the thickness, conditioning the entrance in the ballistic regime along the thickness direction. Unfortunately, we did not pattern the narrowest wires on these films. We could not yet reach the ballistic regime in the width direction of the wire.

4.4 Critical current fluctuations in SQUIDs

Nanobridge SQUIDs were successfully fabricated on the 25 nm thick rhenium film using electron beam lithography. An example of a SQUID is shown in figure 4.19. The two forks of the SQUID are connected by two narrow bridges, with widths smaller than the superconducting coherence length (ξ_0). The fabricated pattern corresponds to figure 4.2 and included 2 SQUIDs. The bridges were designed to be 20 and 50 nm wide. Their dimensions were measured by SEM after fabrication: the narrower bridges were about 40 nm, the wider ones were about 70 nm. The SQUID shown in figure 4.19 has the wider bridges.

Considering that in the superconducting state the current flows in the middle of the the SQUID arms, which measure 200 nm across, the effective area of the SQUID loop is 1.2 μm^2.

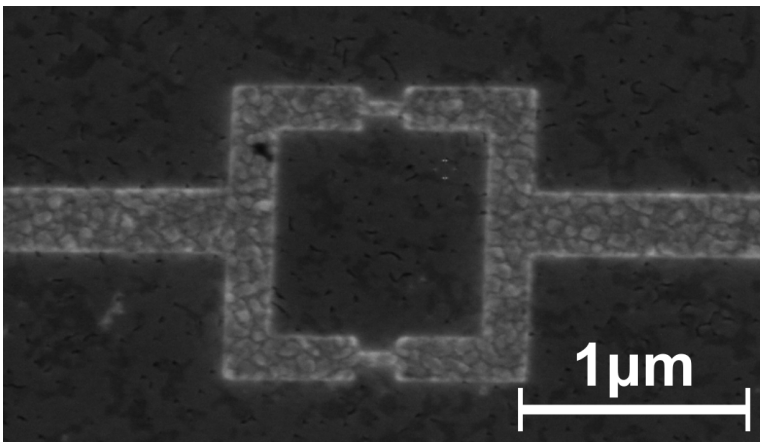

Figure 4.19: SEM image of a SQUID fabricated on the 25 nm thick rhenium thin film.

The switching current of the SQUIDs was measured as the function of the magnetic field in a dilution refrigerator at 250 mK. The main principles of a SQUID and the measurement are described in detail in chapter 3.3.2 and 3.4.2.

A single electrode is used to bias the SQUID and to detect the $\partial V/\partial t$ pulse. One of the connections is schematically indicated in figure 4.20. The measurements were performed using a two-terminal method. In the case of this sample, the ground was connected to the pad marked on the top, and the current bias was connected to pad on the left. In this figure, an SEM image taken of the SQUID is also shown.

The critical current as a function of the magnetic field measured on one of the SQUIDs (SQUID1) are shown in figures 4.21. A low frequency oscillation envelopes a fast critical

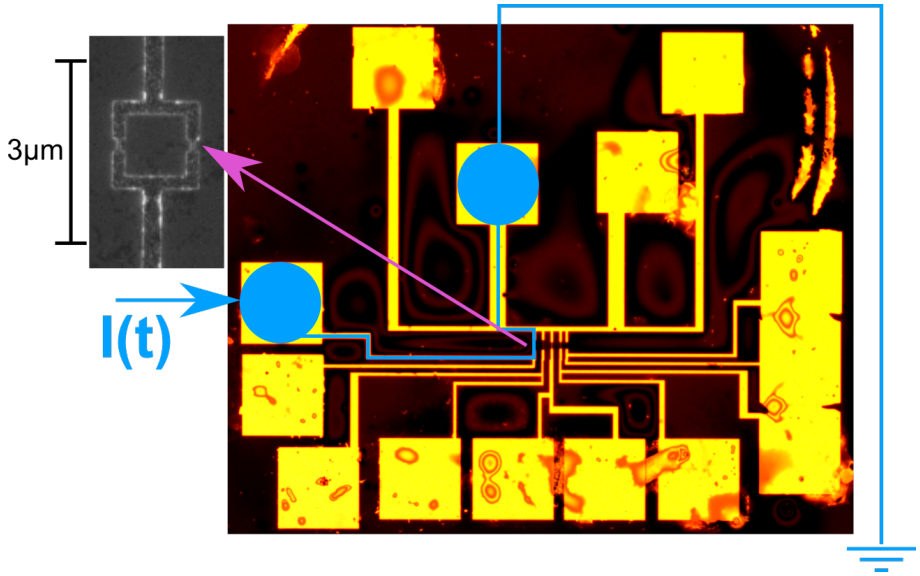

Figure 4.20: The schematics of the electrical connections made to SQUID1 shown on the optical image of the pattern.

current oscillation. The critical current modulation is about 22 μA for both arcs. The period of the fast oscillation is 0.051 mT. The period of the slow component is about 1.4 mT.

The period of the oscillation is defined by the area (S) enclosed by the SQUID:

$$I_c = 2i_c \left| \cos\left(\frac{\pi\Phi}{\Phi_0}\right) \right| = 2i_c \left| \cos\left(\frac{\pi BS}{\Phi_0}\right) \right|, \tag{4.8}$$

where i_c is the critical current through one junction of the SQUID, and $\Phi = \mathbf{BS}$ is the applied flux, given by the dot product of the magnetic induction vector and the vector loop area of the surface. Since these two vectors are parallel, the dot product is simply the product of the magnitudes in equation 4.8.

From the period, the area enclosed by the SQIUD is obtained as follows:

$$S = \frac{\Phi_0}{\Delta B}. \tag{4.9}$$

The periodicity of the fast component corresponds to an area of 40.5 μm^2, which is much larger than the 1.2 μm^2 size of the SQUID. However, the slow oscillation gives an area of 1.4 μm^2, which is in good agreement with the SQUID loop.

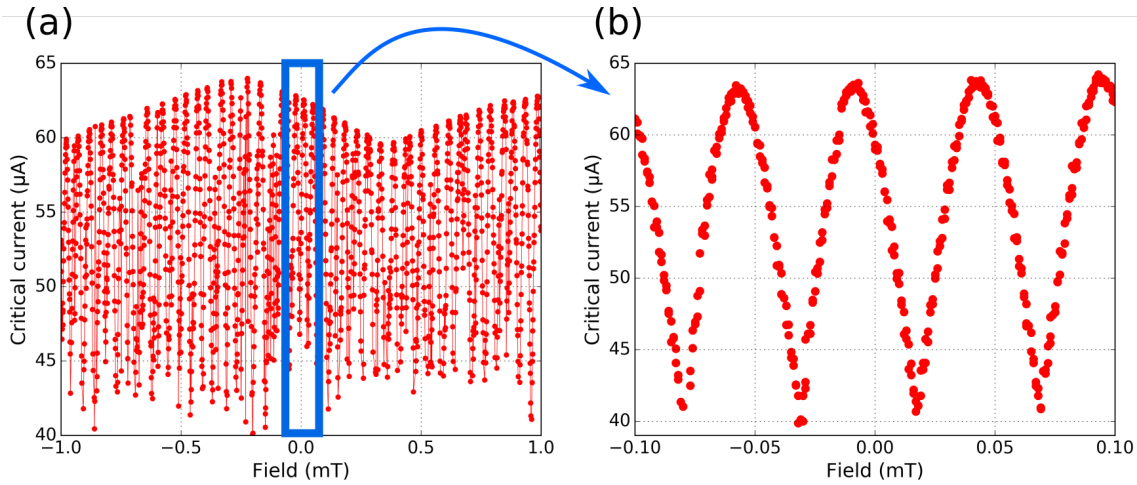

Figure 4.21: The critical current oscillations as a function of the applied field measured on SQUID1. A low frequency component (a) envelops a fast oscillation (b).

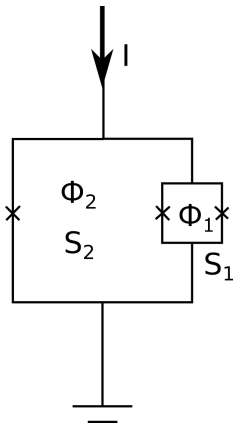

Figure 4.22: Schematics consistent with the data shown in figure 4.21. The small SQUID is connected to either a junction or another SQUID, forming a large SQUID loop.

We are measuring two SQUIDs with different areas. This is shown in figure 4.22. The small SQUID (S_1, Φ_1) is the one that was intentionally fabricated and wired. It is connected to either a Josephson junction or a second SQUID, and together they form a larger SQUID loop (S_2, Φ_2).

On design III, there are two SQUIDs next to each other. They share the ground node, shown in figure 4.20. Their current pads and wires are very close together. It is possible, that there is an electrical connection between either the pads or the wires, that the optical

microscope did not reveal. This way, the supplied current biases both SQUIDs, leading to this double SQUID.

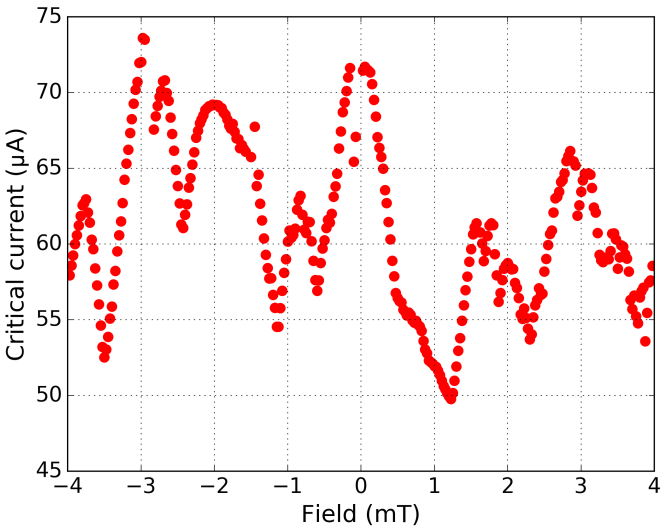

Figure 4.23: The critical current oscillations as a function of the applied field measured on SQUID2.

A second SQUID (SQUID2) was also measured. The critical current is shown in figure 4.23 as the function of the applied magnetic field. The maximum critical current modulation is approximately 20 μA, which is in agreement with SQUID1. The graph shows no obvious periodicity, we suspect a beating of several frequencies. There is a local maximum centred at zero applied field, as expected, and there are maxima on both sides of this peak. Some of these maxima have a clear period, and some do not. To have a clearer picture whether this data shown in this graph have the periodicity corresponding to the size of the SQUID, Fourier transform of the critical current was computed, and is shown in figure 4.24.

The most dominant peak is at 0.385 mT^{-1}, which corresponds to a period of 2.6 mT. The area enclosed by the loop calculated from the period is 0.8 $\mu\mathrm{m}^2$. This value is consistent with the 1.2 $\mu\mathrm{m}^2$ SQUID loop area.

That the $I_c(B)$ graph of SQUID2 in figure 4.23 appears irregular could be explained by left-over rhenium on the surface, that provides alternate path for the current. This has been a problem on other samples.

The switching histogram of the measured SQUIDs are shown in figures 4.25(a) and

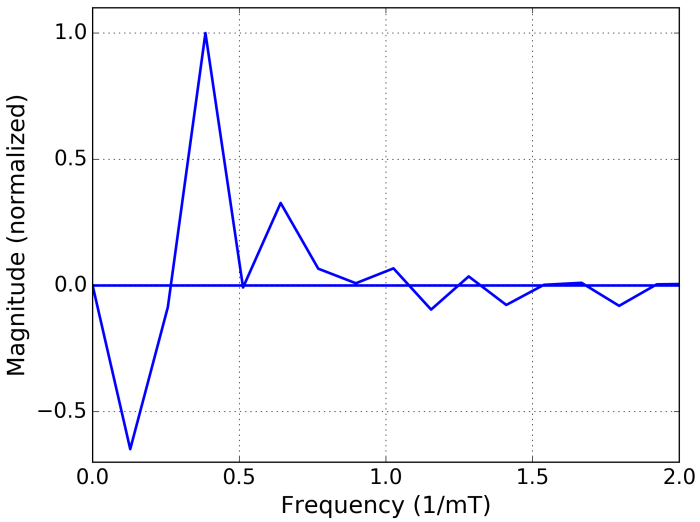

Figure 4.24: Fast Fourier Transform of the $I_c(B)$ curve of SQUID2.

4.25(b). An increasing DC current is injected into the SQUID. As the value of the current approaches the critical current, the probability that the SQUID switches to the normal state increases. The number of switching events exponentially increases with the current until I_c is reached, where the probability of switching is almost 1. As a result, for currents close to the critical current the number of events rapidly decreases [132]. Switching current histograms are asymmetric, exhibit a tail towards the lower currents. In our case the number of switching events measured were low, so the tails are not well defined.

The mean critical current ($\langle I_c \rangle$) and its standard deviation (σ_{I_c}) were extracted from the histograms, and they are shown in figures 4.25(a) and 4.25(b).

From σ_{I_c} the flux noise ($\Delta\Phi$) of the SQUID can be determined using the following expression:

$$\Delta\Phi = \frac{\Delta I_c}{(\frac{\Delta t}{I_c}\frac{dI}{dt})^{1/2}} \frac{1}{\frac{dI_c}{d\Phi}}, \tag{4.10}$$

where Δt is the measurement time interval, dI/dt is the slope of the current ramp used in the measurement [132, 133].

$\frac{dI_c}{d\Phi}$ was determined from the slopes of the $I_c(B)$ curves. For SQUID1 the high frequency oscillations were used. The slope is 1.03 ± 5 mA/mT, which corresponds to (using

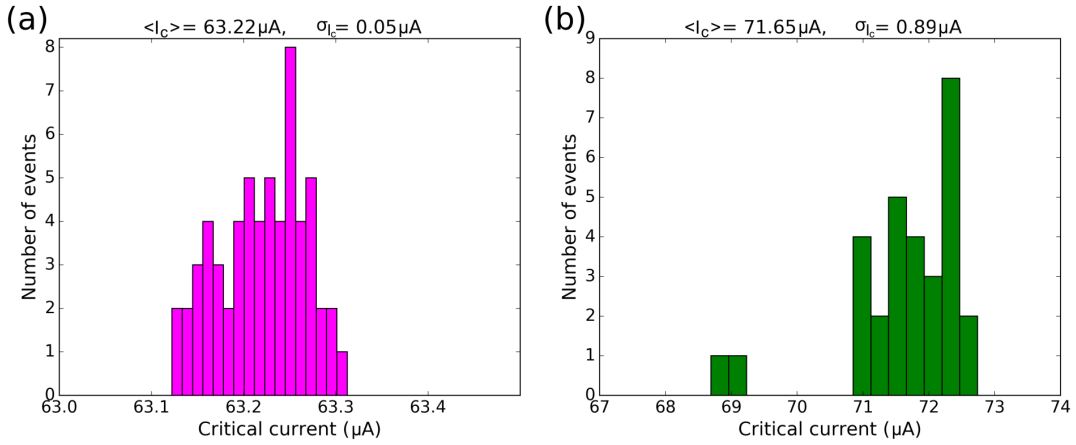

Figure 4.25: Critical current histogram of (a) SQUID1 (b) SQUID2

the area obtained in equation 4.9) 51 μA/Φ_0. For SQUID2, on the positive side of the 0 T peak the slope is 36 μA/mT, and on the negative it is 50μA/mT. Using the obtained loop area, these correspond to 90 μA/Φ_0 and 124 μA/Φ_0, respectively.

The obtained flux noise values are 2.6e−5 $\Phi_0/\mathrm{Hz}^{1/2}$ for SQUID1 and 2.0e−4 $\Phi_0/\mathrm{Hz}^{1/2}$ for the SQUID2.

Theoretically, the highest current a superconductor can carry without dissipation is defined by the depairing mechanism. Superconductivity vanishes when the kinetic energy associated with the supercurrent exceeds the condensation energy (binding energy of the Cooper pairs) [95].

The depairing current density is given by the following expression:

$$j_{dp} = e^* \Psi_0^2 \frac{2}{3} \sqrt{\frac{2}{3} \frac{|\alpha(T)|}{m^*}},$$

where $e^* = 2e$ and $m^* = 2m$ are the charge and mass of the superconducting electron pairs, Ψ_0 is the equilibrium value of the superconducting order parameter, and $\alpha(T)$ is a coefficient from the Ginzburg-Landau theory (see equation 3.8) [95].

Using equations 3.19 and 3.20, the depairing current can be expressed as follows:

$$j_{dp} = \frac{1}{3\sqrt{3}} \frac{1}{\pi} \frac{\Phi_0}{\mu_0 \lambda_L^2(T) \xi_{GL}(T)}, \tag{4.11}$$

where $\mu_0 = 4\pi \cdot 10^{-7}$ Wb/(Am) is the vacuum permeability.

The sample is in the dirty limit, so in equation 4.11, instead of the London penetration depth the effective penetration depth was used, which is obtained by the following equation:

$$\lambda_{eff} = \lambda_L \sqrt{\frac{\xi_0}{l}}. \tag{4.12}$$

The London penetration depth of rhenium thin film was measured by Hykel [134] and Wang [115] by studying vortices, and by Dumur et al. [8] by studying rhenium microwave resonators. They obtained values of 79 nm, 103 nm, and 85 nm for λ_L, respectively. Here, λ_L was assumed to be 90 nm.

Instead of ξ_{GL}, ξ_{eff} was used (dirty limit sample). The coherence lengths, effective coherence lengths and mean free paths of the wires fabricated from this sample was calculated. We took the average values of l, ξ_0 and ξ_{eff} to estimate depairing current density.

A theoretical maximum current density of 4e10 A/m^2 was obtained.

The maximum critical current we measured was about 72 μA. The current flows through the two arms of the SQUID. The cross sectional area of the SQUID arm can be calculated by multiplying the sample thickness (25 nm) with the width of the bridge (70 nm). The critical current density (j_c) is we measured is then

$$j_c = \frac{72\,\mu\text{A}}{2 \cdot 25\text{ nm} \cdot 70\text{ nm}} = 2\text{e}10\text{ A/m}^2. \tag{4.13}$$

The measured current density is half of what an ideal rhenium wire could theoretically carry. This is not surprising, as achieving the theoretical critical current in superconductors is subject of active research. Attempts have been made to reach the depairing current either by reducing the dimensions of the superconductor below the characteristic lengths or by introducing artificial pinning sites to stop the motion of vortices [135], [136], [137].

Conclusion on the SQUID measurements

We have successfully fabricated SQUIDs from rhenium thin films. The critical current oscillations measured on two SQUIDs were imperfect, probably due to contaminations on the surface (left-over rhenium from fabrication or other superconductive particle). The width of the critical current histogram could reach values which make rhenium a promising candidate for low noise μSQUIDs. Rhenium has been shown to have long coherence length and electron mean free path, therefore it would be promising to continue

the study of rhenium SQUIDs on samples that have better crystallographic properties, as the presented sample was a dose test to develop Re SQUID fabrication. Future patterns should include only SQUIDs, with all other superconducting structures as far away as possible. Before these preliminary experiments, the measurement of the wires reduced the number of SQUIDs available, and the sample was handled many times before we could undertake the SQUID experiments.

Conclusion and outlook

Conclusion

In this work, the epitaxial growth of rhenium thin films onto single crystal Al_2O_3 using molecular beam epitaxy was realized and is discussed. An epitaxial relationship was found with orientations (0001)Al_2O_3//(0001)Re and $<2\overline{1}\overline{1}0>Al_2O_3$//$<01\overline{1}0>$Re. This was confirmed using X-ray diffraction. The misfit strain between the lattices is -0.43% at room temperature, which gives a critical thickness of about 15 nm.

The substrates were heated during growth using either a Joule-heated tungsten filament located behind the sample or electron bombardment. An AFM study comparing films grown at temperatures of either 800°C or 900°C revealed that the higher deposition temperature results in a more homogeneous surface. On samples with thicknesses 50 nm and 100 nm, spirals are frequently observed. The diameter of these spirals grew over two fold when the higher deposition temperature was used. An XRD study of the sample films showed that they are all dominated by the epitaxial (0001) orientation. The few secondary orientations have low intensities which in almost all cases decrease with increasing deposition temperature. Deposition at a temperature of 1000°C leads to dewetting of the 50 nm thick sample, and islands with atomically flat surfaces are formed.

The spirals that are often observed on thicker films are most likely the result of steps on the surface caused by screw dislocations. Among the spirals there are deep holes, whose origin is suspected to be partial dewetting and recrystallisation of the film. It was shown by a theoretical model that the temperature of the film starts to increase when the thickness of approximately 10 nm is reached, as the film becomes more opaque. Around this thickness a transformation of the RHEED pattern indicates a crystallographic change, and the observed surface shows signs of dewetting. The surface profile was modeled using Mullins' theory of dewetting, which allowed the determination of the surface diffusion coefficient, 4×10^{-12} cm^2/s.

Wires with widths between 100 nm and 3 μm, and SQUIDs were fabricated on the films using the lithography process. Low temperature transport measurements showed that the fabrication did not affect the superconducting properties. The critical tempera-

ture of the wires was found to vary in a wide range, between 1.43 K and 1.96 K. We found that this correlates with the crystallography and topography of the films. The mean free paths and the superconducting coherence lengths were determined. Two films were in the clean limit, but the wires fabricated on them were in the dirty limit. The mean free paths and the coherence lengths were larger than the thickness of the films for almost all the films and wires conditioning the ballistic regime in the thickness direction. The ballistic regime was not yet obtained in the width direction.

Critical current oscillations of two SQUIDs were measured using a dilution refrigerator. The lowest flux noise value obtained was 2.6×10^{-5} $\Phi_0/\mathrm{Hz}^{1/2}$.

Outlook

The initial intention of this project was to grow epitaxial Re-Al_2O_3-Re junctions. Rhenium is a promising candidate for such junctions as it is known to resist oxidation. To manufacture a junction, a rhenium film with flat surface needs to be deposited, followed by the deposition of an aluminium layer which is subsequently oxidised. However, the epitaxial rhenium films are found experimentally not to have a flat surface. They are covered with spirals and deep holes. This topography is not adequate for the deposition of a second layer.

Welander grew rhenium films onto thick epitaxial niobium layers [5]. His films were relatively flat and smooth, however, displayed several in-plane orientations, and rhenium mixed with niobium at the interface. Our films were flat in the case of grainy structure. The growth of grainy rhenium films is one possible way to avoid holes, and achieve a flat surface. Of course, in this case the aim of fully epitaxial, single crystal junction has to be sacrificed. A second line of investigation could be the use of a seed layer, that prevents the dewetting of rhenium, thus the formation of holes.

We obtained larger mean free path and coherence length values than the thickness of the films, and the width of the thinnest wire, 100 nm. Unfortunately, the 100 nm wide wires were fabricated on a sample which was in the dirty limit, and displayed small λ and ξ values. Wires that are in the ballistic regime in both the thickness and width directions are feasible on a clean limit film, which we can routinely deposit.

The SQUIDs fabricated on a thin film of rhenium showed a flux noise in the range of 10^{-5} $\Phi_0/\mathrm{Hz}^{1/2}$ and 10^{-4} $\Phi_0/\mathrm{Hz}^{1/2}$. Flux noise values reported in literature for low noise μ-SQUIDs and nano-SQUIDs range between 10^{-4} $\Phi_0/\mathrm{Hz}^{1/2}$ and 10^{-6} $\Phi_0/\mathrm{Hz}^{1/2}$ [115, 116, 133, 138–143]. It is very encouraging that our preliminary results fall in this range. By using clean limit films, and refining the lithography parameters, state of art rhenium SQUIDs should be achievable.

A

Ptychography

A.1 Phase problem in crystallography

In a scattering experiment, a sample is subjected to a parallel monochromatic beam with a known wave vector ($\mathbf{k_i}$), therefore known energy and propagation direction. The angle (elastic scattering) and/or the energy distribution (inelastic scattering) of the scattered wave is then studied to draw conclusions regarding the crystallographic (or magnetic or dynamic) properties of the sample.

When the scattering is dominantly elastic, the energy of the incoming wave does not change during the interaction with the sample. This means, the outgoing wave vector has the same length as the incoming wave vector ($|\mathbf{k_i}| = |\mathbf{k_f}|$). Momentum transfer does occur, however, resulting in a directional change. The difference is called the scattering vector:

$$\mathbf{q} = \mathbf{k_f} - \mathbf{k_i}. \tag{A.1}$$

The amplitude of scattered X-ray waves is given by the Fourier transform of the electron density ($f(\mathbf{r})$), where the integral is taken across the illuminated volume (V):

$$A(\mathbf{q}) = \int_V f(\mathbf{r}) e^{i\mathbf{qr}} d\mathbf{r}. \tag{A.2}$$

The Fourier transform is reversible, the inverse Fourier transform of the amplitude could recover the electron density distribution. However, it is the intensity that is recorded by the detectors, which is the absolute modulus of the structure factor:

$$I(\mathbf{q}) = |A(\mathbf{q})|^2. \tag{A.3}$$

Thus, the phase information of the structure factor, which is required for the inverse Fourier transform, is lost upon the measurement. Only the amplitude of the structure factor can be recovered. This is known as the phase problem in crystallography [43].

The consequence of the phase problem is that the electron density, and thus the atomic positions cannot be directly retrieved from the diffraction data. Of course, this has not prevented scientist from trying and succeeding reconstructing structures of materials. Many of the approaches rely on *a priori* information regarding the chemistry of the material, rather than directly recovering the phase [144]. Recovery of both phase and amplitude information is possible by holography, where a reference wave is used to interfere with the scattered wave [145, 146].

The recovery of the phase of the scattered wave is also possible with iterative phase-retrial algorithms. For this, the probing beam needs to be coherent, otherwise the phase is not well-defined. This technique is outlined in this chapter.

A.2 Coherence of the probing beam

Coherence of waves means that there is a known phase relationship. An incoherent beam consists of many coherent waves, between which the phase relationship cannot be defined.

Coherence lengths can be defined in the framework of geometrical optics.

Longitudinal coherence length (ξ_L) is related to the monochromaticity of the beam, this concept is illustrated in figure A.1 Two waves with slightly different wavelengths (λ and $(\lambda - \Delta\lambda)$) are emitted from a point source. They have the same phase at the point of emission. Longitudinal coherence length is defined as the distance it takes for the the two waves to have opposite phases. At a distance twice the coherence length, they will be in phase again. From this criteria longitudinal coherence length can be computed:

$$\xi_L = \left(\frac{\lambda}{\Delta\lambda} - 1\right)\frac{\lambda}{2} \approx \frac{\lambda^2}{2\Delta\lambda} \tag{A.4}$$

Equation A.4 tells us, that higher degree of monochromaticity results in a longer coherence length. Similarly, longer wavelength, therefore lower energy gives longer coherence length. The I13-1 beamline in Diamond Light source uses X-rays in the energy range of 6-20 keV, which corresponds to a wavelength in the range of 2-0.6 Å. $\lambda = 1$ Å midrange. Monochromatic beam is achieved by diffraction through a series of perfect single crystals. A double pass Si(111) monochromator can achieve a bandwidth of $\Delta\lambda/\lambda = 10^{-4}$, resulting in a longitudinal coherence length of 0.5 μm [43, 147].

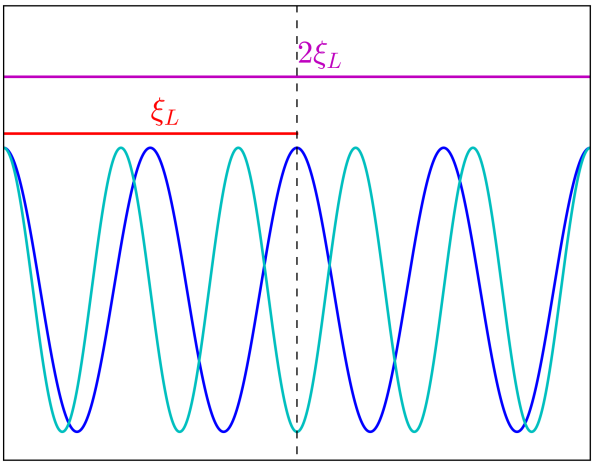

Figure A.1: Longitudinal coherence length.

When producing a monochromatic beam, wavelengths that do not fit in the desired interval are discarded. A narrower bandwidth results in less flux, therefore longer measuring time.

The transverse coherence length (ξ_T) is related to the beam divergence, and is illustrated in figure A.2. Two wave fronts are shown, A and B. Their wavelengths are equal, denoted by λ. They have different directions of propagation, and the difference between them is the angle $\Delta\theta$. Their wavefronts coincide in point P, where they are in phase. The transverse coherence length is defined as the distance we have to travel along wavefront

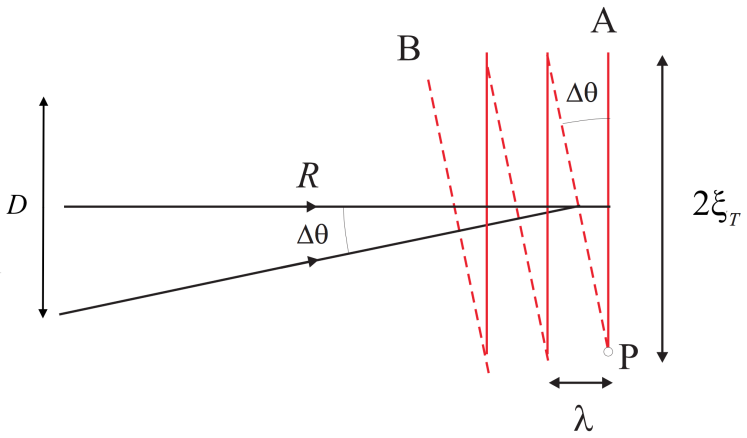

Figure A.2: Transverse coherence length (modified figure from reference [43]).

A, until A and B have opposite phases. Within distance $2\xi_T$ they have the same phase again. Considering the above, the transverse coherence length is $\xi_T = 1/2\ \lambda/\tan\Delta\theta$.

Beam divergence can be caused by the finite size of the source. In figure A.2, D denotes the size of the source, wavefronts A and B are emitted at either ends. R denotes the distance from the source. Using this, $\tan\Delta\theta$ can be expressed as D/2R, and substituting to the previously obtained expression, the transverse coherence length is the following:

$$\xi_T = \frac{\lambda R}{D} \tag{A.5}$$

The transverse coherence length increases with wavelength, lower energy X-rays are favoured. It also increases with distance from the source. This is why the I13-1 experimental hall in Diamond Light Source is located in a separate building about 130 m away from the main building. Lastly, ξ_T is inversely proportional to the size of the source. This motivates reducing the spread of electron bunches in the storage ring, that produce the probing X-ray beam. Alternatively, a slit can be placed close to the source to create a virtual source reducing the size [43, 147, 148]. This is a major motivation for synchrotron facilities to upgrade their ring lattice, such as MAX-IV in Lund and ESRF in Grenoble.

A synchrotron X-ray source measures about 100 μm vertically and 10 μm horizontally. If the wavelength is approximately 1 Å, and the experiment is carried out 100 m away from from the source, the transverse coherence length is 100 μm horizontally, and 1 mm vertically. Specifically for the I13-1 beamline, coherence lengths of 200 μm (horizontal) and 350 μm (vertical) were demonstrated [149].

Synchrotron radiation is only partially coherent. Individual electrons emit coherently, but the batch does not. Coherent beam is produced by inserting a slit of the size of the transverse coherence length in the beam. This only allows the coherent portion through, part of the flux has to be sacrificed [43, 147]. In case of the I13-1 beamline, the initial flux of 7×10^{14} photon per second per 0.1% bandwidth (Ph/s/0.1%BW) is reduced to a coherent flux of about 10^{10} Ph/s/0.1%BW [150].

The diffraction pattern produced by a coherent beam differs from one created by an incoherent beam. A diffraction peak obtained using an incoherent beam is the incoherent sum of the scattering by different domains (n) in the sample ($I(\mathbf{q}) = \sum_n |F_n(\mathbf{q})|^2$). This results in a diffuse pattern. When using a coherent beam, the peak is the coherent sum of the scattering by different domains ($I(\mathbf{q}) = |\sum_n F_n(\mathbf{q})|^2$). The pattern then shows sharp intensity fluctuations, known as speckles [147, 151]. If the scattering object is smaller than the footprint of the beam, fringes related to the shape of the object also appear.

A.3 Coherent diffraction imaging and ptychography

Coherent diffraction imaging (CDI) and ptychography are lensless imaging techniques that allow the reconstruction of the phase information. They are used with electrons and with X-rays as well. In both techniques a coherent X-ray beam is scattered by an object, and the scattered intensity is collected by a 2D detector in the far-field. In case of ptychography the complex amplitude of both the probing and the scattered wavefront can be reconstructed with iterative algorithms. In case of CDI one is assumed to be known (usually the probing wavefront) and the other (usually the scattered wavefront) is recovered.

CDI is used on samples smaller than the footprint of the coherent beam. This way the whole volume of the sample takes part in the scattering process.

Ptychography is the scanning version of CDI. The concept of ptychography was first put forward by Hoppe [152, 153] to be used with scanning transmission microscopy (STEM), and the proof of the concept was demonstrated by Hoppe and Strube [154] using visible light. It was not developed for STEM at the time, because the instrumentation was not sufficiently developed [144]. Thanks to the advances that were made since in X-ray optics and computation, the advantages of ptychography are being discovered.

During the course of a ptychography measurement a large sample is scanned along a predefined path by a coherent beam. The diffraction patterns are collected at each point of the path. The complex amplitude of the scattered and the probing beam is reconstructed.

Redundancy is introduced in the data by partially overlapping the footprint of the beam between the steps in the scan. This overlap is then used as a constraint in the reconstruction algorithm. The ideal degree of overlap was determined to be 60% by Bunk et al. [155], with overlap (o) defined as $o = 2r - a$, where r is the radius of the footprint and a is the centre-to-centre distance.

A.3.1 Oversampling criterion

Retrieval of the phase relies on the concept of oversampling the diffraction pattern.

Nyquist-Shannon theorem states that a continuous function can be completely determined with a sampling frequency twice the highest frequency component of the signal [156]. This frequency is called the Nyquist sampling frequency. It is important to note that we are talking about the probing periodicity of the diffraction plane, which, considering a 2D detector, translates to spatial frequency. This minimum spatial sampling frequency determines the number of detector pixels required per fringe or speckle.

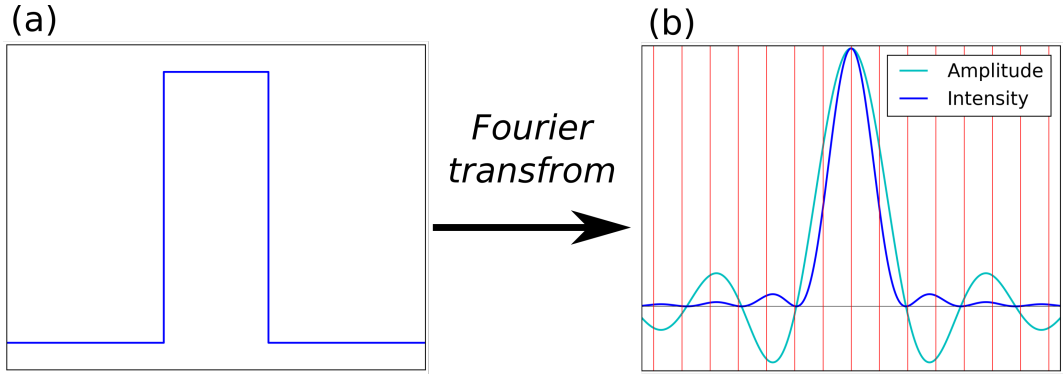

Figure A.3: Nyquist sampling frequency demonstrated on a square function (corresponds to a slit) (a). The square of the Fourier transform is seen by the detector. To fully determine it, it has to be sampled at least once per fringe, shown in red (b).

The concept of the Nyquist sampling frequency is illustrated in figure A.3 with a slit. The Fourier transform of a 1D slit (along x), shown in figure A.3(a), is the function $\sin(x)/x$, shown in light blue in figure A.3(b). What is recorded by the detector is the intensity, the square of the amplitude, shown in darker blue in figure A.3(b). The Nyquist sampling frequency of the intensity function corresponds to one point per fringe, shown by the red marks in figure A.3(b).

When sampling at the Nyquist frequency, the amplitude can be recovered, but half the information, the phase, cannot. Sayre showed that if the diffraction pattern is sampled

at at least twice the Nyquist sampling frequency, the phase of the scattered wave can also be recovered [157].

A.3.2 Phase retrieval methods

The phase problem is solved by applying inverse Fourier transform to the diffraction patterns to recover the complex scattered wavefront ('object') via the use of the convolution theorem.

The first algorithm for ptychography was put forward by Rodenburg and was termed the ptychographic iterative engine (PIE) [158]. It was successful in solving the phase problem, however, it required an accurate knowledge of the incident probing wavefront ('probe') and the stage positions during the scan. The necessity of the accurate knowledge of the probe was removed by the development of the extended ptychographic iterative engine (ePIE), which can recover the probe from a rough estimate as well as the object [159]. Independently of Rodenburg and his coworkers, around the same time Thibault et al. developed their own algorithm based on the difference map algorithm (DM), which is also capable of reconstructing both the probe and the object [160]. Later, it was demonstrated (using ePIE) that errors in samples positions can be corrected for in the algorithm [161]. Furthermore, the DM method was extended by Thibault et al. to take into account partial coherence in both the longitudinal and the transverse directions [162]. This is useful, as it removes the strict restriction on coherence, which limits the flux [163].

Below the two most commonly used iterative reconstruction algorithms, Rodenburg's ePIE and Thibault's DM method, are described.

Both algorithms rely on two assumptions: the interaction between the object function ($O(\mathbf{r})$) and the probe function ($P(\mathbf{r})$) can be modelled by a complex multiplication, and the scattered wavefront can be modelled by the Fourier transform ($\mathcal{F}$).

The extended ptychographic iterative engine

Below the ePIE method is introduced following references [159, 164, 165].

Based on the assumptions above the exit wave is given by the following:

$$\psi(\mathbf{r}) = O(\mathbf{r})P(\mathbf{r} - \mathbf{R}), \tag{A.6}$$

where $\mathbf{R}$ refers to the position of the beam on the sample along the path. The exit wave observed in the far field is:

$$I(\mathbf{q}) = |\mathcal{F}[\psi(\mathbf{r})]|^2. \tag{A.7}$$

The algorithm starts with the initial guesses for the probe ($P_0(\mathbf{r})$) and the object ($O_0(\mathbf{r})$) functions. Both guesses get updated through subsequent iterations that move between the real and the Fourier space.

The J number of diffraction patterns that were collected during the ptychography scan are addressed in a random sequence in the algorithm.

In the first step the guessed scattered wave is calculated from the (updated or initial) shifted probe and the object functions at iteration j:

$$\psi_j(\mathbf{r}) = O_j(\mathbf{r})P_j(\mathbf{r} - \mathbf{R_j}). \tag{A.8}$$

Then Fourier transform is applied:

$$\psi_j(\mathbf{q}) = \mathcal{F}[\psi_j(\mathbf{r})]. \tag{A.9}$$

In the next step, the modulus of the scattered wave in the Fourier space ($\psi_j(\mathbf{q})$) is replaced by the modulus obtained from the measured, corresponding diffraction pattern ($\sqrt{I_j(\mathbf{q})}$):

$$\psi'_j(\mathbf{q}) = \sqrt{I_j(\mathbf{q})}\frac{\mathcal{F}[\psi_j(\mathbf{r})]}{|\mathcal{F}[\psi_j(\mathbf{r})]|}. \tag{A.10}$$

The updated scattered wave is calculated with the inverse Fourier transform:

$$\psi'_j(\mathbf{r}) = \mathcal{F}^{-1}[\psi'_j(\mathbf{q})]. \tag{A.11}$$

Finally the object and probe functions are updated by adding the weighted correction of the wavefront to the guess wavefront. This is expressed by the following two equations:

$$O_{j+1}(\mathbf{r}) = O_j(\mathbf{r}) + \alpha\frac{P_j^*(\mathbf{r} - \mathbf{R_j})}{|P_j(\mathbf{r} - \mathbf{R_j})|^2_{\max}}(\psi'_j(\mathbf{r}) - \psi_j(\mathbf{r})), \tag{A.12}$$

$$P_{j+1}(\mathbf{r}) = P_j(\mathbf{r}) + \beta\frac{O_j^*(\mathbf{r} + \mathbf{R_j})}{|O_j(\mathbf{r} + \mathbf{R_j})|^2_{\max}}(\psi'_j(\mathbf{r}) - \psi_j(\mathbf{r})), \tag{A.13}$$

where $|P_j(\mathbf{r}-\mathbf{R_j})|^2_{\max}$ refers to the maximum value of $|P_j(\mathbf{r}-\mathbf{R_j})|^2$, $P_j^*(\mathbf{r}-\mathbf{R_j})$ is the complex conjugate, and the same stands for $O_j(\mathbf{r})$. α and β are constants that adjusts the step size of the update.

One iteration is complete when the algorithm ran through all J number of diffraction patterns. The updated object and probe functions are the new guesses in the next iteration.

The convergence is monitored by the following metric:

$$E = \frac{\sum_j \sum_{\mathbf{q}} |\sqrt{I_j(\mathbf{q})} - |\psi'_j(\mathbf{q})||^2}{\sum_j \sum_{\mathbf{q}} I_j(\mathbf{q})}, \tag{A.14}$$

The aim is to minimise E.

The difference map algorithm

The DM algorithm is detailed below. The discussion here adheres to references [160, 164, 166, 167].

The DM method also iterates between real and Fourier space using the object and probe functions, but addresses all J diffraction patterns in the same time. It is parallel rather than sequential. The DM algorithm solves the phase problem by searching the intersection point of two constraint sets, one defined in real space, the other in Fourier space. Both constraint sets are associated with a projection operator, that map the iterations onto the constraint sets.

The first constraint set is the Fourier constraint, which relates the observed intensities to the scattered waves via the Fourier transform:

$$I_j(\mathbf{q}) = |\mathcal{F}[\psi_j(\mathbf{r})]|^2, \quad \forall j. \tag{A.15}$$

The second is the overlap constraints, which states that the each scattered wave in the ptychographic scan can be factorised as a probe and an object function:

$$\psi_j(\mathbf{r}) = P(\mathbf{r}-\mathbf{R_j})O(\mathbf{r}), \quad \forall j. \tag{A.16}$$

The task of the algorithm is to find the series of O and P that satisfy these two constraints.

A state vector is defined as $\Psi(\mathbf{r}) = \{\psi_1(\mathbf{r}), \psi_2(\mathbf{r}), \psi_3(\mathbf{r}), ..., \psi_J(\mathbf{r})\}$ using the initial guesses for the the probe and the object functions.

The Fourier constraint is applied where (just as in the ePIE), the modulus of the Fourier transformed wave ($\psi_j(\mathbf{q}) = \mathcal{F}[\psi_j(\mathbf{r})]$) is replaced with the modulus obtained from the measured diffraction patterns. The associated projection (Π_F) takes the following form:

$$\Pi_F(\Psi(\mathbf{q})) : \psi_j(\mathbf{q}) \rightarrow \psi_j^F(\mathbf{q}) = \sqrt{I_j(\mathbf{q})}\frac{\psi_j(\mathbf{q})}{|\psi_j(\mathbf{q})|}, \quad \forall j. \tag{A.17}$$

The overlap projection is determined from the minimisation of distance $|\Psi(\mathbf{r}) - \Psi^O(\mathbf{r})|^2$, where $\Psi^O(\mathbf{r}) = \{\hat{P}(\mathbf{r} - \mathbf{R_j})\hat{O}(\mathbf{r})\}$. Thus, the following equation needs to be minimised with respect to $\hat{P}$ and $\hat{O}$:

$$|\Psi(\mathbf{r}) - \Psi^O(\mathbf{r})|^2 = \sum_j \sum_{\mathbf{r}} |\psi_j(\mathbf{r}) - \hat{P}(\mathbf{r} - \mathbf{R_j})\hat{O}(\mathbf{r})|, \tag{A.18}$$

which defines the overlap projection (Π_O):

$$\Pi_O(\Psi(\mathbf{r})) : \psi_j(\mathbf{r}) \rightarrow \psi_j^O(\mathbf{r}) = \hat{P}(\mathbf{r} - \mathbf{R_j})\hat{O}(\mathbf{r}), \quad \forall j. \tag{A.19}$$

Setting the derivative of equation A.18 to 0, the solution for the minimum is the following equation system:

$$\hat{O}(\mathbf{r}) = \frac{\sum_j \hat{P}^*(\mathbf{r} - \mathbf{R_j})\psi_j(\mathbf{r})}{\sum_j |\hat{P}(\mathbf{r} - \mathbf{R_j})|^2}, \quad \hat{P}(\mathbf{r}) = \frac{\sum_j \hat{O}^*(\mathbf{r} + \mathbf{R_j})\psi_j(\mathbf{r} + \mathbf{R_j})}{\sum_j |\hat{O}(\mathbf{r} + \mathbf{R_j})|^2}. \tag{A.20}$$

O and P cannot be uncoupled analytically. When both the object and the probe are unknowns, the above equations (A.20) are applied in turn to update Ψ.

Using the projections defined in equations A.17 and A.19, the reconstruction is implemented using the the following update rule [168]:

$$\Psi_{n+1} = \Psi_n + \Pi_F[2\Pi_0(\Psi_n) - \Psi_n] - \Pi_O(\Psi_n) \tag{A.21}$$

The convergence is monitored by the difference map error:

$$E_{n+1} = |\Psi_{n+1} - \Psi_n|. \tag{A.22}$$

The aim is the minimise the difference map error.

A.3.3 Sensitivity of the phase to atomic displacement

Ptychography on rhenium was executed in the Bragg geometry, as shown in figure A.4. This technique is known as Bragg Projection Ptychography (BPP).

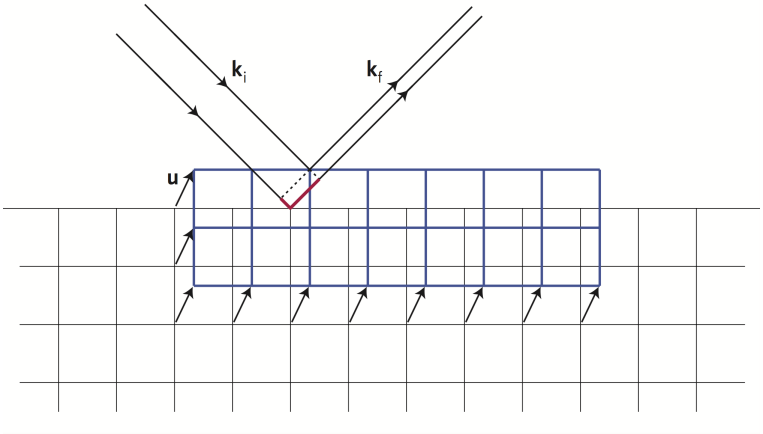

Figure A.4: Sensitivity to the lattice displacement $\boldsymbol{u}$ *in the Bragg geometry [169].*

Intensity distribution from a perfect crystal, where all the atoms are in their ideal positions ($\mathbf{r_0}$), is a periodic function of the reciprocal space coordinates, with Bragg peaks at positions defined by the crystal. The intensity distributions are also symmetric and identical around each Bragg peak. Most crystals, however, are not perfect, and non-symmetric Bragg peaks are often observed.

In a strained crystal atoms are displaced from their ideal positions. A new position is given as $\mathbf{r} = \mathbf{r_0} + \mathbf{u}(\mathbf{r_0})$, where $\mathbf{u}(\mathbf{r_0})$ is the displacement. Substituting $\mathbf{r}$ in the amplitude in equation A.2, the phase in the vicinity of a scattering vector $\mathbf{g}$ becomes the following:

$$\mathbf{q} \cdot \mathbf{r} = \mathbf{q} \cdot \mathbf{r_0} + \mathbf{g} \cdot \mathbf{u}(\mathbf{r_0}) + (\mathbf{q} - \mathbf{g}) \cdot \mathbf{u}(\mathbf{r_0}). \tag{A.23}$$

For small displacements $(\mathbf{q} - \mathbf{g}) \cdot \mathbf{u}(\mathbf{r_0}) \ll 2\pi$ and the third term can be neglected [147]. Thus the scattered amplitude is:

$$A(\mathbf{q}) = \int_V \tilde{f}(\mathbf{r_0}) e^{i\mathbf{q}\mathbf{r_0}} d\mathbf{r_0}, \tag{A.24}$$

where the modified atomic form factor is

$$\tilde{f}(\mathbf{r_0}) = f(\mathbf{r}) e^{i\mathbf{g}\mathbf{u}(\mathbf{r_0})}. \tag{A.25}$$

The modified atomic form factor in case of X-ray scattering is the complex electron density [147, 170].

Non-symmetric Bragg peaks can be decomposed into the symmetric and asymmetric contributions. The symmetric part can be considered to come from the average electron density, and the antisymmetric part is associated with a phase that equals to the projection of the local displacement along the scattering vector **g**. This displacement can be imaged as a real-space map of phase values across the illuminated or scanned area [169].

Over the course of the Bragg ptychography measurement we only recorded the symmetric (002) reflection of rhenium. This reflection only carries information on the displacements along the direction of the surface normal.

It is possible to recover the complex amplitude along the depth of the scattering volume of the scanned area. This technique is known as 3D ptychography, and gives 3 dimensional maps of the modulus and the phase. To achieve this, the ptychographic scans are repeated at and around the Bragg angle along the rocking curve. The technique was successfully demonstrated by Godard et al [171]. This is demanding measurement as it requires precise alignment and stability of the setup over several hours.

Hruszkewycz et al. recently demonstrated that 3D reconstruction is possible form the collection of lateral scans at a single angle [172]. Rocking the sample around the Bragg angle is not necessary.

A.4 I13-1 beamline in Diamond Light Source

Ptychography experiments were carried out on the I13-1 beamline in Diamond Light Source on rhenium thin films.

An areal photograph of the Diamond Light Source is shown in figure A.5(a). The schematics of a beamline is shown in figure A.5(b). The dimensions are specific to the Diamond Light Source and the I13 beamline. The electrons are traveling in the storage ring at an energy of 3 GeV. The ring is not a true circle but a 48 sided polygon. Undulators, shown in figure A.5(c), are composed of a series of dipole magnets with alternating polarity. These are placed in the straight sections of the ring to make the electrons oscillate, and emit X-ray radiation. A specific energy of this radiation is chosen by monochromators, and focused onto the sample under investigation. Most beamlines are located inside the main building, around the storage ring. However, on the I13-1 beamline coherent X-ray radiations is used, which is achieved by placing the experiment far away from the source of the X-ray. The experimental hutch is located in a building separate from the synchrotron storage ring. The total length of the beamline measured

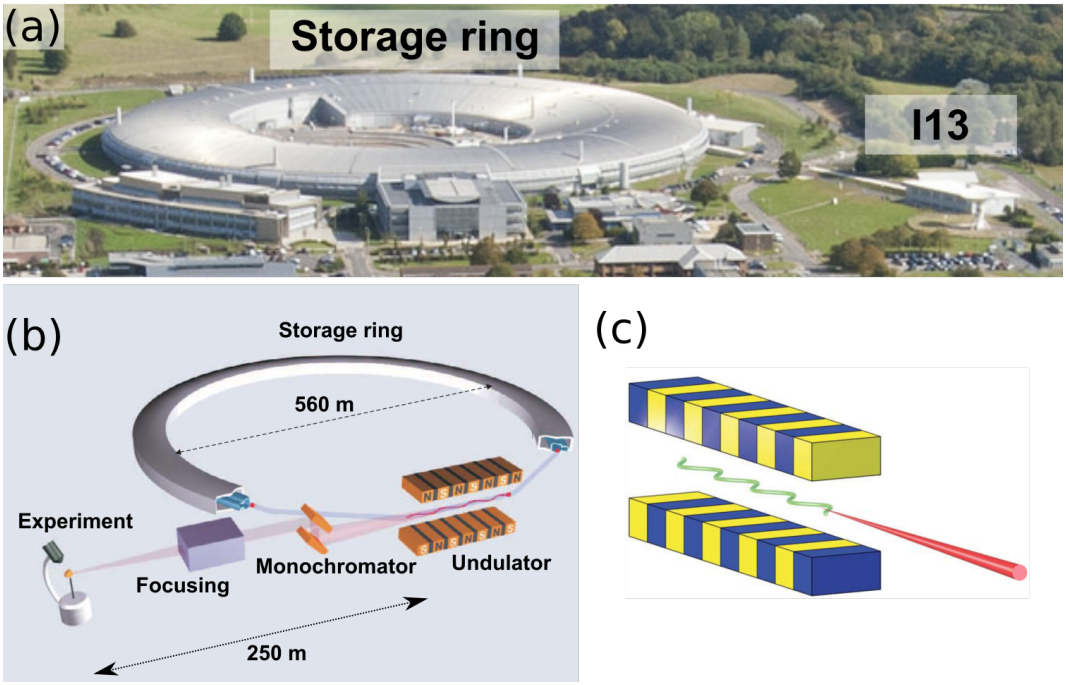

Figure A.5: (a) An areal photograph of Diamond Light Source (source: Science and Technology Facilities Council). (b) Schematics of a synchrotron beamline (dimensions are specific to I13-1 in Diamond Light Source) [43] (c) Undulators are composed of a series of dipole magnets, that make electrons oscillate to generate X-ray radiation [43].

from the source is 250 m.

The experimental setup is shown in figure A.6. The sample stage has a 30° pitch by default with respect to the beam, and can be further tilted by ±15° around the two in-plane axes. Lateral and vertical movement is achieved by two sets XYZ motors, one allows the rough alignment of the sample, another is for fine movements (5 nm resolution) [173, 174].

The detector is placed on an industrial robot arm, part of which is visible in figure A.6. Including this arm, the setup is an 3+2 circle diffractometer, and is able to cover a wide range of *hkl* positions. To achieve sufficient sampling of the diffraction peak, the distance between the sample and the detector can be adjusted. Depending on the Bragg angle, it can be increased up to 5 m, the only limit is the ceiling. Using 9.4 keV X-rays, the Bragg angle for the (002) reflection of rhenium is 17.2°, which allowed a distance of 2 m.

Penetration depth of the X-rays can be obtained as the reciprocal of the attenuation coefficient, which can be found in tables [175]. At this energy for rhenium the penetration

depth is approximately 4 μm, which, taking the angle of incidence into account, gives a probing depth of 1 μm.

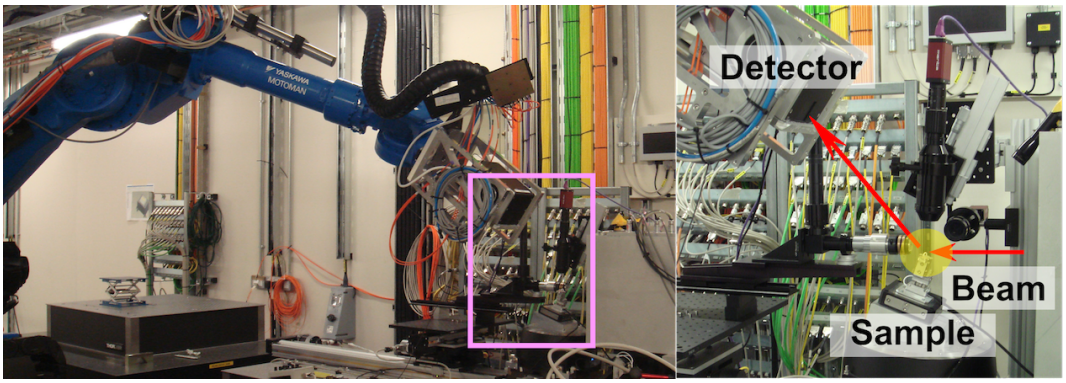

Figure A.6: Experimental setup on the I13-1 beamline.

The detector consists of 3 modules arranged horizontally. Each module contains 2x8 chips, and each chip has 256x256 pixels. This results in a 1536x2048 image. The size of one pixel is 55x55 μm^2 [176].

The X-ray beam was focused onto the sample using a Fresnel-Zone Plate. The spot size was approximately 1 μm horizontally and 0.5 μm vertically. The the horizontal size of the footprint of the beam on the sample is unchanged, the vertical size is increased to $0.5\mu m/\sin(17.2°) = 1.7\mu m$.

A.5 Bragg ptychography on rhenium

Ptychography has been successfully used to study displacement fields in a wide range of materials. Dzhigaev et al. combined finite element method simulations with ptychography to obtain the 3D strain distribution in InGaN/GaN core-shell nanowires, and showed asymmetry in the strain relaxation [177]. Using 3D ptychography Yau et al. observed grain boundary and dislocation dynamics in individual gold grains of a polycrystalline thin film while the sample was subject to heating [178]. Hruszkewycz et al. and Holt et al. used 2D ptychography to map lattice distortions in lithographically engineered epitaxial thin film semiconductor heterostructures [179, 180]. Burdet et al. studied the domains of niobium thin films deposited onto Al_2O_3 substrates [181]. Hruszkewycz et al. also imaged stripped polarization domain pattern in a ferroelectric $PbTiO_3$ thin film [182], and Takahashi et al. succeeded in imaging the strain field of a dislocation in a single crystal silicon [183].

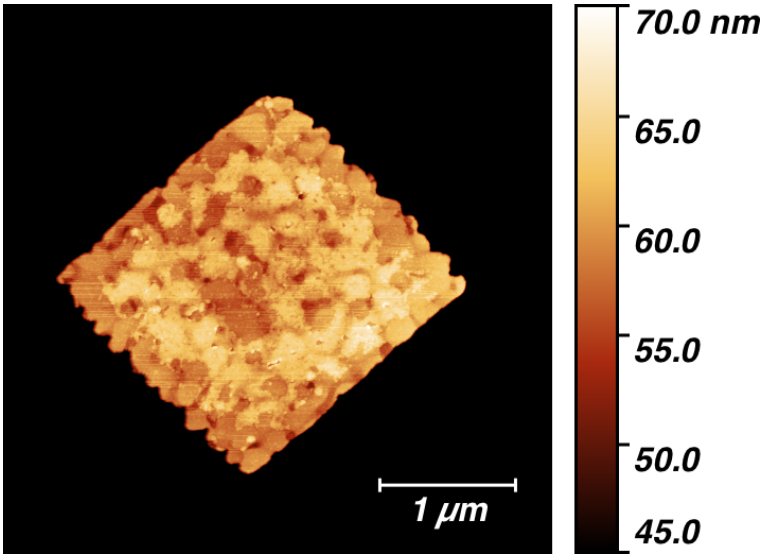

Figure A.7: 4 μm x 4 μm AFM image taken on one of the 2 μm x 2 μm squares fabricated for the ptychography experiments on the a 50 nm sample (sample D).

Spirals decorate the surface of all the rhenium samples that feature a single orientation. An AFM image of a spiral is shown in figure 2.22. Their sizes vary, and are thought to be related to the temperature of deposition, as was shown in section 2.2. Burton et al. explained the growth of spirals by the presence of dislocations with an edge component. This creates a step on the surface, which provides nucleation sites, and allows the spiral to grow [48]. Whether this theory is valid or not in case of our rhenium films could be verified by the technique of ptychography.

Ptychography was preformed on features that were patterned onto the rhenium films using lithography. These clear cut features would allow us to check the resolution and the validity of the measurement.

The features included a square with size 2 μm x 2 μm on the 50 nm sample, which was described in section 2.2.2 (sample D deposited at 900°C). An AFM image taken on one of the squares is shown in figure A.7. A square was scanned with the X-ray beam in a spiral fashion. Spiral path is often used, as it provides good overlap between spots, and eliminates artefacts associated with raster scan.

The spiral scan is shown in figure A.8. At each point of the path a single slice of the (002) reflection of rhenium was recorded on the 2D detector. The colour of the points shown in figure A.8 correspond to the total, summed intensity measured on the detector. The scan started in the middle of the square. Maximum intensity is indeed observed

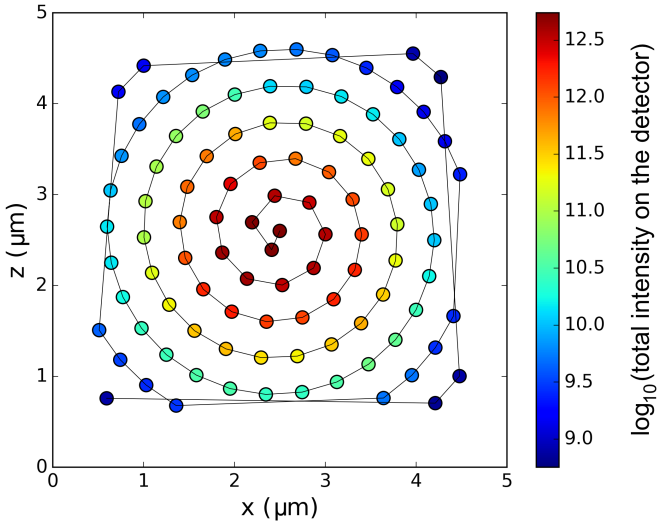

Figure A.8: Spiral ptychography scan on a 2 μm x 2 μm rhenium square: the colour of each point corresponds to the total, summed intensity recorded on the detector.

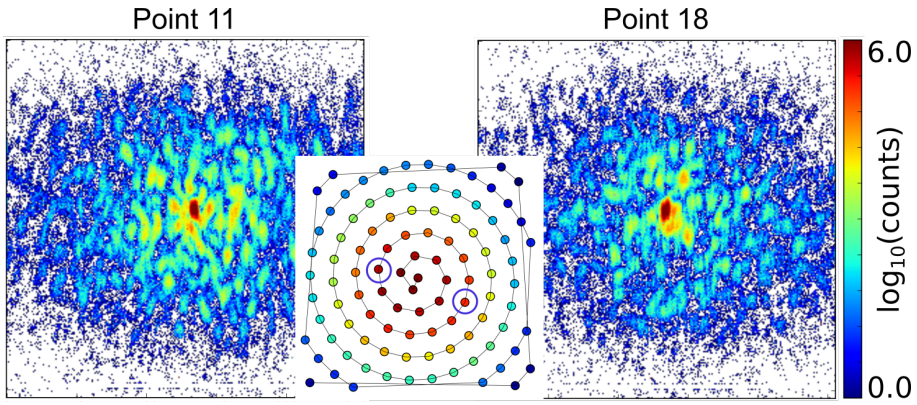

Figure A.9: Two examples of the diffraction pattern recorded on the detector at different points of the scan.

in a 2 μm region of the starting point. Here, the complete footprint of the beam is on the rhenium. As the beam gets further away from the centre, the volume of rhenium that takes part in the diffraction process is reduced, so is the intensity recorded on the detector.

The distance between the consecutive points in the spiral was 0.4 μm, which (with

spot size 1μm) gives the ideal overlap of 60%.

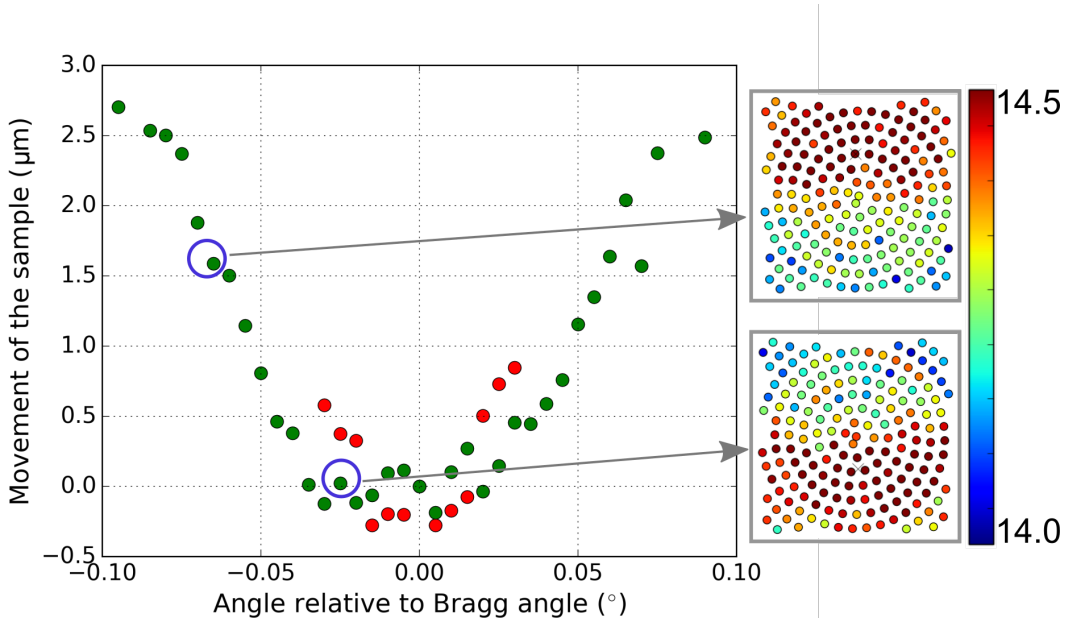

Figure A.10: Movement of the sample during the 3D ptychography scan.

Two examples of the diffraction patterns recorded in two different point of the spiral path are shown in figure A.9. The speckle pattern changes throughout the scan. The centre peak also shows some structure, it appears to be a double peak with small angular separation (approximately 0.002°). The direction and the magnitude of the separation was observed to change along the scan.

We recored scans for 3D ptychography on a 3 μm thick line by repeating the spiral scan at angles around the Bragg angle along the rocking curve. This is a demanding measurement, as it can take several hours, and the sample is required to be stationary, bar the rocking and the scanning motions. To ensure nothing moves, the experimental hutch is kept at a constant temperature by air conditioning, and the robot arm keeps the detector stable. Furthermore, the beam, the centre of the rotation of the stage, and the sample has to be aligned. A camera placed over the sample was used for the alignment. We did not manage to correct all the movements. Figure A.10 shows the position of the sample for each angle. Two of the intensity maps are also shown as a demonstration.

The centre of the line was obtained from the centre-of-mass of the modified intensity map. To correctly detect the middle of the line its weight in the centre-of-mass calculation had to be increased, so intensities below a fixed value were set to zero. This might

indicate that there is some noise in the data, which would prevent the ptychographic reconstruction.

The position of the sample changes consistently with increasing angles in both negative and positive directions. The measurement was repeated latter for the same line, and the points are in close agreement. This suggest that the alignment was the best we could achieve with the setup available.

Reconstruction of the datasets is not a trivial task. To our knowledge, two reconstruction packages are available, both developed for Python environment. Reconstruction was attempted using the *ptypy* package [184] with no success yet. The *pynx* package currently only works for the small angle geometry and is being developed for the Bragg geometry [185, 186]. Analysis of this data is a work in progress.

B

Determination of surface coverage from XPS data

The technique of XPS was introduced in detail in section 1.4.1. The principle of the technique is the following: the sample is irradiated with a known energy X-ray beam, and the electrons (mostly photoelectrons) that escape the material are sorted by their kinetic energies, and counted. From their spectrum the chemical composition of the surface can be determined.

The surface monolayer coverage ($\sigma = \frac{\text{covered surface}}{\text{uncovered surface}}$) of an element (contamination or deposit) can be calculated from the intensity of the corresponding XPS peak. The intensity of a peak arising from the substrate can be expressed as follows:

$$I_{\text{substrate}} \propto (1-\sigma) I^{\infty}_{\text{substrate}} + \sigma I^{\infty}_{\text{substrate}} e^{-\frac{1}{\lambda}}, \tag{B.1}$$

where $I^{\infty}_{\text{substrate}}$ is the intensity that would be detected form the pure material. The first part on the left side of the equation B.1 is reduced by a factor of $(1-\sigma)$, which corresponds to the reduced surface area which is not covered by contamination or deposit. The second part is the intensity that is transmitted through the monolayer coverage, therefore, it is reduced by $e^{-\frac{1}{\lambda}}$, where λ is the inelastic mean free path of the photoelectrons, and can be found in tables.

Intensity that would be detected from a full monolayer can be calculated by integrating the exponential shown below:

$$I_{1\mathrm{ML}} \propto I^{\infty}_{\mathrm{bulk}} \int_0^1 e^{-\frac{z}{\lambda}} dz \propto I^{\infty}_{\mathrm{bulk}}(1 - e^{-\frac{1}{\lambda}}),$$

where $I^{\infty}_{\mathrm{bulk}}$ is the signal that would arise from a pure bulk of the same material.

If only a fraction of the surface is covered by the contamination or deposit, the expression above is simply multiplied by σ:

$$I_{\mathrm{coverage}} \propto \sigma I^{\infty}_{\mathrm{bulk}}(1 - e^{-\frac{1}{\lambda}}).$$

From the ratio of the two intensities (R) the surface coverage can be calculated:

$$R = \frac{I_{\mathrm{substrate}}}{I_{\mathrm{coverage}}} = \frac{I^{\infty}_{\mathrm{substrate}}}{I^{\infty}_{\mathrm{bulk}}} \frac{1 - \sigma(1 - e^{-\frac{1}{\lambda}})}{\sigma(1 - e^{-\frac{1}{\lambda}})}.$$

C

Transformation of the Bravais-Miller indices to Cartesian coordinates

Rhenium is a hexagonal closed-packed material, and the coordinate system of the hexagonal crystal system, shown in figure C.1(a), is not orthogonal. Transformation of the Bravais-Miller indices of a direction to Cartesian coordinates is not trivial, involves trigonometry.

Directions in a hexagonal system are most often given by their four Bravais-Miller indices. In the first step of this transformation, the four Bravais-Miller indices, $[UVTW]$, have to be converted to the three Miller indices, $[uvw]$, using the following formula:

$$u = 2U + V, \quad v = 2V + U, \quad w = W. \tag{C.1}$$

Now we can develop the formula to convert between the two coordinate systems.

The orientation of the Cartesian coordinate system shown in figure C.1(b) was chosen according to the critical thickness calculation detailed in section 1.5.2. Axes x and z are the in-plane orthogonal directions, and axis y is perpendicular to the surface. In the hexagonal crystal system the axis c, of length c lattice parameter, has six fold symmetry. The rhenium films grow along this direction, and therefore the crystal axis c is parallel to axis y. To convert from c to y involves a multiplication by c lattice parameter.

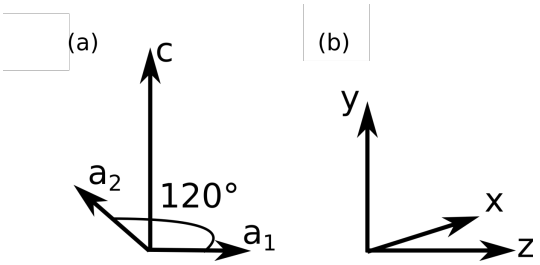

Figure C.1: (a) Coordinate system of the hexagonal crystal system. (b) Cartesian coordinate system of the critical thickness problem.

The other two crystal axes (a_1 and a_2) are perpendicular to axis c, and have a length of a lattice parameter, with a 120° angle between them. Conversion from the axes a_1 and a_2 to x and z requires a rotation.

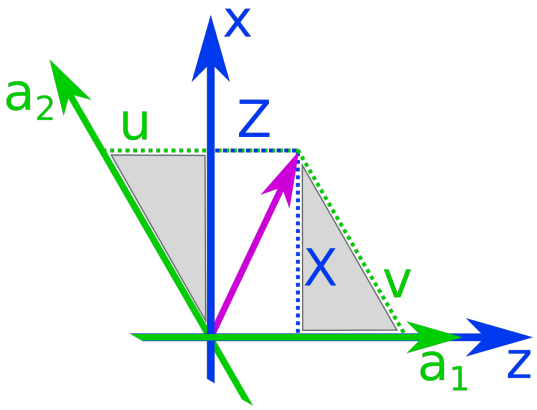

Figure C.2: Transformation of the in-plane hexagonal coordinates to in-plane Cartesian coordinates.

The geometry of the in-plane components of the two coordinate systems is shown in figure C.2. $a1$ is taken parallel to z. The coordinates of the pink vector in the hexagonal system, and in the orthogonal system are (u, v) and (Z, X), respectively. To convert from hexagonal to orthogonal the right-angled triangles, shown in grey in figure C.2, are used. The other two angles in the triangles are 30 and 60°, thus the Cartesian coordinates can be obtained as follows:

$$Z = u - v \sin 30° \quad \text{and} \quad X = v \cos 30°. \tag{C.2}$$

The transformation is demonstrated below, using the indices of a Burgers vector, which is expected to occur in our rhenium films:

$$\begin{array}{ccccc} \text{Bravais-Miller} & \rightarrow & \text{Miller} & \rightarrow & \text{Cartesian} \\ \\ \frac{1}{3}[1\bar{2}10] & \rightarrow & \frac{1}{3}[0\bar{3}0] & \rightarrow & \frac{1}{2}[1a, \overline{\sqrt{3}}a, 0c] \end{array}$$

D

Derivation of the equation system for the heat transfer

To estimate the temperature of the surface of the growing rhenium, a model was developed by Delsol [7]. The complete derivation to obtain the equation system given in chapter 2.4 is given below.

The model is shown in figure D.1. All the parts of the system was assumed to be an infinite plane. The plane noted with F is the furnace. Besides radiosity which is the

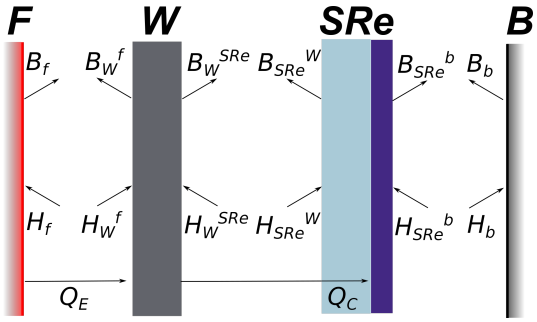

Figure D.1: The model consist of a series of planes: furnace (F), tungsten (W), substrate-rhenium (SRe), and chamber (B). Irradiance and radiosity of the planes is considered.

result of the hot filament, Q_E has to be included in the equations for experiments when electron bombardment is applied. W refers to the tungsten backing on the substrate. SRe is the substrate and rhenium, which is considered as one unit, and conduction of heat through the substrate (Q_C) is included in the model. Finally, B denotes the wall of the vacuum chamber ('bâtiment'), which is at room temperature.

In equilibrium the heat exchange between the surfaces (Q) are equal, and can be expressed using the radiosities:

$$Q = B_f - B_W^f + Q_E, \tag{D.1}$$

$$Q = B_W^{SRe} - B_{SRe}^W + Q_C, \tag{D.2}$$

$$Q = B_{SRe}^b - B_b. \tag{D.3}$$

These three equation give the equation system that needs to be solved. The three unknowns are Q, the temperature of the tungsten layer (T_W), and the temperature of the substrate-rhenium (T_{SRe}). Radiosities need to be expressed as only the function of the unknowns and material parameters.

In equilibrium the heat exchange on the surfaces are also Q, and can be expressed using the irradiance and the radiosity:

$$Q = B_f - H_f + Q_E, \tag{D.4}$$

$$Q = H_W^f - B_W^f + Q_E, \tag{D.5}$$

$$Q = B_W^{SRe} - H_W^{SRe} + Q_C, \tag{D.6}$$

$$Q = H_{SRe}^W - B_{SRe}^W + Q_C, \tag{D.7}$$

$$Q = B_{SRe}^b - H_{SRe}^b, \tag{D.8}$$

$$Q = H_b - B_b. \tag{D.9}$$

Radiosity of a surface is the sum of the thermal radiation due to its temperature ($\epsilon\sigma T^4$), the reflected irradiance (ρH), and transmitted irradiance (τH). According to this the radiosities on the two sides of the substrate-rhenium plane are the following:

$$B^W_{SRe} = \rho_{SRe} H^W_{SRe} + \epsilon_{SRe}\sigma T^4_{SRe} + \tau_{SRe} H^b_{SRe}, \tag{D.10}$$

$$B^b_{SRe} = \rho_{SRe} H^b_{SRe} + \epsilon_{SRe}\sigma T^4_{SRe} + \tau_{SRe} H^W_{SRe}. \tag{D.11}$$

Furthermore, from equations (2.30) and (2.31) the following is true, and is used in the derivation:

$$\epsilon = 1 - \rho - \tau.$$

The chamber wall and the furnace are opaque, their transmittances are 0. The tungsten layer on the backside of the substrate is also thick enough to be considered opaque. Thus, the radiosity (and the irradiance) of the furnace, chamber wall and the two sides of the tungsten layer are given as follows:

$$B_f = \rho_f H_f + \epsilon_f \sigma T^4_f \quad \rightarrow \quad H_f = \frac{1}{\rho_f} B_f - \frac{\epsilon_f}{\rho_f}\sigma T^4_f, \tag{D.12}$$

$$B_b = \rho_b H_b + \epsilon_b \sigma T^4_b \quad \rightarrow \quad H_b = \frac{1}{\rho_b} B_b - \frac{\epsilon_b}{\rho_b}\sigma T^4_b, \tag{D.13}$$

$$B^f_W = \rho_W H^f_W + \epsilon_W \sigma T^4_W \quad \rightarrow \quad H^f_W = \frac{1}{\rho_W} B^f_W - \frac{\epsilon_W}{\rho_W}\sigma T^4_W, \tag{D.14}$$

$$B^{SRe}_W = \rho_W H^{SRe}_W + \epsilon_W \sigma T^4_W \quad \rightarrow \quad H^{SRe}_W = \frac{1}{\rho_W} B^{SRe}_W - \frac{\epsilon_W}{\rho_W}\sigma T^4_W. \tag{D.15}$$

When $\tau = 0$, equation $\epsilon = 1 - \rho - \tau$ is modified as follows:

$$\epsilon = 1 - \rho.$$

As was shown with equation (2.35), a quantity analogue to electric resistance can be defined for opaque objects:

$$R = \frac{1-\epsilon}{\epsilon} = \frac{\rho}{\epsilon}.$$

This definition of resistance is used for the furnace, the chamber wall and the tungsten layer in the derivation.

Equations (D.4) - (D.15) have to be manipulated to obtain expressions for the radiosities that depend only on the 3 unknowns (Q, T_W, T_{SRe}). This can be easily done for the surfaces of the opaque planes.

Using equations (D.4) and (D.12):

$$Q = B_f - H_f + Q_E = \underbrace{\left(1 - \frac{1}{\rho_f}\right)}_{\frac{\rho_f - 1}{\rho_f} = -\frac{\epsilon_f}{\rho_f} = -\frac{1}{R_f}} B_f + \frac{\epsilon_f}{\rho_f}\sigma T_f^4 + Q_E.$$

$$\boxed{B_f = \sigma T_f^4 + R_f(Q_E - Q)} \tag{D.16}$$

Using equations (D.9) and (D.13):

$$Q = H_b - B_b = \underbrace{\left(\frac{1}{\rho_b} - 1\right)}_{\frac{1-\rho_b}{\rho_b} = \frac{\epsilon_b}{\rho_b} = \frac{1}{R_b}} B_b - \frac{\epsilon_b}{\rho_b}\sigma T_b^4.$$

$$\boxed{B_b = \sigma T_b^4 + R_b Q} \tag{D.17}$$

Using equations (D.5) and (D.14):

$$Q = H_W^f - B_W^f + Q_E = \underbrace{\left(\frac{1}{\rho_W} - 1\right)}_{\frac{1-\rho_W}{\rho_W} = \frac{\epsilon_W}{\rho_W} = \frac{1}{R_W}} B_W^f - \frac{1}{R_W}\sigma T_W^4 + Q_E.$$

$$\boxed{B_W^f = \sigma T_W^4 + R_W(Q - Q_E)} \tag{D.18}$$

Using equations (D.6) and (D.15):

$$Q = B_W^{SRe} - H_W^{SRe} + Q_C = \underbrace{\left(1 - \frac{1}{\rho_W}\right)}_{\frac{\rho_W - 1}{\rho_W} = -\frac{\epsilon_W}{\rho_W} = -\frac{1}{R_W}} B_W^{SRe} + \frac{1}{R_W}\sigma T_W^4 + Q_C.$$

$$\boxed{B_W^{SRe} = \sigma T_W^4 + R_W(Q_C - Q)} \tag{D.19}$$

Obtaining the radiosity of the substrate-rhenium is a little more difficult, because due to the non-zero transmittance, the irradiances of the two surfaces mix.

An equation that describes the relationship between the irradiances on the two sides can be obtained by subtracting (D.8) from (D.7) and substituting (D.10) and (D.11):

$$\begin{aligned}
0 &= H_{SRe}^W - B_{SRe}^W + Q_C - B_{SRe}^b + H_{SRe}^b = \\
&= H_{SRe}^W - \rho_{SRe} H_{SRe}^W - \epsilon_{SRe}\sigma T_{SRe}^4 - \tau_{SRe} H_{SRe}^b - \\
&\quad - \rho_{SRe} H_{SRe}^b - \epsilon_{SRe}\sigma T_{SRe}^4 - \tau_{SRe} H_{SRe}^W + H_{SRe}^b + Q_C = \\
&= \underbrace{(1 - \rho_{SRe} - \tau_{SRe})}_{\epsilon_{SRe}} H_{SRe}^W + \underbrace{(1 - \rho_{SRe} - \tau_{SRe})}_{\epsilon_{SRe}} H_{SRe}^b - 2\epsilon_{SRe}\sigma T_{SRe}^4 + Q_C.
\end{aligned}$$

$$0 = H_{SRe}^W + H_{SRe}^b - 2\sigma T_{SRe}^4 + \frac{Q_C}{\epsilon_{SRe}} \tag{D.20}$$

Now the irradiance of one side of the substrate-rhenium can be expressed with the radiosity of the same side.

Expressing H_{SRe}^b from (D.20) and substituting it in equation (D.10):

$$\begin{aligned}
B_{SRe}^W &= \rho_{SRe} H_{SRe}^W + \epsilon_{SRe}\sigma T_{SRe}^4 + \tau_{SRe} H_{SRe}^b = \\
&= \rho_{SRe} H_{SRe}^W + \epsilon_{SRe}\sigma T_{SRe}^4 + \tau_{SRe}\left(2\sigma T_{SRe}^4 - H_{SRe}^W - \frac{Q_C}{\epsilon_{SRe}}\right) = \\
&= (\rho_{SRe} - \tau_{SRe}) H_{SRe}^W + (\epsilon_{SRe} + 2\tau_{SRe})\sigma T_{SRe}^4 - \frac{\tau_{SRe}}{\epsilon_{SRe}} Q_C.
\end{aligned}$$

$$H_{SRe}^W = \frac{1}{\rho_{SRe} - \tau_{SRe}} B_{SRe}^W - \frac{1}{R_{SRe}}\sigma T_{SRe}^4 + \frac{\tau_{SRe}/\epsilon_{SRe}}{\rho_{SRe} - \tau_{SRe}} Q_C \tag{D.21}$$

where, analogous to opaque objects, the notation $R_{SRe} = \frac{\rho_{SRe} - \tau_{SRe}}{\epsilon_{SRe} + 2\tau_{SRe}}$ was used.

Next H^W_{SRe} is expressed from (D.20) and substituted in equation (D.11):

$$\begin{aligned} B^b_{SRe} &= \rho_{SRe} H^b_{SRe} + \epsilon_{SRe}\sigma T^4_{SRe} + \tau_{SRe} H^W_{SRe} = \\ &= \rho_{SRe} H^b_{SRe} + \epsilon_{SRe}\sigma T^4_{SRe} + \tau_{SRe}\left(2\sigma T^4_{SRe} - H^b_{SRe} - \frac{Q_C}{\epsilon_{SRe}}\right) = \\ &= (\rho_{SRe} - \tau_{SRe}) H^b_{SRe} + (\epsilon_{SRe} + 2\tau_{SRe})\sigma T^4_{SRe} - \frac{\tau_{SRe}}{\epsilon_{SRe}} Q_C. \end{aligned}$$

$$H^b_{SRe} = \frac{1}{\rho_{SRe} - \tau_{SRe}} B^b_{SRe} - \frac{1}{R_{SRe}}\sigma T^4_{SRe} + \frac{\tau_{SRe}/\epsilon_{SRe}}{\rho_{SRe} - \tau_{SRe}} Q_C \tag{D.22}$$

Using (D.7) and substituting (D.21) for H^W_{SRe}, the final expression for B^W_{SRe} is obtained:

$$\begin{aligned} Q &= H^W_{SRe} - B^W_{SRe} + Q_C = \\ &= \underbrace{\left(\frac{1}{\rho_{SRe} - \tau_{SRe}} - 1\right)}_{\frac{1-\rho_{SRe}+\tau_{SRe}}{\rho_{SRe}-\tau_{SRe}} = \frac{\epsilon_{SRe}+2\tau_{SRe}}{\rho_{SRe}-\tau_{SRe}} = \frac{1}{R_{SRe}}} B^W_{SRe} - \frac{1}{R_{SRe}}\sigma T^4_{SRe} + \left(1 + \frac{\tau_{SRe}/\epsilon_{SRe}}{\rho_{SRe} - \tau_{SRe}}\right) Q_C. \end{aligned}$$

$$\boxed{B^W_{SRe} = \sigma T^4_{SRe} + R_{SRe}(Q - Q_C) - r_{SRe} Q_C} \tag{D.23}$$

where the notation $r_{SRe} = R_{SRe}\frac{\tau_{SRe}/\epsilon_{SRe}}{\rho_{SRe}-\tau_{SRe}} = \frac{\rho_{SRe}-\tau_{SRe}}{\epsilon_{SRe}+2\tau_{SRe}}\frac{\tau_{SRe}/\epsilon_{SRe}}{\rho_{SRe}-\tau_{SRe}} = \frac{\tau_{SRe}/\epsilon_{SRe}}{\epsilon_{SRe}+2\tau_{SRe}}$ was used.

The final expression for B^b_{SRe} is obtained from equation (D.8) by substituting equation (D.22) for H^b_{SRe}:

$$\begin{aligned} Q &= B^b_{SRe} - H^b_{SRe} = \\ &= \underbrace{\left(1 - \frac{1}{\rho_{SRe} - \tau_{SRe}}\right)}_{\frac{\rho_{SRe}-\tau_{SRe}-1}{\rho_{SRe}-\tau_{SRe}} = -\frac{\epsilon_{SRe}+2\tau_{SRe}}{\rho_{SRe}-\tau_{SRe}} = -\frac{1}{R_{SRe}}} B^b_{SRe} + \frac{1}{R_{SRe}}\sigma T^4_{SRe} - \frac{\tau_{SRe}/\epsilon_{SRe}}{\rho_{SRe} - \tau_{SRe}} Q_C. \end{aligned}$$

$$\boxed{B^b_{SRe} = \sigma T^4_{SRe} - R_{SRe} Q - r_{SRe} Q_C} \tag{D.24}$$

All the radiosities are expressed as the function of only the unknown parameters in equations (D.16), (D.17), (D.18), (D.19), (D.23) and (D.24). The final form of the equations system (D.1), (D.2), (D.3) can be computed.

Rewriting equation (D.1) using (D.16) and (D.18):

$$\begin{aligned} Q &= B_f - B_W^f + Q_E = \\ &= \sigma T_f^4 + R_f(Q_E - Q) - \sigma T_W^4 - R_W(Q - Q_E) + Q_E. \end{aligned}$$

$$\boxed{\boxed{Q = \frac{\sigma T_f^4 - \sigma T_W^4}{1 + R_f + R_W} + Q_E}} \tag{D.25}$$

Rewriting equation (D.2) using (D.19) and (D.23):

$$\begin{aligned} Q &= B_W^{SRe} - B_{SRe}^W + Q_C = \\ &= \sigma T_W^4 + R_W(Q_C - Q) - \sigma T_{SRe}^4 - R_{SRe}(Q - Q_C) + r_{SRe}Q_C + Q_C. \end{aligned}$$

$$\boxed{\boxed{Q = \frac{\sigma T_W^4 - \sigma T_{SRe}^4}{1 + R_W + R_{SRe}} + \left(\frac{r_{SRe}}{1 + R_W + R_{SRe}} + 1\right) Q_C}} \tag{D.26}$$

Finally, rewriting equation (D.3) using (D.17) and (D.24):

$$\begin{aligned} Q &= B_{SRe}^b - B_b = \\ &= \sigma T_{SRe}^4 - R_{SRe}Q - r_{SRe}Q_C - \sigma T_b^4 - R_b Q. \end{aligned}$$

$$\boxed{\boxed{Q = \frac{\sigma T_{SRe}^4 - \sigma T_b^4}{1 + R_B + R_{SRe}} - \frac{r_{SRe}}{1 + R_B + R_{SRe}} Q_C}} \tag{D.27}$$

Notations used throughout this derivation are summarised below:

$$R_f = \frac{\rho_f}{\epsilon_f}, \qquad R_b = \frac{\rho_b}{\epsilon_b}, \qquad R_W = \frac{\rho_W}{\epsilon_W},$$

$$R_{SRe} = \frac{\rho_{SRe} - \tau_{SRe}}{\epsilon_{SRe} + 2\tau_{SRe}}, \qquad r_{SRe} = \frac{\frac{\tau_{SRe}}{\epsilon_{SRe}}}{\epsilon_{SRe} + 2\tau_{SRe}}.$$

Substrate and rhenium was is treated as a single object. The common transmittance and emittance was calculated as follows:

$$\tau_{SRe} = \tau_S \tau_{Re}, \qquad \epsilon_{SRe} = (1 - \tau_{Re})\epsilon_{Re} + \tau_{Re}\epsilon_S.$$

E

Python scripts

In this appendix a selection of scripts and functions that were written in the Python environment to calculate, treat, or simulate the data detailed in this work are presented.

E.1 X-ray diffraction

E.1.1 Extracting data from a SPEC file

Measurement data obtained using the Huber 4-cycle diffractometer is contained in a single file, created by the measurement software, SPEC. The different scans are numbered. The following function extracts scan data from the SPEC file according to its scan number. It fails for scans that were interrupted.

```
import numpy as np

def get_scan_data(lines,scannum):
    "Returns scan data of scan number scannum.
     File needs to be loaded first (lines). See example."
    findit = '#S '+ str(scannum)
    for i in range(np.shape(lines)[0]):
        line = lines[i]
```

```
yes = line.find(findit)

if yes != -1:
    numofline = i
    command = lines[numofline]
    command_arr = command.split(' ')
    numofwords = np.shape(command_arr)[0]

    if numofwords == 15: #a2scan
        numofintervals = int(command_arr[13])
        start_scanned1 = float(command_arr[6])
        stop_scanned1 = float(command_arr[7])
        start_scanned2 = float(command_arr[10])
        stop_scanned2 = float(command_arr[11])

    elif numofwords == 11: #ascan
        numofintervals = int(command_arr[9])
        start_scanned1 = float(command_arr[6])
        stop_scanned1 = float(command_arr[7])
        start_scanned2 = 0
        stop_scanned2 = 0
    else:
        print 'Something is wrong with the number of
               words in the spec command'

    time = lines[numofline+1]
    pos = lines[numofline+8]
    positions = np.array(pos.split(' ')[1:5])
    angles = positions.astype(np.float)
    anglename = ['tth', 'th', 'chi', 'phi']
    names = lines[numofline+10]
    datalinestr = lines[numofline+11]
    datalinearr = np.array(datalinestr.split(' '))
    data = np.zeros([numofintervals+1,
                     np.shape(datalinearr)[0]])
```

```
            for k in range(numofintervals+1):
                datastr = lines[numofline+11+k]
                dataarr = np.array(datastr.split(' '))
                data[k,:] = dataarr.astype(np.float)

            break

        else:
            continue
    return [
            command, numofintervals,
            [start_scanned1, stop_scanned1],
            [start_scanned2, stop_scanned2], time,
            [anglename,angles], names, data
            ]
```

Example:

```
In:
file = open('EJM216')
lines = file.readlines()
file.close
scannum = 10
data = spec.get_scan_data(lines,scannum)

Out:
data[0]
'#S 10  a2scan  tth 32 92  th 16 46  3000 3 \n'
# command - this is the scan command

data[1]
3000
# numofintervals - number of intervals in the data
# number of datapoint is numofintervals+1

data[2]
[32.0, 92.0]
# Start and stop of the first scanned angle, 2theta in this case
```

```
data[3]
[16.0, 46.0]
# Start and stop of the second scanned angle, theta in this case
# [0, 0] when only one angle is scanned

data[4]
'#D Fri Feb 20 12:50:53 2015 \n'
# Date and time of the scan

data[5]
[['tth', 'th', 'chi', 'phi'],
array([  40.6   ,   20.3   , 269.9995,    0.    ])]
# angular positions before the scan

data[6]
'#L Two Theta  Theta  H  K  L  Epoch  Seconds  Detector \n'
# columns of the data

data[7]
array([[3.20000000e+01, 1.60000000e+01, 8.50817000e-06, ...,
        3.46700000e+03, 3.00000000e+00, 7.00000000e+00],
       ...
# the data
```

E.1.2 Functions used to fit X-ray data

Voigt function

The Voigt function was used to fit the θ-2θ diffraction peaks. It is the convolution of a Gauss function and a Lorentz function, and is given in equation 2.10. Both the Gauss and the Lorentz functions are centred on a peak. The discrete convolution only preserves the position of the peak, if that is in the middle of the two arrays. This was considered when defining the Voigt function, which is given below.

```
import numpy as np
import scipy.signal as signal
import scipy.interpolate as interp
```

```
def lorentz(x, c, x0, FWHM):
    "Returns the Lorentz function centred on x0."
    gamma = FWHM/2
    lorentzfunc = np.divide(1, np.pi*gamma * (1 +
                  np.divide( np.square(x - x0), gamma**2)))
    return c*lorentzfunc

def gauss(x, c, x0, FWHM):
    "Returns the Gauss function centred on x0."
    sigma = np.divide(FWHM, 2*np.sqrt(2 * np.log(2)))
    gaussfunc = np.divide(1, sigma*np.sqrt(2*np.pi)) *
                np.exp(-1* np.divide(np.square(x - x0),
                2*sigma**2))
    return c*gaussfunc

def voigt(x, c, x0, FWHM_G, FWHM_L):
    "Returns the Voigt function centred on x0."
    lower = -100
    upper = 100
    nop = 8e3+1
    x_tofit = np.add(np.linspace(lower, upper, nop), x0)
    yl = lorentz(x_tofit, 1, x0, FWHM_L)
    yg = gauss(x_tofit, 1, x0, FWHM_G)
    vv = signal.fftconvolve(yl, yg, 'same')
    yv = c * vv * (upper - lower)/ (nop)
    fv = interp.interp1d(x_tofit, yv, bounds_error = 'False',
         fill_value = 1e7)
    yyv = fv(x)
    # return [x_tofit, yyv, yg, yl, yv]
    return yyv
```

The modified interference function

The interference function, given in equation 1.23, was modified to account for the disorder in the film. A Gaussian distribution of lattice parameters was introduced. The mathematical formula of the thus modified interference function is given in equation 2.17, and is defined below.

```
import numpy as np

def mod_interf(x, c, N, d0, dw, R):
    CuKalpha1 = 0.1540562    # nm
    xq = np.multiply((4*np.pi/CuKalpha1),np.sin(x/2 *np.pi/180))
    f = np.zeros(np.shape(x)[0])
    d_dist = []
    for m in range(R):
        d_sum = 0
        for n in range(int(round(N, 0))):
            d_act = d0 + dw * np.random.normal(0.0, 1, 1)
            d_sum = d_sum + d_act
            d_dist.append(d_act)
            f = f + np.exp(-1j * xq * d_sum)
    intensity = f * np.ma.conjugate(f)
    inten = c * intensity/np.max(intensity)
    return [np.array(np.real(inten)), d_dist]
```

E.1.3 Simulation of the high resolution data

In section 2.2.2 the standard resolution data was simulated from the fit of the high resolution data. Equation 2.20 describes this operation mathematically, and the script is given below.

```
import numpy as np
import scipy.signal as signal

def secondpeak(twotheta1):
    "Returns the angular position of the peak corresponding to
    the CuKalpha2 wavelength. Input and output are in degrees."
    CuKalpha1 = 0.1540562    # nm
```

```
    CuKalpha2 = 0.1544398    # nm
    sintheta2 = (CuKalpha2/CuKalpha1)*
                np.sin(twotheta1/2 *np.pi/180.)
    twotheta2 = 2*np.arcsin(sintheta2) *180/np.pi
    return twotheta2

def func(x):
    "Returns the high resolution fit of the Re(002) and the
    Al2O3(006) peaks."
    f, d_dist = mod_interf(x, 11300., 204, 2.230262, 2.8e-2)
    f = f + lorentz(x, 8.95277495, 41.6910329, 1.15831611e-02)
    return [f, d_dist]

def resolution(x, c, x0, FWHM):
    "Returns an approximation of the resolution of the standard
    XRD setup."
    f = lorentz(x, c, x0, FWHM)
    return f

# calculating the peak positions from the lattice parameter
twotheta = 2*np.arcsin(con.CuKalpha1/(2*2.23022)) *180/np.pi
twotheta2 = secondpeak(twotheta)
dtheta = twotheta2-twotheta

# high-resolution peak normalised
f_hr = func(xx)[0]
f_hr = f_hr/np.max(f_hr)

# standard resolution function normalised
f_res = resolution(xx, 1, twotheta, 0.04)
f_res = f_res/np.max(f_res)

# standard resolution peak from CuKalpha1
lr_func1 = signal.fftconvolve(f_hr,f_res,'same')*0.01
```

```
# standard resolution peak from CuKalpha2
lr_func2 = lr_func1/2
lr_func2 = np.interp(xx, xx+dtheta, lr_func2)

# simulated standard resolution peak
lr_func = lr_func1 + lr_func2
lr_func = 43000*lr_func/np.max(lr_func)
```

E.2 Functions for Mullins' thermal grooving

Below, the script that was used to describe the surface profile that develops during thermal grooving are presented. The theory was detailed in section 1.5.4, and it was applied to a rhenium film in section 2.3.

E.2.1 Evaporation-condenstation

```
import numpy as np
import math
import scipy.special

# Defining the integral errorfunction:
def ierfc(x):
    "Returns the integral errorfunction."
    r = np.multiply(x,scipy.special.erf(x)) +
        np.multiply(1./np.sqrt(np.pi),
        np.exp(-1*np.square(x))) - x
    return r

num_of_x = 50000
datax = np.linspace(0, 18000, num_of_x) # profile line
tt = [5., 30., 90., 120., 180.] *60     # time
beta = math.radians(5)                  # beta in radians
mm = np.tan(beta)

AA = 5e3
At2 = 2*np.sqrt(np.multiply(AA,tt))
```

```
# uu is the argument of the integral errorfunction
uu = np.zeros([num_of_x, np.shape(At2)[0]])
for i in range(np.shape(At2)[0]):
    uu[:,i] = np.divide(datax,At2[i])

# Calculating the integral errorfunction
ierrf = np.zeros([num_of_x, np.shape(At2)[0]])
for i in range(np.shape(At2)[0]):
    for j in range(num_of_x):
        ierrf[j,i] = ierfc(uu[j,i])

# Calculating the profile function
yy = np.zeros([num_of_x, np.shape(At2)[0]])
for i in range(np.shape(At2)[0]):
    yy[:,i] = np.multiply(-1 * mm * At2[i],ierrf[:,i])
```

E.2.2 Surface diffusion

```
import numpy as np
import math
import scipy.special

# Defining the a_n coefficients of the Z function
nn = 51 # number of elements in the a_n series
coef_an = np.zeros([nn]) # contains the a_n coefficients
coef_an[0] = -1/(np.sqrt(2)*math.gamma(5./4))
coef_an[1] = 1
coef_an[2] = -1/(np.sqrt(2**3)*math.gamma(3./4))
coef_an[3] = 0
for i in range(nn-4):
    coef_an[i+4] = coef_an[i]*(i-1)/(4*(i+1)*(i+2)*(i+3)*(i+4))

num_of_x = 50000
datax = np.linspace(0, 18000, num_of_x) # profile line
tt = [5., 30., 90., 120., 180.] *60     # time
beta = math.radians(5)                  # beta in radians
```

```
mm = np.tan(beta)

BB = 1e10
Bt = np.power(np.multiply(BB,tt),0.25)

# uu is the argument of the Z function
uu = np.zeros([num_of_x, np.shape(Bt)[0]])
print np.shape(uu)
for i in range(np.shape(Bt)[0]):
    uu[:,i] = np.divide(datax,Bt[i])

# Calculating the Z function
ZZ = np.zeros([num_of_x, np.shape(Bt)[0]])
for j in range(np.shape(Bt)[0]):
    for i in range(nn):
        aa_n = coef_an[i]
        uu_n = np.power(uu[:,j],i)
        ZZ[:,j] = ZZ[:,j] + np.multiply(aa_n,uu_n)

# Calculating the profile function
yy = np.zeros([num_of_x, np.shape(Bt)[0]])
for i in range(np.shape(Bt)[0]):
    yy[:,i] = np.multiply(mm*Bt[i],ZZ[:,i])
```

E.3 Preparation of the SQUID data

E.3.1 SQUIDbox function

The following function retrieves the parameters of the SQUID critical current measurements. These parameters are used to calculate the critical current.

```
import re

def SQUIDbox(meta_name, n):
    "Returns the parameters of the SQUID box.
    Inputs: file name, n - number of the line 'Periode du squid
    (SQUID Period)"
    meta  = open(meta_name)
```

```
    lines = meta.readlines()
    all   = lines[n:n+8]
    step_start = int(re.search(r'\d+', lines[n+1]).group())
    ramp_start = int(re.search(r'\d+', lines[n+2]).group())
    step_height = int(re.search(r'\d+', lines[n+3]).group())
    ramp_slope = int(re.search(r'\d+', lines[n+4]).group())
    threshold_volt = int(re.search(r'\d+', lines[n+5]).group())
    resistance = int(re.search(r'\d+', lines[n+6]).group())
    gain = int(re.search(r'\d+', lines[n+7]).group())
    meta.close
    return [all, step_start, ramp_start,
            step_height, ramp_slope, resistance]
```

Example:

```
In:
name = '2016-03-18_15-18-38_250p00mK.IcH_cleaned'
meta_name = name[0:len(name)-11] + 'meta'
parameters = SQUIDbox(meta_name, 61)
all the lines corresponding to the SQUID box

Out:
parameters[0]
['Periode du squid (SQUID Period): 255\r\n',
 'T du depart palier (step start time): 35\r\n',
 'T du depart rampe (ramp start time): 103\r\n',
 'hauteur du palier (step height): 8815\r\n',
 'pente de la rampe (slope of the ramp): 2047\r\n',
 'tension de seuil (threshold voltage): 1538\r\n',
 'Resistance [Ohm]: 50000\r\n',
 'gain du pre ampli (Amplifier gain): 1\r\n']
# all the lines corresponding to the SQUID box

parameters[1]
35       # T du depart palier (step start time)

parameters[2]
103      # T du depart rampe (ramp start time)
```

```
parameters[3]
8815      # hauteur du palier (step height)

parameters[4]
2047      # pente de la rampe (slope of the ramp)

parameters[5]
50000     # Resistance [Ohm]
```

E.3.2 Calculating the critical current from the SQUIDbox parameters

When measuring the critical current of a SQUID, the time it takes to reach it is recorded (ramp_stop). The following function calculates the critical current in Amperes using the parameters of the SQUID box and the ramp_stop data.

```
def bit_2_current(ramp_start, ramp_stop, pente, palier, res):
    "Returns the critical current in Amperes from the parameters
    of the SQUID box, and the measured ramp_stop data"
    R_cable = 180
    R_boite = 1000
    time = ramp_stop - ramp_start
    pente_amp = 25e-6*(2.236834e-3)*pente/(R_cable+R_boite+res)
    palier_amp = palier*2.4/(8.0*4096.0)/(R_cable+R_boite+res)
    ic = palier_amp + pente_amp * time
    return ic
```

Bibliography

[1] Edition Michael A. Nielsen and Isaac L. Chuang. *Quantum Computation and Quantum Information*. Cambridge University Press, 2011.

[2] Étienne Dumur. *A V-shape superconducting artificial atom for circuit quantum electrodynamics*. PhD thesis, Universite de Grenoble, 2015.

[3] Grigorij J. Grabovskij, Torben Peichl, Jürgen Lisenfeld, Georg Weiss, and Alexey V. Ustinov. Strain tuning of individual atomic tunneling systems detected by a superconducting qubit. *Science*, 338(6104):232–234, 2012.

[4] Seongshik Oh, Dustin A. Hite, K. Cicak, Kevin D. Osborn, Raymond W. Simmonds, Robert McDermott, Ken B. Cooper, Matthias Steffen, John M. Martinis, and David P. Pappas. Epitaxial growth of rhenium with sputtering. *Thin Solid Films*, 496(2):389 – 394, 2006.

[5] Paul B. Welander. Structural evolution of re (0001) thin films grown on nb (110) surfaces by molecular beam epitaxy. *Journal of Applied Physics*, 108(10):103508, 2010.

[6] A.R. Wildes, J. Mayer, and K. Theis-Bröhl. The growth and structure of epitaxial niobium on sapphire. *Thin Solid Films*, 401(1):7 – 34, 2001.

[7] Benjamin Delsol. *Elaboration et caractérisation de couches minces supraconductrices épitaxiées de rhénium sur saphir*. PhD thesis, Université de Grenoble, 2015.

[8] E. Dumur, B. Delsol, T. Weißl, B. Kung, W. Guichard, C. Hoarau, C. Naud, K. Hasselbach, O. Buisson, K. Ratter, and B. Gilles. Epitaxial rhenium microwave resonators. *IEEE Transactions on Applied Superconductivity*, 26(3):1–4, April 2016.

[9] C. Tonnoir, A. Kimouche, J. Coraux, L. Magaud, B. Delsol, B. Gilles, and C. Chapelier. Induced superconductivity in graphene grown on rhenium. *Phys. Rev. Lett.*, 111:246805, Dec 2013.

[10] W. Noddack, I. Tacke, and O. Berg. Die ekamangane. *Naturwissenschaften*, 13(26):567–574, 1925.

[11] J. Noddack and W. Noddack. Die herstellung von einem gram rhenium. *Zeitschrift für anorganische und allgemeine Chemie*, 183(1):353–375, 1929.

[12] M. A. Korzhinsky, S. I. Tkachenko, K. I. Shmulovich, Y. A. Taran, and G. S. Steinberg. Discovery of a pure rhenium mineral at kudriavy volcano. *Nature*, 369(6475):51–52, 05 1994.

[13] Lin-Gun Liu, Taro Takahashi, and William A. Bassett. Effect of pressure and temperature on the lattice parameters of rhenium. *Journal of Physics and Chemistry of Solids*, 31(6):1345 – 1351, 1970.

[14] G. Audi, O. Bersillon, J. Blachot, and A.H. Wapstra. The nubase evaluation of nuclear and decay properties. *Nuclear Physics A*, 729(1):3 – 128, 2003.

[15] N. N. Greenwood and A. Earnshaw. *Chemistry of the Elements*. Butterworth-Heinemann, 1997.

[16] J. G. Daunt and T. S. Smith. Superconductivity of rhenium. *Phys. Rev.*, 88:309–311, Oct 1952.

[17] E. Lerner, J. G. Daunt, and E. Maxwell. Magnetic properties of superconducting mo-re alloys. *Phys. Rev.*, 153:487–492, Jan 1967.

[18] V. S. Neshpor, V. I. Novikov, V. A. Noskin, and S. S. Shalyt. Superconductivity of some alloys of the tungsten-rhenium-carbon system. *Soviet Physics JETP*, 27:13, 1968.

[19] `http://jp-minerals.org/vesta/en/`.

[20] T. Huang, W. Parrish, N. Masciocchi, and P. Wang. *Adv. X-Ray Anal.*, 33:295, 1990.

[21] J. R. Arthur. Molecular beam epitaxy. *Surface Science*, 500(1–3):189 – 217, 2002.

[22] A. Y. Cho. 20 years of quantum cascade lasers (QCLs) anniversary workshop, Zurich, Switzerland. 2014.

[23] W. Patrick McCray. MBE deserves a place in the history books. *Nature Nanotechnology*, 2(5):259–261, 05 2007.

[24] R. J. Collins, F. W. Reynolds, and G. R. Stilwell. Electrical and optical properties of *GaSb* films. *Phys. Rev.*, 98:227–227, 1955.

[25] K. G. Günther. Aufdampfschichten aus halbleitenden III–V-verbindungen. *Naturwissenschaften*, 45(17):415–416, 1958.

[26] J. R. Arthur. Interaction of *Ga* and As_2 molecular beams with *GaAs* surfaces. *Journal of Applied Physics*, 39(8):4032–4034, 1968.

[27] J. R. Arthur and J. J. LePore. *GaAs*, *GaP*, and $GaAs_xP_{1-x}$ epitaxial films grown by molecular beam deposition. *Journal of Vacuum Science and Technology*, 6(4):545–548, 1969.

[28] A. Y. Cho. Morphology of epitaxial growth of *GaAs* by a molecular beam method: The observation of surface structures. *Journal of Applied Physics*, 41(7):2780–2786, 1970.

[29] A. Y. Cho. *GaAs* epitaxy by a molecular beam method: Observations of surface structure on the (*001*) face. *Journal of Applied Physics*, 42(5):2074–2081, 1971.

[30] D. C. Tsui, H. L. Stormer, and A. C. Gossard. Two-dimensional magnetotransport in the extreme quantum limit. *Phys. Rev. Lett.*, 48:1559–1562, 1982.

[31] F. Capasso. Band–gap engineering via graded gap, superlattice, and periodic doping structures: Applications to novel photodetectors and other devices. *Journal of Vacuum Science and Technology B*, 1(2):457–461, 1983.

[32] J. Faist, F. Capasso, D. L. Sivco, C. Sirtori, A. L. Hutchinson, and A. Y. Cho. Quantum cascade laser. *Science*, 264(5158):553–556, 1994.

[33] L. Goldstein, F. Glas, J. Y. Marzin, M. N. Charasse, and G. Le Roux. Growth by molecular beam epitaxy and characterization of $InAs/GaAs$ strained–layer superlattices. *Applied Physics Letters*, 47(10):1099–1101, 1985.

[34] N. N. Ledentsov, V.M. Ustinov, A. Y. Egorov, A. E. Zhukov, M. V. Maksimov, I. G. Tabatadze, and P.S. Kop'ev. Optical properties of heterostructures with $InGaAs - GaAs$ quantum clusters. *Semiconductors*, 28:832–834, 1994.

[35] A. Fert. The origin, development and future of spintronics, Nobel lecture. 2007.

[36] P. A. Grünberg. From spinwaves to giant magnetoresistance (GMR) and beyond, Nobel lecture. 2007.

[37] Mohamed Henini, editor. *Molecular beam epitaxy: from research to mass production.* Elsevier, 2013.

[38] John F. Moulder, William F Stickle, Peter E. Sobol, and Kenneth D. Bomben. *Handbook of X-ray photoelectron spectroscopy.* Perkin-Elmer Corporation.

[39] J. Sólyom. *Fundamentals of the Physics of Solids*, volume I. Structure and Dynamics. Springer-Verlag, first edition, 2009.

[40] Ayahiko Ichimiya and Philip I. Cohen. *Reflection high energy electron diffraction.* Cambridge university Press, 1st edition, 2004.

[41] *Scanning probe microscopy training notebook.* Digital Instruments, Veeco Metrology Group, 2000.

[42] `http://gwyddion.net`.

[43] J. Als-Nielsen and D. McMorrow. *Elements of Modern X-ray Physics.* Wiley, 2nd edition, 2011.

[44] M. A. Herman and H. Sitter. *Molecular beam epitaxy: Fundamentals and current status.* Springer-Verlag, 1989.

[45] D. Hull and D. J. Bacon. *Introduction to dislocations.* Butterworth-Heinemann, 5th edition, 2011.

[46] L. B. Freund and S. Suresh. *Thin film materials: stress, defect formation and surface evolution.* Cambridge University Press, 1st edition, 2003.

[47] A. Pimpinelli and J. Villain. *Physics of crystal growth.* Cambridge University Press, 1st edition, 1998.

[48] W. K. Burton, N. Cabrera, and F. C. Frank. The growth of crystals and the equilibrium structure of their surfaces. *Philosophical Transactions of the Royal Society of London A: Mathematical, Physical and Engineering Sciences*, 243(866):299–358, 1951.

[49] W. W. Mullins. Theory of thermal grooving. *Journal of Applied Physics*, 28(3):333–339, 1957.

[50] M. Yoshimoto, T. Maeda, T. Ohnishi, H. Koinuma, O. Ishiyama, M. Shinohara, M. Kubo, R. Miura, and A. Miyamoto. Atomic scale formation of ultrasmooth surfaces on sapphire substrates for high quality thin film fabrication. *Applied Physics Letters*, 67(18):2615–2617, 1995.

[51] J.R. Heffelfinger, M.W. Bench, and C.B. Carter. Steps and the structure of the (*0001*) α–alumina surface. *Surface Science*, 370(1):L168 – L172, 1997.

[52] J. R. Heffelfinger and C. B. Carter. Mechanisms of surface faceting and coarsening. *Surface Science*, 389(1–3):188 – 200, 1997.

[53] L. P. Van, O. Kurnosikov, and J. Cousty. Evolution of steps on vicinal (*0001*) surfaces of α–alumina. *Surface Science*, 411(3):263 – 271, 1998.

[54] P. R. Ribič and G. Gvido Bratina. Behavior of the (*0001*) surface of sapphire upon high-temperature annealing. *Surface Science*, 601(1):44 – 49, 2007.

[55] F. Cuccureddu, S. Murphy, I.V. Shvets, M. Porcu, H.W. Zandbergen, N.S. Sidorov, and S.I. Bozhko. Surface morphology of c−plane sapphire (α–alumina) produced by high temperature anneal. *Surface Science*, 604(15–16):1294 – 1299, 2010.

[56] X.-G. Wang, A. Chaka, and M. Scheffler. Effect of the environment on $\alpha - Al_2O_3$ (*0001*) surface structures. *Phys. Rev. Lett.*, 84:3650–3653, 2000.

[57] C. Scheu. Manipulating bonding at a $Cu/(0001)\alpha - Al_2O_3$ interface by different substrate cleaning processes. *Interface Science*, 12(1):127–134, 2004.

[58] P. J. Eng, T. P. Trainor, G. E. Brown Jr., G. A. Waychunas, M. Newville, S. R. Sutton, and M. L. Rivers. Structure of the hydrated $\alpha - Al_2O_3$ (*0001*) surface. *Science*, 288(5468):1029–1033, 2000.

[59] S. H. Oh, C. Scheu, T. Wagner, and M. Rühle. Control of bonding and epitaxy at copper/sapphire interface. *Applied Physics Letters*, 91(14), 2007.

[60] S. Neretina, R. A. Hughes, J. F. Britten, N. V. Sochinskii, J. S. Preston, and P. Mascher. The role of substrate surface termination in the deposition of (*111*) *CdTe* on (*0001*) sapphire. *Applied Physics A*, 96(2):429–433, 2009.

[61] C.F. Walters, K.F. McCarty, E.A. Soares, and M.A. Van Hove. The surface structure of $\alpha - Al_2O_3$ determined by low–energy electron diffraction: aluminum termination and evidence for anomolously large thermal vibrations. *Surface Science*, 464(2–3):L732 – L738, 2000.

[62] T Toofan and P. R. Watson. The termination of the $\alpha - Al_2O_3$ (0001) surface: a LEED crystallography determination. *Surface Science*, 401(2):162 – 172, 1998.

[63] H. Hertz. *Ann. Phys.*, 17:177, 1882.

[64] David R. Lide, editor. *CRC Handbook of Chemistry and Physics*. CRC Press, 84 edition, 2004.

[65] Carl L. Yaws, editor. *Handbook of Vapor Pressure*, volume 4: Inorganic compounds and elements. Gulf Publishing Company, 1995.

[66] E.R. Plante and R. Szwarc. Vapor pressure and heat of sublimation of rhenium. *J. Res. Nat. Bur. Stand.*, 70A, 03 1966.

[67] Murli H. Manghnani, Keith Katahara, and Edward S. Fisher. Ultrasonic equation of state of rhenium. *Phys. Rev. B*, 9:1421–1431, Feb 1974.

[68] Touloukian Y. S., Kirby R. K., Taylor R. E., and P. D. Desai. *Thermophysical Properties of Matter*, volume 12. Thermal Expansion: Metallic Elements and Alloys. Defense Technical Information Center, 1st edition, 1975.

[69] Touloukian Y. S., Kirby R. K., Taylor R. E., and P. D. Desai. *Thermophysical Properties of Matter*, volume 13. Thermal Expansion; Nonmetallic Solids. Defense Technical Information Center, 1st edition, 1977.

[70] Mario Birkholz. *Thin film analysis by X-ray Scattering*. Wiley-VCH, 2005.

[71] G.K Williamson and W.H Hall. X-ray line broadening from filed aluminium and wolfram. *Acta Metallurgica*, 1(1):22 – 31, 1953.

[72] B. E. Warren and B. L. Averbach. The separation of coldâĂŘwork distortion and particle size broadening in xâĂŘray patterns. *Journal of Applied Physics*, 23(4):497–497, 1952.

[73] Th. H. de Keijser, J. I. Langford, E. J. Mittemeijer, and A. B. P. Vogels. Use of the voigt function in a single-line method for the analysis of x-ray diffraction line broadening. *J. Appl. Cryst.*, 15:308–314, 1982.

[74] P Scherrer. Bestimmung der größe und der inneren struktur von kolloidteilchen mittels röntgenstrahlen. *Nachrichten von der Gesellschaft der Wissenschaften zu Göttingen, Mathematisch-Physikalische Klasse*, 1918:98–100, 1918.

[75] V. Soleimanian and S. R. Aghdaee. Comparison methods of variance and line profile analysis for the evaluation of microstructures of materials. *Powder Diffraction*, 23(1):41–51, 003 2008.

[76] J.T. Goldstein and G. Ehrlich. Atom and cluster diffusion on re(0001). *Surface Science*, 443(1–2):105 – 115, 1999.

[77] W. R. Tyson and W. A. Miller. Surface free energies of solid metals: Estimation from liquid surface tension measurements. *Surface Science*, 62(1):267–276, 1977.

[78] F.R. de Boer, R. Boom, W.C.M. Mattens, A.R. Miedema, and A.K. Niessen. *Cohesion in Metals*. North-Holland, 1988.

[79] L. Vitos, A.V. Ruban, H.L. Skriver, and J. Kollár. The surface energy of metals. *Surface Science*, 411(1–2):186 – 202, 1998.

[80] John H. Lienhard IV and John H. Lienhard V. *A Heat Transfer Textbook*. Phlogiston Press, 3rd edition, January 2004.

[81] Touloukian Y. S., Kirby R. K., Taylor R. E., and P. D. Desai. *Thermophysical Properties of Matter*, volume 2. Thermal Conductivity, Nonmetallic Solids. Defense Technical Information Center, 1st edition, 1977.

[82] Edward D. Palik, editor. *Handbook of Optical Constants of Solids*. Academic Press, 1998.

[83] D. T. F. Marple. Spectral emissivity of rhenium. *J. Opt. Soc. Am.*, 46(7):490–494, Jul 1956.

[84] Yanina Kisler, Lenn C. Kupferberg, Gordon Mackenzie, and Chia M. Chen. Direct emissivity measurements of ir materials, 1999.

[85] A. M. Wittenberg. Total hemispherical emissivity of sapphire. *J. Opt. Soc. Am.*, 55(4):432–435, Apr 1965.

[86] Elena R. Dobrovinskaya, Leonid A. Lytvynov, and Valerian Pishchik. *Sapphire Material, Manufacturing, Applications*. Springer, 2009.

[87] Erik Lassner and Wolf-Dieter Schubert. *ner, Erik. Tungsten - Properties, Chemistry, Technology of the Element, Alloys, and Chemical Compounds*. Kluwer Academic / Plenum Publishers, 1999.

[88] D. van Delft. Little cup of helium, big science. *Physics Today*, 61:36, March 2008.

[89] H. Kamerlingh Onnes. *Commun. Phys. Lab. Univ. Leiden*, 120b, April 1911.

[90] D. van Delft and P. Kes. The discovery of superconductivity. *Physics Today*, 63:38, September 2010.

[91] H. Kamerlingh Onnes. *Commun. Phys. Lab. Univ. Leiden*, 133d, May 1913.

[92] H. Kamerlingh Onnes. *Comm. Phys. Lab. Univ. Leiden*, 139f, Feb 1914.

[93] W. Meissner and R. Ochsenfeld. Ein neuer effekt bei eintritt der supraleitfähigkeit. *Naturwissenschaften*, 21:787, November 1933.

[94] F. London and H. London. The electromagnetic equations of the supraconductor. *Proceedings of the Royal Society of London A: Mathematical, Physical and Engineering Sciences*, 149(866):71–88, 1935.

[95] Tinkham M. *Introduction to superconductivity.* Dover Publications, second edition, 1996.

[96] V. L. Ginzburg and L. D. Landau. *Zh. Eksp. Teor. Fiz.*, 20:1064, 1950.

[97] A. A. Abrikosov. *Zh. Eksp. Teor. Fiz.*, 32:1442, 1957.

[98] J. Bardeen, L. N. Cooper, and J. R. Schrieffer. Microscopic theory of superconductivity. *Phys. Rev.*, 106:162–164, Apr 1957.

[99] J. Bardeen, L. N. Cooper, and J. R. Schrieffer. Theory of superconductivity. *Phys. Rev.*, 108:1175–1204, Dec 1957.

[100] Leon N. Cooper. Bound electron pairs in a degenerate fermi gas. *Phys. Rev.*, 104:1189–1190, Nov 1956.

[101] L.D. Landau. *Zh. Eksp. Teor. Fiz.*, page 19, 1937.

[102] L. P. Gor'kov. *Zh. Eksp. Teor. Fiz.*, 36:1918, 1959.

[103] Emanuel Maxwell. Isotope effect in the superconductivity of mercury. *Phys. Rev.*, 78:477–477, May 1950.

[104] C. A. Reynolds, B. Serin, W. H. Wright, and L. B. Nesbitt. Superconductivity of isotopes of mercury. *Phys. Rev.*, 78:487–487, May 1950.

[105] H. Fröhlich. Theory of the superconducting state. i. the ground state at the absolute zero of temperature. *Phys. Rev.*, 79:845–856, Sep 1950.

[106] H Fröhlich. Isotope effect in superconductivity. *Proceedings of the Physical Society. Section A*, 63(7):778, 1950.

[107] J E Hirsch. Did herbert fröhlich predict or postdict the isotope effect in superconductors? *Physica Scripta*, 84(4):045705, 2011.

[108] P.W. Anderson. Theory of dirty superconductors. *Journal of Physics and Chemistry of Solids*, 11(1):26 – 30, 1959.

[109] B. G. Lazarev, A. I. Sudovtsev, and A. P. Smirnov. *Zh. Eksp. Teor. Fiz.*, 33:1059, 1958.

[110] B.T. Matthias, E.A. Wood, E. Corenzwit, and V.B. Bala. Superconductivity and electron concentration. *Journal of Physics and Chemistry of Solids*, 1(3):188 – 190, 1956.

[111] Bascom S. Deaver and William M. Fairbank. Experimental evidence for quantized flux in superconducting cylinders. *Phys. Rev. Lett.*, 7:43–46, Jul 1961.

[112] J. Sólyom. *Fundamentals of the Physics of Solids*, volume ll: Electronic Properties. Springer-Verlag, first edition, 2009.

[113] U. Essmann and H. Träuble. The direct observation of individual flux lines in type ii superconductors. *Physics Letters A*, 24(10):526 – 527, 1967.

[114] B.D. Josephson. Possible new effects in superconductive tunnelling. *Physics Letters*, 1(7):251 – 253, 1962.

[115] Zhao-Sheng Wang. *Superconducting properties of iron-based Ba-122 by transport measurements and scanning nano-SQUID microscopy.* PhD thesis, Université de Grenoble, 2012.

[116] K Hasselbach, C Veauvy, and D Mailly. Microsquid magnetometry and magnetic imaging. *Physica C: Superconductivity*, 332(1–4):140 – 147, 2000.

[117] `http://neel.cnrs.fr/IMG/pdf/Table-top_Helium_3_cryostat.pdf`.

[118] `https://en.wikipedia.org/wiki/Dilution_refrigerator`.

[119] P. Rai-Choudhury, editor. *Handbook of Microlithography, Micromachining, and Microfabrication.*, volume 1: Microlithography. Institution Of Engineering And Technology, 1997.

[120] Adam J. Schwartz, Mukul Kumar, Brent L. Adams, and David P. Field, editors. *Electron Backscatter Diffraction in Materials Science*. Springer, second edition, 2009.

[121] N. A. Tulina. Influence of purity on the magnetic properties of rhenium in the superconducting state. *Phys. Met. Metall.*, 50(4):62–68, 1980.

[122] E. Purushotham and N. Gopi Krishna. Mean square amplitudes of vibration and associated debye temperatures of rhenium, osmium and thallium. *Physica B: Condensed Matter*, 405(16):3308 – 3311, 2010.

[123] J. K. Hulm and B. B. Goodman. Superconducting properties of rhenium, ruthenium, and osmium. *Phys. Rev.*, 106:659–671, May 1957.

[124] N. E. Alekseevskii, Mikheeva M. N., and Tulina N. A. The superconducting properties of rhenium. *Soviet Physics JETP*, 25(4):575–579, October 1967.

[125] T. V. Kopetskii, M. M. Myshlyaev, N. I. Novochatskai, N. A. Tulina, and V. A. Yukhanov. Critical temperature of superconducting transition in plastically deformed rhenium single crystals. *physica status solidi (a)*, 15(1):307–314, 1973.

[126] I. N. Khlyustikov and A. I. Buzdin. Localized superconductivity of twin metal crystals. *Sov. Phys. Usp.*, 38:409–433, 1988.

[127] A. Ul Haq and O. Meyer. Electrical and superconducting properties of rhenium thin films. *Thin Solid Films*, 94(2):119 – 132, 1982.

[128] C. W. Chu, T. F. Smith, and W. E. Gardner. Study of fermi-surface topology changes in rhenium and dilute re solid solutions from T_c measurements at high pressure. *Phys. Rev. B*, 1:214–221, Jan 1970.

[129] L. F. Mattheiss. Band structure and fermi surface for rhenium. *Phys. Rev.*, 151:450–464, Nov 1966.

[130] Masaki Mito, Hideaki Matsui, Kazuki Tsuruta, Tomiko Yamaguchi, Kazuma Nakamura, Hiroyuki Deguchi, Naoki Shirakawa, Hiroki Adachi, Tohru Yamasaki, Hideaki Iwaoka, Yoshifumi Ikoma, and Zenji Horita. Large enhancement of superconducting

transition temperature in single-element superconducting rhenium by shear strain. 6:36337 EP –, 11 2016.

[131] N.A. Tulina. Point-contact spectroscopy of renium single crystal. *Solid State Communications*, 41(4):313 – 315, 1982.

[132] Wilfried Rabaud. *Courants permanents dans des anneaux mésoscopiques connectés.* PhD thesis, Université Joseph-Fourier, 2001.

[133] D. Hazra, J. R. Kirtley, and K. Hasselbach. Nano-superconducting quantum interference devices with suspended junctions. *Applied Physics Letters*, 104(15):152603, 2014.

[134] Danny Hykel. *Microscopie à micro-SQUID: étude de la coexistence de la supraconductivité et du ferromagnétisme dans le composé UCoGe.* PhD thesis, L'Université de Grenoble, 2011.

[135] R. B Dinner, A. P. Robinson, S. C. Wimbush, J. L. MacManus-Driscoll, and M. G. Blamire. Depairing critical current achieved in superconducting thin films with through-thickness arrays of artificial pinning centers. *Superconductor Science and Technology*, 24(5):055017, 2011.

[136] S. Nawaz, R. Arpaia, T. Bauch, and F. Lombardi. Approaching the theoretical depairing current in yba2cu3o7âĹŠx nanowires. *Physica C: Superconductivity*, 495:33 – 38, 2013.

[137] Ke Xu, Peigen Cao, and James R. Heath. Achieving the theoretical depairing current limit in superconducting nanomesh films. *Nano Letters*, 10(10):4206–4210, 2010. PMID: 20738113.

[138] M. B. Ketchen, M. Bhushan, S. B. Kaplan, and W. J. Gallagher. Low noise dc squids fabricated in nb-al/sub 2/o/sub 3/-nb trilayer technology. *IEEE Transactions on Magnetics*, 27(2):3005–3008, March 1991.

[139] Amit Finkler, Yehonathan Segev, Yuri Myasoedov, Michael L. Rappaport, Lior Ne'eman, Denis Vasyukov, Eli Zeldov, Martin E. Huber, Jens Martin, and Amir Yacoby. Self-aligned nanoscale squid on a tip. *Nano Letters*, 10(3):1046–1049, 2010. PMID: 20131810.

[140] L. Hao, J. C. Macfarlane, J. C. Gallop, D. Cox, J. Beyer, D. Drung, and T. Schurig. Measurement and noise performance of nano-superconducting-

quantum-interference devices fabricated by focused ion beam. *Applied Physics Letters*, 92(19):192507, 2008.

[141] D. Hazra, J. R. Kirtley, and K. Hasselbach. Nano-superconducting quantum interference devices with continuous read out at millikelvin temperatures. *Applied Physics Letters*, 103(9):093109, 2013.

[142] D. J. Hykel, Z. S. Wang, P. Castellazzi, T. Crozes, G. Shaw, K. Schuster, and K. Hasselbach. Microsquid force microscopy in a dilution refrigerator. *Journal of Low Temperature Physics*, 175(5):861–867, Jun 2014.

[143] D. Hazra, J. R. Kirtley, and K. Hasselbach. Retrapping current in bridge-type nano-squids. *Phys. Rev. Applied*, 4:024021, Aug 2015.

[144] J.M. Rodenburg. Ptychography and related diffractive imaging methods. volume 150 of *Advances in Imaging and Electron Physics*, pages 87 – 184. Elsevier, 2008.

[145] D. Gabor. A new microscopic principle. *Nature*, 161:777–778, May 1948.

[146] D. Gabor. Microscopy by reconstructed wave-fronts. *Proceedings of the Royal Society of London A: Mathematical, Physical and Engineering Sciences*, 197(1051):454–487, 1949.

[147] Maxime Dupraz. *Coherent X-ray diffraction applied to metal physics*. PhD thesis, Université Grenoble Alpes, 2015.

[148] Ian K. Robinson. Optimisation of coherent x-ray diffraction imaging at ultrabright synchrotron sources. *Zeitschrift für Kristallographie Supplements*, 27:27–35, February 2008.

[149] U. H. Wagner, A. Parsons, J. Rahomaki, U. Vogt, and C. Rau. Characterising the large coherence length at diamond's beamline i13l. *AIP Conference Proceedings*, 1741(1):050022, 2016.

[150] C. Rau, U. Wagner, and Z. Pešić. The imaging and coherence beamline i13 at diamond. *AIP Conference Proceedings*, 1365(1):132–135, 2011.

[151] M. Sutton, S. G. J. Mochrie, T. Greytak, S. E. Nagler, L. E. Berman, G. A. Held, and G. B. Stephenson. Observation of speckle by diffraction with coherent x-rays. *Nature*, 352(6336):608–610, 08 1991.

[152] W. Hoppe. Beugung im inhomogenen Primärstrahlwellenfeld. I. Prinzip einer Phasenmessung von Elektronenbeungungsinterferenzen. *Acta Crystallographica Section A*, 25(4):495–501, Jul 1969.

[153] W. Hoppe and G. Strube. Beugung in inhomogenen Primärstrahlenwellenfeld. II. Lichtoptische Analogieversuche zur Phasenmessung von Gitterinterferenzen. *Acta Crystallographica Section A*, 25(4):502–507, Jul 1969.

[154] W. Hoppe. Beugung im inhomogenen Primärstrahlwellenfeld. III. Amplituden- und Phasenbestimmung bei unperiodischen Objekten. *Acta Crystallographica Section A*, 25(4):508–514, Jul 1969.

[155] Oliver Bunk, Martin Dierolf, Søren Kynde, Ian Johnson, Othmar Marti, and Franz Pfeiffer. Influence of the overlap parameter on the convergence of the ptychographical iterative engine. *Ultramicroscopy*, 108(5):481 – 487, 2008.

[156] C. E. Shannon. Communication in the presence of noise. *Proceedings of the IRE*, 37(1):10–21, Jan 1949.

[157] D. Sayre. Some implications of a theorem due to Shannon. *Acta Crystallographica*, 5(6):843, Nov 1952.

[158] J. M. Rodenburg and H. M. L. Faulkner. A phase retrieval algorithm for shifting illumination. *Applied Physics Letters*, 85(20):4795–4797, 2004.

[159] Andrew M. Maiden and John M. Rodenburg. An improved ptychographical phase retrieval algorithm for diffractive imaging. *Ultramicroscopy*, 109(10):1256 – 1262, 2009.

[160] Pierre Thibault, Martin Dierolf, Oliver Bunk, Andreas Menzel, and Franz Pfeiffer. Probe retrieval in ptychographic coherent diffractive imaging. *Ultramicroscopy*, 109(4):338 – 343, 2009.

[161] Fucai Zhang, Isaac Peterson, Joan Vila-Comamala, Ana Diaz, Felisa Berenguer, Richard Bean, Bo Chen, Andreas Menzel, Ian K. Robinson, and John M. Rodenburg. Translation position determination in ptychographic coherent diffraction imaging. *Opt. Express*, 21(11):13592–13606, Jun 2013.

[162] Pierre Thibault and Andreas Menzel. Reconstructing state mixtures from diffraction measurements. *Nature*, 494(7435):68–71, 02 2013.

[163] Aaron Parsons. *Coherent Diffraction Imaging using a High Harmonic Source at 40 eV*. PhD thesis, University of Southampton, 2014.

[164] Laura Shemilt. *Coherent Diffraction Imaging and Ptychography of Human Metaphase Chromosomes*. PhD thesis, University College London, 2014.

[165] Sandra Stephan. *High-Resolution 3D Ptychography*. PhD thesis, Technischen Universität Dresden, 2013.

[166] Martin Johannes Dierolf. *Ptychographic X-ray Microscopy and Tomography*. PhD thesis, Technischen Universität München, 2015.

[167] Pierre Thibault. *Algorimethric methods in diffraction microscopy*. PhD thesis, Cornell University, 2007.

[168] Veit Elser. Phase retrieval by iterated projections. *J. Opt. Soc. Am. A*, 20(1):40–55, Jan 2003.

[169] Ian Robinson and Ross Harder. Coherent x-ray diffraction imaging of strain at the nanoscale. *Nat Mater*, 8(4):291–298, 04 2009.

[170] Satio Takagi. A dynamical theory of diffraction for a distorted crystal. *Journal of the Physical Society of Japan*, 26(5):1239–1253, 1969.

[171] P. Godard, G. Carbone, M. Allain, F. Mastropietro, G. Chen, L. Capello, A. Diaz, T. H. Metzger, J. Stangl, and V. Chamard. Three-dimensional high-resolution quantitative microscopy of extended crystals. 2:568 EP –, 11 2011.

[172] Stephan Hruszkewycz, Marc Allain, Martin Holt, Conal Murray, J Holt, P H. Fuoss, and Virginie Chamard. High resolution three dimensional structural microscopy by single angle bragg ptychography. 11 2016.

[173] Z D Pešić, A De Fanis, U Wagner, and C Rau. Experimental stations at i13 beamline at diamond light source. *Journal of Physics: Conference Series*, 425(18):182003, 2013.

[174] C. Rau, U. H. Wagner, J. Vila-Comamala, A. Bodey, A. Parson, M. García-Fernández, A. De Fanis, and Z. Pešić. Imaging in real and reciprocal space at the diamond beamline i13. *AIP Conference Proceedings*, 1696(1):020047, 2016.

[175] `https://physics.nist.gov/PhysRefData/FFast/html/form.html`.

[176] C. Rau, U. H. Wagner, J. Vila-Comamala, A. Bodey, A. Parson, M. García-Fernández, A. De Fanis, Z. Pešić, I. Zanette, and M. Zdora. Micro- and nano-imaging at the diamond beamline i13l-imaging and coherence. *AIP Conference Proceedings*, 1741(1):030008, 2016.

[177] Dmitry Dzhigaev, Tomaš Stankevič, Zhaoxia Bi, Sergey Lazarev, Max Rose, Anatoly Shabalin, Juliane Reinhardt, Anders Mikkelsen, Lars Samuelson, Gerald Falkenberg, Robert Feidenhans'l, and Ivan A. Vartanyants. X-ray bragg ptychography on a single InGaN/GaN core–shell nanowire. *ACS Nano*, March 2017. PMID: 28264155.

[178] Allison Yau, Wonsuk Cha, Matthew W. Kanan, G. Brian Stephenson, and Andrew Ulvestad. Bragg coherent diffractive imaging of single-grain defect dynamics in polycrystalline films. *Science*, 356(6339):739–742, 2017.

[179] S. O. Hruszkewycz, M. V. Holt, C. E. Murray, J. Bruley, J. Holt, A. Tripathi, O. G. Shpyrko, I. McNulty, M. J. Highland, and P. H. Fuoss. Quantitative nanoscale imaging of lattice distortions in epitaxial semiconductor heterostructures using nanofocused x-ray bragg projection ptychography. *Nano Letters*, 12(10):5148–5154, 2012. PMID: 22998744.

[180] Martin V. Holt, Stephan O. Hruszkewycz, Conal E. Murray, Judson R. Holt, Deborah M. Paskiewicz, and Paul H. Fuoss. Strain imaging of nanoscale semiconductor heterostructures with x-ray bragg projection ptychography. *Phys. Rev. Lett.*, 112:165502, Apr 2014.

[181] Jesse N. Clark Xiaojing Huang Ross Harder Nicolas Burdet, Xiaowen Shi and Ian Robinson. Bragg projection ptychography on niobium phase domains. *Phys. Rev. B*, Accepted, 2017.

[182] S. O. Hruszkewycz, M. J. Highland, M. V. Holt, Dongjin Kim, C. M. Folkman, Carol Thompson, A. Tripathi, G. B. Stephenson, Seungbum Hong, and P. H. Fuoss. Imaging local polarization in ferroelectric thin films by coherent x-ray bragg projection ptychography. *Phys. Rev. Lett.*, 110:177601, Apr 2013.

[183] Yukio Takahashi, Akihiro Suzuki, Shin Furutaku, Kazuto Yamauchi, Yoshiki Kohmura, and Tetsuya Ishikawa. Bragg x-ray ptychography of a silicon crystal: Visualization of the dislocation strain field and the production of a vortex beam. *Phys. Rev. B*, 87:121201, Mar 2013.

[184] http://ptycho.github.io/ptypy/.

[185] http://pynx.sourceforge.net.

[186] Vincent Favre-Nicolin, Johann Coraux, Marie-Ingrid Richard, and Hubert Renevier. Fast computation of scattering maps of nanostructures using graphical processing units. *Journal of Applied Crystallography*, 44(3):635–640, Jun 2011.